

The Effect of Oxygen in Sweet Corrosion of Carbon Steel for Enhanced Oil Recovery  
Applications

A dissertation presented to  
the faculty of  
the Russ College of Engineering and Technology of Ohio University

In partial fulfillment  
of the requirements for the degree  
Doctor of Philosophy

Nor Roslina Rosli

December 2015

© 2015 Nor Roslina Rosli. All Rights Reserved.

This dissertation titled  
The Effect of Oxygen in Sweet Corrosion of Carbon Steel for Enhanced Oil Recovery  
Applications

by

NOR ROSLINA ROSLI

has been approved for  
the Department of Chemical and Biomolecular Engineering  
and the Russ College of Engineering and Technology by

Srdjan Nesic

Professor of Chemical and Biomolecular Engineering

Dennis Irwin

Dean, Russ College of Engineering and Technology

## ABSTRACT

ROSLI, NOR ROSLINA, Ph.D., December 2015, Chemical Engineering

The Effect of Oxygen in Sweet Corrosion of Carbon Steel for Enhanced Oil Recovery

Applications

Director of Dissertation: Srdjan Nestic

The primary objective of this work is to investigate the corrosion behavior of carbon steel in simulated CO<sub>2</sub>-EOR environments when O<sub>2</sub> is present in the CO<sub>2</sub> supply. A preliminary study was first conducted at low pressure to investigate the effect of O<sub>2</sub> on the protectiveness of iron carbonate (FeCO<sub>3</sub>) corrosion product layers in mild steel CO<sub>2</sub> corrosion. Carbon steel (UNS G10180) samples were immersed in a CO<sub>2</sub> saturated 1 wt.% NaCl electrolyte for 2 days to facilitate formation of a protective FeCO<sub>3</sub> layer on the steel surface. Temperature and pH were maintained at 80°C and 6.6, then 1 ppm O<sub>2</sub> was introduced to the electrolyte. The impact of the oxidant(s) was studied after samples were exposed for one week to test conditions. Electrochemical measurements indicated increased corrosion rates over the first two days of O<sub>2</sub> exposure, with a decrease in corrosion rate thereafter due to corrosion product formation that conferred some degree of protection to the steel surface. When O<sub>2</sub> was introduced after carbonate formation, the corrosion rate did not increase. Although the final corrosion rates of all tests were relatively low (less than 0.2 mm/y), localized corrosion was observed. Surface analysis showed attack of iron carbonate crystals and formation of iron (III) oxides. This degradation of initially formed FeCO<sub>3</sub> occurred concurrently with the development of localized corrosion features as deep as 80 μm.

High pressure experiments were then conducted at CO<sub>2</sub>-EOR simulated downhole conditions. The effect of O<sub>2</sub> (4 vol. %) on the corrosion performance of mild steel (UNS G10180) in CO<sub>2</sub>-saturated brine was investigated using a 4-liter autoclave at two different temperatures (25 and 80°C) and pressures (40 and 90 bar). Experiments at 25°C are categorized as 'FeCO<sub>3</sub>-free' while experiments at 80°C are termed 'FeCO<sub>3</sub>-forming'. The work included electrochemical measurements, weight loss determination, and characterization of the corrosion products. Severe corrosion was observed on the steel specimen after 48 hours of exposure to the corrosive environments. Tests at FeCO<sub>3</sub>-forming conditions exhibited localized corrosion, while the FeCO<sub>3</sub>-free experiments displayed severe general corrosion. Corrosion prediction using Multicorp© software was performed and the output corrosion rate data were compared against experimental results. Reasonable correlation was observed with the experimental data in anoxic conditions.

## DEDICATION

*Elmira, Eshal and Fatin, my patient and understanding little girls.*

*and*

*Zafri, for your constant love and support through thick and thin.*

## ACKNOWLEDGMENTS

I wish to express my sincere gratitude to my supervisors, Professor Srdjan Nesic, Dr David Young, and Dr Yoon-Seok Choi, who have given support and encouragement to a student like me, who is loaded with family commitments. I wish to acknowledge the considerable contributions made by many of my colleagues at the Institute for Corrosion and Multiphase Technology (ICMT). Among them are Steve Upton, Cody Shafer, and Alexis Barxias who have spent substantial time and energy in helping me get my setup to work in proper order because the autoclave is never an easy equipment to work with. I humbly thank the Center for Electrochemical Engineering Research (CEER) for letting me utilize their X-ray diffraction and Raman spectroscopy instrumentation for specimen analyses. Special thanks have to go to my dissertation committee members Dr John Staser, Dr Michael Jensen, and Dr Dina López for their invaluable technical advice. Editorial help from Dr David Young, Dr Bert Pots and Dr Joseph Lee are much appreciated, and essential to the completion of this dissertation. I am grateful to the research team from PETRONAS, namely Muhammad Firdaus Suhor, Azmi Mohammed Nor, and Ahmad Zaki Abbas, for their help and feedback relating to high pressure sweet corrosion. Scholarship and financial support from the Ministry of Education, Malaysia has made it possible for me to complete my studies. Finally, a thank you to all the other members at the ICMT that are not mentioned, for all their feedback and support and making my graduate school years an unforgettable experience.

## TABLE OF CONTENTS

	Page
Abstract.....	3
Dedication.....	5
Acknowledgments.....	6
List of Tables .....	11
List of Figures.....	12
Chapter 1: Introduction.....	21
1.1    Background.....	21
1.1.1    Cost of Corrosion in the Oil and Gas Industry .....	21
1.1.2    Oxygen and Carbon Dioxide's Role in Corrosion.....	22
1.2    Layout of Dissertation.....	23
Chapter 2: Literature Review.....	24
2.1    CO <sub>2</sub> -Enhanced Oil Recovery (CO <sub>2</sub> -EOR) .....	24
2.2    Carbon Capture and Storage (CCS).....	27
2.3    CO <sub>2</sub> Corrosion.....	30
2.3.1    Water Chemistry .....	31
2.3.2    Electrochemistry .....	33
2.3.3    Factors Affecting CO <sub>2</sub> Corrosion Rate .....	34

	8
2.3.4 Corrosion Product Prediction using Pourbaix Diagrams .....	36
2.3.5 CO <sub>2</sub> Corrosion at EOR Conditions .....	38
2.4 Properties of CO <sub>2</sub> – O <sub>2</sub> Mixtures .....	41
2.5 Oxygen Corrosion of Steel.....	41
2.5.1 Iron Oxides.....	43
2.5.2 Effect of O <sub>2</sub> on CO <sub>2</sub> Corrosion .....	44
2.6 Chapter Summary .....	46
Chapter 3: Objectives and Hypotheses .....	47
3.1 Problem Statement and Research Gap.....	47
3.2 Objectives of the Study.....	47
3.3 Research Hypothesis.....	47
Chapter 4: Low Pressure Corrosion Experiments .....	51
4.1 Sample Material .....	52
4.2 Experimental Design.....	53
4.3 Electrochemical Measurements .....	59
4.4 Results and Discussions: FeCO <sub>3</sub> -Free Experiments .....	60
4.5 Results and Discussions: FeCO <sub>3</sub> -Forming Experiments.....	63
4.5.1 Test A: Baseline CO <sub>2</sub> Corrosion Experiment .....	64
4.5.2 Test B: O <sub>2</sub> Ingress from Day 2.....	70

	9
4.5.3 Test C: O <sub>2</sub> Ingress from Day 0.....	80
4.5.4 Results Summary .....	93
4.6 Proposed Corrosion Mechanism.....	96
4.7 Chapter Summary .....	101
Chapter 5: High Pressure Corrosion Tests.....	102
5.1 Introduction.....	102
5.2 Sample Material and Preparation.....	104
5.3 Experimental Set-up and Instrumentation .....	105
5.4 Measurements and Test Matrix.....	108
5.5 Results and Discussion .....	110
5.5.1 Experiment 1: 25°C, 40 bar pCO <sub>2</sub> , with and without 4% O <sub>2</sub> .....	110
5.5.2 Experiment 2: 25°C, 90 bar pCO <sub>2</sub> , with and without 4% O <sub>2</sub> .....	116
5.5.3 Experiment 3: 80°C, 40 bar pCO <sub>2</sub> , with and without 4% O <sub>2</sub> .....	121
5.5.4 Experiment 4: 80°C, 90 bar pCO <sub>2</sub> , with and without 4% O <sub>2</sub> .....	129
5.6 The Proposed Corrosion Mechanism.....	136
5.7 The Effect of Flow .....	139
5.8 Chapter Summary and Conclusions.....	149
Chapter 6: Modeling.....	151
6.1 Simulation at Low Pressure .....	151

	10
6.2 Simulation at High Pressure.....	154
6.2.1 Multicorp© High Pressure Simulation for Tests at 25°C .....	155
6.2.2 Multicorp© High Pressure Simulation for Tests at 80°C .....	161
6.2.3 Multicorp© Simulation on the Effect of Flow .....	164
6.3 Chapter Summary .....	168
Chapter 7: Conclusion and Recommendations .....	169
7.1 Overall Summary/Conclusion.....	169
7.2 Future Work/Recommendations .....	170
References.....	173
Appendix A: AES Analysis of Steel Specimen .....	183
Appendix B: Calculation of O <sub>2</sub> Content in Water from Orbisphere Data .....	184
Appendix C: Clarke Solution Treatment (ASTM G1-03) .....	187
Appendix D: Sample Calculation of Corrosion Rate from Weight Loss.....	188
Appendix E: Sample Calculation of Corrosion Rate from Polarisation Resistance .....	189
Appendix F: Predicted O <sub>2</sub> Solubility in Water .....	191
Appendix G: Sample calculation for Pitting Ratio Determination .....	196
Appendix H: Determination of O <sub>2</sub> Consumption from Weight Loss of Steel .....	197

## LIST OF TABLES

	Page
Table 1: Composition of CO <sub>2</sub> from Different Capture Processes [26]. .....	29
Table 2: Estimated CO <sub>2</sub> -O <sub>2</sub> Mixture Critical Properties from REFPROP9 Database .....	42
Table 3: Iron Oxides and their Characteristics [79]. .....	44
Table 4: Overview of O <sub>2</sub> -CO <sub>2</sub> Corrosion Tests in the Literature. ....	45
Table 5: Composition of Steel (Balance Fe). .....	53
Table 6: Test Matrix for Low Pressure Corrosion Test. ....	56
Table 7: Summary of Corrosion Rate Results. ....	94
Table 8: Test Matrix for High Pressure Corrosion Test. ....	110
Table 9: Results Summary of High Pressure Corrosion Experiments .....	149

## LIST OF FIGURES

	Page
Figure 1. Schematic of CO <sub>2</sub> -EOR with alternating water injection.....	25
Figure 2. Typical CO <sub>2</sub> and water injection well [5].....	26
Figure 3. CO <sub>2</sub> capture options in the electric power industry.....	28
Figure 4. Pourbaix diagram for Fe-O <sub>2</sub> -H <sub>2</sub> O system at 25°C.....	37
Figure 5. Pourbaix diagram of CO <sub>2</sub> -O <sub>2</sub> -H <sub>2</sub> O system generated using OLIAnalyzer 3.2..	38
Figure 6. Carbon dioxide phase diagram .....	39
Figure 7. Schematic for hypothesis at low pressure .....	49
Figure 8. Schematic of hypothesis at high pressure.....	49
Figure 9. Steel specimens for glass cell tests.....	52
Figure 10. Glass cell setup (Courtesy of Cody Shafer, ICMT) .....	54
Figure 11. Oxygen meter, Orbisphere 410.....	55
Figure 12. Different tests for FeCO <sub>3</sub> -forming experiments.....	57
Figure 13. Effect of O <sub>2</sub> on corrosion rates at FeCO <sub>3</sub> -free condition (pH 4, 25°C).....	61
Figure 14. Nyquist plots relative to the reference electrode (pH 4, 25°C) .....	62
Figure 15. Polarization curves versus Ag/AgCl reference electrode (pH 4, 25°C).....	63
Figure 16. LPR mean corrosion rates for Test A (Baseline CO <sub>2</sub> Corrosion, 80°C, pH 6.6, 0 ppm O <sub>2</sub> , 50 ppm initial Fe <sup>2+</sup> concentration).....	65
Figure 17. Mean corrosion potential for Test A (Baseline CO <sub>2</sub> Corrosion, 80°C, pH 6.6, 0 ppm O <sub>2</sub> , 50 ppm initial Fe <sup>2+</sup> concentration).....	65

Figure 18. Solution pH for Test A, (80°C, pH 6.6, 0 ppm O <sub>2</sub> , 50 ppm initial Fe <sup>2+</sup> concentration) .....	66
Figure 19. Total iron ion concentration in the solution for Test A (80°C, pH 6.6, 0 ppm O <sub>2</sub> , 50 ppm initial Fe <sup>2+</sup> concentration).....	67
Figure 20. SEM image and EDS spectra of sample for Test A (80°C, pH 6.6, 0 ppm O <sub>2</sub> , 50 ppm initial Fe <sup>2+</sup> concentration) .....	68
Figure 21. SEM image of steel surface for Test A after corrosion product removal.....	69
Figure 22. Cross-section view of steel specimen for Test A .....	69
Figure 23. LPR mean corrosion rate for Test B (O <sub>2</sub> introduced on Day 2).....	71
Figure 24. Mean corrosion potential for Test B (O <sub>2</sub> introduced on Day 2).....	71
Figure 25. Solution pH for Test B (O <sub>2</sub> introduced on Day 2).....	72
Figure 26. FeCO <sub>3</sub> crystals on steel surface at 24 h in Test B.....	73
Figure 27. FeCO <sub>3</sub> crystals on steel surface at 48 h before O <sub>2</sub> introduction in Test B.....	74
Figure 28. Oxide clusters on FeCO <sub>3</sub> layer at 168 h in Test B.....	74
Figure 29. SEM image and EDS spectra of sample at the end of Test B .....	75
Figure 30. Cross-section of the sample from Test B .....	76
Figure 31. X-ray diffraction of the specimen after 7 day immersion for Test B.....	77
Figure 32. SEM image of the bare steel surface from Test B.....	78
Figure 33. Surface profile of pits on specimen from Test B.....	79
Figure 34. Initial electrolyte color change from colorless to yellow to black in Test C...	80
Figure 35. Reddish brown precipitate at the bottom of the glass cell.....	81
Figure 36. LPR mean corrosion rate for Test C.....	82

	14
Figure 37. Mean corrosion potential for Test C.....	83
Figure 38. Bulk solution pH for Test C. ....	84
Figure 39. Total iron concentration in solution of Test C.....	84
Figure 40. Steel surface at the end of Day 2 in Test C. ....	85
Figure 41. Steel surface at the end of Day 4 in Test C. ....	86
Figure 42. Steel surface at the end of Day 6 in Test C. ....	86
Figure 43. Steel surface at the end of Day 8 in Test C. ....	87
Figure 44. SEM image and EDS spectra of sample recovered after 8 days in Test C.....	88
Figure 45. Imperfectly formed FeCO <sub>3</sub> crystals covered with iron oxides .....	88
Figure 46. X-ray diffraction of the specimen recovered after 7 days in Test C. ....	89
Figure 47. Raman spectra of specimen recovered after 7 days in Test C.....	90
Figure 48. Cross-section of specimen recovered after 7 days of Test C.....	90
Figure 49. Schematic of a tubercle based on a study described by Herro [68].....	91
Figure 50. SEM image of steel surface for Test C after corrosion product removal.....	92
Figure 51. Pit depth analysis of specimen recovered at the end of Test C. ....	93
Figure 52. Corrosion rates comparison of Tests A, B and C. ....	94
Figure 53. Corrosion potential of test A, B and C. ....	95
Figure 54. Comparison of test solution pH for Tests A, B and C.....	96
Figure 55. Proposed tuberculation mechanism in CO <sub>2</sub> corrosion with O <sub>2</sub> intrusion. ....	97
Figure 56. Cylindrical and flat steel specimens for high pressure experiments. ....	104
Figure 57. Dimensions of steel specimens used in the high pressure tests.....	105
Figure 58. 4-L stainless steel autoclave diagram (Courtesy of Cody Shafer, ICMT) ....	106

Figure 59. The 4-L autoclave in ICMT.....	107
Figure 60. Piping and instrumentation diagram of the autoclave setup.....	107
Figure 61. Boundary conditions of experiment in the CO <sub>2</sub> phase diagram .....	109
Figure 62. LPR corrosion rate with time for experiments at 25°C, 40 bar pCO <sub>2</sub> , with and without 4% O <sub>2</sub> .....	111
Figure 63. Weight loss corrosion rates compared to LPR time-integrated corrosion rates for experiments at 25°C, 40 bar pCO <sub>2</sub> , with and without 4% O <sub>2</sub> . .....	111
Figure 64. Corrosion potential for experiments at 25°C, 40 bar pCO <sub>2</sub> , with and without 4% O <sub>2</sub> .....	112
Figure 65. Bluish-green corrosion product on a recovered steel specimen for experiment at 25°C, 40 bar pCO <sub>2</sub> , with 4% O <sub>2</sub> .....	113
Figure 66. SEM and EDS analysis of steel surface at the end of 25°C, 40 bar pCO <sub>2</sub> , with and without 4% O <sub>2</sub> experiments. ....	113
Figure 67. Steel cross-sections at 25°C, 40 bar pCO <sub>2</sub> , with and without 4% O <sub>2</sub> .....	114
Figure 68. XRD analysis for specimen at 25°C, 40 bar pCO <sub>2</sub> , with 4% O <sub>2</sub> for 48 h. ....	115
Figure 69. Profilometry of specimen at 25°C, 40 bar pCO <sub>2</sub> , with 4% O <sub>2</sub> after 48 h. ....	115
Figure 70. LPR corrosion rate with time for experiments at 25°C, 90 bar pCO <sub>2</sub> , with and without 4% O <sub>2</sub> .....	116
Figure 71. Weight loss corrosion rates compared to LPR time-integrated corrosion rates for experiments at 25°C, 90 bar pCO <sub>2</sub> , with and without 4% O <sub>2</sub> . ....	117
Figure 72. Corrosion potential with time for experiments at 25°C, 90 bar pCO <sub>2</sub> , with and without 4% O <sub>2</sub> .....	118

Figure 73. SEM micrographs and EDS analysis of steel surface at the end of 25°C, 90 bar pCO <sub>2</sub> , with and without 4% O <sub>2</sub> experiments. ....	119
Figure 74. Steel cross-sections at the end of 25°C, 90 bar pCO <sub>2</sub> , with and without 4% O <sub>2</sub> tests. ....	120
Figure 75. XRD analysis for specimen at 25°C, 90 bar pCO <sub>2</sub> , with 4% O <sub>2</sub> , 48h. ....	120
Figure 76. Profilometry of steel specimen at at 25°C, 90 bar pCO <sub>2</sub> , with 4% O <sub>2</sub> , 48h ..	121
Figure 77. Corrosion rates of steel at 80°C and 40 bar CO <sub>2</sub> with and without O <sub>2</sub> .....	122
Figure 78. Corrosion potential of steel at 80°C and 40 bar CO <sub>2</sub> with and without O <sub>2</sub> . ..	123
Figure 79. Corrosion rates measured using weight loss technique compared with integrated LPR results for conditions with and without O <sub>2</sub> at 80°C, 40 bar CO <sub>2</sub> after 2 days of test. ....	124
Figure 80. Steel surface after being exposed to 80°C, 40 bar CO <sub>2</sub> , 4% O <sub>2</sub> in solution for 48 hours.....	125
Figure 81. Cross-sectional view of steel specimen for tests conditions at (a) 80°C, 40 bar pCO <sub>2</sub> , 1.7 bar O <sub>2</sub> and (b) 80°C, 40 bar pCO <sub>2</sub> .....	126
Figure 82. XRD analysis for specimen at the end of 80°C, 40 bar pCO <sub>2</sub> , with 4% O <sub>2</sub> experiment.....	127
Figure 83. Raman spectra at two different locations on the steel specimen (785 nm laser excitation energy at 50 mW laser power, 20 s integration time). ....	127
Figure 84. Surface profilometry of bare steel for test conditions 80°C, 40 bar pCO <sub>2</sub> , 1.7 bar O <sub>2</sub> .....	129
Figure 85. Corrosion rates of steel at 80°C and 90 bar CO <sub>2</sub> with and without O <sub>2</sub> .....	130

Figure 86. Corrosion rates measured using weight loss technique compared with integrated LPR results for conditions with and without O <sub>2</sub> at 80°C, 90 bar CO <sub>2</sub> after 2 days of test. ....	131
Figure 87. Corrosion potential of steel at 80°C and 90 bar CO <sub>2</sub> with and without O <sub>2</sub> ...	132
Figure 88. Steel samples after 2 days of immersion without (left) and with O <sub>2</sub> (right)..	132
Figure 89. Micrograph of steel surface at 80°C, 90 bar CO <sub>2</sub> in 1 wt% NaCl solution for 48 with and without the presence of 4% O <sub>2</sub> .....	133
Figure 90. Cross-section of steel at 80°C, 90 bar CO <sub>2</sub> in 1 wt% NaCl solution for 48 with and without the presence of 4% O <sub>2</sub> .....	134
Figure 91. Analysis of steel surface using XRD for the specimen recovered at the end of the 80°C, 90 bar pCO <sub>2</sub> , with 4% O <sub>2</sub> experiment.....	134
Figure 92. Hematite peaks detected using Raman spectroscopy with 532 nm laser excitation energy at 2 mW laser power, 20 s integration time.....	135
Figure 93. Surface profilometry of bare steel for test conditions 80°C, 90 bar pCO <sub>2</sub> , 1.7 bar O <sub>2</sub> . ....	135
Figure 94. Localized corrosion on steel surface as seen under SEM.....	136
Figure 95. Proposed corrosion mechanism at low temperature and high pCO <sub>2</sub> with O <sub>2</sub> ingress in a closed system. ....	137
Figure 96. Proposed corrosion mechanism at high temperature and high pCO <sub>2</sub> with O <sub>2</sub> ingress in a closed system. ....	138
Figure 97. Effect of 1000 rpm flow rotational speed on the corrosion rates in equivalent CO <sub>2</sub> systems. ....	140

Figure 98. Effect of 1000 rpm flow on the corrosion rates in equivalent CO <sub>2</sub> /O <sub>2</sub> systems. .....	140
Figure 99. Effect of flow and O <sub>2</sub> on weight loss corrosion rate. ....	141
Figure 100. Steel specimens at 80°C 90 bar CO <sub>2</sub> , 4% O <sub>2</sub> , and 1000 rpm speed. ....	142
Figure 101. SEM of steel surface at 80°C 90 bar CO <sub>2</sub> , 4% O <sub>2</sub> , and 1000 rpm speed.....	142
Figure 102. EDS of steel surface at 80°C, 90 bar CO <sub>2</sub> , 4% O <sub>2</sub> , and 1000 rpm rotational speed. ....	143
Figure 103. SEM of steel surface at 80°C 90 bar CO <sub>2</sub> , and 1000 rpm rotational speed.	144
Figure 104. EDS analysis of two points on the steel as labeled in the previous Figure.	144
Figure 105. Cross-sectional views of coupon comparing the effect of flow at 80°C and 90 bar CO <sub>2</sub> .....	145
Figure 106. Cross-sectional views of coupon comparing the effect of flow in CO <sub>2</sub> -O <sub>2</sub> system at 80°C, 90 bar CO <sub>2</sub> and 4% O <sub>2</sub> . ....	145
Figure 107. Surface profilometry of steel for experiment at 80°C, 90 bar CO <sub>2</sub> , 2 days, 1000 rpm .....	146
Figure 108. Surface profilometry of steel for experiment at 80°C, 90 bar CO <sub>2</sub> , 2 days, 4% O <sub>2</sub> , 1000 rpm.....	147
Figure 109. Surface profilometry of another specimen for experiment at 80°C, 90 bar CO <sub>2</sub> , 2 days, 4% O <sub>2</sub> , 1000 rpm .....	148
Figure 110. Comparison of corrosion rates between Freecorp© and experimental data at 25°C, 1 bar, pH 4.0, with and without 3 ppm O <sub>2</sub> .....	152

Figure 111. The effect of 3 ppm O <sub>2</sub> in CO <sub>2</sub> system at 25°C, 1 bar shown in Tafel plots using Freecorp©.....	152
Figure 112. Comparison of corrosion rates between Multicorp© and experimental data of test at 80°C, pH 6.6 and 0.5 bar CO <sub>2</sub> , with and without O <sub>2</sub> .....	154
Figure 113. Simulated surface pH and porosity at 80°C, pH 6.6, and 0.5 bar CO <sub>2</sub> .....	154
Figure 114. Comparison of simulated corrosion rate with experimental results for experiment at 40 bar CO <sub>2</sub> , 25°C, autogenous pH for 48 hours.....	156
Figure 115. Comparison of simulated corrosion rate with experimental results for experiment at 90 bar CO <sub>2</sub> , 25°C, autogenous pH for 48 hours.....	156
Figure 116. Predicted corrosion rates using Multicorp© at varying pressures at 25°C, autogenous pH for 2 days .....	157
Figure 117. Predicted corrosion rates using Multicorp© at varying pressures at 25°C, autogenous pH for 60 days .....	158
Figure 118. Simulated surface porosity at 25°C and autogenous pH for 60 days .....	159
Figure 119. Predicted surface pH at 25°C and autogenous solution pH for 60 days.....	160
Figure 120. Predicted bulk and surface pH at 25°C.....	160
Figure 121. Predicted corrosion rates using Multicorp© at varying pressures at 80°C, autogenous pH .....	161
Figure 122. Simulated surface porosity at 80°C and autogenous pH for 30 days .....	162
Figure 123. Predicted surface pH at 80°C and autogenous solution pH for 30 days.....	163
Figure 124. Predicted bulk and surface pH using Multicorp©.....	163

Figure 125. Simulated corrosion rate at varying flow velocities for non-FeCO <sub>3</sub> forming condition (25°C, 90 bar CO <sub>2</sub> , autogenous pH, 60 days).....	165
Figure 126. Simulated corrosion rate at varying flow velocities for FeCO <sub>3</sub> forming condition (80°C, 90 bar CO <sub>2</sub> , autogenous pH, 30 days).....	165
Figure 127. Evolution of simulated corrosion rate at varying flow velocities and non-FeCO <sub>3</sub> forming condition (25°C, 90 bar CO <sub>2</sub> , autogenous pH, 60 days) .....	166
Figure 128. Simulated surface porosity at various flow velocities at 25°C, 90 bar CO <sub>2</sub> , autogenous pH for 60 days .....	167
Figure 129. Simulated surface pH at various flow velocities at 25°C, 90 bar CO <sub>2</sub> and autogenous pH for 60 days .....	167
Figure 130. Predicted corrosion rate at various flow velocity at 80°C, 90 bar CO <sub>2</sub> , for 2 days at autogenous pH .....	168

## CHAPTER 1: INTRODUCTION

### 1.1 Background

Steel has been used since ancient times due to its durability and, as smelting methods developed, availability. Over time, metallurgical processes have also evolved, resulting in the production of steels with enhanced hardness, strength, ductility, and resistance to corrosion (stainless steel). Today, steel remains a material of choice in many industries, and is used in various physically and chemically harsh environments. Economic factors do often limit the use of high-end corrosion resistant alloy (CRA) steels in such environments. Therefore, carbon steel is generally the preferred and economic choice, but only feasible for aggressive environments if used in conjunction with appropriate mitigation strategies. This applies in particular to the oil and gas industry where massive amounts of steels are required for both downhole and surface facilities.

#### 1.1.1 Cost of Corrosion in the Oil and Gas Industry

In 2002, a study undertaken by NACE, and backed by the U.S. Federal Highway Administration, estimated the total cost of corrosion associated with oil and gas exploration and production in the United States to be \$1.4 billion annually. The cost of corrosion in gas and liquid transmission pipelines was determined to be much higher at \$7 billion [1]. Corrosion accounts for about 25% of the infrastructure failures in the oil and gas industry [2].

### 1.1.2 Oxygen and Carbon Dioxide's Role in Corrosion

Oxygen,  $O_2$ , the gas that is vital to life, is the main culprit for material failure by its reaction with steel in the presence of moisture, producing rust as corrosion product. Carbon dioxide,  $CO_2$ , generally accepted as the culprit behind global warming, also plays a major role in corrosion of carbon steel.  $CO_2$  is generally co-produced with oil and gas, or injected for enhanced oil recovery, causing internal corrosion in tubulars, pipelines, and other equipment. When  $CO_2$  gas dissolves in water, it produces an acidic solution that drives a type of corrosion called 'sweet corrosion'. Its corrosion product may provide a degree of protection against further deterioration of the steel, depending on, among other controlling factors, temperature and water chemistry. A mixture of  $O_2$  and  $CO_2$  dissolved in water may cause relatively severe corrosion due to a mixture of reactions and mechanisms; this is discussed in detail in the next chapter.

Since each case of corrosion has the potential to be unique, extensive and systematic investigations are essential. The mechanisms have to be fully understood in order to prevent and find mitigation strategies that act against the hazards of corrosion. Presently, there is limited understanding of corrosion that involves the mixture of two different corrosive gases, such as when  $O_2$  is a contaminant in a  $CO_2$ -containing environment. Addressing this gap is the key objective of the research described in this dissertation.

## 1.2 Layout of Dissertation

The work presented in this dissertation covers the investigation of CO<sub>2</sub> corrosion of steel with O<sub>2</sub> ingress for high pressure downhole conditions. The following chapters present the different aspects of this research work:

Chapter 2: Literature review. This chapter provides a detailed review of topics relevant to this research including CO<sub>2</sub>-EOR, CCS technology, CO<sub>2</sub> corrosion, and corrosion caused by O<sub>2</sub>.

Chapter 3: Hypotheses and Objectives. The goals and the proposed hypotheses of the effect of O<sub>2</sub> on CO<sub>2</sub> corrosion at CO<sub>2</sub>-EOR conditions are presented separately.

Chapter 4: Low Pressure Corrosion Tests. The details of the preliminary corrosion experiments that were conducted at atmospheric pressure conditions are discussed.

Chapter 5: High Pressure Corrosion Test. Experiments were conducted in a high pressure stainless steel vessel to simulate downhole conditions of an EOR field.

Chapter 6: Modeling. Results from experiments are compared to output from available in-house simulation software.

Chapter 7: Summary and Conclusion. The overall conclusions and recommendations of prospective work are presented.

## CHAPTER 2: LITERATURE REVIEW

This chapter addresses the connection between carbon dioxide (CO<sub>2</sub>) corrosion in the oil and gas industry relating to enhanced oil recovery (EOR) and carbon capture and storage (CCS). It is organized into several subtopics. The first part of the chapter provides an overview of CO<sub>2</sub> enhanced oil recovery (CO<sub>2</sub>-EOR). This is then followed by a section that describes related technology that is used to lessen global warming effects, *i.e.*, CCS. In each case, there is a risk of corrosion by CO<sub>2</sub> and oxygen (O<sub>2</sub>) particularly when anthropogenic sources of CO<sub>2</sub> are injected downhole. Theoretical descriptions of corrosion in such systems are then presented and discussed.

### 2.1 CO<sub>2</sub>-Enhanced Oil Recovery (CO<sub>2</sub>-EOR)

Since the 1940s, an increasing number of oil reservoirs around the world have been abandoned upon their depletion. A depleted, or matured, reservoir is a term coined for a reservoir that has typically undergone extensive oil production *via* conventional primary and secondary extraction techniques. Nevertheless, these matured reservoirs are not fully exhausted as they still contain as much as 50% of the original oil in place (OOIP), trapped within the host geologic formation [3]. The remaining trapped oil can be recovered by means of tertiary methods such as injection of high pressure carbon dioxide (CO<sub>2</sub>) into the reservoir, thereby extending field life. The technology referred to as CO<sub>2</sub>-EOR has been a method of choice since the 1970s. When the trapped oil in the reservoir rocks comes into contact with the injected high pressure CO<sub>2</sub>, it becomes less viscous and swells up, enabling it to permeate through the rocks into the oil wells. This method of oil

recovery, which was once considered uneconomic, became increasingly feasible as oil prices soared. A notable CO<sub>2</sub>-EOR example is the Scurry Area Canyon Reef Operators Committee (SACROC) unit in Kelly Snyder Field, Scurry County, Texas. The unit started its operations in 1948 using gas drive as its primary recovery method, followed by water-flooding, a secondary recovery technique, in 1954. In 1972, operations switched to a tertiary mode of oil recovery, CO<sub>2</sub> injection [4]–[6]. Its source of CO<sub>2</sub> was initially supplied from the Val Verde Basin gas field, and later to a more consistent CO<sub>2</sub> supply from McElmo Dome in Colorado [7], [8].

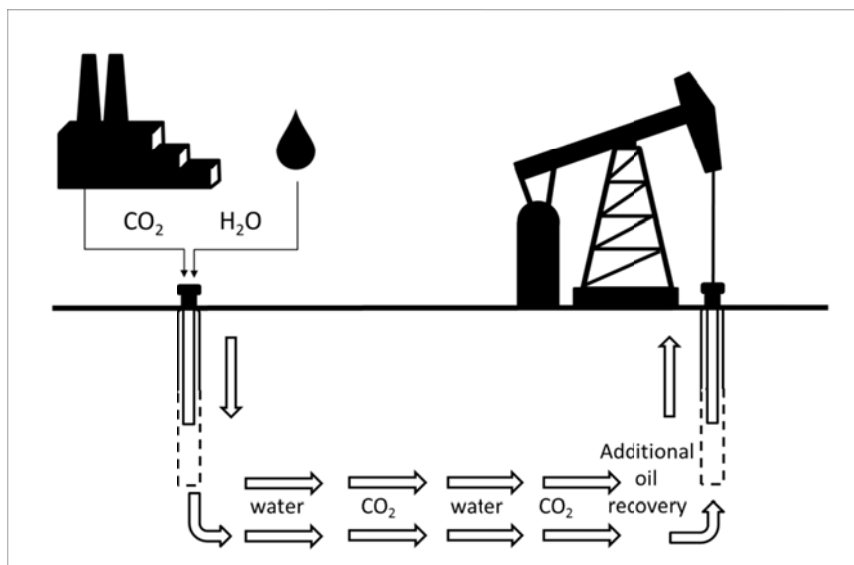


Figure 1. Schematic of CO<sub>2</sub>-EOR with alternating water injection.

The use of CO<sub>2</sub> injection, however, poses a new corrosion risk to the casing and tubing of injection wells. CO<sub>2</sub>, in combination with any aqueous phase, creates an acidic environment that can cause damage and failure to the tubing and casing material. This phenomenon is called CO<sub>2</sub> corrosion or ‘sweet corrosion’.

Like hydrocarbon transmission pipelines, the well casings and production tubing of injection wells are typically constructed from carbon steel. Carbon steel is durable, easily shaped, and can withstand high pressures. Due to its strength, tubing and casing walls can be thinner, thus reducing construction costs tremendously. This makes carbon steel a more economical choice compared to other materials such as corrosion resistant alloys (CRAs) and stainless steels [9]–[11]. Carbon steel in CO<sub>2</sub>-EOR applications needs to be consistently treated with corrosion inhibitor due to constant sequential exposures to CO<sub>2</sub> and water as shown in Figure 2. Alternating cycles of CO<sub>2</sub> and water injection is a usual scheme in CO<sub>2</sub>-EOR sites. This technique is called the water alternating gas (WAG) process. The water aids in moving the oil that was previously swollen by its contact with CO<sub>2</sub> [12].

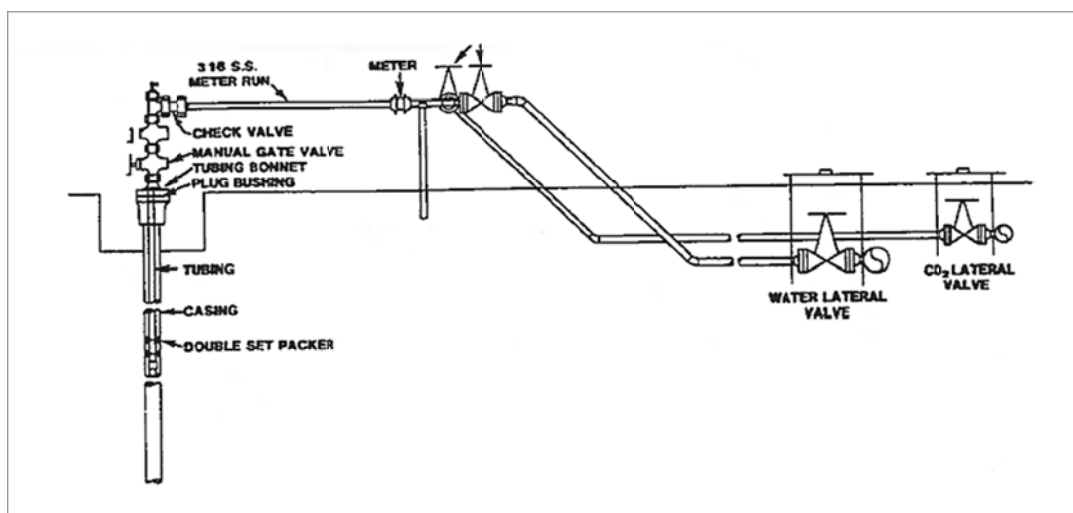


Figure 2. Typical CO<sub>2</sub> and water injection well [5]  
 (Reproduced with permission from NACE International, Houston, TX. All rights reserved. L.E. Newton, SACROC CO<sub>2</sub> project - Corrosion problems and solutions, in: Advanced CO<sub>2</sub> Corrosion, 1985. © NACE International 1985.)

## 2.2 Carbon Capture and Storage (CCS)

Emission of CO<sub>2</sub> into the atmosphere primarily stems from human activities, potentially causing climate change and contributing to global warming. Carbon Capture and Storage (CCS) involves a combination of technologies to combat this threat. CCS involves capturing CO<sub>2</sub> from large-scale industrial processes and injecting it into subterranean geologic formations either for sequestration or further utilization. Captured CO<sub>2</sub> could potentially be used to stimulate oil production from matured reservoirs, thus adding a revenue source to, for example, power plants. An example of a major CO<sub>2</sub>-EOR project is the IEA GHG Weyburn-Midale CO<sub>2</sub> Monitoring and Storage Project which is located in Saskatchewan, Canada [13], [14]. The CO<sub>2</sub> is supplied from a coal gasification plant in North Dakota and transported by over 300 miles of pipeline across the US-Canadian border. The project started in the year 2000 and is currently the world's largest CO<sub>2</sub>-EOR/CCS project. The Boundary Dam integrated CCS project, which was commissioned in October 2014, similarly supplies CO<sub>2</sub> to the Weyburn-Midale field but from a post-combustion CO<sub>2</sub> capture process.

The capture of CO<sub>2</sub> from power plants can be done either before or after the fuel combustion process *via* three different processes: pre-combustion, post-combustion or oxyfuel; these are illustrated in Figure 3. The CO<sub>2</sub> product from all three processes can contain impurities such as oxygen (O<sub>2</sub>), hydrogen sulfide (H<sub>2</sub>S), sulfur dioxide (SO<sub>2</sub>) and water. A review of the impurities in CO<sub>2</sub> supplies from a range of CCS technologies indicated that the concentration of O<sub>2</sub> can be as high as 3 vol.%, as Table 1 shows. This has the potential to lead to severe corrosion of steel pipes [15]–[17]. It has been reported

that corrosion rate increases proportionally with increasing dissolved  $O_2$  concentration [18]–[20]. This is because higher concentrations of  $O_2$  leads to formation of ferric oxides and suppresses the growth of protective ferrous carbonate corrosion product layers; thus,  $O_2$  increases the corrosion rate of carbon steel [21]. Performance of corrosion inhibitors decreases in the presence of  $O_2$ ; increased inhibitor dosage or special formulation is needed to combat corrosion [22], [23].

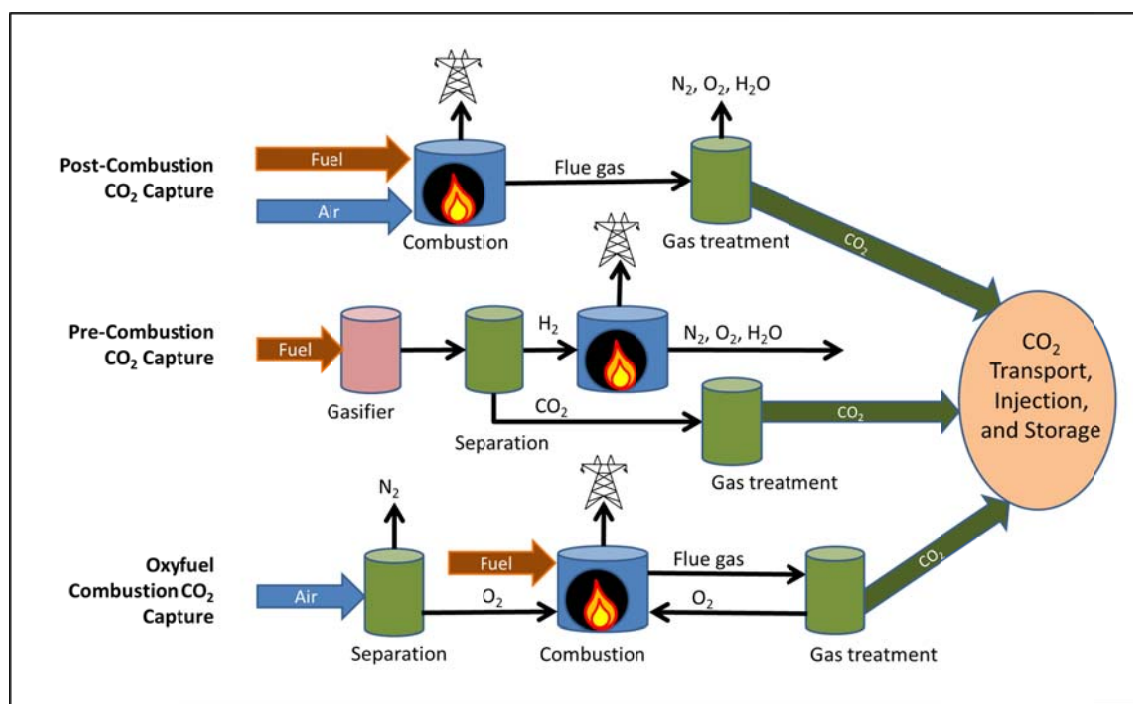


Figure 3. CO<sub>2</sub> capture options in the electric power industry.

Although techniques to eliminate the remaining impurities in the CO<sub>2</sub> gas are available, this is generally not economical. Further purification would include more sophisticated separation units and involve higher energy use and cooling water

consumption which further increase operating costs. Therefore, the current practice for CCS operators is to adhere to the minimum concentration of impurities allowable for transportation and sequestration as well as to comply with environmental and legal requirements [24], [25].

Table 1: Composition of CO<sub>2</sub> from Different Capture Processes [26].

<b>Component</b>	<b>Post combustion</b>	<b>Pre-combustion</b>	<b>Oxyfuel</b>
CO <sub>2</sub>	>99% v%	>95.6 v%	>90 v%
CH <sub>4</sub>	<100 ppmv	<350 ppmv	0
N <sub>2</sub>	<0.17 v%	<0.6%	<7 v%
H <sub>2</sub> S	Trace	<3.4%	Trace
C <sub>2</sub> <sup>+</sup> *	<100 ppmv	<0.01 v%	0
CO	<10 ppmv	<0.4 v%	Trace
O <sub>2</sub>	<0.01 v%	Trace	<3 v%
NO <sub>x</sub>	<50 ppmv	0	<0.25 v%
SO <sub>x</sub>	<10 ppmv	0	<2.5 v%
H <sub>2</sub>	Trace	<3 v%	Trace
Ar	Trace	<0.05 v%	<5 v%
S	N/A	N/A	N/A

\*Hydrocarbon with two or more carbon atoms.

Transportation of CO<sub>2</sub> from its sources to geological storage or EOR injection wells is typically done *via* miles of carbon steel pipeline at operating conditions between 75 and 200 bar CO<sub>2</sub> and temperatures up to 30°C [27]. CO<sub>2</sub> well casing and tubing, also consisting of steel elements, can be exposed to operating conditions up to 500 bar CO<sub>2</sub> and temperatures up to 150°C [27]. The extreme conditions make corrosion of steel by CO<sub>2</sub> inevitable and it is important to understand the mechanism of the corrosion process.

### 2.3 CO<sub>2</sub> Corrosion

Dry CO<sub>2</sub>, whether in gaseous, liquid or solid phase, is harmless to steel. However, when water is present, CO<sub>2</sub> dissolves therein to create a weak acidic solution called carbonic acid which is corrosive to steel. The overall reactive phenomenon between CO<sub>2</sub>, water, and steel is referred to as CO<sub>2</sub> corrosion.

An acid's ability to lose a hydrogen ion (H<sup>+</sup>), or proton, defines the strength of the acid. Strong acids, such as hydrochloric acid (HCl), completely dissociate in water, while weak acids such as carbonic acid (H<sub>2</sub>CO<sub>3</sub>) dissociate incompletely in water. Carbonic acid constantly provides a reservoir of hydrogen ions, which leads to a higher corrosion rate than strong acid solutions under the same pH condition. In other words, corrosion rates at the same pH conditions is higher due to the increased accessibility of hydrogen ions to the active steel surface [28].

### 2.3.1 Water Chemistry

The water chemistry of CO<sub>2</sub> corrosion can be described from the following reaction equations:



Reaction (1) is CO<sub>2</sub> dissolution in water, followed by hydration to form carbonic acid (2). Carbonic acid dissociates to form hydrogen ions and bicarbonate (3). The bicarbonate further dissociates to form carbonate ions and more hydrogen ions (4). When the carbonic acid reacts with steel, primarily Fe, it forms a thin layer of crystals called iron carbonate (FeCO<sub>3</sub>) on the steel surface, provided that the ion concentrations are saturated. The overall reaction can be expressed as follows:



Incorporating electrochemical and precipitation processes, this is the overall reaction involving CO<sub>2</sub>, water and steel in CO<sub>2</sub> corrosion. The electrochemical reactions themselves are discussed in the next section.

The layer of  $\text{FeCO}_3$ , also known as siderite, forms on the steel surface and confers some protection by slowing down the corrosion process as a result of mass transfer resistance set by the layer, blocking the steel surface and making it unavailable for corrosion. This has been studied by many researchers since the 1970's [29]–[34]. Solid  $\text{FeCO}_3$  forms when the concentrations of  $\text{Fe}^{2+}$  and  $\text{CO}_3^{2-}$  exceed the solubility limit according to the following reaction [35]:



The precipitation of  $\text{FeCO}_3$  also depends on its saturation, which is defined by:

$$S_{\text{FeCO}_3} = \frac{[\text{Fe}^{2+}][\text{CO}_3^{2-}]}{K_{sp}} \quad (7)$$

$\text{FeCO}_3$  will not form if the saturation value is less than 1. The solubility product constant,  $K_{sp}$ , is a function of temperature,  $T_k$ , and ionic strength,  $I$ , and can be calculated by [36]:

$$\log K_{sp} = -59.3498 - 0.41377T_k - \frac{2.1963}{T_k} + 24.5724 \log T_k + 2.518I^{0.5} - 0.657I \quad (8)$$

The degree of protection that the  $\text{FeCO}_3$  layer provides has been investigated in terms of its shear stress, adhesion properties, dissolution in flowing conditions, and other parameters [11], [37]–[39]. However, limited research has been done on the integrity of this film with respect to  $\text{O}_2$  exposure especially at high pressure.

### 2.3.2 Electrochemistry

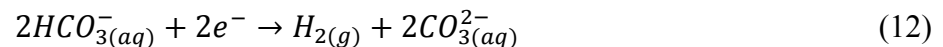
In an electrochemical reaction, there is a transfer of electrons at anodic and cathodic sites on the steel surface. In a mild steel corrosion process, iron loses two of its electrons when it is oxidized in the anodic reaction.



Ferrous ions,  $Fe^{2+}$ , migrates into the solution that is adjacent to the steel surface. In an acidic solution, hydrogen ions ( $H^{+}$ ) diffuse to the steel surface to receive the electrons released by the iron via the following reduction reaction:

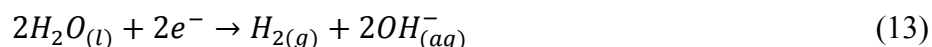


This reduction results in hydrogen gas evolution. Other reduction reactions involving carbonates have been proposed, called the ‘direct’ reduction of carbonic acid and bicarbonate ion, respectively [29], [40]:



This mechanism was later dismissed by others as to not actually take place [41]. The observed dominant cathodic reaction was the reduction of  $H^+$  that was provided by the dissociation of carbonic acid. This is referred to as the ‘buffering effect’.

Another cathodic reaction can occur due to the direct reduction of water.



This reaction is purely charge transfer controlled because water is present in abundance at the steel surface [42]. The reaction is too slow and occurs at potentials below -1000 mV [40], which is well below the typical corrosion potential seen in  $CO_2$  corrosion.

In this discussion of the electrochemistry of  $CO_2$  corrosion, water is assumed to be oxygen-free. In the occasion that  $O_2$  is present in the system, an additional  $O_2$  reduction reaction will occur; this is discussed later in this chapter.

### 2.3.3 Factors Affecting $CO_2$ Corrosion Rate

Many factors affect the rate of  $CO_2$  corrosion, which include, but are not limited to, temperature, pH, pressure, impurities, and salinity. Temperature affects gas solubility, reaction kinetics, and equilibrium constants. As temperature increases, the solubility of  $O_2$  and  $CO_2$  decreases, thus reducing their concentrations in solution. Nevertheless, corrosion rates generally increase with temperature as reaction rates increase more strongly with temperature than the solubility decreases [18], [43]. The phase identity and morphology of corrosion products also changes with temperatures [44]. At elevated

temperature, the corrosion product layer may become protective and reduce corrosion rates, depending on flow, pH, and ferrous iron concentration [35], [45], [46].

At low pH, say around pH 4, corrosion rate increases as temperature increases and protection by corrosion products will be less than for a higher pH; this is due to the nature of the corrosion product, which is generally porous and loose and does not offer any protection to the steel surface. Previous researchers indicated that corrosion rates at pH 4 increase rapidly from 25 to 90°C but increase at a slower rate between 90 and 125°C due to changes in the iron oxidation reaction [42]. At higher pH, the corrosion rate will generally drop at higher temperature due to the formation of a dense and compact corrosion product that can be very adherent to the steel surface and thus provides a form of self-mitigation against further corrosion. This physical barrier restricts the diffusion of aggressive species as well as prevents further dissolution of steel and leads to blocking of the steel surface, impeding iron dissolution [29], [46], [47].

Corrosion rate may increase slightly as salt concentration is increased up to 3 wt% due to a higher electrical conductivity of the solution. Further increase in the salt concentration would limit the solubility of gases such as O<sub>2</sub>, which then lowers the corrosion rate [18], [43]. Retarded anodic and cathodic reactions have been reported at 25 wt% NaCl concentration as well [48].

The increase in the partial pressure of CO<sub>2</sub> generally increases the overall corrosion rate of steel for conditions without a protective corrosion product layer; this is due to the increased carbonic acid concentration in the solution. Several different factors

influence the corrosion behavior at high pressure conditions, which will be discussed in detail later in this chapter.

The above factors not only affect the corrosion rate, but also determine the type of corrosion product that would evolve. Knowledge of chemical equilibria for the involved species and electrochemistry can be combined in the form of a plot called a Pourbaix diagram, and can be applied to predict the thermodynamically stable species, including the corrosion products.

#### 2.3.4 Corrosion Product Prediction using Pourbaix Diagrams

A Pourbaix diagram, or a potential-pH diagram, is a map that can be created by plotting equilibrium relationships in a plot of potential *versus* pH. The diagram can be used to predict the type of corrosion products that form at different pH values and potentials. The use of the Pourbaix diagram is the key in assisting in experimental design and interpretation of results. Electrochemical equilibrium transition lines follow from the Nernst equation, while chemical reaction transitions follow from chemical equilibria, (K values). The Pourbaix diagram for Fe-O<sub>2</sub>-H<sub>2</sub>O is given in Figure 4. The lines represent the equilibrium conditions when the activities of species are equal across the line. Various computer software options exist to produce such diagrams, an example is shown in Figure 5. Based on these two diagrams, iron will not corrode and stays in the form of Fe when the potential is very low due to the high availability of electrons. Increase in potential would lead to dissolution of iron into Fe<sup>2+</sup> at low pH values, or precipitate as oxides of iron at higher pH values. The driving force for the evolution of a stable species

becomes enhanced as the combined pH and potential conditions move further away from each equilibrium line.

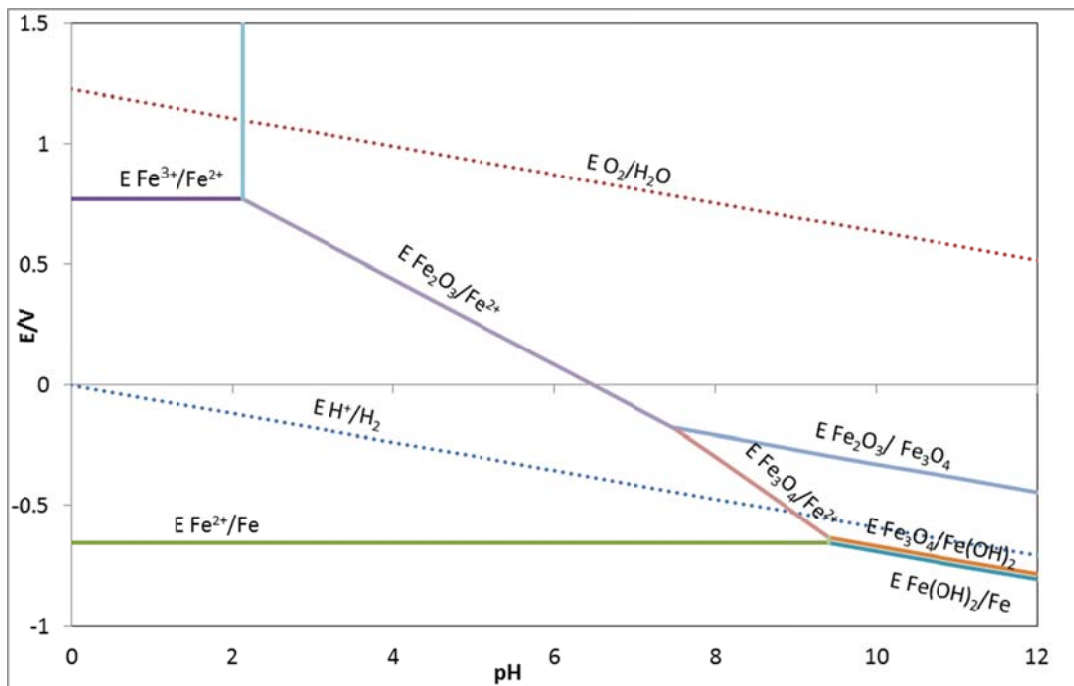


Figure 4. Pourbaix diagram for Fe-O<sub>2</sub>-H<sub>2</sub>O system at 25°C

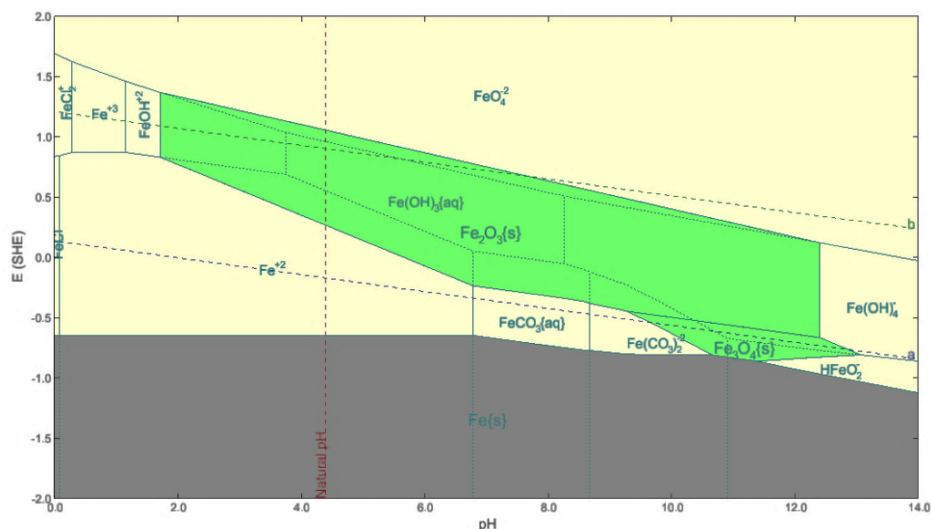


Figure 5. Pourbaix diagram of  $\text{CO}_2\text{-O}_2\text{-H}_2\text{O}$  system generated using OLIAnalyzer 3.2.

### 2.3.5 $\text{CO}_2$ Corrosion at EOR Conditions

Carbon dioxide can exist in different physical states depending on temperature and pressure, as shown in a phase diagram in Figure 6.  $\text{CO}_2$  becomes a supercritical fluid (SCF) at conditions above its critical pressure and critical temperature ( $P_c = 7.39$  MPa,  $T_c = 31^\circ\text{C}$ ) [49]. When  $\text{CO}_2$  is heated and compressed to these conditions, it will demonstrate unique characteristics in terms of compressibility, homogeneity, and its ability to continuously transform its properties from gas-like to liquid-like [50]. SCFs exhibit a liquid-like density with gas-like solvent capacity. The higher solubility of supercritical  $\text{CO}_2$  in water at elevated pressure increases the concentration of carbonic acid in the solution, thus causing corrosion. Besides the increased solubility, the mass transfer rate is also higher due to elevated diffusivity of the SCF. Wetting properties are also increased due to the low viscosities comparable to gases. All of these superior properties of SCF make a corrosion process kinetically faster [51].

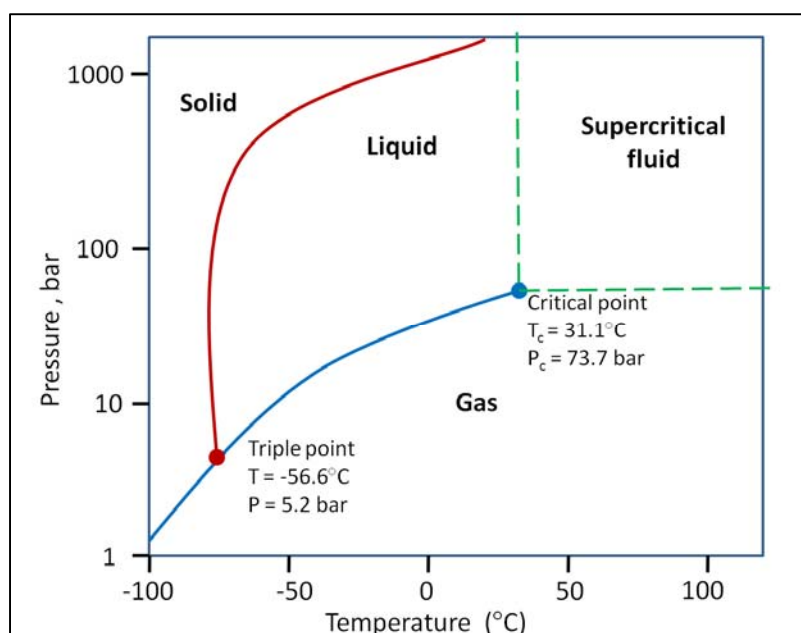


Figure 6. Carbon dioxide phase diagram

In EOR applications, the injected CO<sub>2</sub> mostly exists as a high pressure gas or in a supercritical state. For example, the CO<sub>2</sub> supply at the SACROC unit in Texas was delivered through a 220 mile, 16 inch pipeline at 165 bar in its supercritical state [52].

Since CO<sub>2</sub> at elevated pressure (including supercritical conditions) behaves rather differently than at atmospheric standard conditions, the corrosion behavior of steel will be affected. Corrosion studies in these regimes are currently limited and are preliminary. Studies have found that the corrosion mechanism and carbonate corrosion product formation at elevated pressure are similar to those at lower pressure [53], [54]. One study used electrochemical impedance to elucidate the similarities between corrosion mechanisms at high pressure and low pressure by comparing the shape of the impedance

loop [54]. Various magnitudes of corrosion rates at high pressure have been reported by research scholars with corrosion rates as high as 40 mm per year [55]–[57].

In ‘scale-free’ CO<sub>2</sub> corrosion, the corrosion rate of steel is proportional to the partial pressure of CO<sub>2</sub> up to about 10 bars. This is explained by the increased concentration of carbonic acid in the solution that leads to the increase in cathodic reactions in the system. This pattern changes as the CO<sub>2</sub> partial pressure increases beyond 10 bars, especially in a more alkaline environment when the corrosion rate starts to decline due to the formation of a protective FeCO<sub>3</sub> layer on the steel surface. At this condition, the increase in concentration of bicarbonate and carbonate ions causes supersaturation and precipitation to occur, thus forming a layer of FeCO<sub>3</sub> that provides protection against corrosion [31], [58]. Most corrosion prediction models are designed for low pressure applications. For partial pressures of CO<sub>2</sub> above say 10 bar, over prediction of the corrosion rate is to be expected. This is because these models do not take some factors into consideration such as the effect of water wetting and protectiveness of the corrosion product layer. Modifications can be done to these models by introducing particular factors, such as the fugacity coefficients, as well as using equilibrium constants that are valid at elevated pressures [59].

One study reported that UNS G10180 carbon steel experiences corrosive attack due to its exposure to water-saturated supercritical CO<sub>2</sub> [60]. In another study, it was reported that there existed a layer of cementite (iron carbide) with intergrown siderite (iron carbonate) at 80 bar CO<sub>2</sub> (supercritical) [59]. Researchers also observed that the

coverage of iron carbonate was more thorough with supercritical CO<sub>2</sub> than for liquid CO<sub>2</sub>, which also causes a significant reduction in corrosion rate of X65 steel [61].

While the physical and chemical properties of the corrosion product layer continue to be studied, the effect of external factors, such as O<sub>2</sub> intrusion on the corrosion product layer, has been given less attention.

#### 2.4 Properties of CO<sub>2</sub> – O<sub>2</sub> Mixtures

The physical properties of mixtures differ from pure substances. Table 2 shows the changes in mixture properties at different ratios of CO<sub>2</sub> and O<sub>2</sub> relating to supercriticality. Note that the critical point changes and mixtures are less dense at the critical point as the O<sub>2</sub> concentration increases. Physical property data of CO<sub>2</sub>-O<sub>2</sub> mixtures such as molar volume, viscosity, and diffusion coefficients is limited, especially at pressures above 1 bar [27], [62]. Phase diagrams of CO<sub>2</sub> mixtures relevant to CCS have been published where it has been observed that boiling and condensing behavior will change due to impurities. [63]. Vapor-liquid equilibria of CO<sub>2</sub> mixtures have been published in articles since the 1970s [64]–[66], however, the temperature and pressure range is still limited.

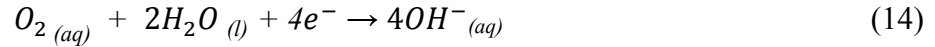
#### 2.5 Oxygen Corrosion of Steel

When iron is in contact with air and moisture, it oxidizes into what is generally known as rust. Iron and O<sub>2</sub> react with each other to form different oxides and oxyhydroxides, turning the metal surface brittle and resulting in spallation.

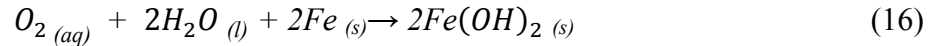
Table 2: Estimated CO<sub>2</sub>-O<sub>2</sub> Mixture Critical Properties from REFPROP9 Database

Mol fraction (%)		Estimated Critical Properties		
CO <sub>2</sub>	O <sub>2</sub>	T <sub>c</sub> (°C)	P <sub>c</sub> (bar)	Density (kg/m <sup>3</sup> )
100	0	30.978	73.773	467.6
95	5	27.083	80.918	466.36
90	10	22.812	87.377	465.09
80	20	13.137	97.968	462.47
70	30	1.953	105.28	459.72
60	40	-10.739	109.12	456.84
50	50	-24.939	109.35	453.82

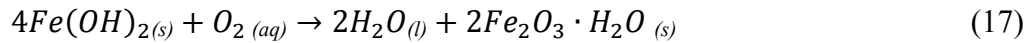
The study of corrosion of iron by O<sub>2</sub> has a history since the early 19<sup>th</sup> century. The anodic and cathodic reactions of oxygen with steel and water are as follows:



Electrons in the O<sub>2</sub> reduction process are supplied by the iron oxidation reaction. The overall reaction can be expressed as:



O<sub>2</sub> dissolves readily in water and when in excess, reacts with ferrous hydroxide to produce hydrated ferric oxide (brown rust).



The presence of  $O_2$  also causes other reactions to occur, forming various types of iron oxides.

The corrosion rate of iron generally increases as the concentration of dissolved  $O_2$  in water increases. Localized corrosion occurs when poor mass transport exists under deposits and crevices [67]. Tubercles are the typical morphology of the corrosion product observed on steel surfaces in the form of small, rounded, hollow protrusions [68]–[72]. Other factors such as water velocity, temperature, pH, and dissolved minerals affect the corrosion process [73].

### 2.5.1 Iron Oxides

Iron can commonly occur in ferrous (+2 oxidation state) or ferric (+3) forms. The ferric form generally has very low solubility [74]. Under oxidizing conditions, iron precipitates as ferric hydroxide. Typically, iron oxides have an octahedral structural unit in which Fe atoms are surrounded by six oxide ( $O^{2-}$ ) and/or hydroxide ( $OH^-$ ) anions. The  $O^{2-}$  and  $OH^-$  ions are arranged in layers that are either in a  $\alpha$ -phase or  $\gamma$ -phase. The  $\alpha$ -phase arrangement is hexagonally close-packed (*hcp*), whereas the  $\gamma$ -phase is cubic close-packed (*ccp*). For example, goethite ( $\alpha$ -FeOOH) and hematite ( $\alpha$ -Fe<sub>2</sub>O<sub>3</sub>) are in *hcp* form, while lepidocrocite ( $\gamma$ -FeOOH) and maghemite ( $\gamma$ -Fe<sub>2</sub>O<sub>3</sub>) are in *ccp* form [75]. There are 16 different iron oxide or oxyhydroxide phases that have been reported to exist in nature. Nine of the oxides have been reported to be detected on corrosion products of steel, namely goethite, hematite, lepidocrocite, maghemite, iron (II) hydroxide (Fe(OH)<sub>2</sub>), iron (III) hydroxide (Fe(OH)<sub>3</sub>), akaganeite ( $\beta$ -FeOOH), feroxyhite ( $\delta$ -FeOOH), and magnetite

(Fe<sub>3</sub>O<sub>4</sub>) [76]. The mechanism of iron oxide and oxyhydroxide formation on low alloy steel in aqueous solution has been studied by previous researchers [77], [78].

Pigment quality iron oxide crystals have been studied and characterized with different morphologies and sizes [79]. Table 3 summarizes the characteristics of the iron oxides in terms of their morphologies and typical crystal size.

Table 3: Iron Oxides and their Characteristics [79].

Compound (Pure)	Chemical formula	Morphology	Size (μm)
Goethite	α-FeOOH	Needle-like	<0.1
Maghemite	γ-Fe <sub>2</sub> O <sub>3</sub>	Pseudo-cubic	<1
Magnetite	Fe <sub>3</sub> O <sub>4</sub>	Pseudo-cubic	<0.1
Hematite	α-Fe <sub>2</sub> O <sub>3</sub>	Pseudo-cubic	<0.05

### 2.5.2 Effect of O<sub>2</sub> on CO<sub>2</sub> Corrosion

Reservoir injection processes, such as water-flooding and CO<sub>2</sub> -EOR, often inject O<sub>2</sub>-contaminated fluids into host formations, thus promoting O<sub>2</sub> corrosion with simultaneous sweet corrosion. O<sub>2</sub> is a strong oxidizer and is able to accelerate metal damage as the kinetics of O<sub>2</sub> reduction on metal are fast [80]. Many researchers have indicated that a trace amount of O<sub>2</sub> is enough to have a detrimental effect on CO<sub>2</sub> corrosion of mild steel [20], [81], [82]. Some have reported that low O<sub>2</sub> concentrations in CO<sub>2</sub> saturated aqueous solution caused iron carbonate to lose its protectiveness, thus increasing the corrosion rate [83]–[85]. The general corrosion rate tends to increase sharply in the first several hours of a test, which then drops to a steady state general

corrosion rate after about 20 hours of test time [81]. O<sub>2</sub> intrusion also accelerates corrosion in sour (H<sub>2</sub>S) systems [23]. CO<sub>2</sub> corrosion with O<sub>2</sub> intrusion is controlled by both mass and charge transfer, as demonstrated by the higher corrosion rate in highly turbulent systems than in a stagnant system [81]. Pits were observed in both stagnant and turbulent O<sub>2</sub>-CO<sub>2</sub> systems under a layer of red, loose, and porous iron oxide [69], [81]. It was further reported that deeper pits occurred in correlation with increasing O<sub>2</sub> concentration [81].

Table 4: Overview of O<sub>2</sub>-CO<sub>2</sub> Corrosion Tests in the Literature.

No.	pCO <sub>2</sub> , MPa	T, °C	H <sub>2</sub> O content	O <sub>2</sub> content	Steel type	Time, hours	Flow, rpm	CR, mm/y	Ref.
1	1	25		0.2 ppm 0.4 ppm 0.6 ppm 0.8 ppm 1.4 ppm	1018	24	0	0.86 0.99 1.14 1.45 2.06	[23]
2	8	35	100 g	3 vol%	304L 316L X42, X60	120	100	0.031 0.028 0.32 0.26	[20]
3	10	50	100 g	3 vol%	304L 316L X42 X60	120	100	0.032 0.042 0.99 0.93	[20]
4	8	50	sat	4 vol%	X65, 13Cr	24 120	0	19.3 14.1	[86], [87]
5	2.5	120	sat	0.5 MPa	N80	120	1 m/s	4.47	[88]
6	1	90	sat	0.05 MPa	N80	72	0	1.43	[82]
7	1	90	sat	0.05 MPa	N80	72	2 m/s	3.36	[82]
8	0.92	60	sat	5 vol%	3Cr	120	0	1.36	[89]
9	0.05	80	sat	1 ppm	1018	168	0	1.07	[90]
10	7.58	40	1000 ppmv	100 ppm	1010	5	0	2.3	[91]

In corrosion control, inhibitors lose their efficiency with increases in  $O_2$  concentration in  $CO_2$  environments [92]. Almost all corrosion inhibitors do not work well when  $O_2$  is present. Observed corrosion products were reported to be porous and non-protective. Still, limited investigations have been conducted to study the effect of  $O_2$  on sweet corrosion of steel at elevated pressure, including conditions where supercritical  $CO_2$  is present. Awareness and quantification of the amount of  $O_2$  ingress in a  $CO_2$ - $H_2O$  system is key to prevent potential catastrophic corrosion failures.

## 2.6 Chapter Summary

The discussion in this chapter covered the connection between  $O_2$  ingress in  $CO_2$  corrosion related to the oil and gas industry and carbon capture technology;  $CO_2$ -EOR was described. Discussion of  $CO_2$  corrosion covered the related electrochemical and chemical reactions, thermodynamics, and the effect of high pressure. Mechanisms relating to  $O_2$  corrosion were discussed, which included the different types of oxides that can form during the corrosion process. The effect of  $O_2$  ingress on  $CO_2$  corrosion was also discussed. Limited work has been done to investigate mechanisms relating to  $O_2$  ingress in high pressure  $CO_2$  corrosion. The intention of this dissertation is to expand knowledge within this research area. High pressure  $CO_2$  will simulate the conditions of  $CO_2$ -EOR fields. The presence of  $O_2$  will act as the impurity in the  $CO_2$  supply. The following chapters elaborate the methodology and research strategy that was applied to explore how  $O_2$  affects  $CO_2$  corrosion in high pressure systems.

## CHAPTER 3: OBJECTIVES AND HYPOTHESES

### 3.1 Problem Statement and Research Gap

Limited studies have thus far been conducted relating to establishing the mechanism of CO<sub>2</sub>-O<sub>2</sub> corrosion in both low and high pressure systems. In particular, how tuberculation and blistering of the corrosion product layer occurs is poorly understood. The research reported in this dissertation seeks to contribute to knowledge in this area.

### 3.2 Objectives of the Study

This project aims to investigate the corrosion behavior of carbon steel in CO<sub>2</sub>/O<sub>2</sub>/brine mixtures at ambient and simulated EOR conditions. A qualitative mechanistic model of the corrosion process will be described. This study is expected to provide knowledge and useful information beneficial for the future development of corrosion control in CO<sub>2</sub>/O<sub>2</sub>/brine systems at elevated pressure, particularly in the oil and gas industry.

The scope of this work includes electrochemical measurements, as well as surface analysis of corrosion products in order to characterize their morphologies, phase identities, and chemical properties.

### 3.3 Research Hypothesis

Dissolved O<sub>2</sub> in water is highly reactive and readily converts Fe<sup>2+</sup> to Fe<sup>3+</sup> ions, adversely impeding the formation of a protective layer of iron carbonate, FeCO<sub>3</sub>. Full

coverage of  $\text{FeCO}_3$  on a steel surface will be absent, thus exposing selective areas to corrosive species. Dissolution of already formed  $\text{FeCO}_3$  crystals may also occur, weakening the protective layer, leading to localized corrosion at crystal boundaries. This is illustrated in Figure 7, which shows a thin layer of  $\text{FeCO}_3$  in  $\text{CO}_2$ -saturated solution that is damaged and/or dissolved in the presence of  $\text{O}_2$ . Researchers [69], [81] have reported that  $\text{O}_2$  causes localized corrosion and have also reported morphologies corresponding to tubercles in their ambient pressure glass cell tests.

Iron carbonate layers on steel were reported to be thicker at high  $\text{CO}_2$  partial pressures [61]. It is speculated that the thickness of this layer will decrease in the presence of  $\text{O}_2$  since it oxidizes  $\text{Fe}^{2+}$  into  $\text{Fe}^{3+}$  ions, thereby impeding the formation of  $\text{FeCO}_3$ . Produced  $\text{Fe}^{3+}$  will result in formation of loose iron oxide,  $\text{Fe}_x\text{O}_y$ , particles. This is illustrated in Figure 8 where the thicker layer of  $\text{FeCO}_3$  is also dissolved in the presence of  $\text{O}_2$ . The dissolution of  $\text{FeCO}_3$  weakens the protective layer, especially at its crystal grain boundaries resulting in penetration of  $\text{Fe}_x\text{O}_y$  deeper into the steel in association with creation of deeper pits.

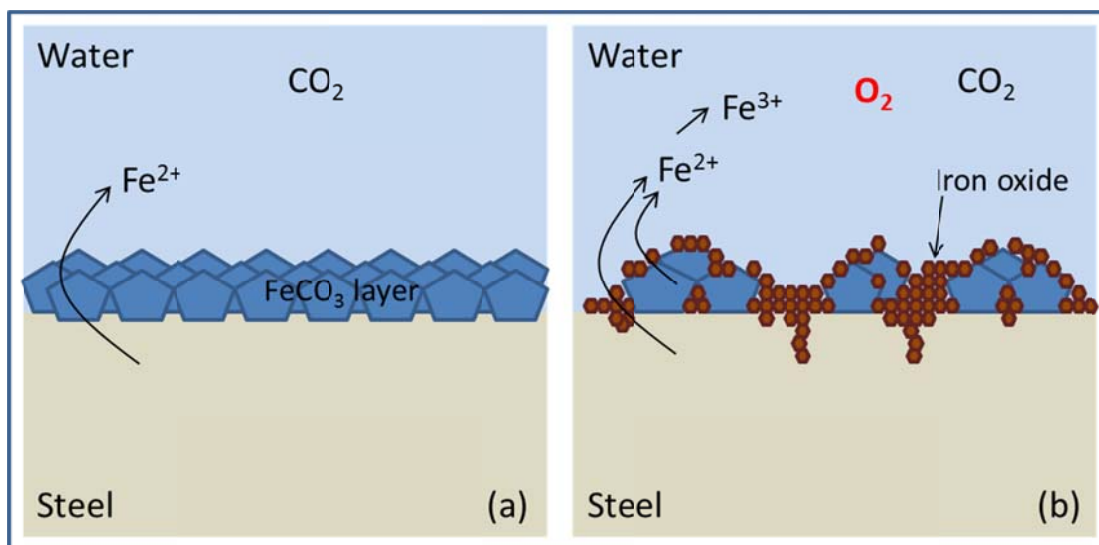


Figure 7. Schematic for hypothesis at low pressure

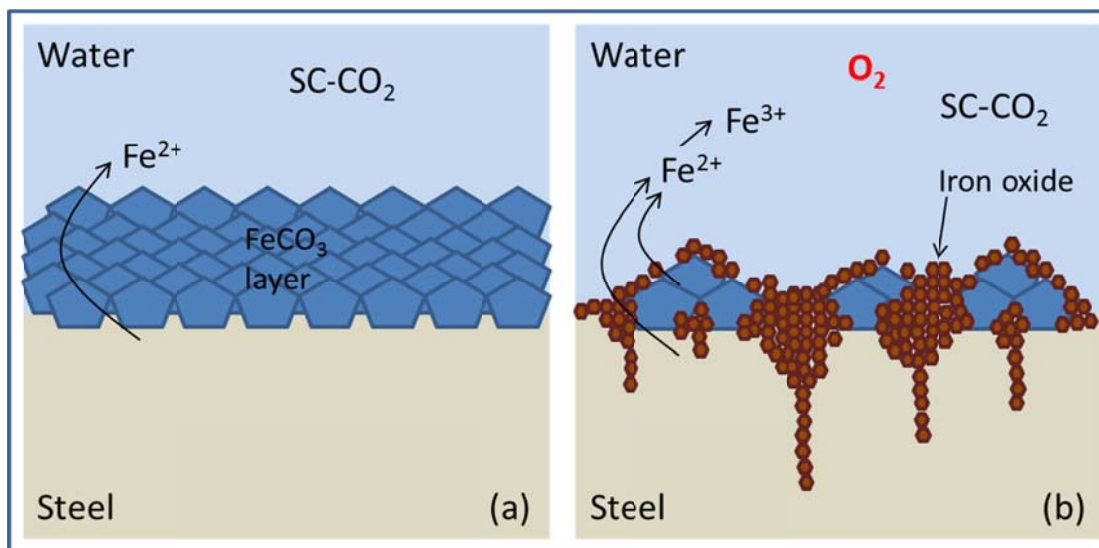


Figure 8. Schematic of hypothesis at high pressure

Although previous researchers have investigated the effect of  $\text{O}_2$  on  $\text{CO}_2$  corrosion, attempts to describe its mechanism are limited. Many questions are still left unanswered. The following questions were addressed in this research:

1. What iron oxides form in an  $O_2/CO_2$  environment?
2. Do different kinds of oxides form at elevated pressure?
3. What is the solubility of  $O_2$  in various phases of  $CO_2$ ?
4. How severe is the corrosion?
5. Do the phenomena agree with generated Pourbaix diagrams?
6. Does  $O_2$  cause pitting corrosion?
7. What causes tuberculation and blistering on the corrosion product layer?

## CHAPTER 4: LOW PRESSURE CORROSION EXPERIMENTS

This chapter describes the experiments that were conducted at atmospheric pressure. Four different types of experiment are discussed. The first is a preliminary experiment that was conducted to determine the effect of O<sub>2</sub> on CO<sub>2</sub> corrosion of steel at a condition that does not promote growth of a protective iron carbonate layer on the steel surface. This condition will be referred to as 'FeCO<sub>3</sub>-free'. Other experiments were then conducted for multiple sets of 'FeCO<sub>3</sub>-forming' conditions.

The experimental methodology is discussed first, followed by the results and their discussion. Corrosion mechanisms for mild steel with oxygen (O<sub>2</sub>) intrusion in different scenarios are then elaborated.

The objective of this study is to investigate the corrosion mechanism and the stability of iron carbonate (FeCO<sub>3</sub>) on mild steel with simulated ingress of ppm levels of O<sub>2</sub> at 1 bar total pressure as a prelude to conducting experiments that simulate high pressure environments.

Parts of this chapter have been presented at an international conference, CORROSION 2014, in San Antonio, Texas [90]. (Reproduced with permission from NACE International, Houston, TX. All rights reserved. N.R. Rosli, Y.-S. Choi, D. Young, Paper Number C2014-4299 presented at CORROSION/2014, San Antonio, TX. © NACE International 2014.)

#### 4.1 Sample Material

The type of steel that was used in this study is grade UNS G10180, its corrosion behavior was investigated using electrochemical techniques, surface analysis, and weight loss measurements. The specimens for electrochemical measurements were cylindrical-shaped while the specimens for weight loss and surface analyses were square-shaped, as shown in Figure 9. The composition of the steel was evaluated using Atom Emission Spectroscopy (AES), conforming to the requirements of UNS G10180, as shown in Table 5. The steel possesses a ferritic-pearlitic microstructure. The full report of the analysis is in Appendix A.

Sample preparation involved polishing of the steel specimens with up to 600 grit silicon carbide (SiC) paper, rinsing to remove any debris with isopropyl alcohol in an ultrasonic bath, and finally drying with a heat gun. The dimensions and masses of the specimens were measured using a scale with accuracy of 0.001 g.



Figure 9. Steel specimens for glass cell tests

Table 5: Composition of Steel (Balance Fe).

Element	Wt. %
Al	0.008
As	0.006
C	0.18
Co	0.003
Cr	0.12
Cu	0.18
Mn	0.75
Mo	0.02
Nb	0.002
Ni	0.065
P	0.011
S	0.021
Sb	0.009
Si	0.16
Sn	0.009
Ta	0.028
Ti	0.002
V	0.003
W	0.014
Zn	0.004
Zr	0.003

## 4.2 Experimental Design

A three-electrode glass cell setup, as shown in Figure 10, was utilized to conduct the low-pressure corrosion tests described in this chapter. A Teflon<sup>TM</sup> lid was fabricated with slots to hold multiple electrodes in place, as labeled in the diagram in Figure 10. These include the pH electrode, thermocouple, gas inlet and outlet, reference electrode, counter electrode, and holders for the working electrode and weight loss steel samples.

The electrolyte that was used for the system was 2 liters of 1 wt.% NaCl solution. Before the start of each experiment, CO<sub>2</sub> or a CO<sub>2</sub> and O<sub>2</sub> mixture was sparged through

the solution for at least 1 hour until the desired stable concentration of  $O_2$  is achieved. The sparger was used to reduce the size of the gas bubbles to speed up the process of saturating the solution with gas. The  $O_2$  concentration was monitored using an oxygen sensor, an Orbisphere 410, which gives the  $O_2$  concentration in the water phase at  $25^\circ C$ . This value was then recalculated to determine the actual concentration of  $O_2$  in the glass cell at the set temperature. A sample calculation is included in Appendix B. A solution that was  $CO_2$ -saturated recorded a reading of less than 10 ppb of  $O_2$  in the gas phase ( $25^\circ C$ ). Gas was continuously bubbled into the system for the duration of the tests.

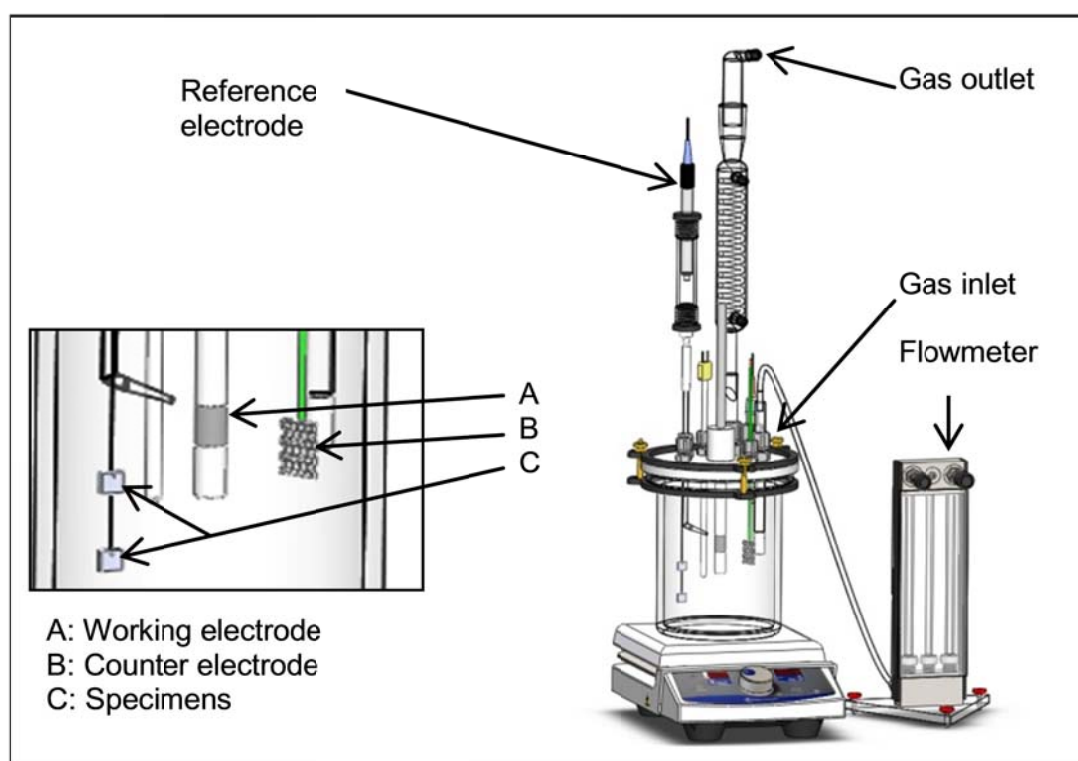


Figure 10. Glass cell setup (Courtesy of Cody Shafer, ICMT)



Figure 11. Oxygen meter, Orbisphere 410.

The desired temperature was maintained using a hotplate, controlled with a thermocouple immersed into the solution. Once the solution temperature stabilized, its pH was adjusted by adding deoxygenated reagent grade  $\text{NaHCO}_3$  or  $\text{HCl}$ . Deoxygenated ferrous chloride ( $\text{FeCl}_2 \cdot 4\text{H}_2\text{O}$ ) solution was added to provide additional  $\text{Fe}^{2+}$  ions in order to achieve a high initial  $\text{FeCO}_3$  saturation value; this accelerated the formation of a protective layer, thus reduced the experiment time. The test matrix for the  $\text{FeCO}_3$ -free and  $\text{FeCO}_3$ -forming experiments is shown in Table 6.

Table 6: Test Matrix for Low Pressure Corrosion Test.

Parameters	FeCO <sub>3</sub> -free condition	FeCO <sub>3</sub> -forming condition
Temperature	25°C	80°C
Initial pH	4.0	6.6
Total Pressure	1 bar	1 bar
CO <sub>2</sub> Partial Pressure	0.90 bar	0.53 bar
O <sub>2</sub> Concentration in liquid phase	3 ppm at 25°C	1 ppm at 80°C
O <sub>2</sub> Partial Pressure	0.07 bar	0.04 bar
Electrolyte	1 wt.% NaCl	1 wt.% NaCl
Water vapor pressure	0.03 bar	0.47 bar
Initial Fe <sup>2+</sup> Concentration	Not measured	50 ppm
Initial FeCO <sub>3</sub> Saturation	Not available	277
Duration	4 hours	7 days
Flow Rate	Stagnant	Stagnant

The FeCO<sub>3</sub>-forming corrosion experiments were conducted according to three different procedures, labeled as follows, and illustrated schematically in Figure 12:

- a) Test A: Baseline CO<sub>2</sub> experiment, no O<sub>2</sub> intrusion.

- b) Test B:  $O_2$  was added into the system after 2 days of  $CO_2$  corrosion and formation of the  $FeCO_3$  layer on the steel surface. The objective of this test is to determine the effect of  $O_2$  intrusion on the  $FeCO_3$  layer.
- c) Test C:  $CO_2$ - $O_2$  mixture from the beginning of the experiment. This study was conducted to investigate the effect of  $O_2$  impurity on  $CO_2$  corrosion of steel without any pre-corrosion.

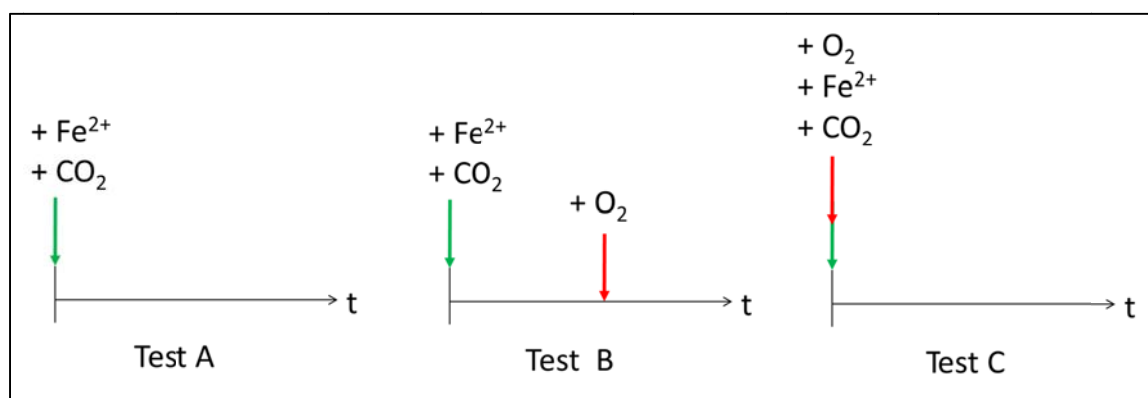


Figure 12. Different tests for  $FeCO_3$ -forming experiments.

Electrochemical measurements were conducted using a GAMRY Reference 600 potentiostat to determine the corrosion parameters of the experiments. Detailed explanation of this technique is described in the next sub-topic.

The test specimens were promptly removed from the electrolyte at the end of the experiments, rinsed with isopropyl alcohol, and dried to prevent the onset of further corrosion processes. The test specimens were then analyzed using scanning electron microscopy (SEM), energy dispersive X-ray spectroscopy (EDS), X-ray diffraction (XRD) and Raman spectroscopy.

Besides electrochemical measurements, the corrosion rate of the steel was also determined by measuring the weight loss at the end of the experiments. The weight loss of the steel is measured by completely removing the corrosion product from the steel surface in order to determine the difference in weight. The layers of corrosion product on the steel surface were removed using Clarke solution (ASTM G1-03). The Clarke solution consists of a mixture of hydrochloric acid (HCl), antimony trioxide (Sb<sub>2</sub>O<sub>3</sub>), and stannous chloride (SnCl<sub>2</sub>). The HCl removes the rust, Sb<sub>2</sub>O<sub>3</sub> works as an inhibitor to prevent HCl attack on the steel, while SnCl<sub>2</sub> is a reducing agent to convert ferric chloride to ferrous ions to avoid further reaction between ferric ions and fresh steel. A sample plot of weight change during the treatment using Clarke solution is provided in Appendix C.

Weight loss from the specimens in all tests were recorded and translated into corrosion rate using the following formula:

$$CR = \frac{W}{D \cdot A \cdot T} \quad (18)$$

The letter  $W$  represents the weight loss in grams,  $D$  is the density of the steel specimen in units of g/cm<sup>3</sup>,  $A$  is the area of the specimen in cm<sup>2</sup>, and  $T$  is the experimental time in seconds. The corrosion rate in cm/s was converted into units of mm/y with appropriate unit conversion. Treated specimens were also characterized by profilometry, using a 3D microscope, to determine the surface profile of the corroded steel surface. The penetration rate was calculated from observable areas showing a pitting attack. A sample

calculation of a corrosion rate from a weight loss measurement is provided in Appendix D.

### 4.3 Electrochemical Measurements

The working electrode was polarized at  $\pm 5$  mV *versus* the open circuit potential (OCP) at a scan rate of 0.125 mV/s. The value of the polarization resistance obtained from this technique is the total polarization resistance,  $R_{p,total}$ , which includes the solution resistance,  $R_s$ . To calculate the corrosion rate, the true polarization resistance,  $R_p$ , was determined by subtracting the solution resistance from the total polarization resistance that was obtained from linear polarization resistance (LPR) measurements.

$$R_p = R_{p,total} - R_s \quad (19)$$

The solution resistance was obtained by conducting Electrical Impedance Spectroscopy (EIS) on the specimen. The corrosion current,  $i$ , was then calculated using the Stern-Geary equation:

$$i = \frac{B}{R_p} = \frac{\beta_a \times \beta_c}{2.3 \times R_p \times (\beta_a + \beta_c)} \quad (20)$$

Where  $\beta_a$  and  $\beta_c$  are the anodic and cathodic Tafel slopes, set to a value of 0.12 V/decade each, resulting in a Stern-Geary constant,  $B$ , value of 0.026 V. This value corresponds to a corrosion rate that was controlled by both charge transfer and mass transfer.

The corrosion current density,  $i_{corr}$ , in units of  $A/m^2$ , is obtained by dividing the current with the surface area of the steel specimen that is exposed to the solution.

$$i_{corr} = \frac{i}{A} \quad (21)$$

The corrosion rate is then calculated using the equation [46]:

$$CR = \frac{i_{corr} M_{Fe}}{\rho n F} \cdot \left[ \frac{mm}{year} \right] = i_{corr} \cdot 1.16 \quad (22)$$

Where  $M_w$  is molar mass of the iron (Fe) in g/mol,  $\rho$  is the density in  $g/m^3$ ,  $n$  is the number of charges per mol of iron loss, and  $F$  is the Faraday's constant, 96,485 C/mol. For every kmol of iron lost, 2 kmol of electrons are released, hence the number of charge,  $n$ , is 2. A sample calculation of corrosion rate from polarization resistance value is given in Appendix E.

#### 4.4 Results and Discussions: FeCO<sub>3</sub>-Free Experiments

CO<sub>2</sub> corrosion tests at total pressure of 1 bar have already been conducted by previous researchers with reports of increased corrosion rate of carbon steel with the intrusion of O<sub>2</sub> [69], [81], [84]. This set of short term tests was conducted to understand the effect of O<sub>2</sub> on CO<sub>2</sub> corrosion of bare steel.

As expected, the corrosion rate increased with O<sub>2</sub> ingress. Figure 13 compares the corrosion rate of steel as measured using LPR. The chart indicates that O<sub>2</sub> ingress

increased the corrosion rate by 40% when measured at the end of a 4-hour experiment. Simulation of results using Freecorp© indicated that 3 ppm O<sub>2</sub> lead to about 30% increase in the corrosion rate; this is discussed separately in Chapter 6.

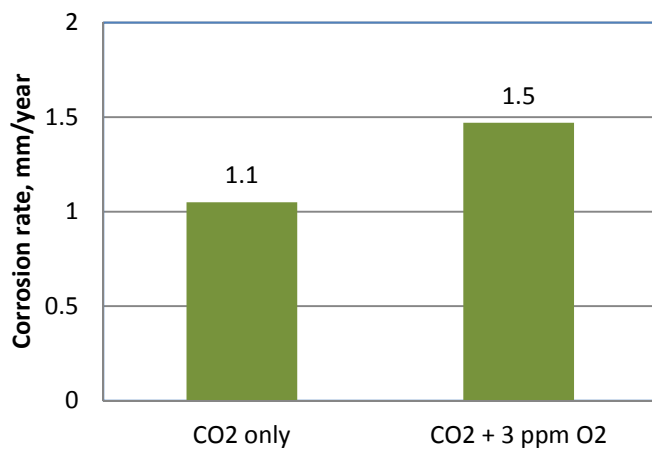
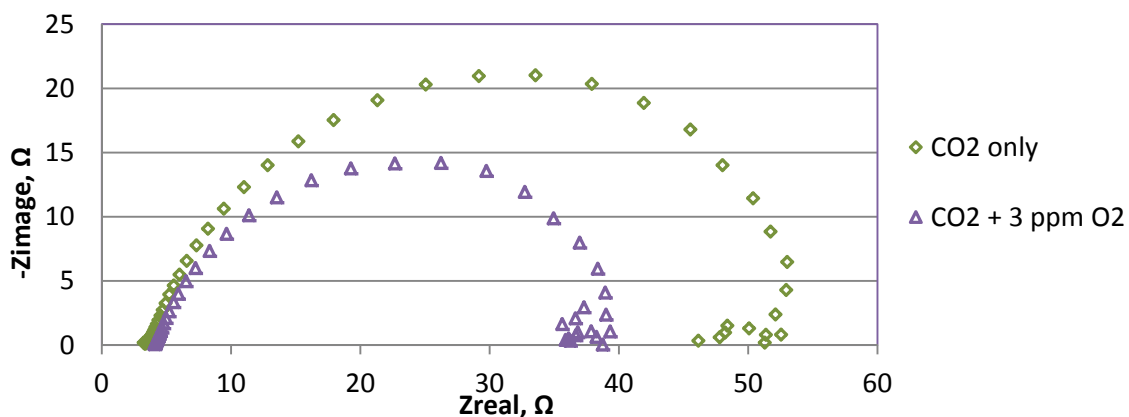


Figure 13. Effect of O<sub>2</sub> on corrosion rates at FeCO<sub>3</sub>-free condition (pH 4, 25°C)

The Nyquist plot, shown in Figure 14, which was obtained from EIS measurements, showed lower polarization resistance,  $R_p$ , when O<sub>2</sub> was present in the system, which implies to a higher corrosion rate. The solution resistance,  $R_s$ , did not show any significant difference in values.



	$R_p, \Omega$	$R_s, \Omega$
CO <sub>2</sub>	53.4	3.45
CO <sub>2</sub> + O <sub>2</sub>	38.2	4.08

Figure 14. Nyquist plots relative to the reference electrode (pH 4, 25°C)

Potentiodynamic sweeps were carried out to analyze the behavior of the anodic and cathodic reactions of the corrosion process. The sweeps were conducted towards the end of experiments due to their destructive effect to the specimens. The steel specimen was first polarized negatively from 0 to -500 mV with respect to the  $E_{oc}$ . The OCP was later monitored until it returned to its original OCP before the polarization. The specimen was then positively polarized from 0 to 300 mV. The resulting polarization curves, shown in Figure 15, exhibited higher corrosion current density in the presence of O<sub>2</sub>; this translates to a higher corrosion rate. This is because the cathodic curve for the O<sub>2</sub>-CO<sub>2</sub> system slightly shifted to the right. The overall shape of the curves did not change in the presence of O<sub>2</sub>, showing a mixed mass transfer and charge transfer mechanism. Previous researcher had found the cathodic curve shifted further when O<sub>2</sub> concentration in CO<sub>2</sub>-saturated solution was increased from 40 ppb to 3 ppm [81]. The potentiodynamic

sweep measurement was not repeated, however, the experimental results were compared with simulated results using Multicorp© which is discussed in Chapter 6.

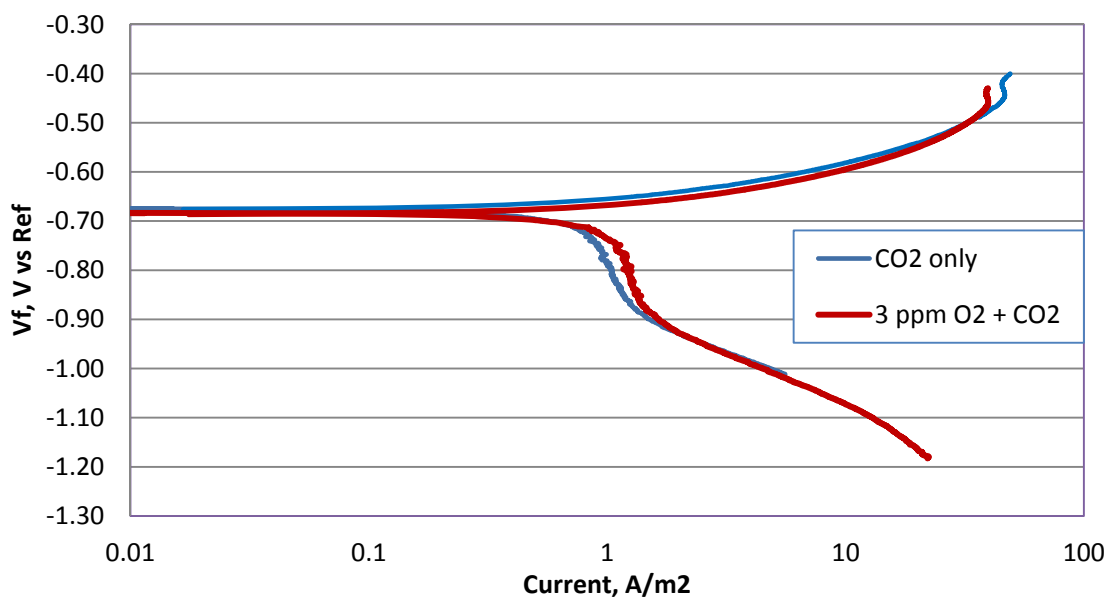


Figure 15. Polarization curves versus Ag/AgCl reference electrode (pH 4, 25°C)

In general,  $O_2$  ingress showed an increase in the corrosion rate of steel due to the additional cathodic reaction causing accelerated consumption of electrons at the steel surface, thus promoting further oxidative dissolution of iron.

#### 4.5 Results and Discussions: $FeCO_3$ -Forming Experiments

This set of experiments was conducted at conditions where the formation of a protective  $FeCO_3$  layer on the steel surface is expected; see Table 6 for the test matrix. This enabled the investigation of the integrity of the protective  $FeCO_3$  with the presence of  $O_2$  as an impurity. The results from each of three different conditions will be described

separately in dedicated sub-sections. The electrochemical measurements, and generated surface analysis results provide a basis for the proposed corrosion mechanism at the end of this chapter.

#### 4.5.1 Test A: Baseline CO<sub>2</sub> Corrosion Experiment

The plot shown on Figure 16 shows that the corrosion rate for the baseline CO<sub>2</sub> corrosion test kept on decreasing monotonously until the end of the 8-day experiment to *ca.* 0.1 mm/y. These average values are based on two repeated tests, with error bars indicating minimum and maximum values. The time-integrated corrosion rate value corresponds to 0.26 mm/year while the weight loss corrosion rate value was 0.11 mm/year. Theoretically, the drop of the corrosion rate was due to coverage by FeCO<sub>3</sub> on the steel surface that slowed the corrosion process. The corrosion potential, shown in Figure 17 as the mean values out of two repeats, was relatively stable at around -0.7 mV.

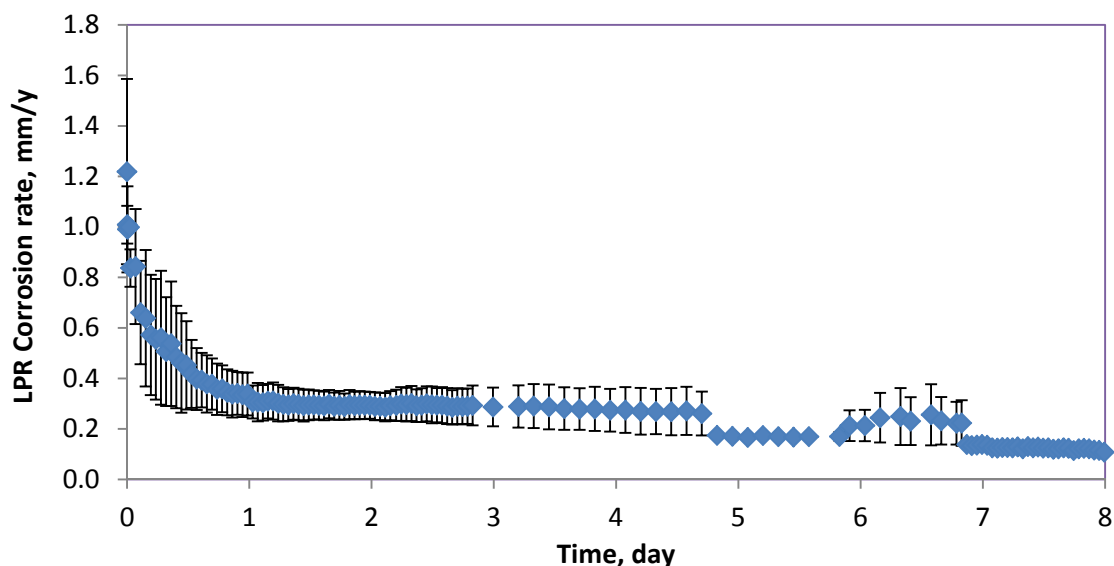


Figure 16. LPR mean corrosion rates for Test A (Baseline CO<sub>2</sub> Corrosion, 80°C, pH 6.6, 0 ppm O<sub>2</sub>, 50 ppm initial Fe<sup>2+</sup> concentration).

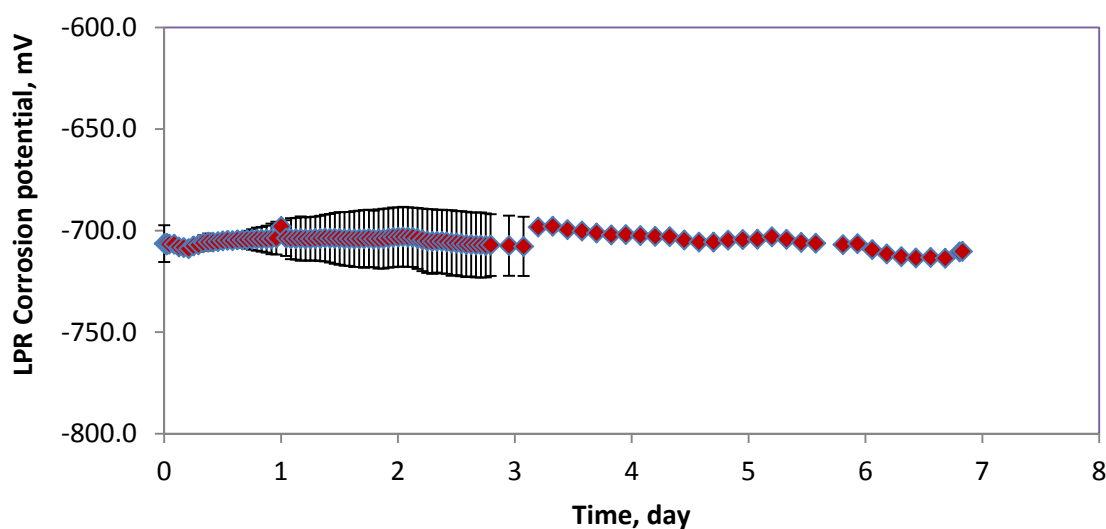


Figure 17. Mean corrosion potential for Test A (Baseline CO<sub>2</sub> Corrosion, 80°C, pH 6.6, 0 ppm O<sub>2</sub>, 50 ppm initial Fe<sup>2+</sup> concentration).

The pH values of the bulk solution, measured during one of the tests, constantly dropped slowly from about 6.63 to 6.55 as shown in Figure 18. The total iron ion

concentration ( $\text{Fe}^{2+}$  and  $\text{Fe}^{3+}$ ) in the solution, measured using a spectrophotometer, showed a decline from the initial 50 mg/L to 2.8 mg/L at the end of the experiment as shown in Figure 19. The gradual decline in the iron concentration in this baseline test was due to the continuous consumption of the initially added 50 mg/L of  $\text{Fe}^{2+}$  ions to form  $\text{FeCO}_3$ . The layer of protective  $\text{FeCO}_3$  slowed down the release of more  $\text{Fe}^{2+}$  into the solution.

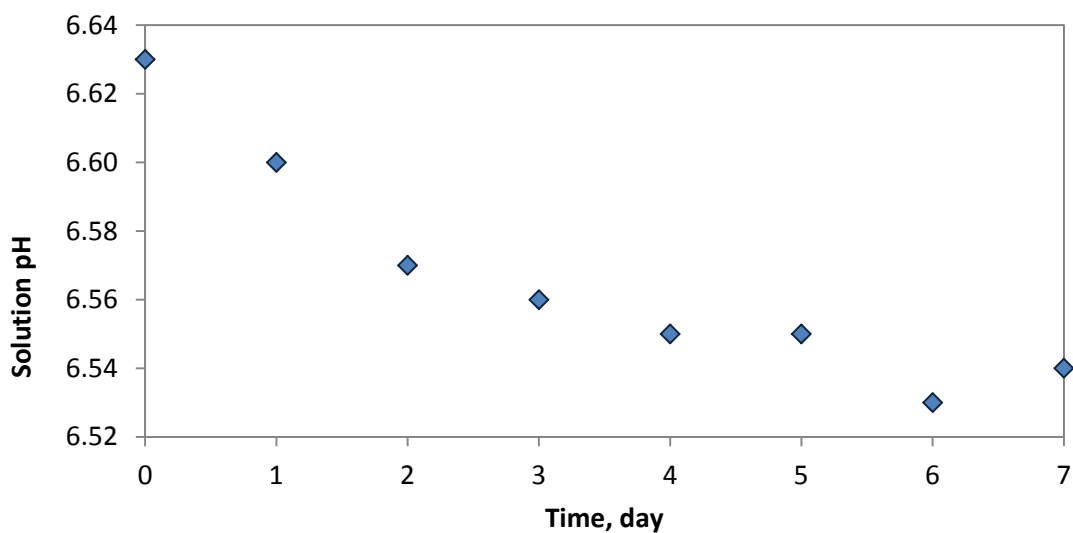


Figure 18. Solution pH for Test A, ( $80^{\circ}\text{C}$ , pH 6.6, 0 ppm  $\text{O}_2$ , 50 ppm initial  $\text{Fe}^{2+}$  concentration).

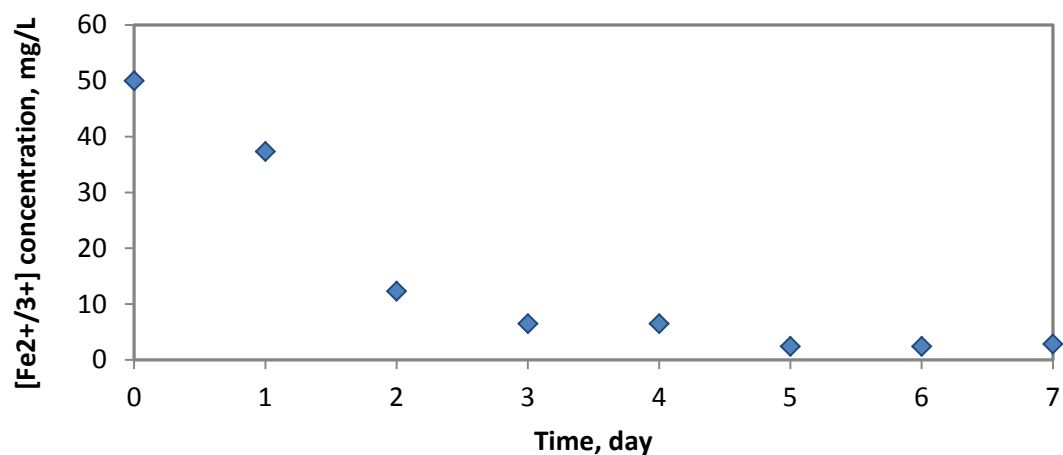


Figure 19. Total iron ion concentration in the solution for Test A (80°C, pH 6.6, 0 ppm O<sub>2</sub>, 50 ppm initial Fe<sup>2+</sup> concentration).

At the end of the 7-day experiment, the steel surface was found to be densely coated with prismatic crystals of morphology typical of FeCO<sub>3</sub>, as shown in Figure 20. The overall full coverage by FeCO<sub>3</sub> provided adequate protection to the steel surface and lowered the final corrosion rate. The EDS analysis showed Fe, C and O in the crystals. Removal of this corrosion product using a Clarke solution treatment revealed a surface that showed general corrosion over the entire steel surface with no signs of pitting, as shown in Figure 21. Polishing marks were still visible on the steel surface. The thickness of the corrosion product was measured from the cross-section of the specimen under SEM, as shown in Figure 22, measuring about 6.6 μm.

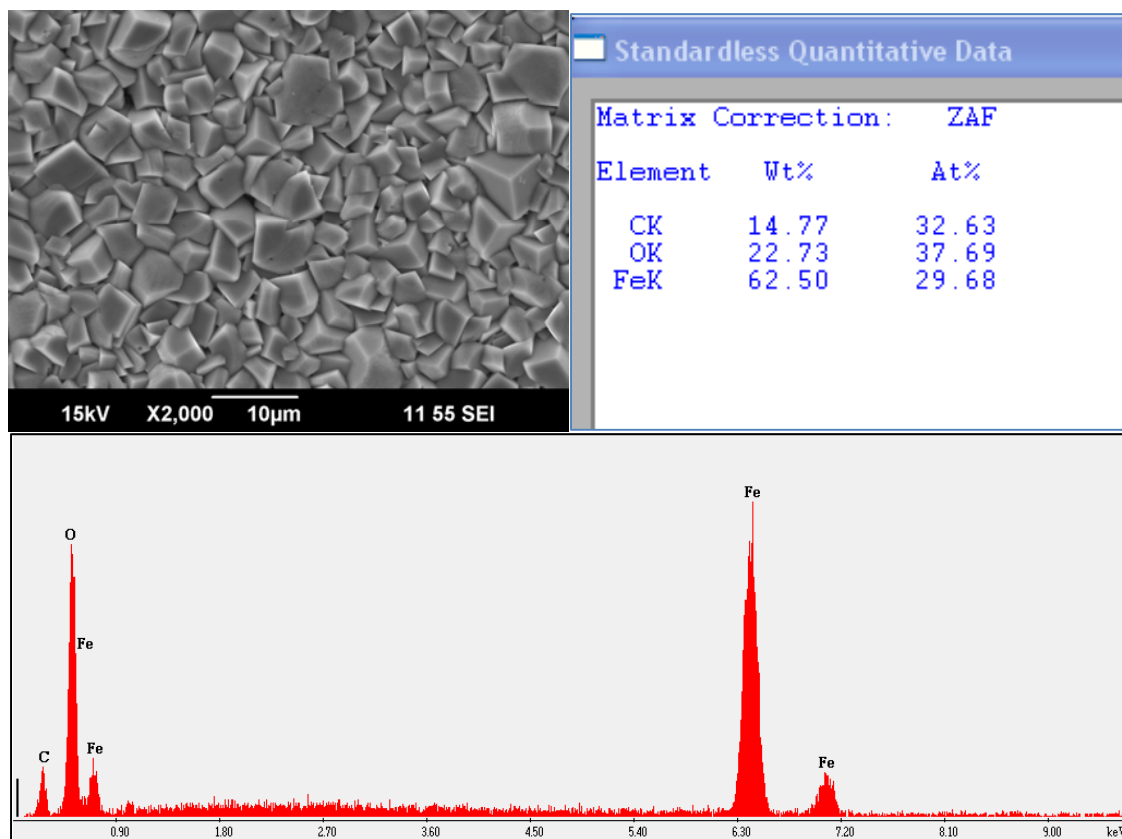


Figure 20. SEM image and EDS spectra of sample for Test A (80°C, pH 6.6, 0 ppm O<sub>2</sub>, 50 ppm initial Fe<sup>2+</sup> concentration)

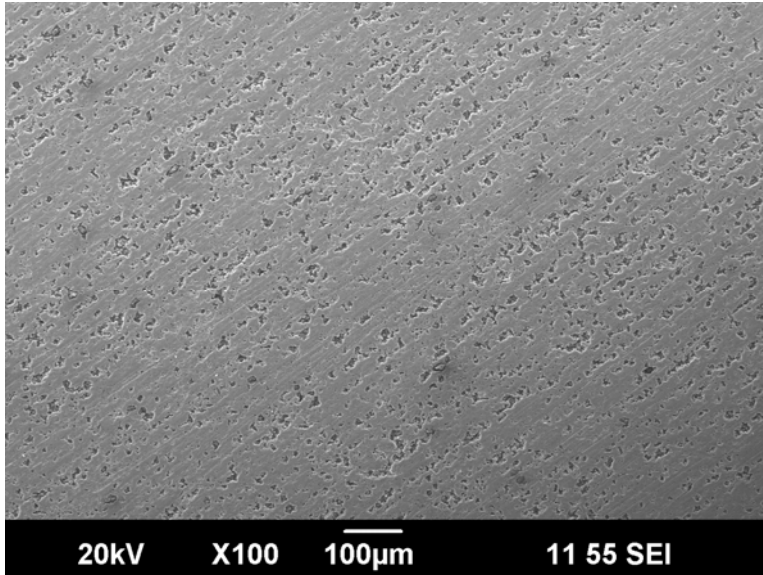


Figure 21. SEM image of steel surface for Test A after corrosion product removal

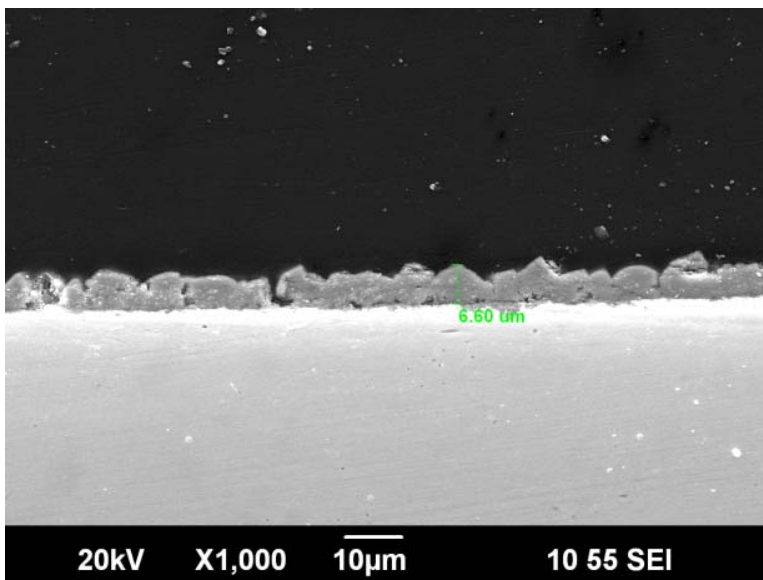


Figure 22. Cross-section view of steel specimen for Test A

#### 4.5.2 Test B: O<sub>2</sub> Ingress from Day 2

When O<sub>2</sub> was introduced into the glass cell on Day 2, the clear, colorless solution turned colored and murky due to the conversion of the available Fe<sup>2+</sup> ions in the solution into insoluble ferric precipitates that were suspended in the electrolyte. Figure 23 shows that the introduction of 1 ppm O<sub>2</sub> to the pre-corroded specimen caused the corrosion rate to instantly spike and then settled at a relatively constant value of around 0.5 mm/year. It is noteworthy that there was a greater scatter of corrosion rate values after the addition of O<sub>2</sub>. Similar observations of instant increase in corrosion rate with higher degree of scatter have been reported by previous researchers [69], [84].

The calculated time-averaged value from the corrosion rate measurement was 0.33 mm/year. There was also an immediate shift in the potential as O<sub>2</sub> was added to the system, shown in Figure 24, similar to the findings observed by another researcher [69]. The error bars shown in the plot represent the maximum and minimum recorded values. The weight loss measurements recorded a corrosion rate of 0.77 mm/year, this is a value that is higher than what was observed in Test A.

Figure 25 shows the variation in the solution pH that was measured during one the tests at this condition. The pH dropped slightly in the beginning before the introduction of O<sub>2</sub>, consistent with the pH in the baseline experiment, Test A. The pH then gradually increased once the system became oxidic with a recorded final pH of about 6.6.

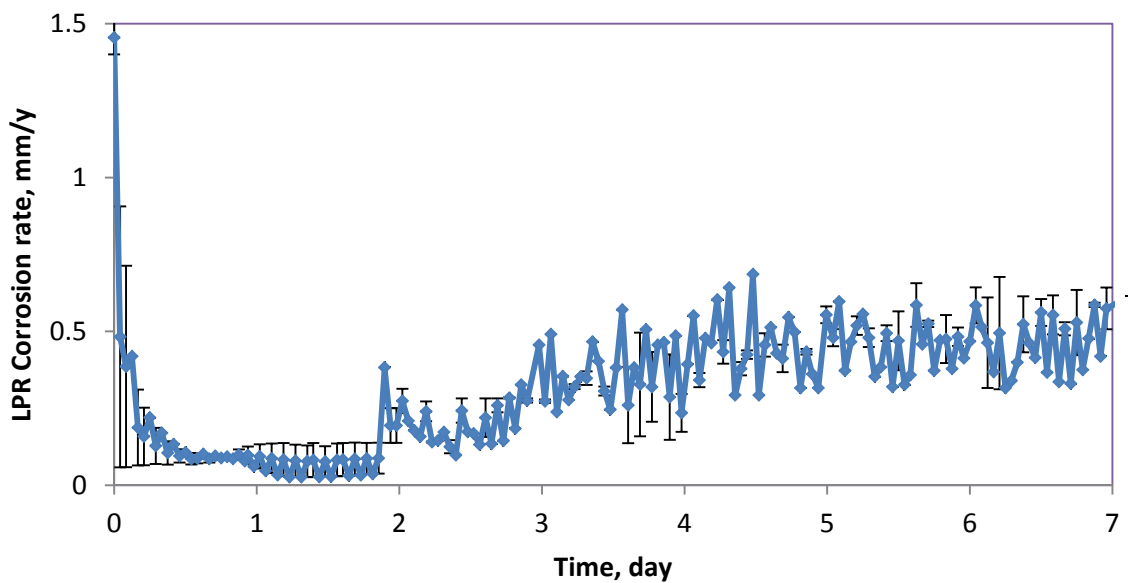


Figure 23. LPR mean corrosion rate for Test B ( $O_2$  introduced on Day 2).

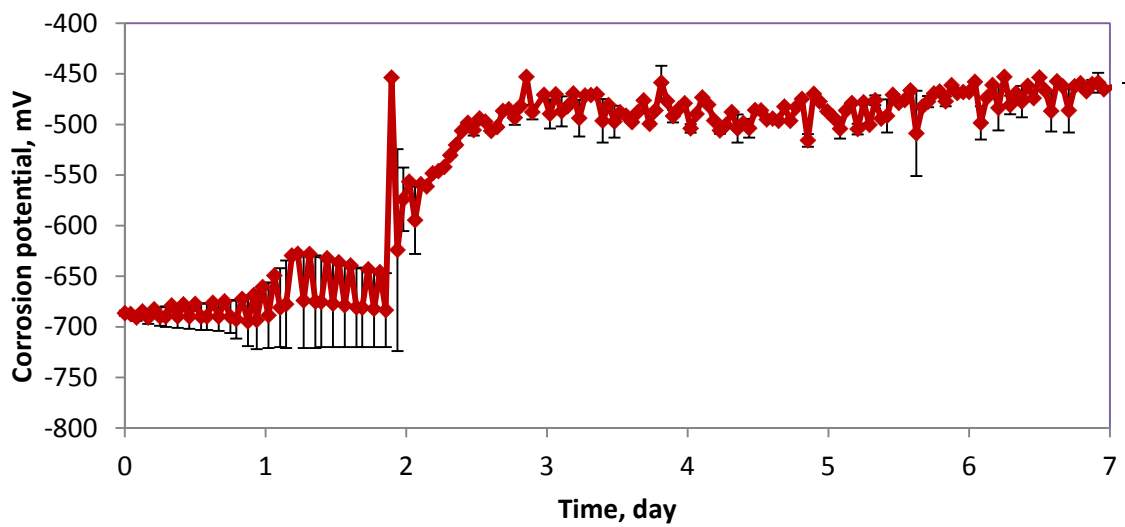


Figure 24. Mean corrosion potential for Test B ( $O_2$  introduced on Day 2).

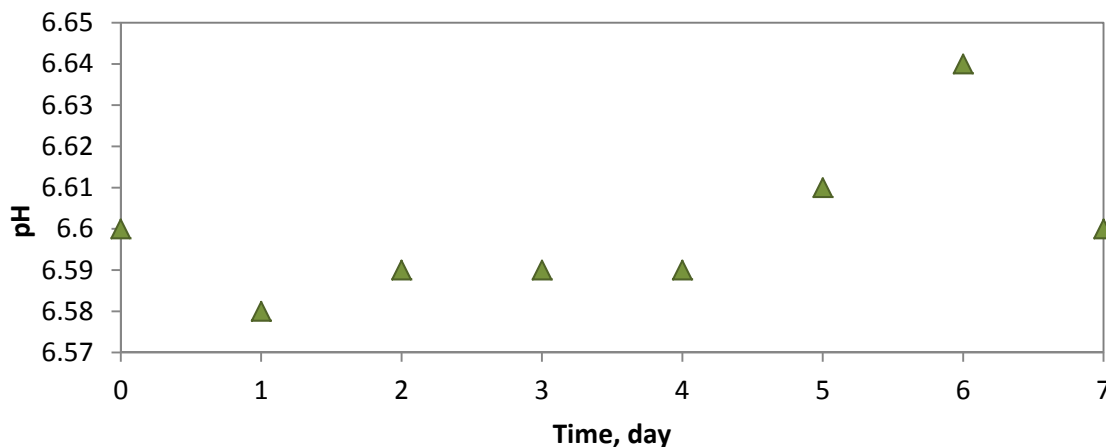


Figure 25. Solution pH for Test B ( $O_2$  introduced on Day 2).

Figure 26 shows the surface of the steel that was partially covered by prismatic  $FeCO_3$  crystals that had formed after 24 hours of test duration. Figure 27 shows dense coverage by  $FeCO_3$  crystals across almost the entire steel surface, right before the addition of  $O_2$ . The formation of  $FeCO_3$  in this first two days of the test provided some protection to the steel surface, hence the drop in the corrosion rate as demonstrated in the electrochemical measurements shown in Figure 24.

The  $FeCO_3$  layer was then perturbed by iron oxide formation on Day 2, which caused the increase in the general corrosion rate after  $O_2$  was introduced to the system. By the end of the test on Day 7, features such as tubercles and mounds of deposits were observed on the steel surface. Small globular-shaped pseudo-cubic crystals were found deposited in clusters on top of the prismatic  $FeCO_3$  crystals. These clusters of crystals tend to accumulate and form mounds and craters as demonstrated in Figure 28 and Figure 29. The EDS analysis, shown in Figure 29, of the smaller pseudo-cubic crystals showed a

higher intensity O peak and lower intensity carbon C peak, compared to the EDS analysis of the larger prismatic crystals, which indicates the presence of iron oxide. Nevertheless, this result is questionable due to the thin and porous morphological characteristics of the formed iron oxide.

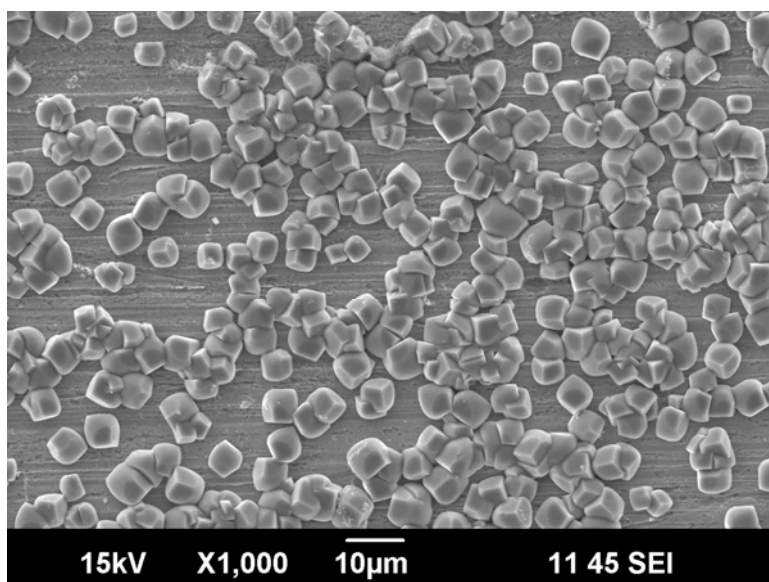


Figure 26. FeCO<sub>3</sub> crystals on steel surface at 24 h in Test B.

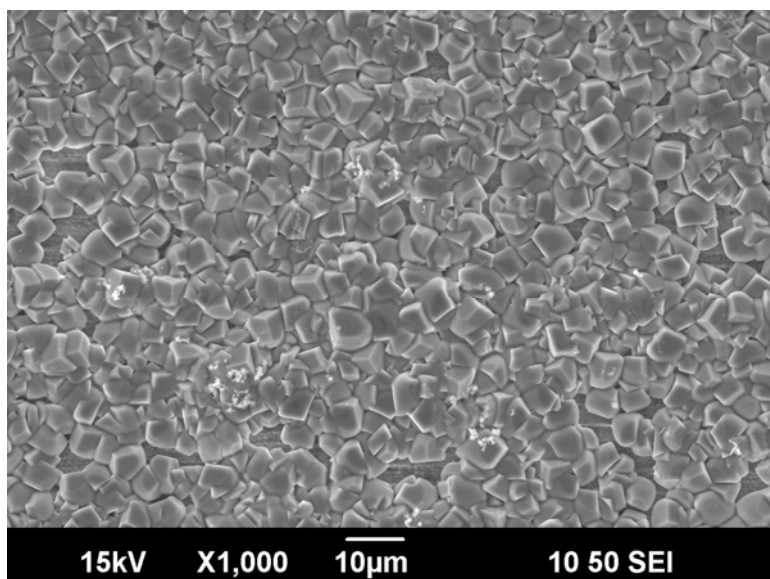


Figure 27. FeCO<sub>3</sub> crystals on steel surface at 48 h before O<sub>2</sub> introduction in Test B.

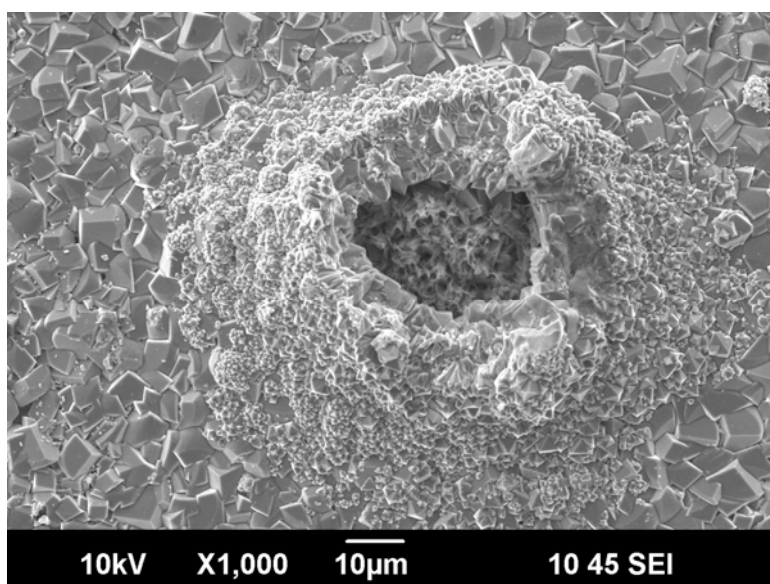


Figure 28. Oxide clusters on FeCO<sub>3</sub> layer at 168 h in Test B

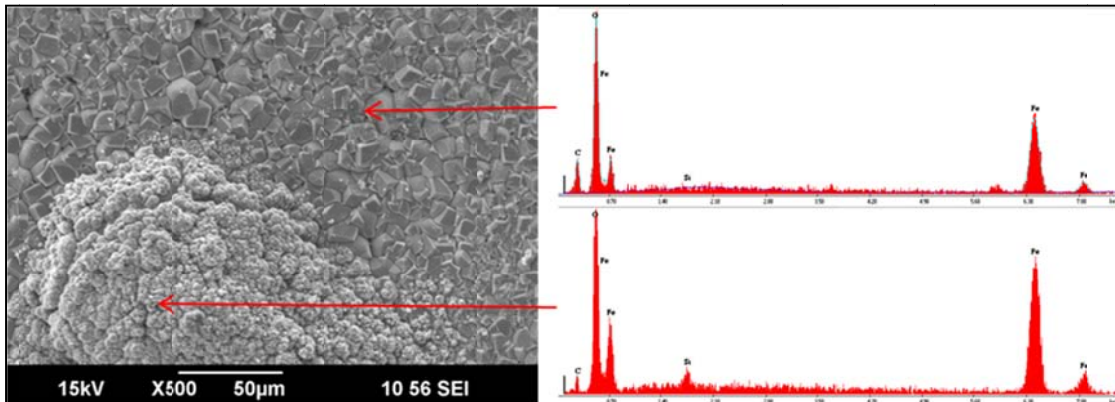


Figure 29. SEM image and EDS spectra of sample at the end of Test B

The cross-sectional view of the corrosion product on the steel surface shown in Figure 30 demonstrates a dome-like hollow tubercular structure. The different shades of grey shown in the SEM backscatter image are indicative of compositional variation in the corrosion product layer. Heavy elements scatter electrons more effectively than light elements, hence the appearance of lighter shades of gray. Therefore, there is a correlation between the atomic numbers of the elements present and the contrasting shades of gray observed in SEM images [93], [94]. The epoxy that was used to impregnate the specimen appeared black on the image due to the lesser amount of backscattered electrons from a surface constituted from light elements (C, H, O). The steel, consisting overwhelmingly of Fe, is a light gray. Iron oxide and iron carbonate corrosion products were of intermediate shading. A thin oxide layer is noticeable on top of the tubercular structure in light grey.

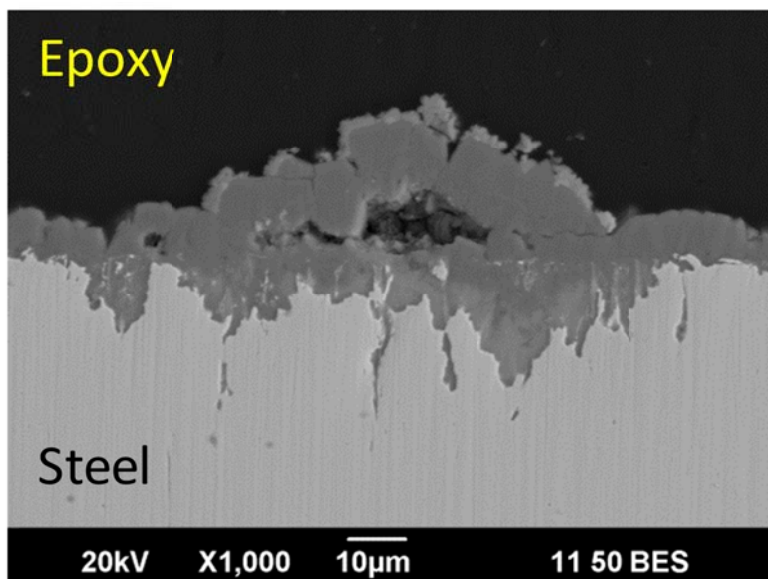


Figure 30. Cross-section of the sample from Test B

Elemental analyses using EDS provided an initial determination of the chemical compositions of the corrosion product; however, the results were inconclusive since it failed to provide accurate identification of the phases present. Although the identity of the chemical compounds can be deduced based on the measured atomic ratios, this can be misinterpreted – particularly if more than one phase is present or if polymorphism is possible. X-ray diffraction (XRD) was then utilized to confirm the presence, or absence, of particular phases.

Figure 31 corresponds to the XRD patterns of specimens removed at the end of the experiments corresponding to Test B. The analyses revealed a pattern characteristic of siderite ( $\text{FeCO}_3$ ) as the main component in the corrosion product layer of the recovered specimen for Test B, while hematite ( $\text{Fe}_2\text{O}_3$ ) and magnetite ( $\text{Fe}_3\text{O}_4$ ) were detected as the

main components in Test C. Substrate  $\alpha$ -Fe peaks were notably absent, consistent with formation of a thick corrosion product layer.

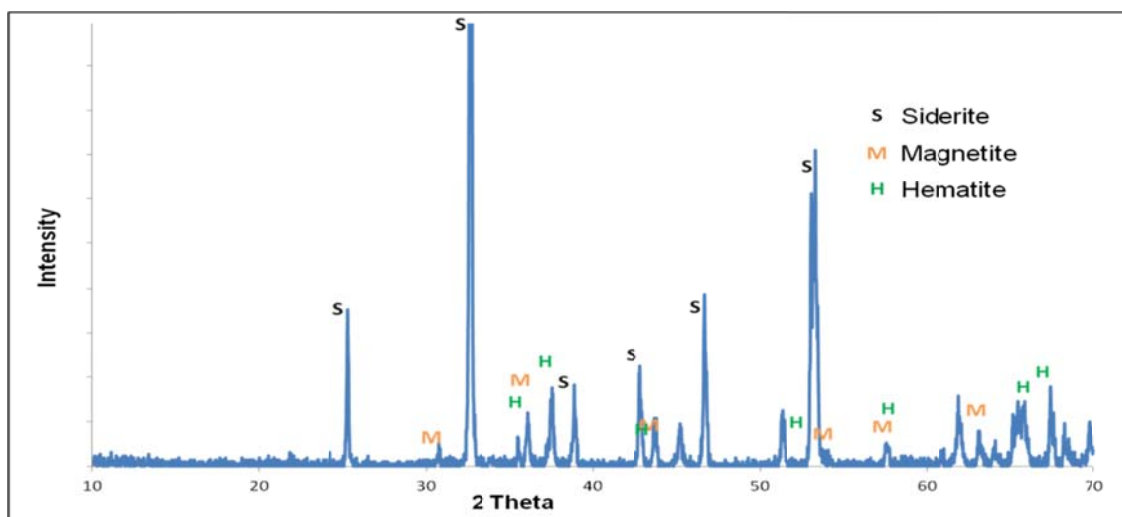


Figure 31. X-ray diffraction of the specimen after 7 day immersion for Test B.

Figure 32 shows the steel surface of the specimens after Clarke solution treatment. It was apparent that iron oxide was able to partially remove and penetrate through the formed  $\text{FeCO}_3$ , leading to the damage that can be seen as a mottled appearance to the steel surface. The attack was observed in the form of wide and shallow localized corrosion features.

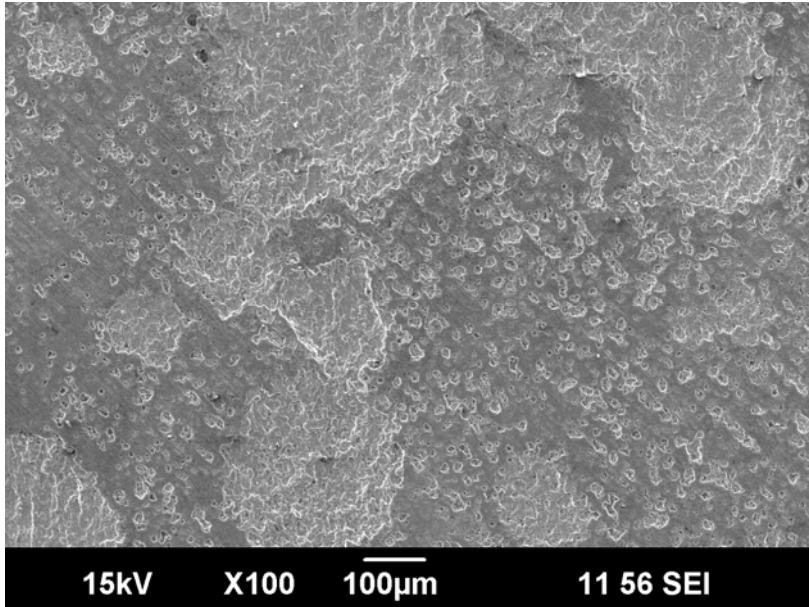


Figure 32. SEM image of the bare steel surface from Test B

The pit depth and surface profile was investigated using a 3D microscope, as a profilometer, as shown in Figure 33. The maximum pit depth found was about 95  $\mu\text{m}$ , which corresponds to a penetration rate of 4.2 mm/y. Visual inspection of the pits shows that they are relatively wide. False color images were also produced to help distinguish subtle variations by expanding the range of visible hues.

Similar findings have been observed before by another researcher who introduced two different concentration of  $\text{O}_2$  after 4 days of  $\text{FeCO}_3$  layer formation on steel surface. In that study, pits had been observed to occur more frequently underneath tubercles, and the severity of the pits amplified when the  $\text{O}_2$  concentration was increased from 4 ppm to 8 ppm [69].

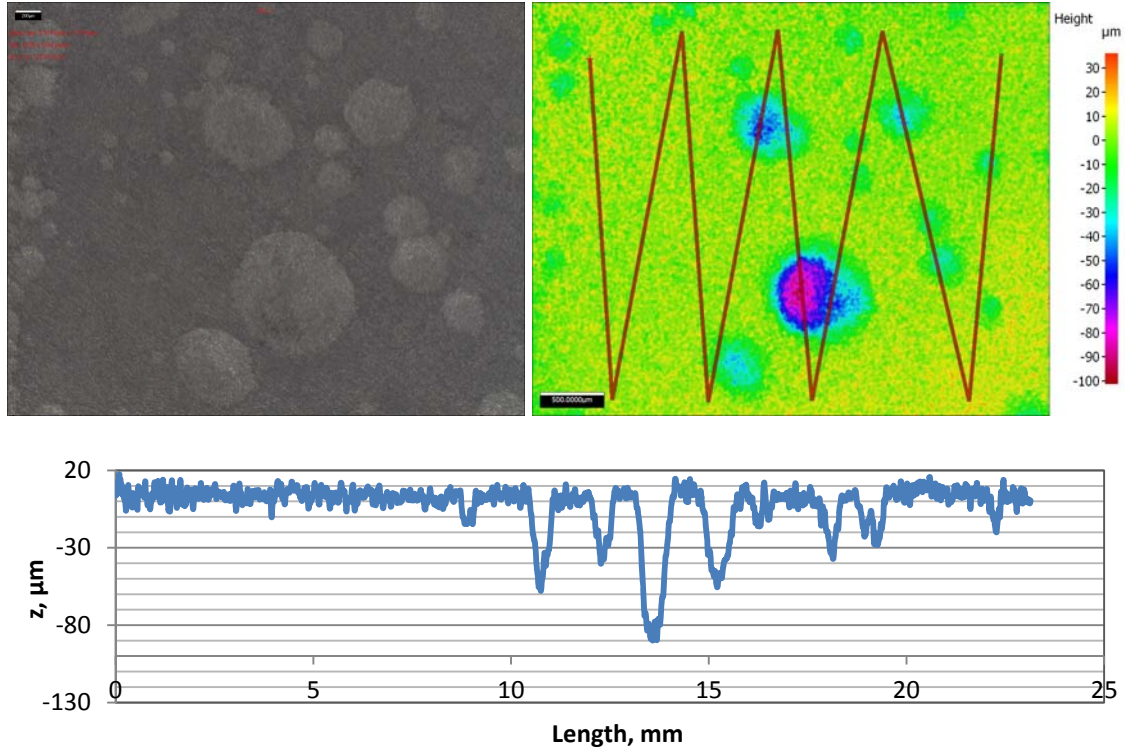


Figure 33. Surface profile of pits on specimen from Test B.

One proposed method to determine the severity of localized corrosion is by measuring the pitting factor, which is the ratio of the pit penetration to the average penetration obtained from weight loss of the metal [95]. A pitting factor of lower than 3 suggests uniform corrosion while higher values (greater than 5) suggest localized corrosion. However, one should not depend on this ratio as it is not an absolute confirmation of localized corrosion [95]. With the resulting corrosion rate from weight loss calculation (1.31 mm/y), the pitting factor of this test was found to be 3.4. This would be consistent with low severity, or low risk of localized corrosion.

#### 4.5.3 Test C: O<sub>2</sub> Ingress from Day 0

When a deaerated FeCl<sub>2</sub> solution was added to an electrolyte that was saturated with the CO<sub>2</sub> and O<sub>2</sub> gas mixture to confer a 50 ppm concentration of Fe<sup>2+</sup>, the solution immediately turned yellowish then pitch black and remained that way for about 10 minutes as shown in Figure 34. This is because O<sub>2</sub> is a strong oxidizer that rapidly converted Fe<sup>2+</sup> to Fe<sup>3+</sup>, which is considerably less soluble. The solution became clearer after 10 minutes as the black precipitate settled to the bottom of the glass cell. By the end of the 7 day test, Figure 35, the precipitate at the bottom of the glass cell was of a reddish brown hue.

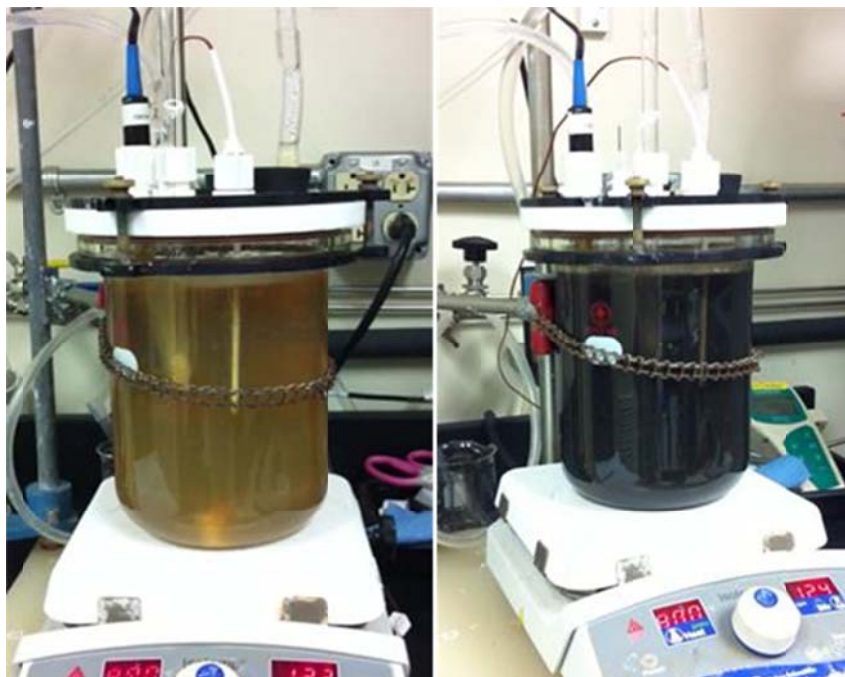


Figure 34. Initial electrolyte color change from colorless to yellow to black in Test C



Figure 35. Reddish brown precipitate at the bottom of the glass cell.

Corrosion rates, measured using LPR, are shown in Figure 36. Similar to Test A and Test B, the corrosion rate showed a rapid decrease over the first few hours. However, the decrease was less pronounced for Test C, with the corrosion rate holding relatively steady at an average of around 0.8 mm/y until Day 4. Interestingly, the corrosion rate then significantly decreased between Day 4 and Day 5 to a mean value of 0.2 mm/year, where it remained relatively constant until the end of the experiment. Based on these observations, it was concluded that the presence of  $O_2$  delayed the formation of a protective layer on the steel surface.

The weight loss and time-averaged corrosion rates were 1.07 mm/year and 0.63 mm/year respectively. Both values were high compared to those for Test A and Test B.

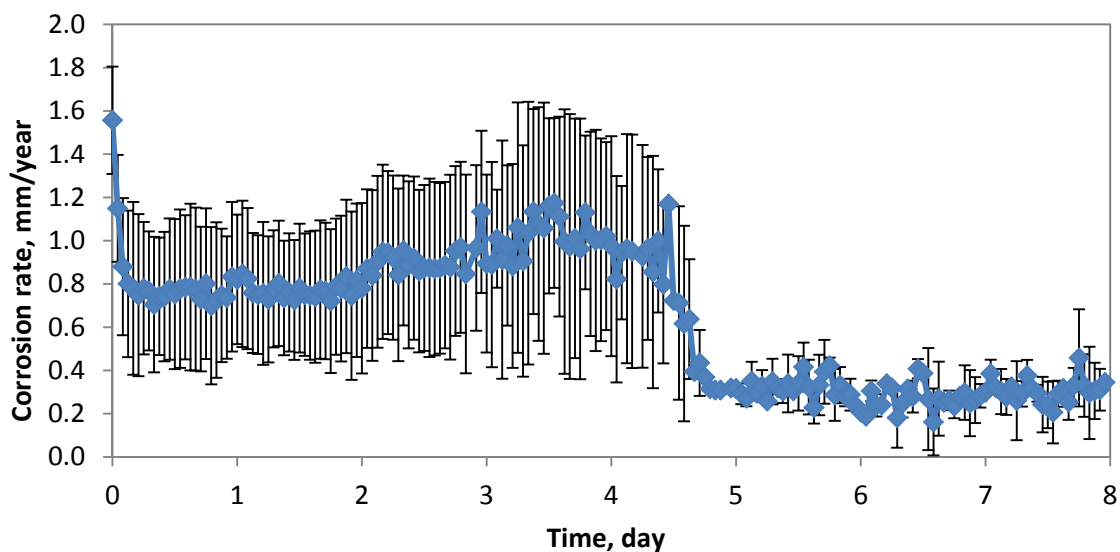


Figure 36. LPR mean corrosion rate for Test C

The change in the open circuit potential was insignificant in the initial part of the experiment but exhibited an abrupt shift between Day 4 and Day 5, shown in Figure 37, concurrent with the dip in the corrosion rate shown in Figure 36. The abrupt shift to more positive potential from *ca.* -690 mV to *ca.* -475 mV is indicative of alterations in the nature of the corrosion product on the steel surface.

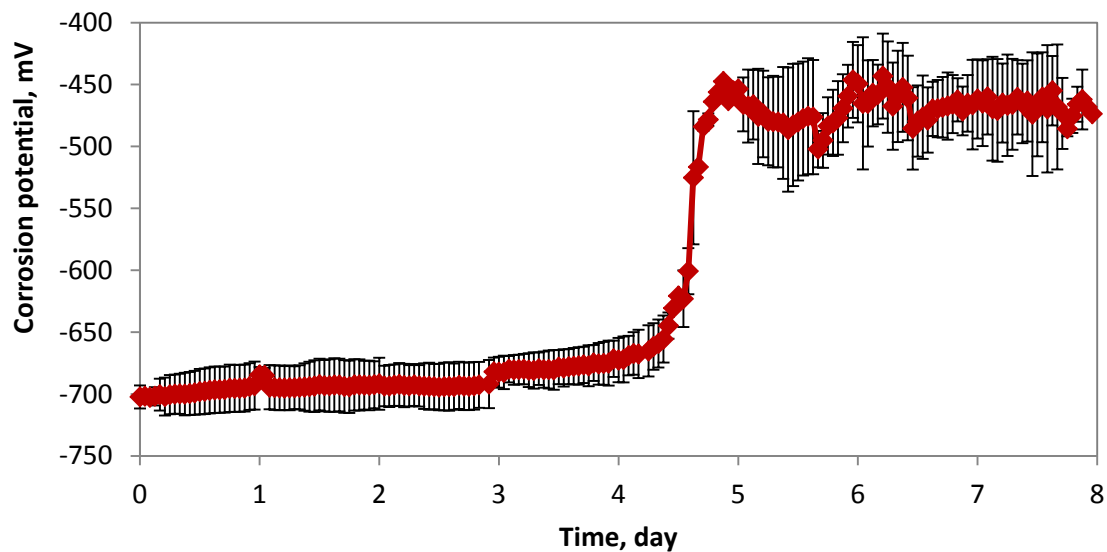


Figure 37. Mean corrosion potential for Test C

The pH of the solution remained relatively constant throughout the duration of the experiment, see Figure 38. The final pH was similar to that measured in Test B.

The total dissolved iron ion concentration recorded a drastic drop from 50 ppm to a very low value, as shown in Figure 39, consistent with the rapid conversion of ferrous ions to insoluble ferric precipitates. It should be noted that these low values represent the combined  $\text{Fe}^{2+}$  and  $\text{Fe}^{3+}$  concentrations in the bulk solution is opposed to their concentrations at, or in the proximity of, the actively corroding steel surface.

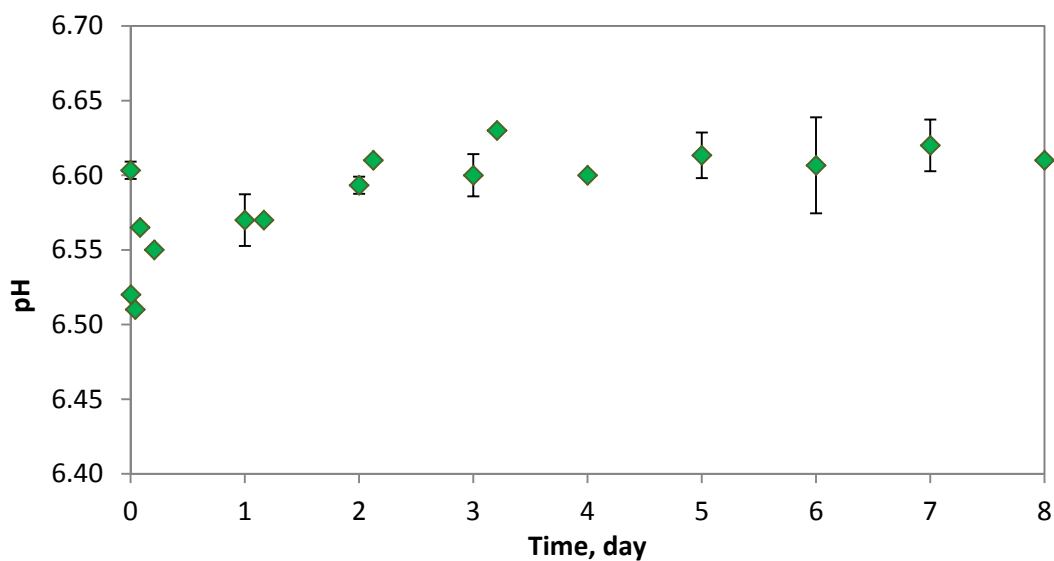


Figure 38. Bulk solution pH for Test C.

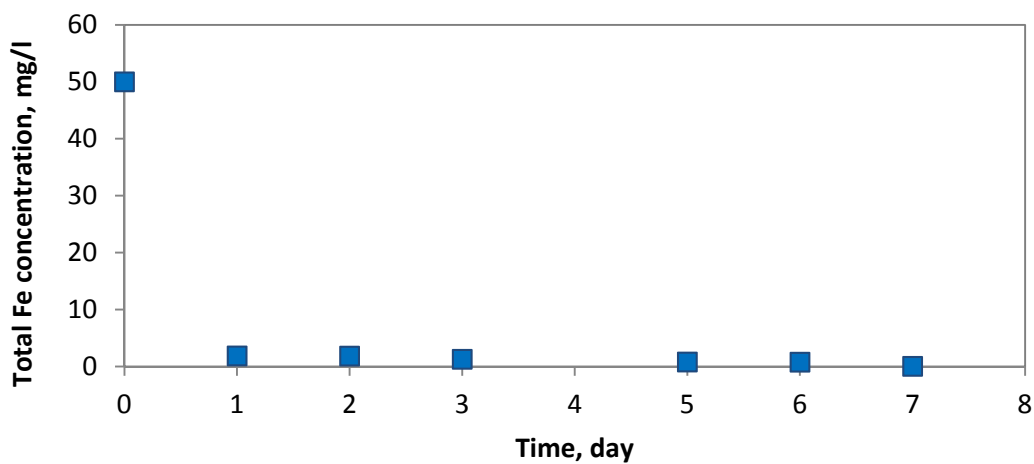


Figure 39. Total iron concentration in solution of Test C.

The presence of 1 ppm  $O_2$  did not completely impede the formation of  $FeCO_3$  crystals on the steel surface, as can be seen in Figure 40 through Figure 43. However, coverage by the  $FeCO_3$  crystals was incomplete, as observed on the steel specimen that

was retrieved at the end of Day 2, as shown in Figure 40. The surface was instead covered by a combination of prismatic and smaller sized plate-like crystals. The iron oxide crystals obstructed the formation of  $\text{FeCO}_3$  and resulted in partial coverage by  $\text{FeCO}_3$  of the steel surface. The attack by  $\text{O}_2$  was more rapid than the formation of  $\text{FeCO}_3$  as a corrosion product. A denser coverage of corrosion product was observed on the specimen that was retrieved on Day 4, which consists of a mixture of prismatic  $\text{FeCO}_3$  crystals and smaller globular-shaped crystals, shown in Figure 41. Tubercular features were non-existent at this stage. Between Day 6 and Day 8 oxide encrusted tubercles were observed to develop on the steel specimens, as shown in Figure 42 and Figure 43.

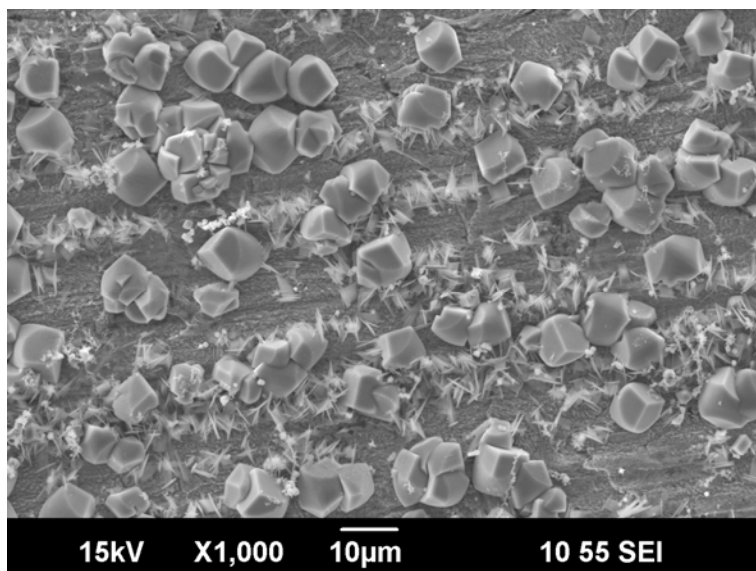


Figure 40. Steel surface at the end of Day 2 in Test C.

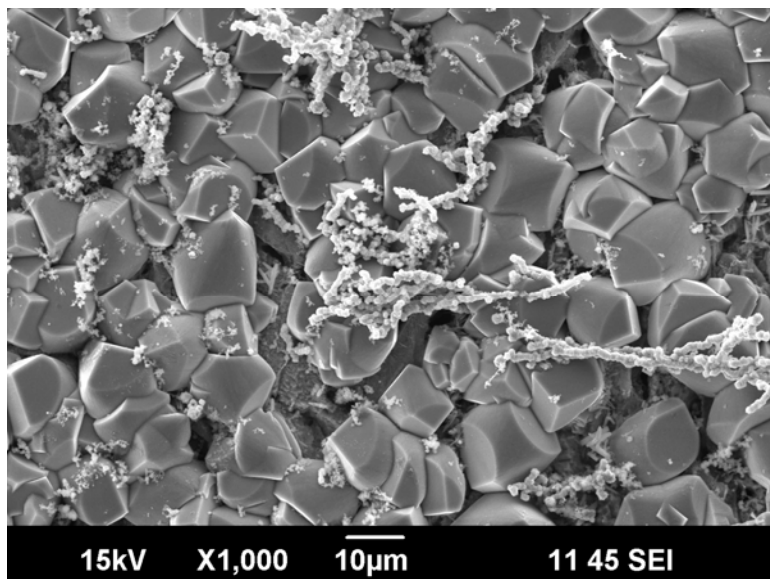


Figure 41. Steel surface at the end of Day 4 in Test C.

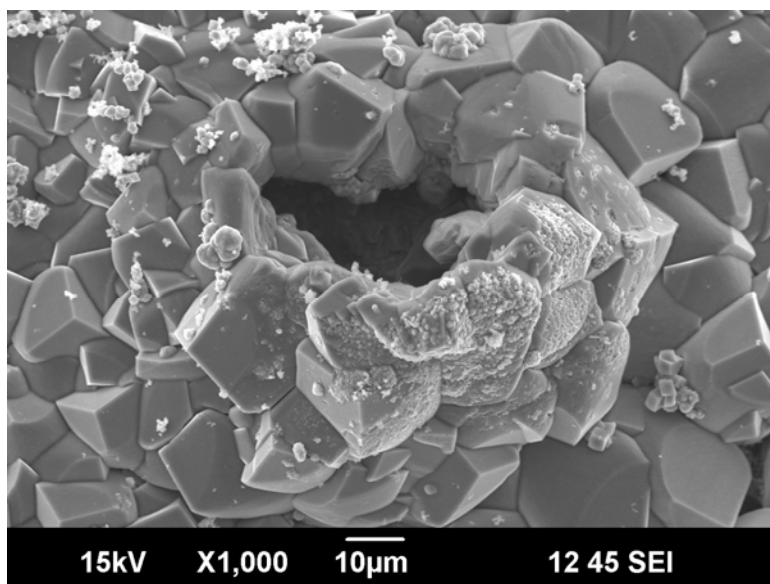


Figure 42. Steel surface at the end of Day 6 in Test C.

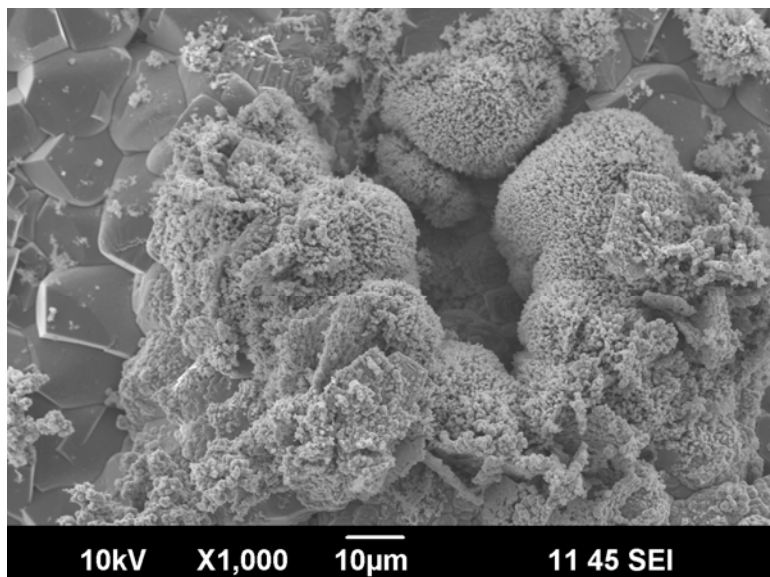


Figure 43. Steel surface at the end of Day 8 in Test C.

EDS spectra shown in Figure 44 provided a good indication of the presence of iron oxides on the steel surface. When the two different morphologies were analyzed, the smaller crystals exhibited a lower content of C (carbon) as compared to the larger prismatic crystals, indicative of possible formation of iron oxides.

Further investigation of the corrosion product layer showed the obstructive nature of iron oxide towards  $\text{FeCO}_3$  crystals. The  $\text{FeCO}_3$  prisms also appeared imperfectly formed, as shown in Figure 45. Iron oxides, such as  $\text{Fe}_2\text{O}_3$  and  $\text{Fe}_3\text{O}_4$ , were hypothesized to grow simultaneously with  $\text{FeCO}_3$  resulting in mixed crystal constituents within the corrosion product layer.

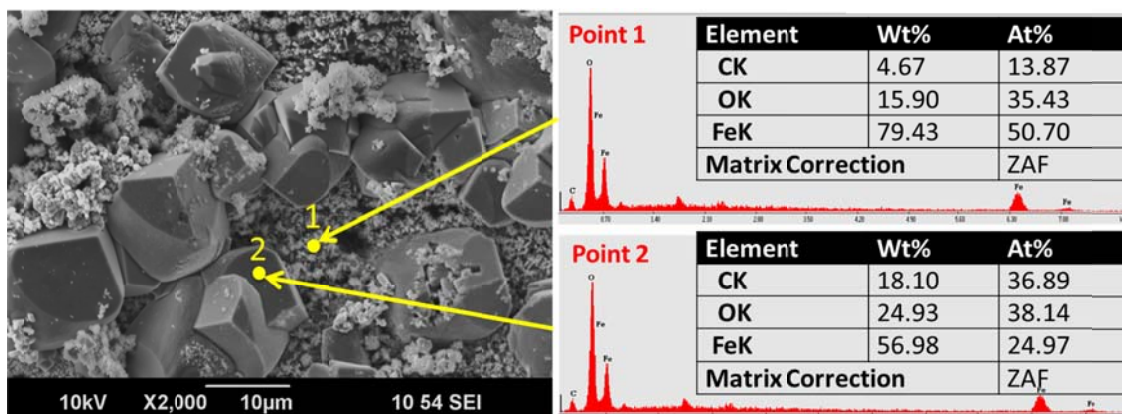


Figure 44. SEM image and EDS spectra of sample recovered after 8 days in Test C

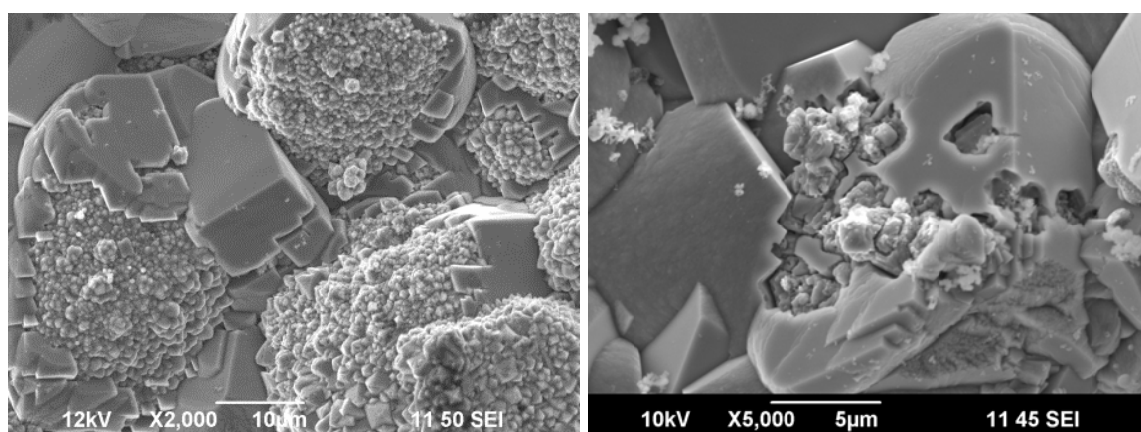


Figure 45. Imperfectly formed  $\text{FeCO}_3$  crystals covered with iron oxides

Post analysis of the specimen using XRD, Figure 46, revealed intense diffraction peaks consistent with the presence of hematite ( $\alpha\text{-Fe}_2\text{O}_3$ ) and magnetite ( $\text{Fe}_3\text{O}_4$ ), and weaker peaks of siderite ( $\text{FeCO}_3$ ), and goethite ( $\alpha\text{-FeO(OH)}$ ).

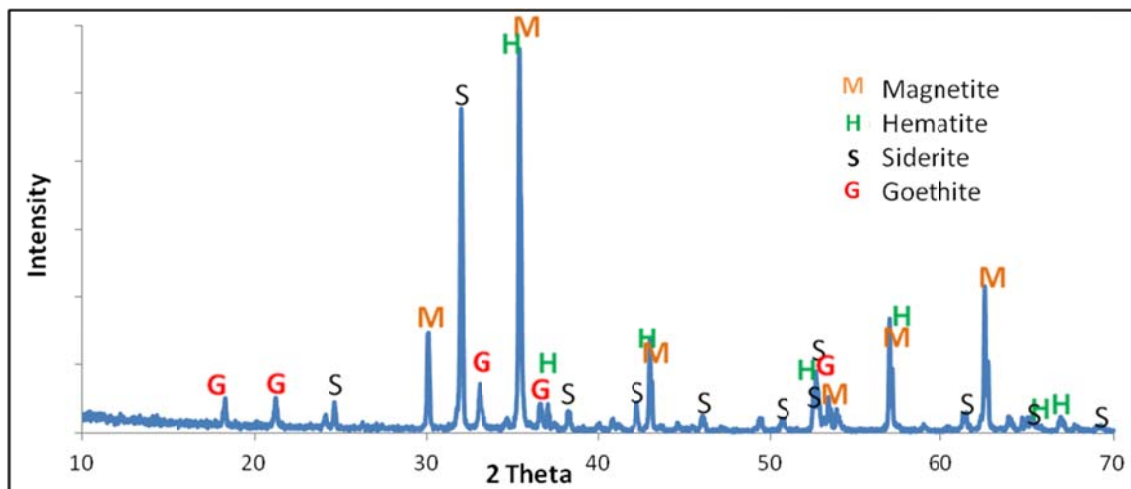


Figure 46. X-ray diffraction of the specimen recovered after 7 days in Test C.

Raman spectroscopy was utilized to complement the XRD data. Peaks for hematite, magnetite, goethite and siderite were identified, as shown in Figure 47. Note the absence of a strong vibrational mode at *ca.*  $1086\text{ cm}^{-1}$ , which is diagnostic for the presence of carbonate ( $\text{CO}_3^{2-}$ ). Taken in conjunction with the XRD data, the collected Raman data would be consistent with the presence of a primarily hematite-type ferric oxide ( $\text{Fe}_2\text{O}_3$ ) overlying the formed iron carbonate ( $\text{FeCO}_3$ ).

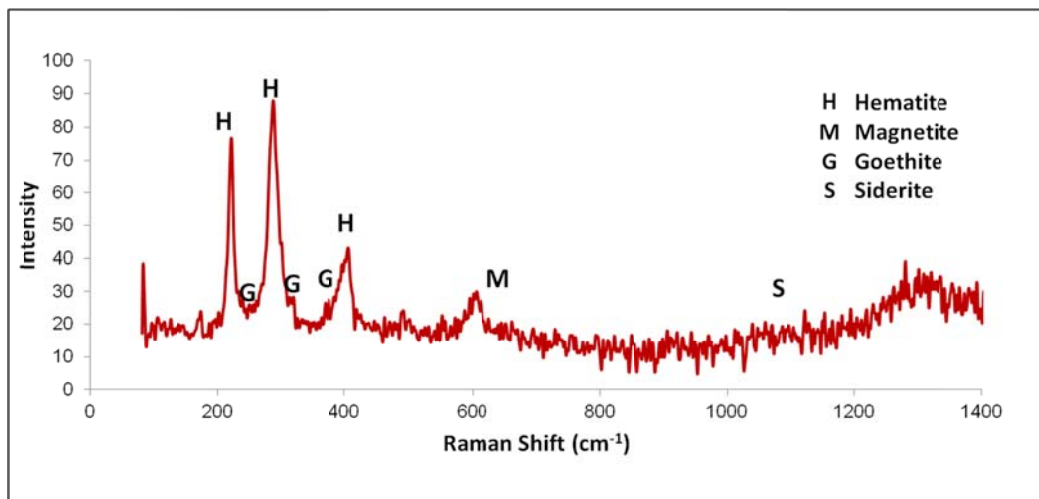


Figure 47. Raman spectra of specimen recovered after 7 days in Test C.

A cross-section of the specimen recovered at the conclusion of the experiment was characterized by SEM using back-scattered electrons to provide information on the compositional difference of the corrosion product layer, as shown in Figure 48. The contrasting shades produced by the SEM backscattered image shows formation of an oxide-encrusted corrosion product tubercle on top of a wide pit.

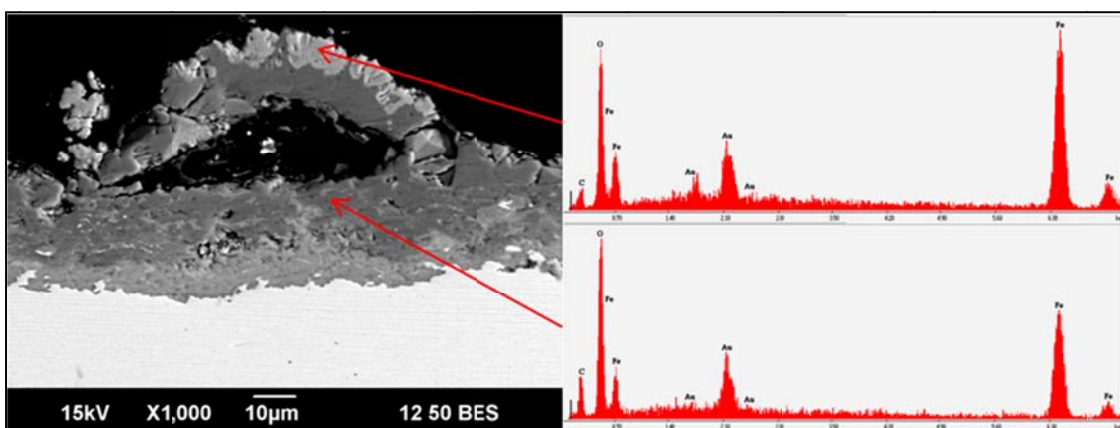


Figure 48. Cross-section of specimen recovered after 7 days of Test C

The compositional characteristic of the observed tubercles were in relatively close agreement with models reported by previous corrosion researchers [68], [70], [96]–[99]. One model suggested that tubercles commonly consist of five structural features; an outer crust ( $\text{Fe}_2\text{O}_3$ , hematite), inner shell ( $\text{Fe}_3\text{O}_4$ , magnetite), core ( $\text{FeCO}_3$ , siderite &  $\text{Fe}(\text{OH})_2$ , ferrous hydroxide), fluid cavity and steel floor, as shown in Figure 49 [68]. The fluid filled cavity can be seen in Figure 48 as a black region that has been filled by epoxy. The lighter colored region at the top of the tubercle can be speculated to be magnetite, with EDS analyses showing a low intensity C peak. Smaller particles on the outermost region of the tubercle were too porous to be meaningfully analyzed by EDS since they are filled with carbon-containing epoxy. Specimens recovered from Test B and Test C showed similar tubercle characteristics.

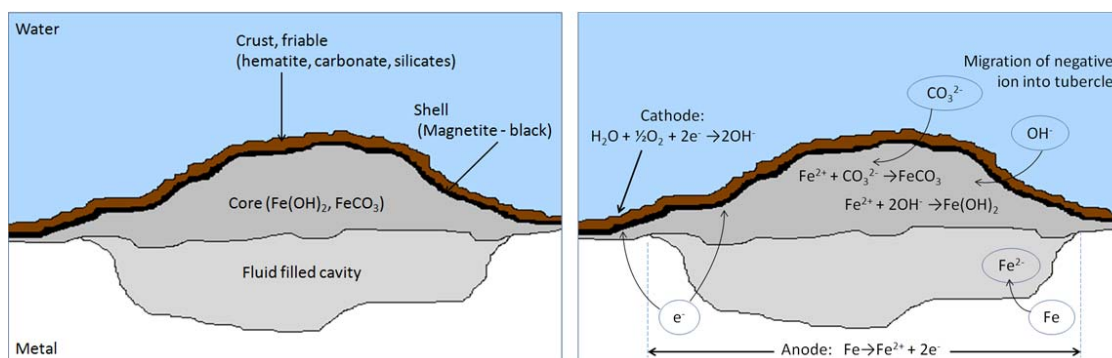


Figure 49. Schematic of a tubercle based on a study described by Herro [68].

The model shown in Figure 49 does not fully represent the phenomena that were observed in this study. The cross-section view in Figure 48 showed that the fluid filled

cavity was not in direct contact with steel floor, but was separated by another layer of corrosion product.

The entire steel surface underneath the corrosion product layer was severely damaged, as shown in Figure 50 for the specimen recovered at the conclusion of the test and treated with Clarke solution. Polish marks could no longer be seen on the surface of this specimen. The surface profile showed penetration depths approaching 100  $\mu\text{m}$ , as shown in Figure 51. The true depth of penetration was unable to be confirmed due to the unidentified original height of the surface.

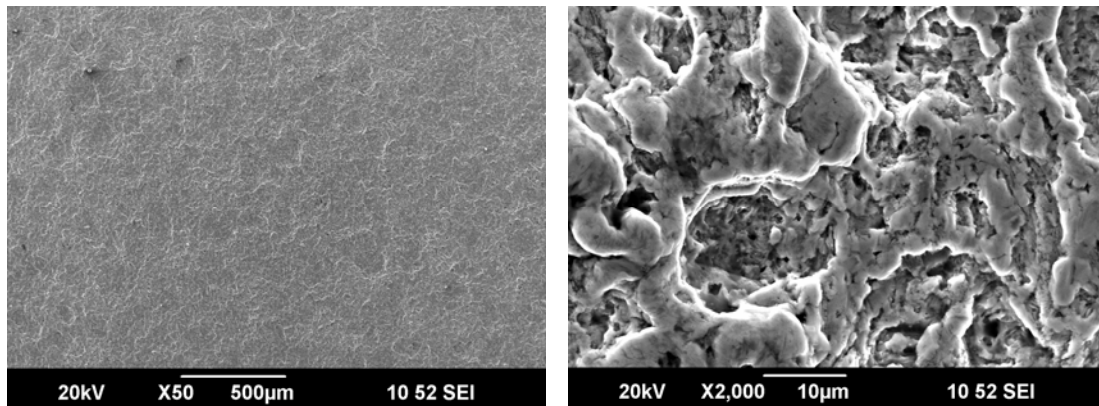


Figure 50. SEM image of steel surface for Test C after corrosion product removal

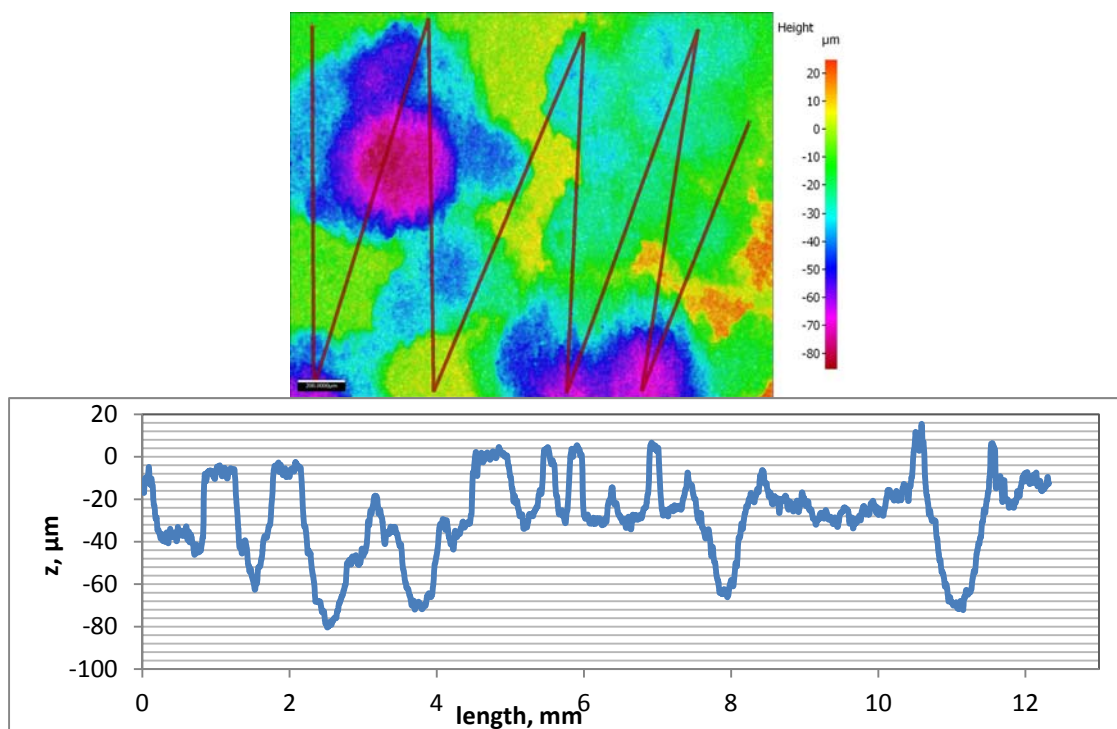


Figure 51. Pit depth analysis of specimen recovered at the end of Test C.

#### 4.5.4 Results Summary

The results from Test A, B and C can be analyzed by making comparisons between them for each condition. Figure 52 shows that the presence of  $O_2$  caused the final corrosion rate to be higher than the baseline,  $CO_2$  only, condition. This effect was also supported by the recorded corrosion rate based on the weight loss of the specimens as presented in Table 7. The corresponding corrosion rates of the specimens in Test B and Test C (oxic conditions) were one order of magnitude greater than for Test A (anoxic). Test C recorded the highest corrosion rate due to the longer exposure to  $O_2$ , while Test B had some form of protection against corrosion before the introduction of  $O_2$  into the system.

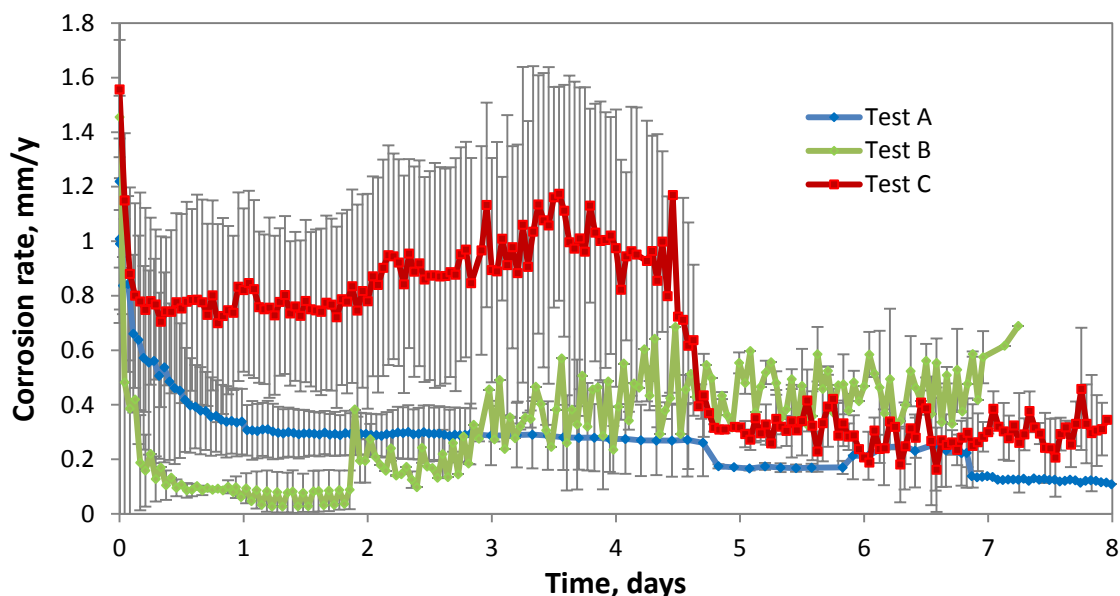


Figure 52. Corrosion rates comparison of Tests A, B and C.

Table 7: Summary of Corrosion Rate Results.

Experiment	Time-averaged corrosion rate from LPR, mm/y	Weight loss corrosion rate, mm/y
Test A	0.26	0.11
Test B	0.33	0.77
Test C	0.63	1.07

The corrosion potential in both Tests B and C ended in the same range of less negative values as compared to the potential in the baseline condition, shown in Figure 53. Although both oxidic conditions showed sudden shift in potential, the shift occurred at different times of the experiments. The shift in potential that occurred in Test B was due to the sudden introduction of  $O_2$  into the system, while the shift in Test C could be due to the change in the solution water chemistry and the compositional change on the steel surface due to corrosion products.

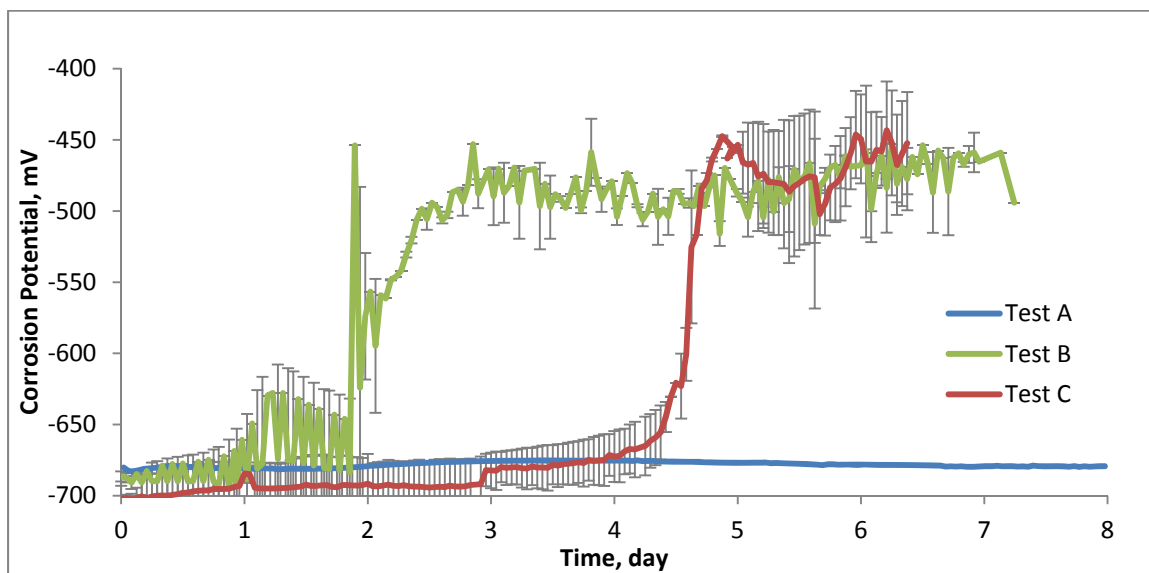


Figure 53. Corrosion potential of test A, B and C.

Figure 54 shows that the test solution also had relatively higher bulk pH due to the presence of  $O_2$ . This could be due to the oxidation of  $O_2$  in water that produces hydroxide ions ( $OH^-$ ) as mentioned in Equation (14).

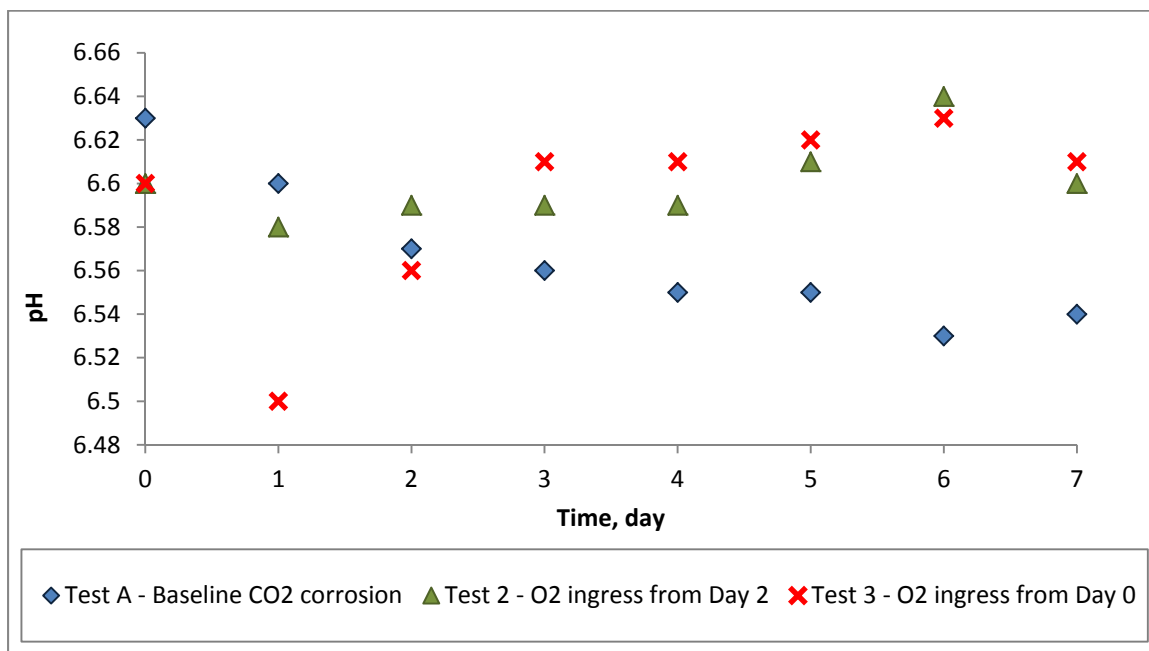


Figure 54. Comparison of test solution pH for Tests A, B and C.

#### 4.6 Proposed Corrosion Mechanism

Tuberculation, which has been associated with microbiologically induced corrosion [68] as well as corrosion in water distribution systems [70], [73], [96], [99], is caused by localized electrochemical processes at distinguishable anodic and cathodic sites. An  $O_2$  deficient region below the tubercle creates an anodic site, while cathodic sites are created around the surrounding area of the tubercle.

In this work, essentially the same principle was adopted to describe the corrosion mechanism in a  $CO_2$  system with  $O_2$  ingress. The mechanism can be described in six distinguishable steps, illustrated in Figure 55:

- 1) Formation of iron carbonate,  $FeCO_3$ .
- 2) Formation of iron oxides.

- 3) Volume reduction of solid material.
- 4) Pressure build-up in void spaces forming dome-like structures.
- 5) Rupture of top shell.
- 6) Underdeposit pitting caused by a galvanic effect

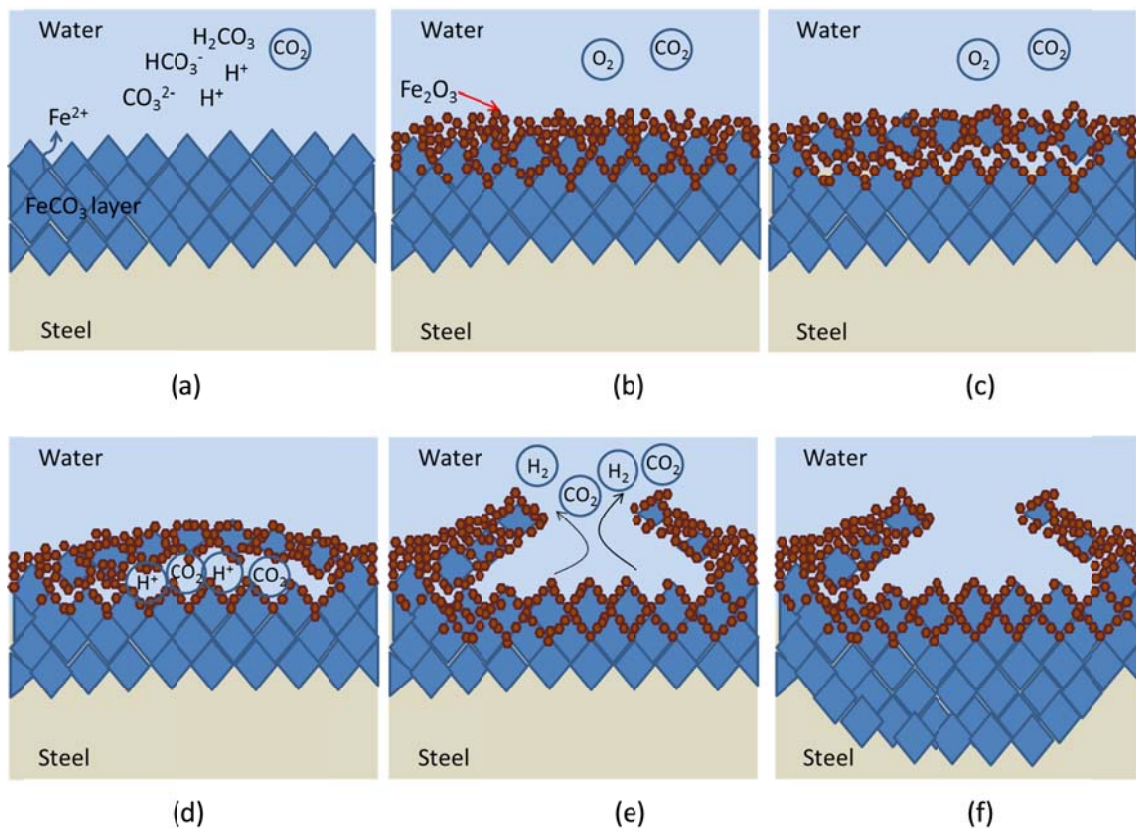


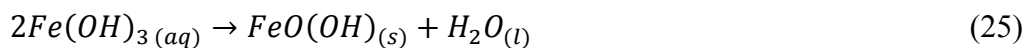
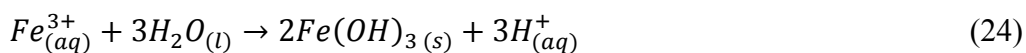
Figure 55. Proposed tuberculation mechanism in CO<sub>2</sub> corrosion with O<sub>2</sub> intrusion.

In an ideally anoxic and CO<sub>2</sub>-saturated solution, FeCO<sub>3</sub> will form on the surface of steel by electrochemical and chemical reactions (Figure 55(a)) in accordance with the

following steps. CO<sub>2</sub> gas dissolves in water and is hydrated into carbonic acid (H<sub>2</sub>CO<sub>3</sub>), which then dissociates into a bicarbonate ion (HCO<sub>3</sub><sup>-</sup>), which itself further dissociates into a carbonate ion (CO<sub>3</sub><sup>2-</sup>). Associated generated hydrogen ions (H<sup>+</sup>) undergo reduction concurrently with oxidation of iron, evolving H<sub>2</sub> gas. As the concentration of Fe<sup>2+</sup> and CO<sub>3</sub><sup>2-</sup> exceeds the solubility limit, a FeCO<sub>3</sub> layer is formed on the steel surface, see reaction (6) in Chapter 2, sub-section 2.3.1.

The ingress of O<sub>2</sub> adds an additional cathodic reaction, reduction of oxygen, see reaction (14) in section 2.5. With this additional cathodic reaction, the rate of anodic reaction will increase to compensate for the additional consumption of electrons.

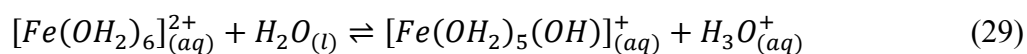
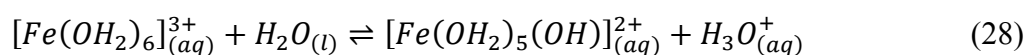
The available O<sub>2</sub> also causes the precipitation of highly insoluble iron oxides and oxyhydroxides, which then grows/settles on the FeCO<sub>3</sub> layer (Figure 55 (b)). Ferrous ions in the solution rapidly convert to ferric ions due to the oxidizing power of O<sub>2</sub>, which then precipitates into insoluble, loose, and porous Fe<sub>2</sub>O<sub>3</sub>, known as hematite.



The author found evidence of FeCO<sub>3</sub> dissolution by O<sub>2</sub> from observing oxide crystals on the faces of the FeCO<sub>3</sub> crystals, which was reported earlier in this chapter. The degradation of FeCO<sub>3</sub> crystals is expressed in the following reaction:



On a molar basis, the volume change from the conversion of 2 moles  $FeCO_3$  into 1 mole  $Fe_2O_3$  was determined. About 48.8% volume reduction of the occupied solid takes place during the conversion. It can be hypothesized that this volume change creates void spaces in between the  $FeCO_3$  crystals with a micro-environment that is lower in pH than in the bulk solution (Figure 55(c)). The lower pH value in the confined space is due to iron ion aquation and subsequent dissociation reactions that produce hydrogen ions. The creation of the aqua acids, hexaaquairon (II) ( $[Fe(H_2O)_6]^{2+}$ ) and hexaaquairon (III) ( $[Fe(H_2O)_6]^{3+}$ ), contributes to the lowering of the pH value. The iron (III) aqua ion has a  $pK_a$  value of 2.2, and is more acidic than the iron (II) ion ( $pK_a$  value of 8.3) [100] due to the greater positive charge of the central metal ion in the complex.



The acidic micro-environment promotes the dissolution of  $FeCO_3$  and releases  $CO_2$  gas. Hydrogen ions are also cathodically converted to  $H_2$  gas in this void space. The corrosion product layer above the cavity impedes the migration of the gases into the bulk solution, causing pressure build-up in the cavity, creating a dome-like structure (Figure 55(d)).

Localized regions of metal loss are capped with accumulated corrosion products and deposits of precipitates.

The cathodic reaction continues to consume the  $O_2$  that is confined in the cavity underneath the tubercle and becomes depleted with  $O_2$ , which results in a differential aeration cell. The area underneath the tubercle with the lower  $O_2$  concentration becomes the anode while the larger surface area of the steel that is directly exposed to the aerated bulk solution becomes the cathode. Anodic reaction increases the concentration of ferrous ions,  $Fe^{2+}$  and further decreases the pH of the micro-environment. The low pH accelerates the dissolution of metal and promotes crevice or localized corrosion. The  $FeCO_3$  layer becomes thicker under the deposit due to the saturation of  $Fe^{2+}$  and  $CO_3^{2-}$  ions in the confined space.

As the pressure inside the cavity continues to rise, the thin top shell of the dome loses its integrity and ruptures, releasing the trapped gases and ions into the bulk solution (Figure 55(e)). The system now has a galvanic effect between the damaged tubercle and the rest of the metal surface.  $FeCO_3$  forms downwards into the actively corroding steel, creating the broad depression that was observed underneath the tubercles (Figure 55(f)). The rupture of the tubercle's top shell may also be caused by stress at the crystal boundaries, which is a consequence of the previously discussed volume reduction.

All of these hypothesized corrosion mechanisms will require further investigation to confirm their validity. Amongst the phenomena that can be explored are hydrogen gas evolution, surface/pit pH changes, galvanic effects, and tubercle integrity.

#### 4.7 Chapter Summary

The above described sequence of corrosion process steps provides a basis for comparison with investigation of O<sub>2</sub> ingress in sweet corrosion environments at high pressure conditions, simulating the conditions in a CO<sub>2</sub>-EOR field. The observed influence of O<sub>2</sub> on sweet corrosion at low pressure was profound and must be seriously considered when selecting materials and performing corrosion control of mild steel. Localized corrosion was observed although the corrosion rates at the conclusion of all tests were relatively low. Surface analysis showed degradation of FeCO<sub>3</sub> crystals and formation of iron oxides. This degradation of initially formed FeCO<sub>3</sub> occurred concurrently with the development of localized corrosion features as deep as 100 μm. XRD and Raman confirm the formation of magnetite (Fe<sub>3</sub>O<sub>4</sub>), hematite (α-Fe<sub>2</sub>O<sub>3</sub>), and goethite (α-FeOOH) along with siderite (FeCO<sub>3</sub>) in corrosion products.

## CHAPTER 5: HIGH PRESSURE CORROSION TESTS

This chapter describes and discusses high pressure CO<sub>2</sub> corrosion experiments in the presence and absence of O<sub>2</sub>. Similar to the previous chapter, experimental methodologies and design are initially described, followed by discussion of results and a mechanistic description.

The set of experiments described herein investigates the corrosion behavior of carbon steel in simulated CO<sub>2</sub>-EOR environments with the presence of O<sub>2</sub> as an impurity in the CO<sub>2</sub> supply. The contaminant corresponds to the amount of O<sub>2</sub> that can be present in CO<sub>2</sub> from an oxyfuel combustion flue gas, in particular.

### 5.1 Introduction

The CO<sub>2</sub> utilized in CO<sub>2</sub>-EOR can be derived from natural or anthropogenic sources, for example, CO<sub>2</sub>-rich geologic reservoirs or byproduct gas from an industrial process. The SACROC unit of the Kelly-Snyder field in Texas receives its CO<sub>2</sub> supply from natural gas fields in southwest Texas [101], whilst the Weyburn-Midale fields in Saskatchewan, Canada receive CO<sub>2</sub> from a coal gasification plant in North Dakota [102]. However, unlike the above example, CO<sub>2</sub> sourced from power plants may contain significant levels of impurities, such as oxygen (O<sub>2</sub>), that pose a higher risk of corrosion to injection/production wells and related infrastructure. O<sub>2</sub> concentration in a CO<sub>2</sub> stream from the oxyfuel process can be as high as 3 vol.% [16] and further purification of the gas to eliminate the O<sub>2</sub> is considered unfeasible.

Previous studies have found that the existence of O<sub>2</sub> in sweet corrosion systems accelerated the corrosion rate of steel [20], [23], [55], [86], [87], [103] and caused pitting corrosion [82], [88]–[90]. The effect of O<sub>2</sub> on the corrosion mechanisms, especially at high CO<sub>2</sub> partial pressure, has not been thoroughly investigated.

The casing and tubing of injection wells are normally constructed out of carbon steel due to its high strength, durability in high pressure environments, low cost, ease of use in fabrication, and range of available corrosion mitigation strategies (*e.g.*, inhibitors). This makes carbon steel the preferred choice of material as compared to other materials such as corrosion resistant alloys (CRAs) [9]. Carbon steel grades J-55 and N-80 are typical examples of tubing/casing materials used in CO<sub>2</sub> injection [104], [105]. However, Kapusta and Canter [105] documented that corrosion was observed at Shell's CO<sub>2</sub>-EOR field in Mississippi after only 10 months of production. Their laboratory experiments conducted on J-55 and N-80 grade tubing from the CO<sub>2</sub>-EOR field showed high corrosion rates in their flow-through system (50 mm/year) and static system (13 mm/year).

In this work, the effect of O<sub>2</sub> (4 vol.%) on the corrosion performance of mild steel (UNS G10180) in CO<sub>2</sub>-saturated brine was investigated using a 4-liter autoclave in experiments of 48 hours duration. Experiments were conducted at temperature and pressure combinations that correspond to subcritical-supercritical conditions.

## 5.2 Sample Material and Preparation

Carbon steel UNS G10180 was again used to represent casing and tubing material, and has a ferritic/pearlitic microstructure that is similar to J-55 steel.

Cylindrical steel specimens were utilized in the corrosion study using electrochemical methods, while rectangular steel specimens were utilized for weight loss measurement and surface analysis, as shown in Figure 56. The dimensions of the steel samples are shown in Figure 57. The specimens were polished with a 600 grit silicon carbide (SiC) paper, cleaned with isopropanol in an ultrasonic bath, and dried using a heat gun prior to the experiments. Following the cleaning process, the mass and the dimensions of the specimens were measured and recorded.



Figure 56. Cylindrical and flat steel specimens for high pressure experiments.

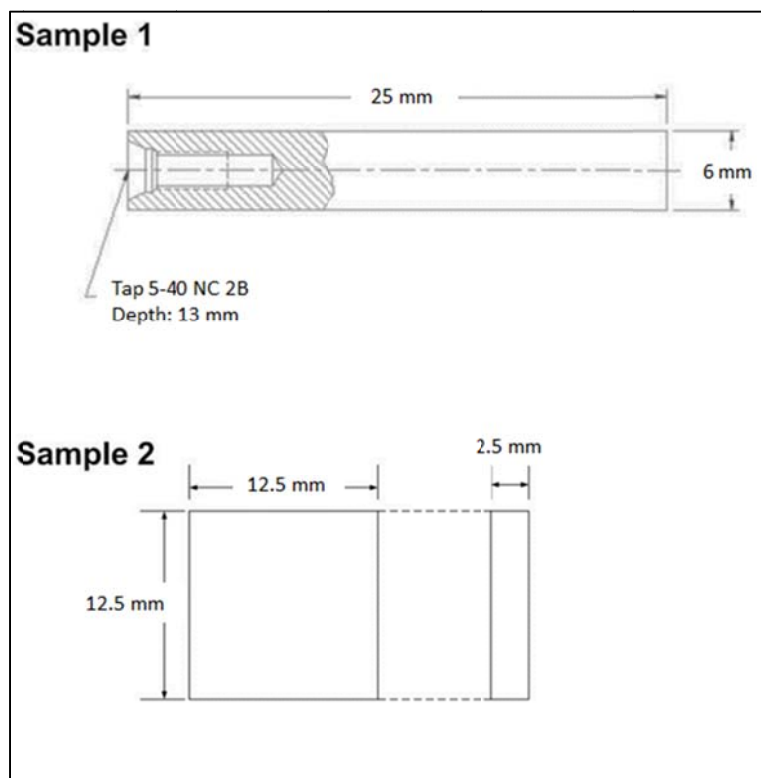


Figure 57. Dimensions of steel specimens used in the high pressure tests.

### 5.3 Experimental Set-up and Instrumentation

All high pressure tests in this set of experiments were conducted in a 4-liter stainless steel autoclave as illustrated in Figure 58 and Figure 59. The set-up consisted of a Pt-coated Nb counter electrode, a shaft for the steel specimen as the working electrode, a high pressure high temperature (HPHT) Ag/AgCl reference electrode, and a HPHT glass pH electrode that were all inserted through the stainless steel lid of the autoclave. The electrodes were immersed in 3 liters of solution (1 wt.% NaCl) that was saturated with CO<sub>2</sub> for at least 2 hours before the start of each experiment. O<sub>2</sub> was then bubbled into the sealed autoclave until the desired partial pressure was achieved. The O<sub>2</sub> gas input

was then shut off for the entire duration of the test. High pressure CO<sub>2</sub> was then added into the autoclave by a booster pump until the desired total pressure was achieved. The total pressure of the system was the sum of the partial pressures of O<sub>2</sub>, CO<sub>2</sub>, and water vapor. The vessel and solution temperature was controlled by a digital controller that was connected to the autoclave. The piping and instrumentation diagram of the setup is shown in Figure 60.

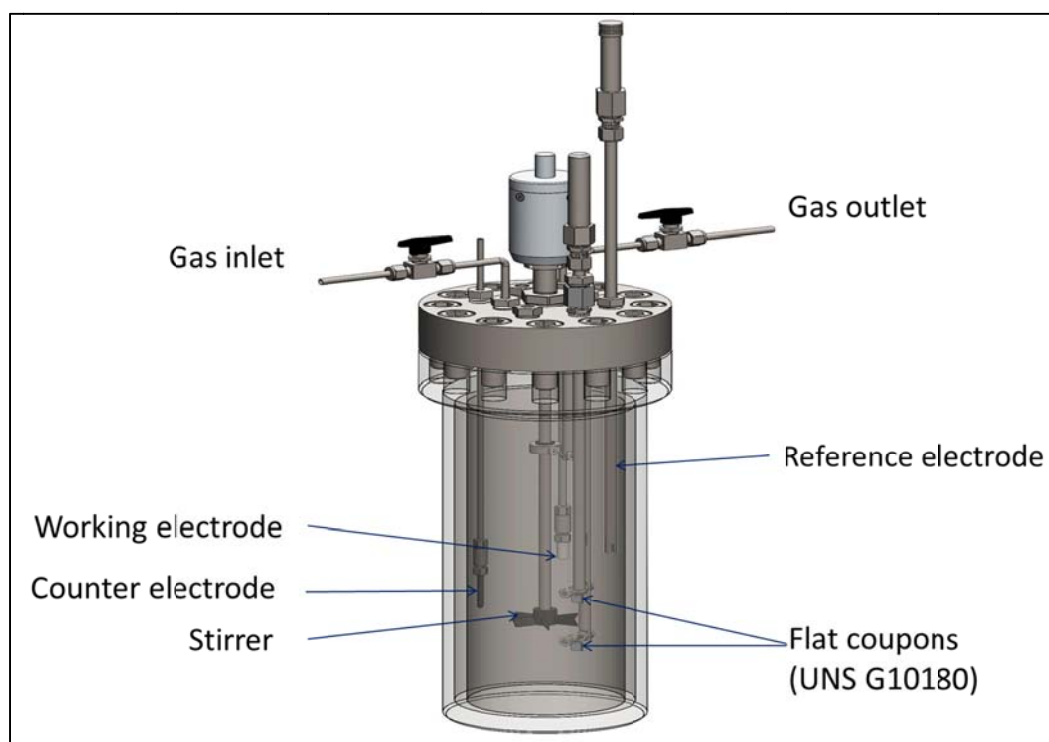


Figure 58. 4-L stainless steel autoclave diagram (Courtesy of Cody Shafer, ICMT)



Figure 59. The 4-L autoclave in ICMT

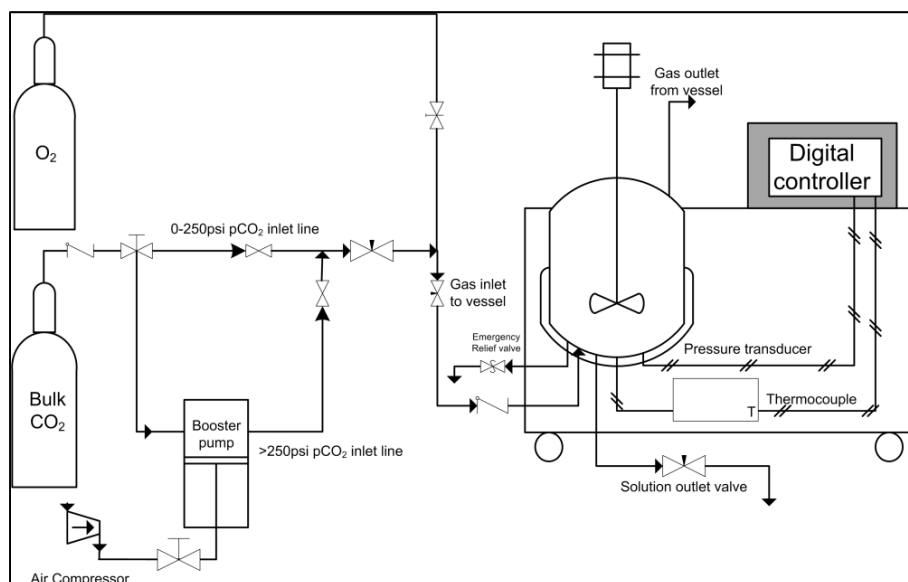


Figure 60. Piping and instrumentation diagram of the autoclave setup

#### 5.4 Measurements and Test Matrix

Experiments were conducted at two different temperatures (25°C and 80°C) and two different CO<sub>2</sub> partial pressures (40 and 90 bar). These temperature and pressure combinations encompass three different phases of CO<sub>2</sub>, illustrated as the corner points for the shaded region in the CO<sub>2</sub> phase diagram in Figure 61. The test matrix is shown in Table 8. All tests were compared with a baseline condition without the presence of O<sub>2</sub>. The presence of 4% O<sub>2</sub> only slightly shifts the critical points of the CO<sub>2</sub>/O<sub>2</sub> mixture, maintaining the same three phases of CO<sub>2</sub> in the different experiments.

Corrosion rates were measured continuously using the linear polarization resistance (LPR) method. A Gamry Reference 600 potentiostat was utilized for this purpose. The OCP was monitored throughout the experiment to ensure a stable condition for accurate electrochemical measurements. The potential was polarized at  $\pm 5$  mV with respect to the OCP at a 0.125 mV/s scan rate, as mentioned in Chapter 4. The Stern-Geary coefficient,  $B$  value, used in the calculation of corrosion rates in this work was 26 mV. Previous high pressure corrosion tests performed using this value had corrosion rates that corresponded to the weight loss corrosion rates [106]. Electrochemical impedance spectroscopy (EIS) was conducted to determine the value of the solution resistance in order to correct the polarization resistance values obtained from LPR measurements. Besides LPR, the average corrosion rates were also determined *via* weight loss at the end of the 48-hour tests. Steel specimens were removed from the autoclave at the completion of the high-pressure tests, rinsed with isopropanol, placed in individual nitrogen-purged bags, and stored in a dry cabinet. Post-test analyses of the specimens

were conducted using scanning electron microscopy (SEM), energy dispersive X-ray spectroscopy (EDS), Raman spectroscopy, and X-ray diffraction (XRD). The surface of the steel underneath the corrosion product was exposed using a Clarke solution (ASTM G1-03). The uncovered steel surface was characterized using SEM and by profilometry with an optical 3D measurement device.

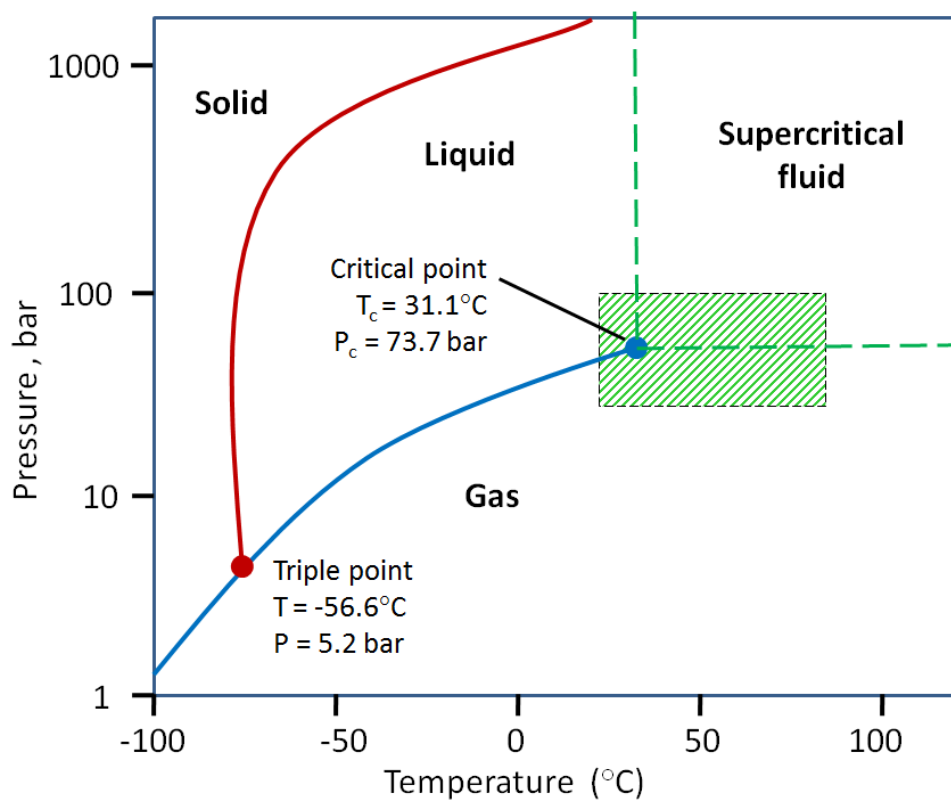


Figure 61. Boundary conditions of experiment in the CO<sub>2</sub> phase diagram

Table 8: Test Matrix for High Pressure Corrosion Test.

Expt. No.	T (°C)	pCO <sub>2</sub> (bar)	pO <sub>2</sub> (bar)	CO <sub>2</sub> Phase
1	25	40	0 & 1.7	Gas
2	25	90	0 & 3.75	Liquid
3	80	40	0 & 1.7	Gas
4	80	90	0 & 3.75	Supercritical

## 5.5 Results and Discussion

### 5.5.1 Experiment 1: 25°C, 40 bar pCO<sub>2</sub>, with and without 4% O<sub>2</sub>.

In this experiment, the CO<sub>2</sub> is in its gaseous state. Figure 62 shows the variation of the mean corrosion rate with time for the cases with and without O<sub>2</sub> at 40 bar CO<sub>2</sub> and 25°C, as measured using LPR. Error bars on the plot indicate maximum and minimum recorded values. The presence of O<sub>2</sub> in the system showed an increase in the overall corrosion rate of the steel sample. These values were integrated over time and were comparable to the weight loss corrosion rate that was measured at the end of the 48-hour experiments, as shown in Figure 63. The corrosion potential of both oxic and anoxic systems, however, did not show a significant difference between each set of experiments, see Figure 64.

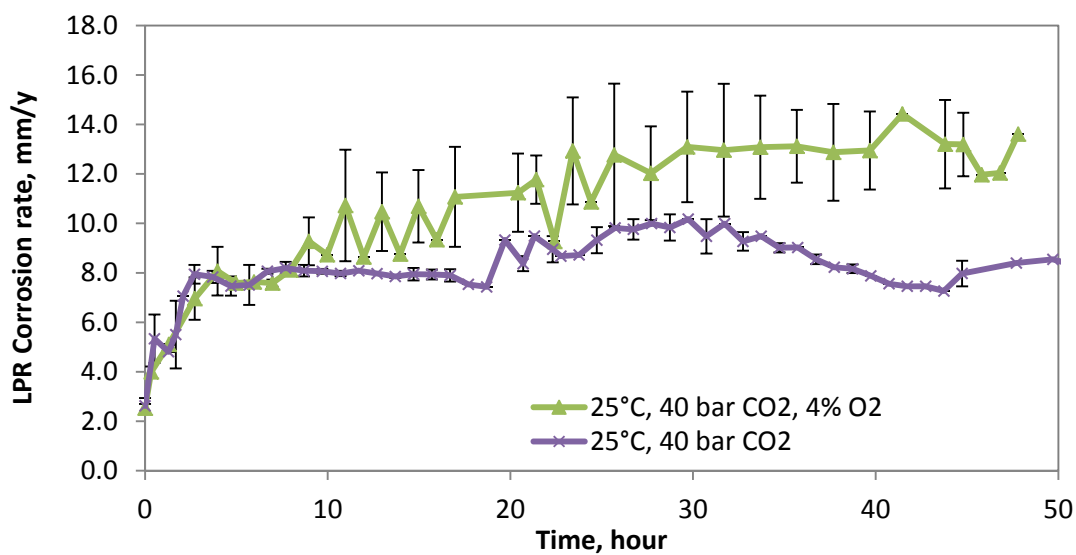


Figure 62. LPR corrosion rate with time for experiments at 25°C, 40 bar pCO<sub>2</sub>, with and without 4% O<sub>2</sub>.

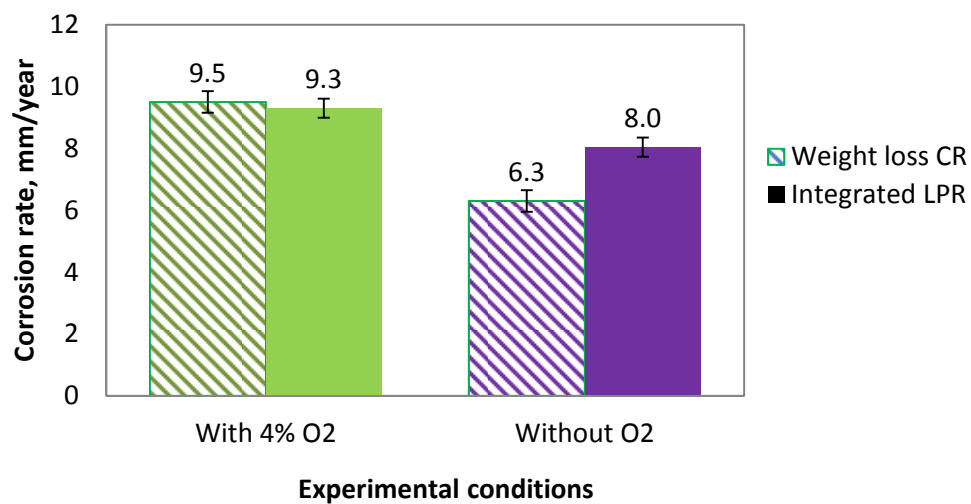


Figure 63. Weight loss corrosion rates compared to LPR time-integrated corrosion rates for experiments at 25°C, 40 bar pCO<sub>2</sub>, with and without 4% O<sub>2</sub>.

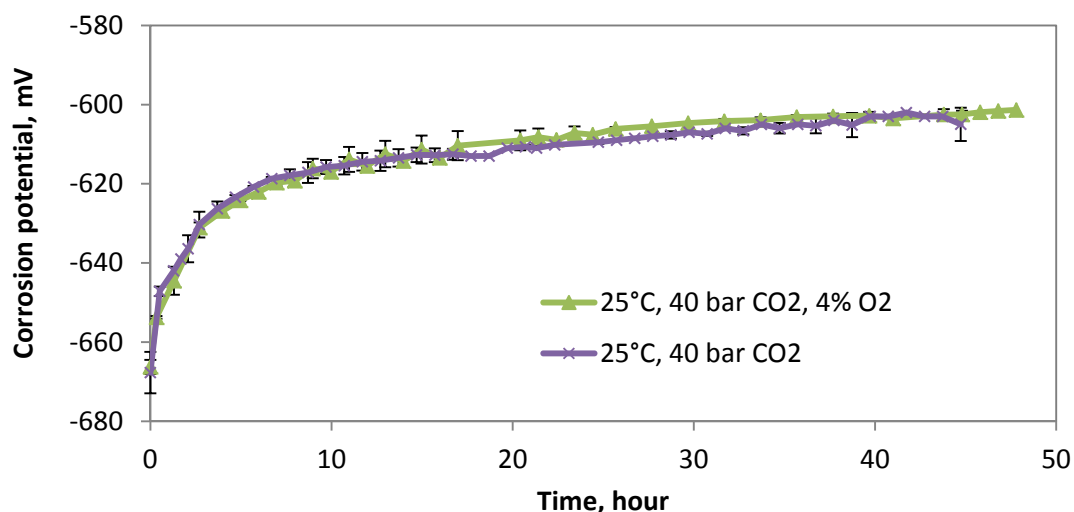


Figure 64. Corrosion potential for experiments at 25°C, 40 bar pCO<sub>2</sub>, with and without 4% O<sub>2</sub>.

By visual inspection, the steel sample that was exposed to the anoxic environment for 48 hours appeared clear of any obvious corrosion products on its surface, as can be seen by the absence of any crystalline features on the surface of the specimens shown in Figure 66. On the other hand, the steel sample from the CO<sub>2</sub>/O<sub>2</sub> experiments appeared to have a thin layer of bluish-green corrosion products that turned yellowish after about 20 to 30 minutes post-recovery. Elemental analysis using EDS, shown in Figure 66, revealed a higher percentage of oxygen, O, that can be due to the presence of a thin iron oxide film on the steel surface. Alloying elements such as molybdenum, manganese, and copper were also detected on the steel surface. Using a 3D optical microscope, the surface profile of the bare steel surface was measured, and exhibited uniform corrosion across the whole steel surface.



Figure 65. Bluish-green corrosion product on a recovered steel specimen for experiment at 25°C, 40 bar pCO<sub>2</sub>, with 4% O<sub>2</sub>

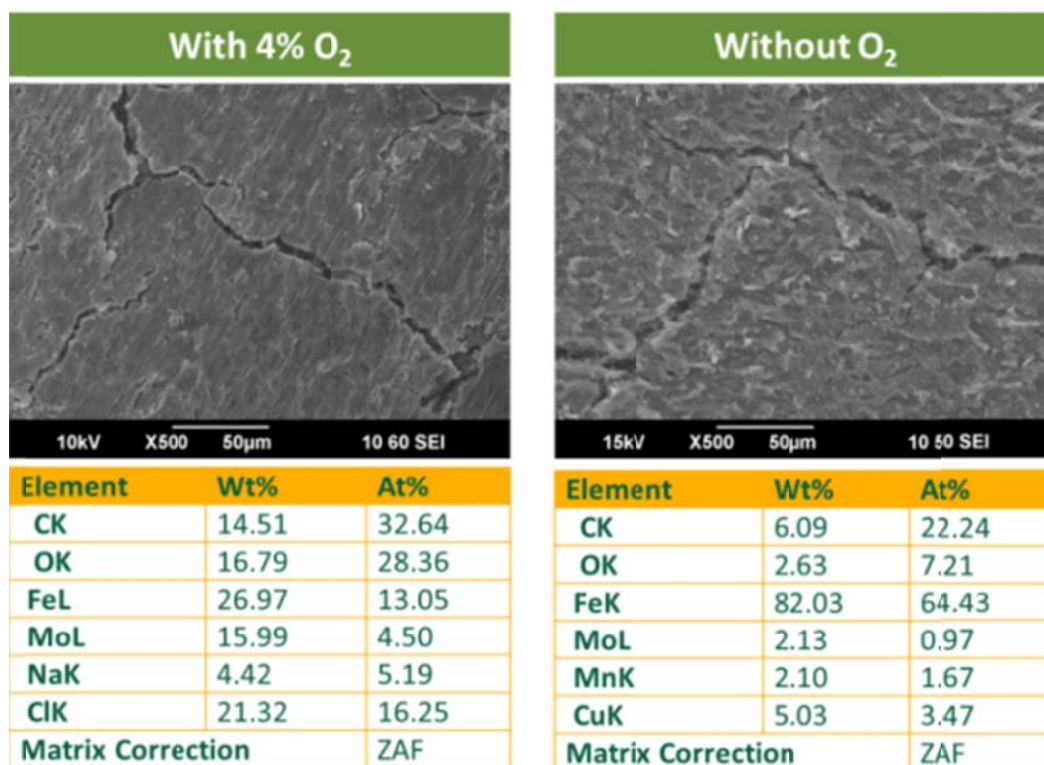


Figure 66. SEM and EDS analysis of steel surface at the end of 25°C, 40 bar pCO<sub>2</sub>, with and without 4% O<sub>2</sub> experiments.

Cross-sectional analysis of the steel samples exhibited a layer on top of the steel surface having morphological features that were loose and fragile, typical of skeletal iron

carbide. The thickness of the corrosion product, as seen in Figure 67, did not conform to an expected thickness of residual carbide on the steel surface. Due to its fragile nature, some amount of iron carbide was probably lost during the tests. The amount of iron loss in the O<sub>2</sub> experiment, based on the weight loss corrosion rate, corresponded to an approximate 52 μm thickness, as compared to the 15 μm thick layer of carbide/alloying element residue observed under SEM. This suggests that some of the iron carbide must have been lost or spalled off from the steel surface due to its fragility. The calculated iron loss for the experiment without O<sub>2</sub> was 34 μm, which corresponds to the 40 μm thickness shown in the cross-section. The presence of this iron carbide layer was confirmed by XRD analysis, as shown in Figure 68.

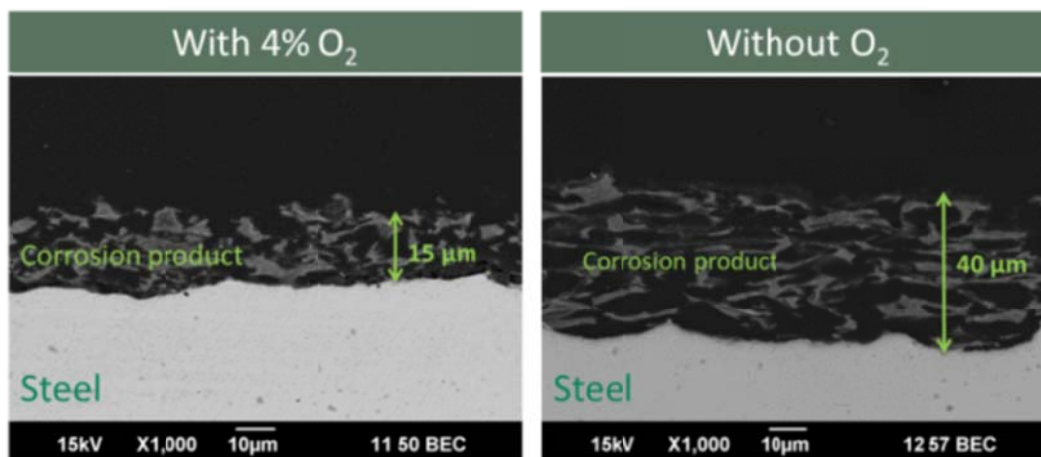


Figure 67. Steel cross-sections at 25°C, 40 bar pCO<sub>2</sub>, with and without 4% O<sub>2</sub>

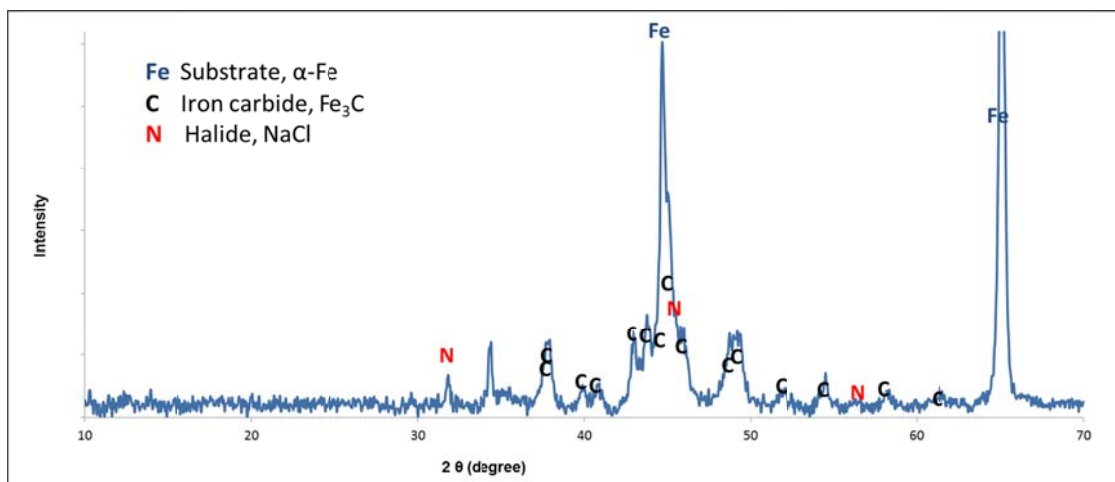


Figure 68. XRD analysis for specimen at 25°C, 40 bar  $\text{pCO}_2$ , with 4%  $\text{O}_2$  for 48 h.

Although the presence of  $\text{O}_2$  caused the corrosion rate to increase, the occurrence of pits or localized corrosion were not detected, as shown in Figure 69. The overall steel surface was uniformly corroded and the polishing lines were no longer visible.

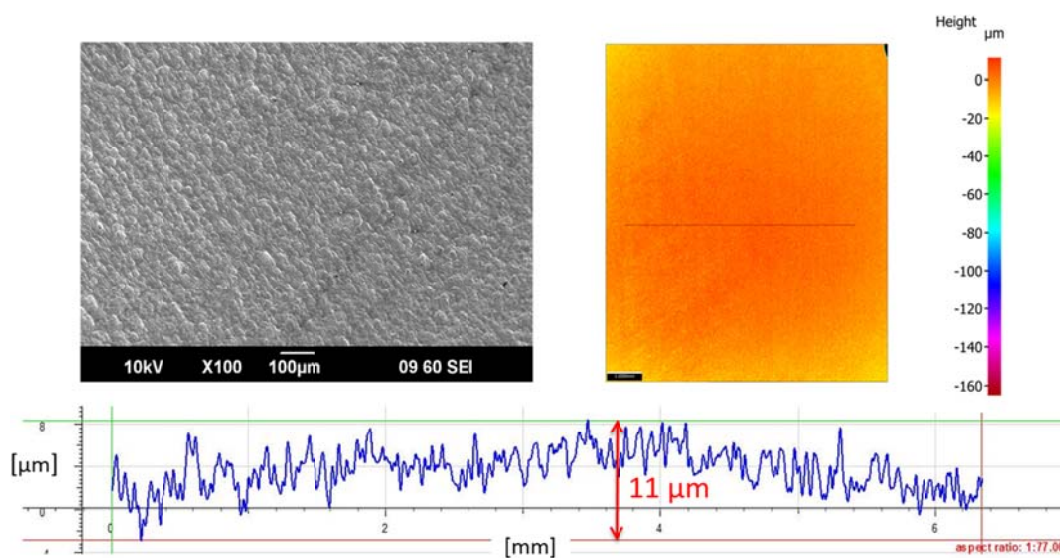


Figure 69. Profilometry of specimen at 25°C, 40 bar  $\text{pCO}_2$ , with 4%  $\text{O}_2$  after 48 h.

### 5.5.2 Experiment 2: 25°C, 90 bar pCO<sub>2</sub>, with and without 4% O<sub>2</sub>.

At this condition, CO<sub>2</sub> was in its liquid state. The corrosion rates, measured by LPR, showed a similar trend of higher corrosion rates of steel observed in the presence of O<sub>2</sub>, as was seen in the previous sub-section. Figure 70 shows a relatively constant and stable corrosion rate values for both oxic and anoxic condition. An almost similar test, conducted at 25°C and 80 bar CO<sub>2</sub>, reported similar findings where the corrosion rate stayed relatively constant at 5 mm/year [61]. The calculated time-integrated value of the LPR corrosion rate was 7.2 mm/year and 12.9 mm/year for the anoxic and oxic experiments, respectively.

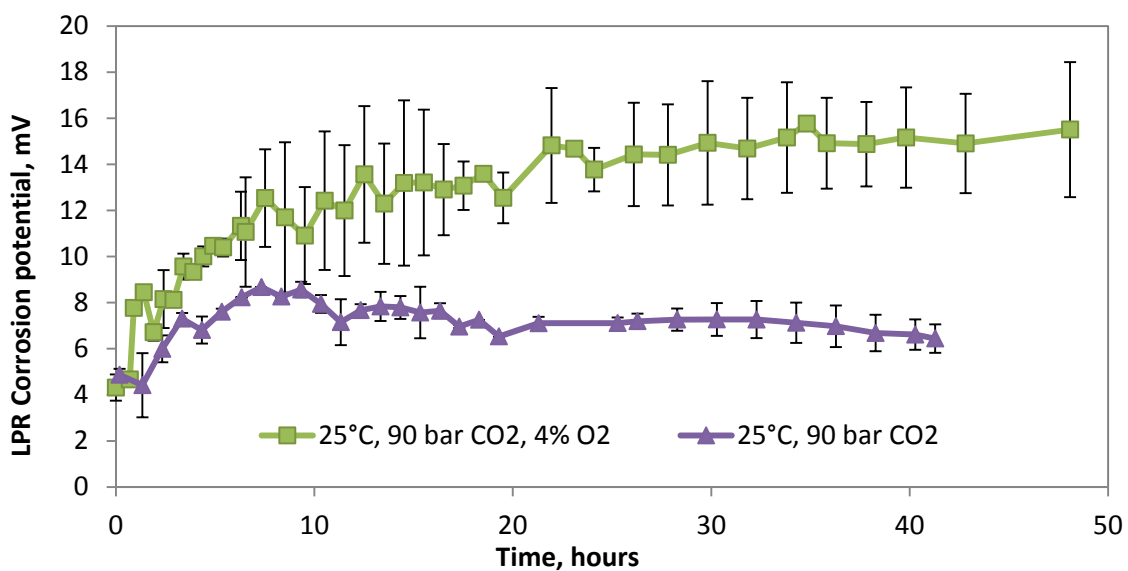


Figure 70. LPR corrosion rate with time for experiments at 25°C, 90 bar pCO<sub>2</sub>, with and without 4% O<sub>2</sub>.

The time-integrated values were compared with the weight lost corrosion rate, shown in Figure 71, showing that the presence of O<sub>2</sub> resulted in higher corrosion rates. In an almost similar test, conducted at 25°C, 80 bar pCO<sub>2</sub>, it reported a maximum LPR corrosion rate of 7 mm/year [106], comparable with the time-integrated corrosion rate of the anoxic experiment at a slightly higher CO<sub>2</sub> partial pressure. There is a high discrepancy between the weight loss corrosion rate for the experiment without O<sub>2</sub> with the corrosion rate measured using LPR. However, the repeatability of this particular condition was high, and observed in three separate repeat experiments. This deviation in value could be due to technical error during preparation and handling of the test specimen.

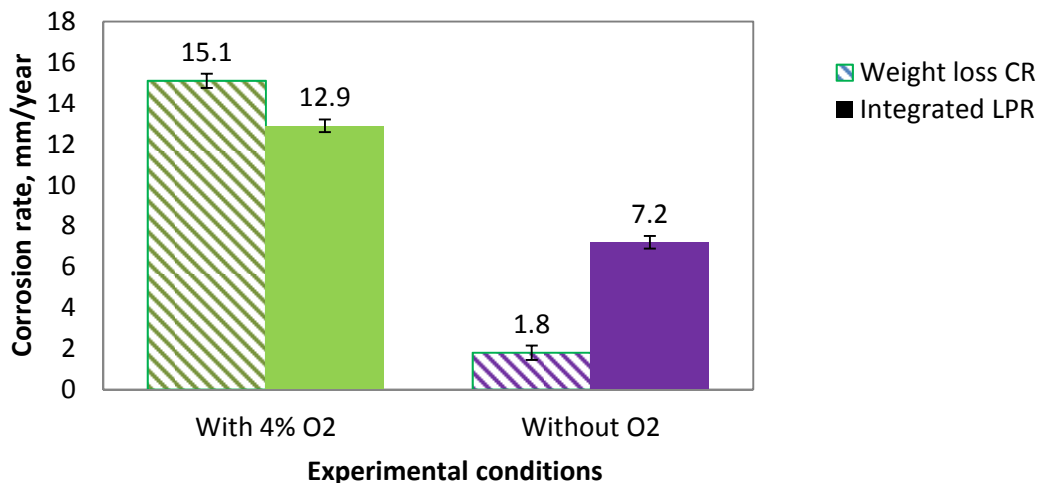


Figure 71. Weight loss corrosion rates compared to LPR time-integrated corrosion rates for experiments at 25°C, 90 bar pCO<sub>2</sub>, with and without 4% O<sub>2</sub>.

The presence of  $O_2$  did not significantly affect the corrosion potential, as shown in Figure 72. Similar behavior was discussed in the previous sub-section for the experiments at 40 bar  $CO_2$ .

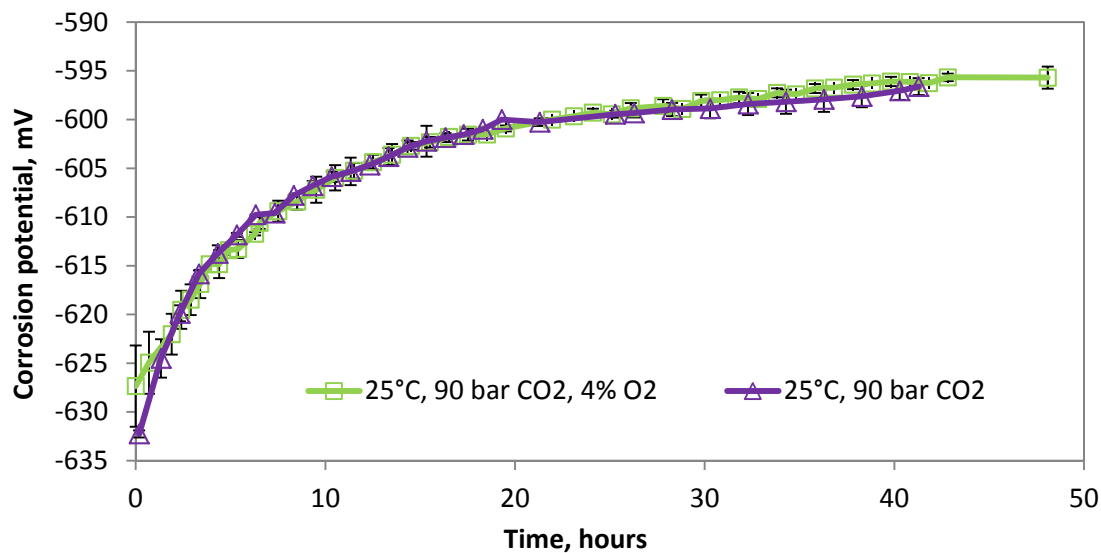


Figure 72. Corrosion potential with time for experiments at 25°C, 90 bar  $pCO_2$ , with and without 4%  $O_2$ .

The condition of each steel surface at the end of the experiments was similar to what was observed at 40 bar  $CO_2$ . No obvious crystalline features or precipitate accumulation were found when observed using SEM, as can be seen in Figure 73. EDS indicated that O was more abundant on the specimen that was exposed to oxic conditions. Higher percentages of the alloying elements copper, molybdenum, and nickel were also detected on the steel surface.

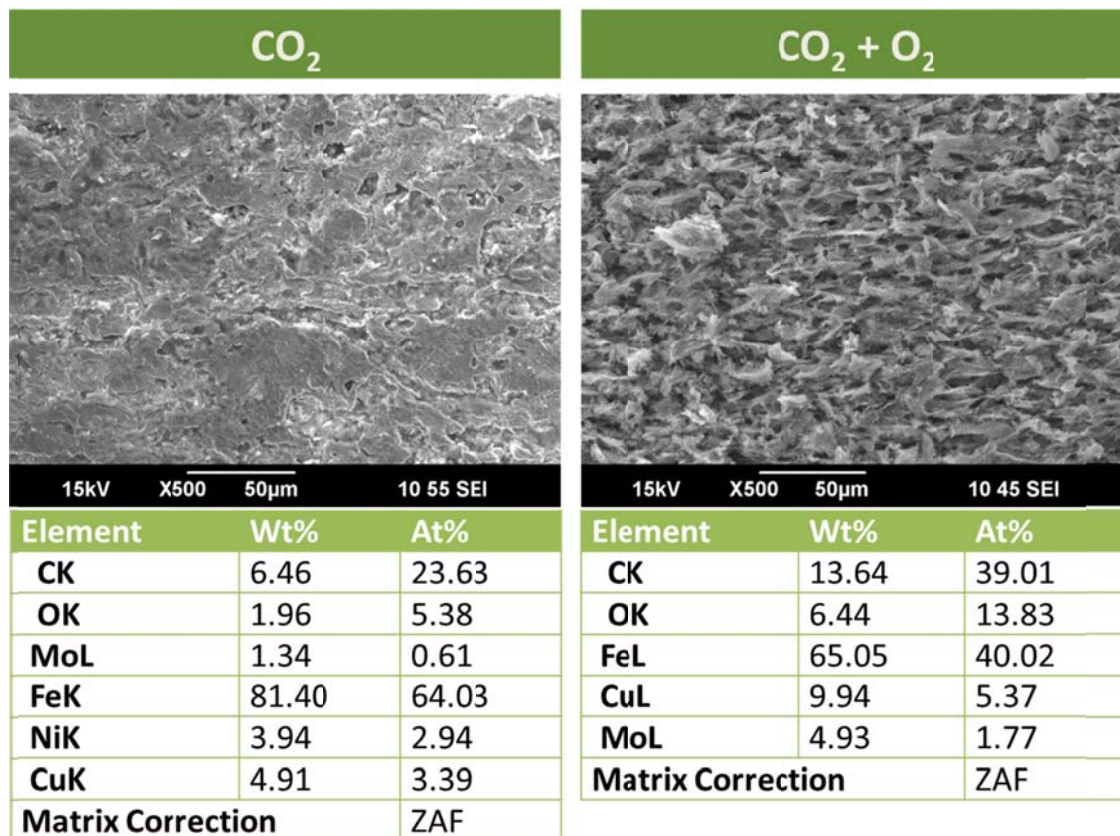


Figure 73. SEM micrographs and EDS analysis of steel surface at the end of 25°C, 90 bar pCO<sub>2</sub>, with and without 4% O<sub>2</sub> experiments.

The cross-sectional view of the specimens showed typical features of skeletal iron carbide layers on the steel surface, as shown in Figure 74. The presence of this fragile iron carbide layer was confirmed by the obvious peaks that were observed through XRD analysis, shown in Figure 75. The corresponding iron loss was calculated using values of weight loss corrosion rate and was compared with the thickness of the corrosion product that was observed on the cross-sectional view of the specimens. The amount of iron losses for the specimen in the anoxic and oxic are 10 µm and 78 µm, respectively. These values are greater than the values shown in the cross-sections of the steel specimen,

possibly due to the fragile nature of iron carbide that could have been removed during the course of the experiments.

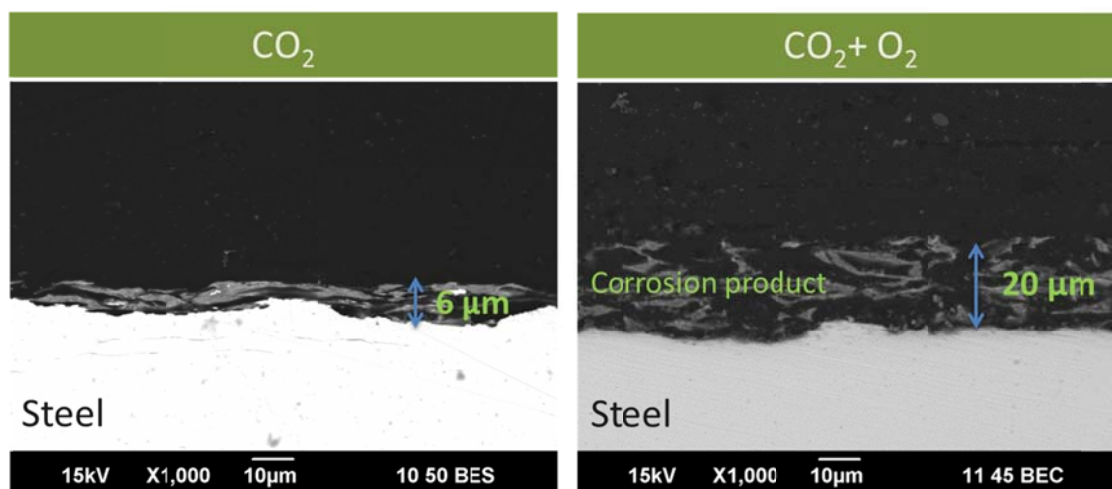


Figure 74. Steel cross-sections at the end of 25°C, 90 bar pCO<sub>2</sub>, with and without 4% O<sub>2</sub> tests.

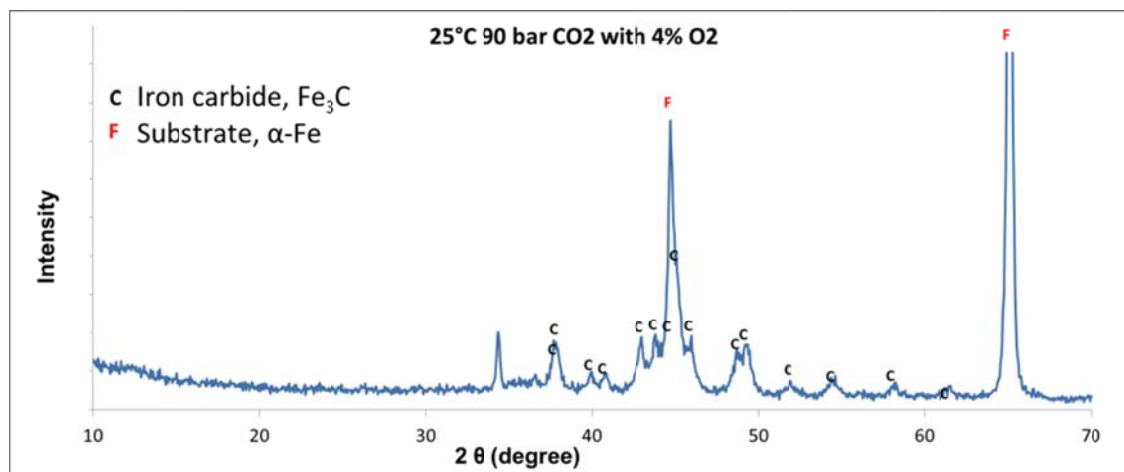


Figure 75. XRD analysis for specimen at 25°C, 90 bar pCO<sub>2</sub>, with 4% O<sub>2</sub>, 48h.

When corrosion product removal treatment was applied on the steel, it revealed uniform corrosion on the bare steel surface with no obvious pits, as shown in Figure 76, an observation that is similar to the condition at 40 bar CO<sub>2</sub>.

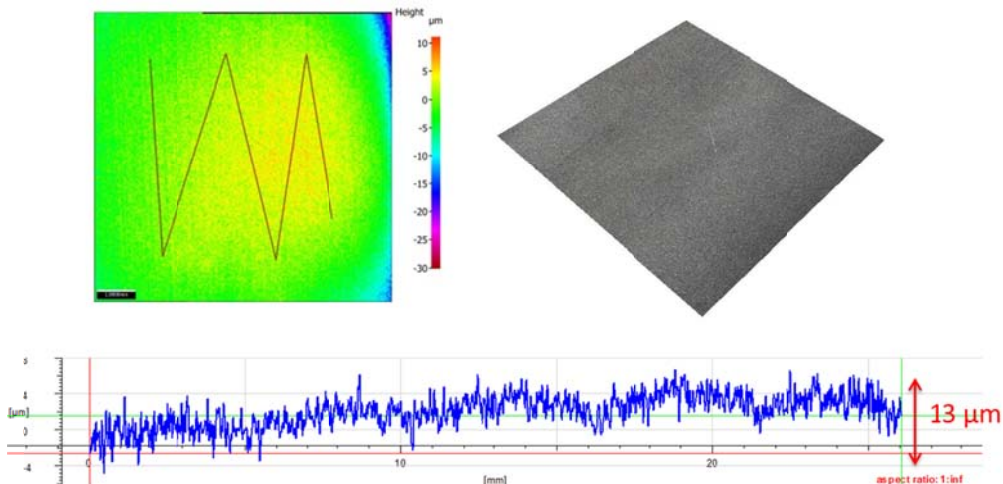


Figure 76. Profilometry of steel specimen at at 25°C, 90 bar pCO<sub>2</sub>, with 4% O<sub>2</sub>, 48h

### 5.5.3 Experiment 3: 80°C, 40 bar pCO<sub>2</sub>, with and without 4% O<sub>2</sub>.

In this experiment, the CO<sub>2</sub> is in its gaseous state. Figure 77 shows the electrochemical measurements using LPR, note the changes of the corrosion rate throughout the duration of the experiment for tests conducted with and without the presence of 4% O<sub>2</sub>. Both conditions showed the same trends of high corrosion rate during the first several hours of the experiment which then dropped to values less than 0.5 mm/year. This drop of corrosion rate values is an indication of a corrosion product that had formed on the surface of steel, serving as a protective barrier against further corrosion. This drop of corrosion rate was not observed in the previous experiment at 25°C due to the absence of a protective corrosion product layer, *i.e.* FeCO<sub>3</sub>, on the steel

surface. The kinetics of  $\text{FeCO}_3$  formation is much slower at low temperature. Corrosion rates with  $\text{O}_2$  ingress reached a maximum of about 47 mm/year as compared to 18 mm/year for baseline  $\text{CO}_2$  corrosion.  $\text{O}_2$  ingress exhibited higher final LPR corrosion rate (0.7 mm/year) than the baseline condition (0.1 mm/year).

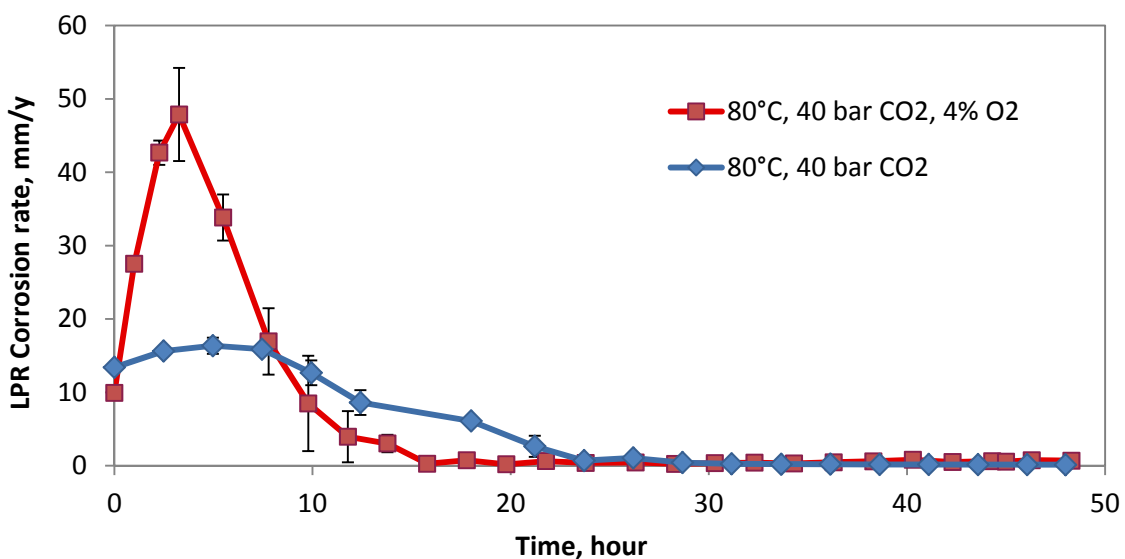


Figure 77. Corrosion rates of steel at 80°C and 40 bar  $\text{CO}_2$  with and without  $\text{O}_2$ .

Figure 78 represent the corrosion potential that was measured throughout the duration of each experiment. Both systems exhibited a steady increase of the potential due to the formation of protective layers on the steel surface from the 10<sup>th</sup> hour to the 20<sup>th</sup> hour, concurrent with the decrease of corrosion rate. The slow increase in the corrosion potential (about 150 mV) until the 40<sup>th</sup> hour, as seen in the baseline experiment, then became relatively constant at about -440 mV. This may be due to the development of a passive corrosion product layer that provided protection to the steel surface. The presence of  $\text{O}_2$  resulted in a sharp increase (about 400 mV) in the corrosion potential which later

dropped after the 20<sup>th</sup> hour and then became constant at about -420 mV around the 40<sup>th</sup> hour. Based on the potential change, the formation of a corrosion product layer with the presence of O<sub>2</sub> is more rapid due to the increase in oxidizer concentration in the system that produces excessive amounts of precipitation and corrosion products.

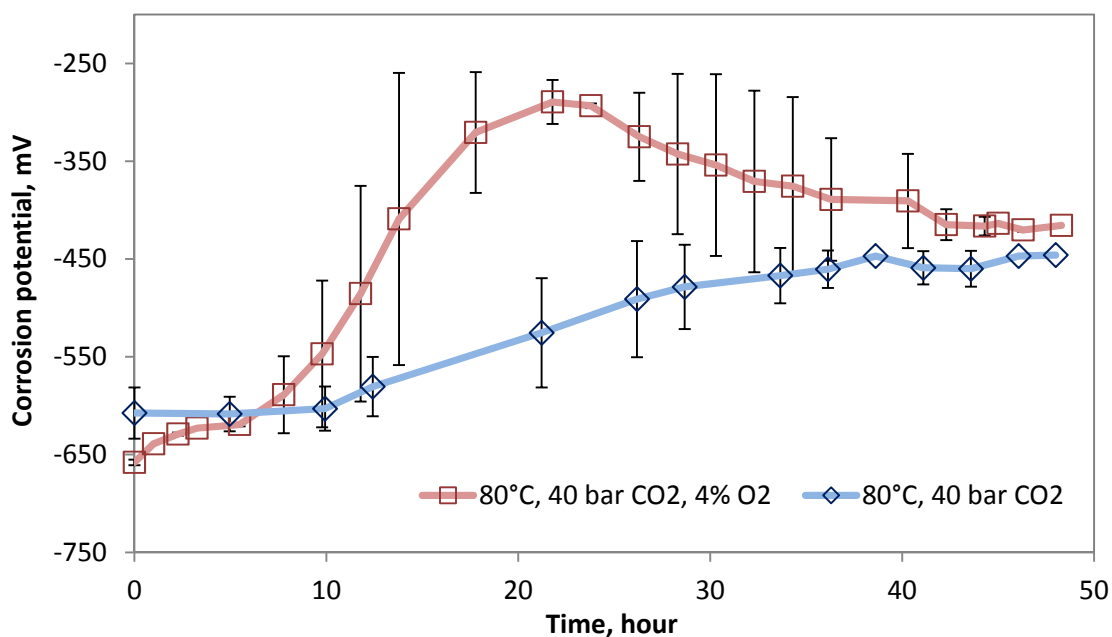


Figure 78. Corrosion potential of steel at 80°C and 40 bar CO<sub>2</sub> with and without O<sub>2</sub>.

Corrosion rate was also measured by weight loss method, which was then compared with the integrated values of corrosion rates from the LPR measurements. The weight loss method represented the value of the overall corrosion rate during the 48-hour period whereas the LPR corrosion rates were measured continuously throughout the test duration. The comparison, which can be seen in Figure 79, showed that the weight loss corrosion rates were comparable with the LPR corrosion rates. The presence of O<sub>2</sub> in this experiment resulted in a higher CO<sub>2</sub> corrosion rate.

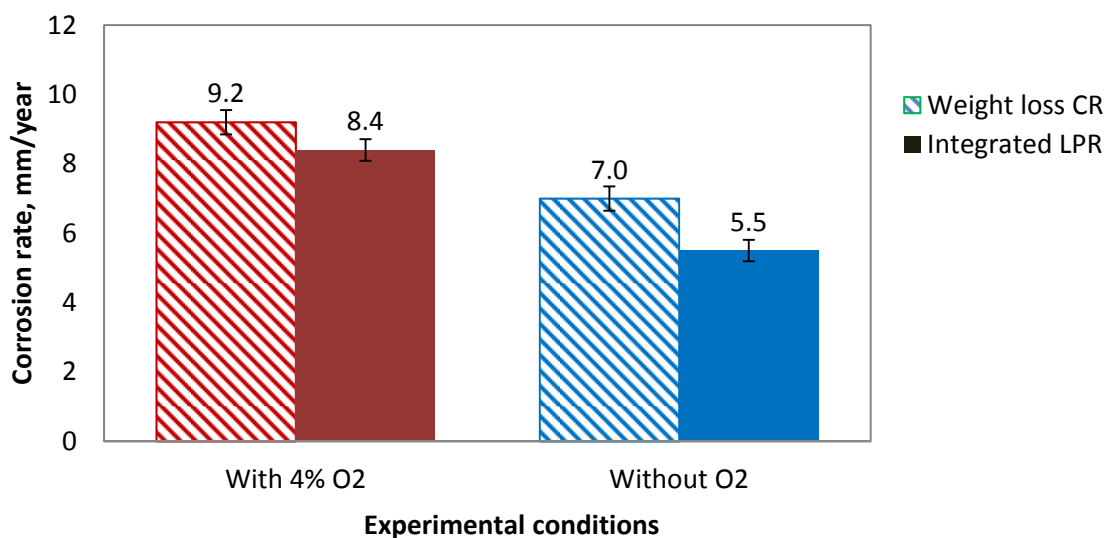


Figure 79. Corrosion rates measured using weight loss technique compared with integrated LPR results for conditions with and without O<sub>2</sub> at 80°C, 40 bar CO<sub>2</sub> after 2 days of test.

At the end of the oxic experiment, the steel specimens were covered with loose red products that were easily dislodged when rinsed with isopropyl alcohol. This is a preliminary indication that iron oxides were produced during the test. The reddish layer was loose, porous, and prone to dislodge, exposing the grayish inner corrosion product layer. Further observations of the specimen surface using scanning electron microscopy (SEM) revealed two different kinds of crystal morphologies (Figure 80). The non-adherent top layer consists of globular crystals that are typical of iron oxides while the features underneath the top layer were of prism-like crystals of a morphology characteristic of FeCO<sub>3</sub>.

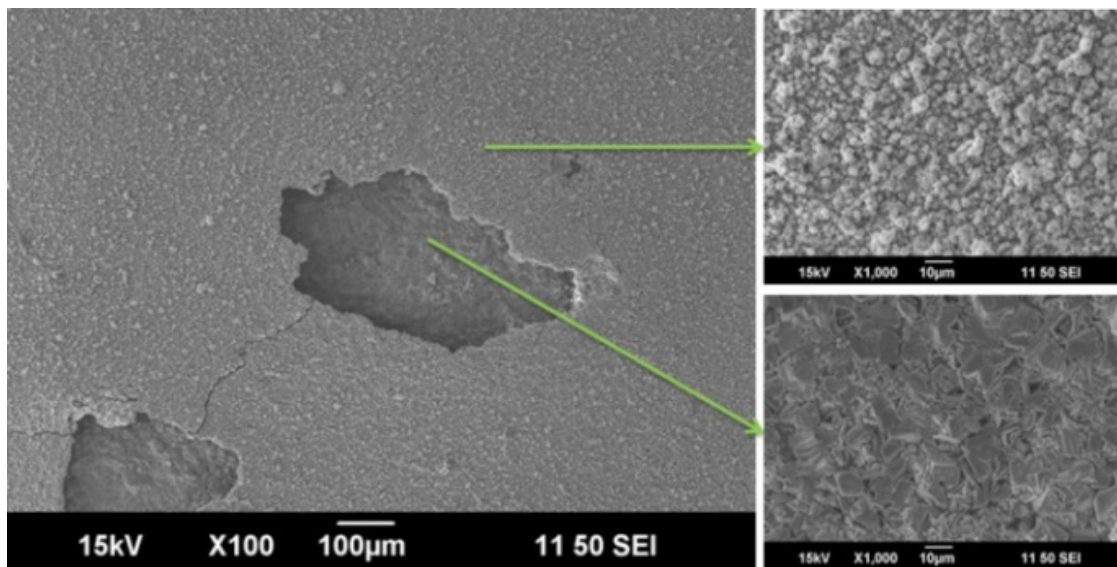


Figure 80. Steel surface after being exposed to 80°C, 40 bar CO<sub>2</sub>, 4% O<sub>2</sub> in solution for 48 hours.

The thickness and compositional characteristics of the corrosion product were determined by preparing a cross-section of the specimen which was then analyzed under SEM using backscattered electrons as shown in Figure 81. The thickness of the corrosion product derived from the CO<sub>2</sub>/O<sub>2</sub> environment was relatively thinner (43 µm) than the corrosion product that was not subjected to O<sub>2</sub> (78 µm). The amount of iron lost, calculated from weight loss, was 50 µm and 38 µm for the conditions with O<sub>2</sub> and without O<sub>2</sub>, respectively. Most of the iron lost from the oxidic experiment was probably converted into loose iron oxide and had spalled off of the steel surface.

The backscatter image in Figure 81(a) suggests different compositions and layers of the corrosion product based on the different shades of gray. The lighter shade of gray at the top layer indicates a heavier compound than the layer next to the steel surface. This is a good indication that the top layer consists of oxides, Fe<sub>x</sub>O<sub>y</sub>, while the layer closest to

the steel surface is iron carbonate,  $\text{FeCO}_3$ . The bottom-most layer was observed to be more coherent and compact than the top-most layer, providing a good protection to the steel surface.

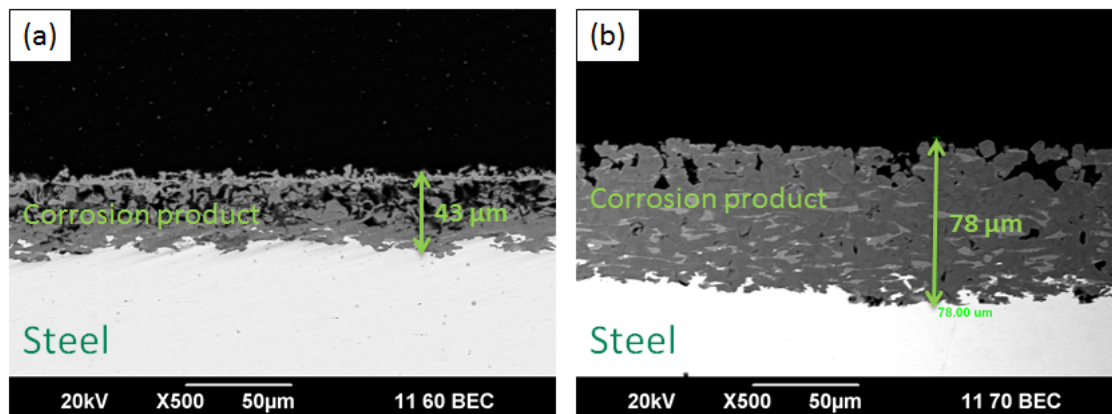


Figure 81. Cross-sectional view of steel specimen for tests conditions at (a) 80°C, 40 bar  $\text{pCO}_2$ , 1.7 bar  $\text{O}_2$  and (b) 80°C, 40 bar  $\text{pCO}_2$ .

X-ray diffraction (XRD) was utilized to determine the type of corrosion product that was formed on the steel surface. The diffraction pattern in Figure 82 indicated intense peaks of  $\text{FeCO}_3$ , which confirmed the coherent layer of compact corrosion product that was observed in the backscatter micrograph in Figure 81(a). Iron oxides and hydroxide were also detected on the steel surface. However, the intensities of the magnetite and hematite peaks were low and difficult to distinguish between each another. Raman spectroscopy was later utilized to investigate the corrosion product crystals. Analysis was conducted on different locations on the steel sample using 785 nm laser excitation energy at 50 mW laser power and 20 s integration time. The reddish-colored top layer picked up peaks that are characteristic of hematite ( $\text{Fe}_2\text{O}_3$ ), while the grey-

colored layer (underneath the dislodged top layer) recorded strong peaks of iron carbonate,  $\text{FeCO}_3$ , as shown in Figure 83.

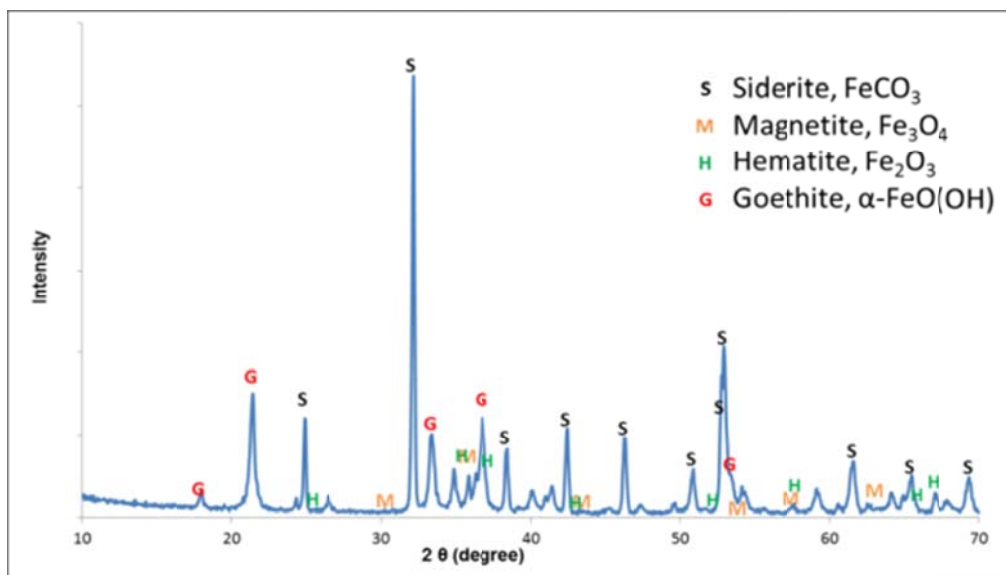


Figure 82. XRD analysis for specimen at the end of 80°C, 40 bar  $\text{pCO}_2$ , with 4%  $\text{O}_2$  experiment.

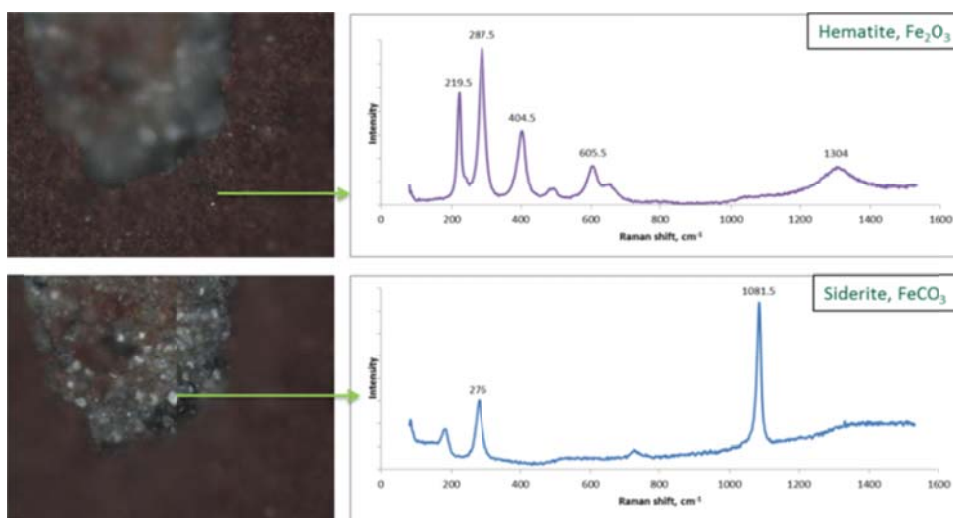


Figure 83. Raman spectra at two different locations on the steel specimen (785 nm laser excitation energy at 50 mW laser power, 20 s integration time).

Further investigations were carried out to observe the surface profile of the steel underneath the corrosion product after exposure to experimental conditions with O<sub>2</sub> present. After carefully chemically removing the corrosion product, the bare steel surface was analyzed using optical 3D profilometry. Localized corrosion was observed on the bare steel surface and the surface profile, Figure 84, showed a pit depth up to 386 μm. This maximum pit depth value converts to about 70 mm/year of penetration rate. The occurrence of localized corrosion could be due to the heterogeneity of the corrosion product layer on the steel surface, which could create highly localized environment for initiation of pits.

Localized corrosion was quantified by calculating the pitting ratio (PR) using the following method [95]:

$$PR = \frac{\text{Pit penetration rate}}{\text{Weight loss corrosion rate}} = \frac{70}{9.2} = 7.6 \quad (33)$$

According to the definition, if the PR value is greater than 5, it is a sign of localized corrosion. If the PR value is lower than 3 this implies no localized corrosion. If the PR value falls between 3 and 5, there is a probability for localized corrosion to occur [95]. In this case, the PR value indicates the existence of localized corrosion.

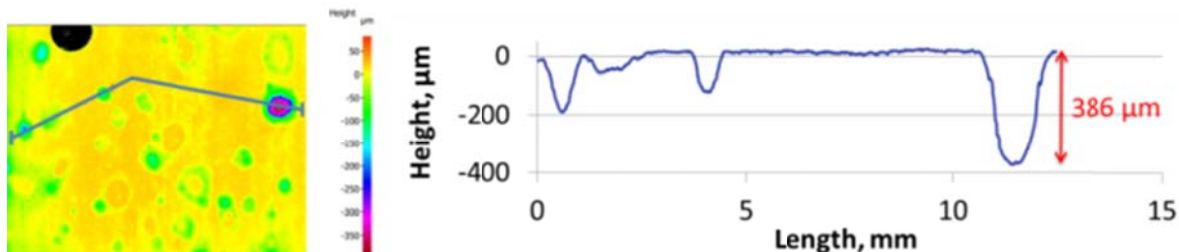


Figure 84. Surface profilometry of bare steel for test conditions 80°C, 40 bar pCO<sub>2</sub>, 1.7 bar O<sub>2</sub>

To summarize the results, the presence of 4% O<sub>2</sub> in 40 bar CO<sub>2</sub> at 80°C can be detrimental to steel integrity. Even though low corrosion rate was recorded at the end of the experiment, severe localized corrosion was observed and can consequently cause material failure, although the coherent and compact layer of FeCO<sub>3</sub> on the steel provides some protection to the steel, thus lowering the uniform corrosion rate.

#### 5.5.4 Experiment 4: 80°C, 90 bar pCO<sub>2</sub>, with and without 4% O<sub>2</sub>.

In this experiment CO<sub>2</sub> is in the supercritical phase. Figure 85 shows the corrosion rates measured by LPR for 48 hours at 90 bar CO<sub>2</sub> and 80°C; the error bars mark the maximum and minimum values of corrosion rates. The behavior of the corrosion rates at 90 bar CO<sub>2</sub> showed slightly similar behavior as the experiments done at 40 bar CO<sub>2</sub>, as discussed in the previous section. Higher corrosion rate was observed in the first 5 hours of experiment for the oxygenated system as compared to the anoxic system. Corrosion rates with O<sub>2</sub> ingress reached a maximum of over 50 mm/year as opposed to the maximum of about 30 mm/year for the baseline CO<sub>2</sub> experiment. However, the drop in corrosion rate occurred earlier in the presence of O<sub>2</sub> and therefore resulting in a much

lower time-integrated corrosion rate value as shown in Figure 86. The weight loss corrosion rate also showed lower corrosion rate when  $O_2$  is present in supercritical  $CO_2$ . This differing observation could be caused by the complex nature of supercritical  $CO_2$  which affects the overall chemistry of the solution.

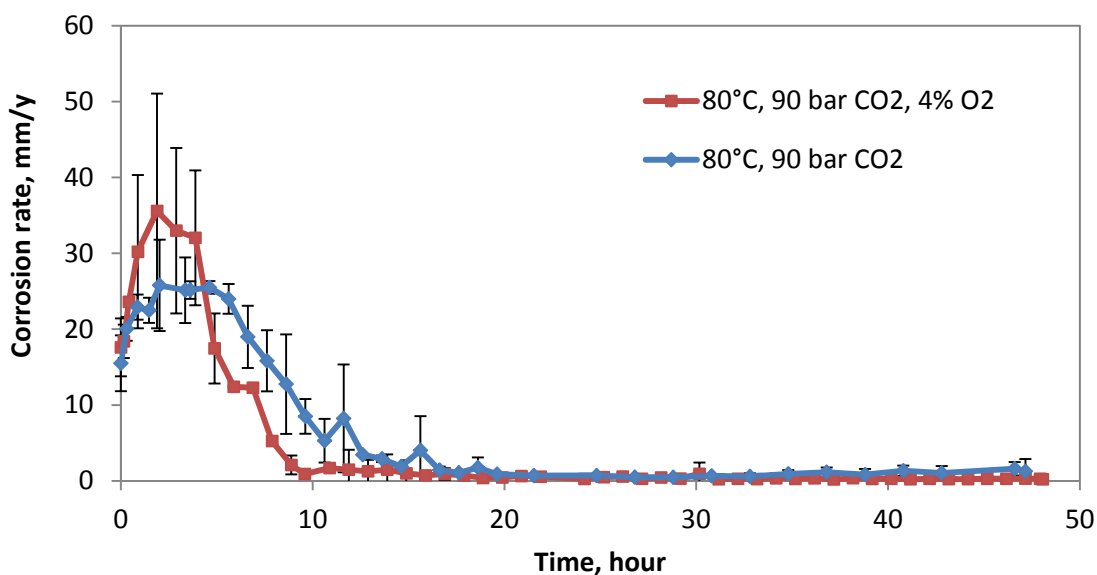


Figure 85. Corrosion rates of steel at 80°C and 90 bar  $CO_2$  with and without  $O_2$ .

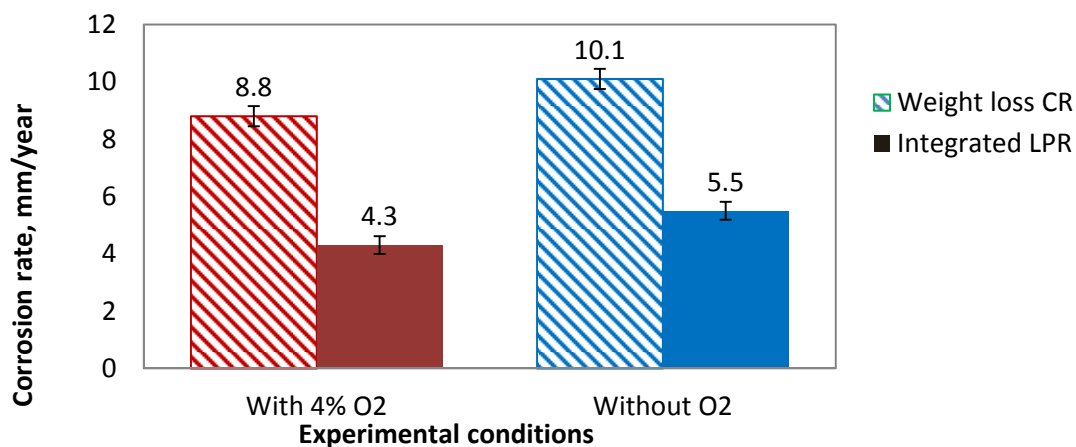


Figure 86. Corrosion rates measured using weight loss technique compared with integrated LPR results for conditions with and without O<sub>2</sub> at 80°C, 90 bar CO<sub>2</sub> after 2 days of test.

The corrosion potential showed a similar trend as was observed in the 40 bar CO<sub>2</sub> experiments, see Figure 87. The potential increased positively about 400 mV during the first 24 hours, and gradually declined to a fairly constant value of -300 mV. The presence of O<sub>2</sub> had caused conversion of ferrous to ferric ions, and consequently to oxides of iron on the steel surface, thus affecting the observed potential change.

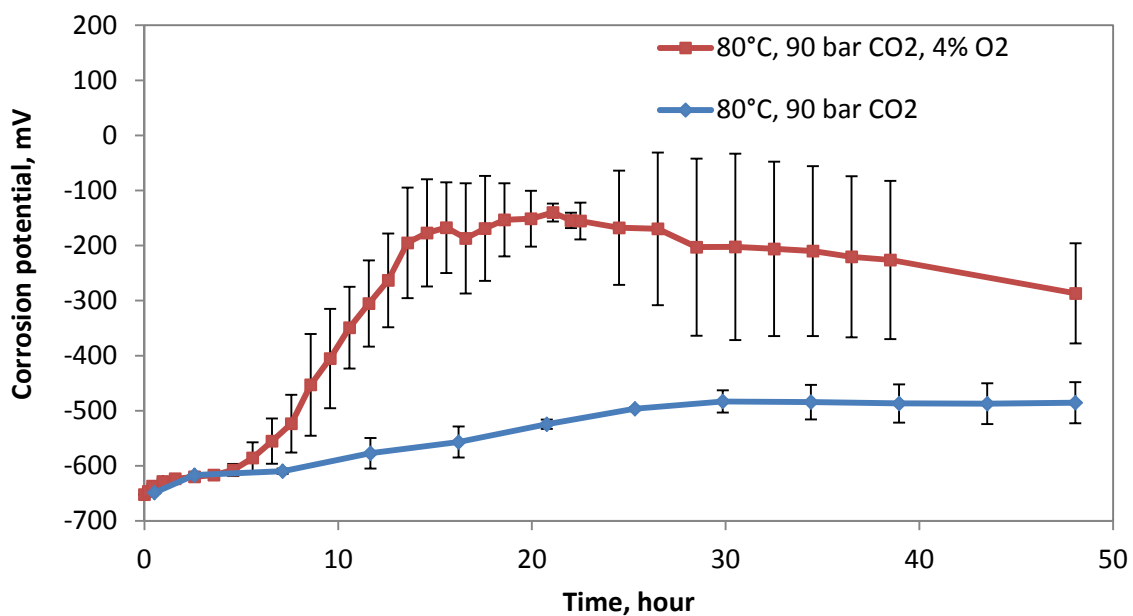


Figure 87. Corrosion potential of steel at 80°C and 90 bar CO<sub>2</sub> with and without O<sub>2</sub>

The steel specimen was covered with a thick layer of reddish precipitate that was loose and porous. This readily washed off of the steel surface when rinsed with isopropanol, leaving a brownish red steel surface, as shown in Figure 88. A comparison of the steel surface, observed using SEM, is shown in Figure 89.



Figure 88. Steel samples after 2 days of immersion without (left) and with O<sub>2</sub> (right).

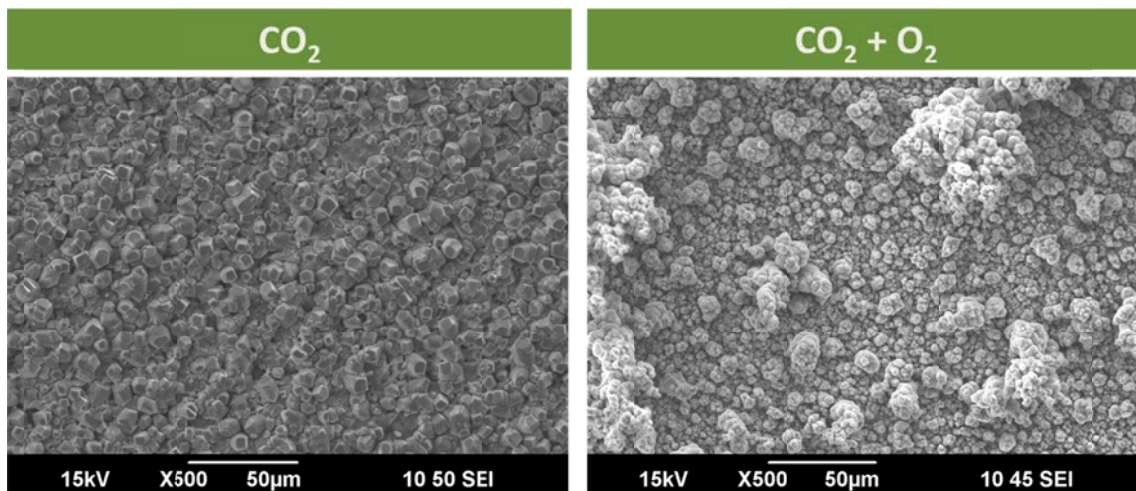


Figure 89. Micrograph of steel surface at 80°C, 90 bar CO<sub>2</sub> in 1 wt% NaCl solution for 48 with and without the presence of 4% O<sub>2</sub>.

Distinct layers of corrosion product were identified using backscatter SEM based on the different shades of gray on top of the steel surface shown in Figure 90. These findings were similar to those at 40 bar CO<sub>2</sub> at the same temperature. The cross-section shows that the thickness of the corrosion product is about 60 µm and 50 µm for the conditions without and with O<sub>2</sub>, respectively. The predicted thickness of iron loss was also calculated from the weight loss data and compared with the thickness observed in the cross-sections. The calculated iron loss matches well with the thickness of the corrosion product layer. The condition without O<sub>2</sub> resulted in 56 µm of iron loss, while the presence of O<sub>2</sub> showed 48 µm of iron loss.

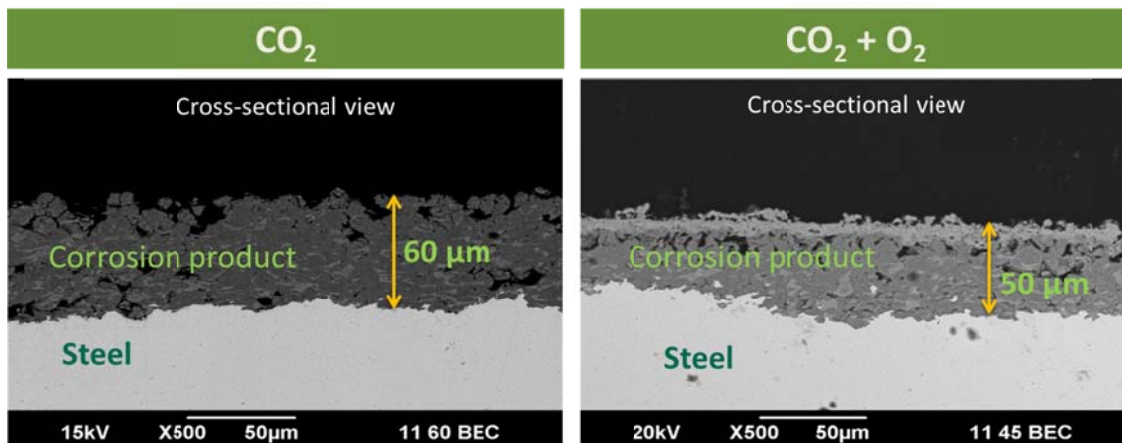


Figure 90. Cross-section of steel at 80°C, 90 bar CO<sub>2</sub> in 1 wt% NaCl solution for 48 with and without the presence of 4% O<sub>2</sub>.

The identity of the corrosion product was confirmed by XRD (Figure 91) and Raman spectroscopy (Figure 92). Due to the thickness of the top oxide layer, hematite was the only compound that was detected by Raman spectroscopy.

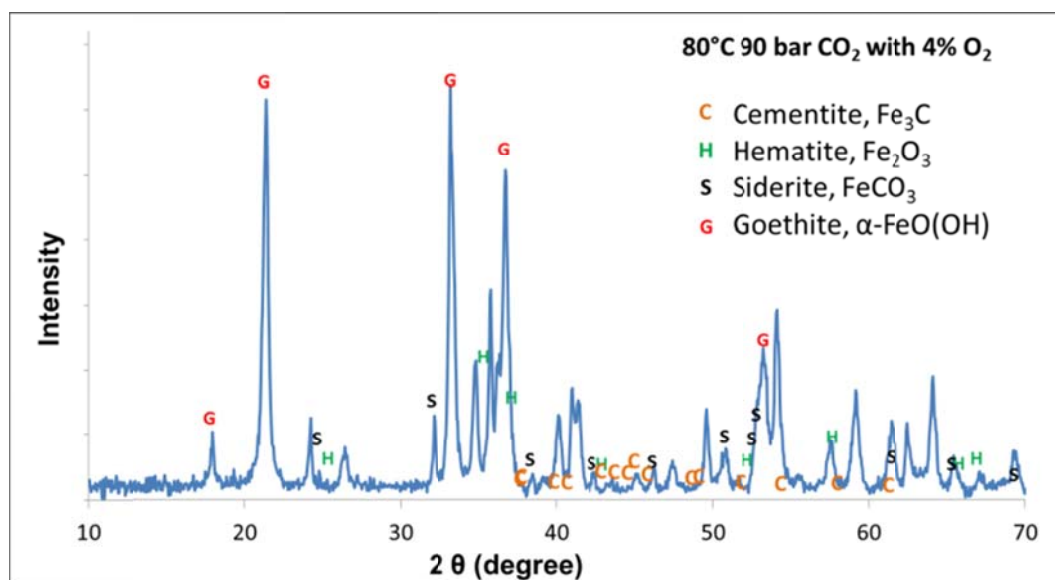


Figure 91. Analysis of steel surface using XRD for the specimen recovered at the end of the 80°C, 90 bar pCO<sub>2</sub>, with 4% O<sub>2</sub> experiment.

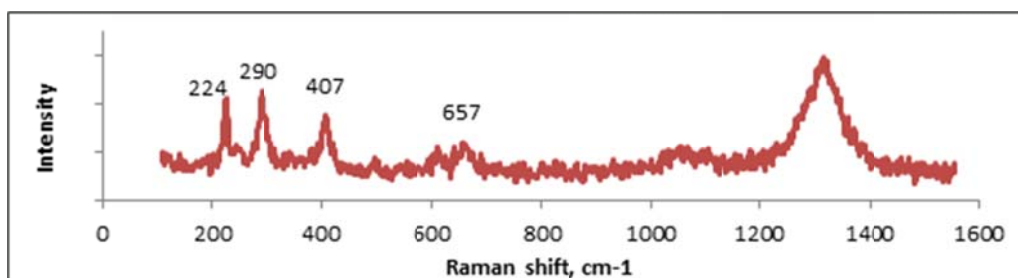


Figure 92. Hematite peaks detected using Raman spectroscopy with 532 nm laser excitation energy at 2 mW laser power, 20 s integration time.

Pit-like features as deep as 162  $\mu\text{m}$  occurred on the surface of the steel specimen as shown in Figure 93. The calculated penetration rate based on the maximum observed depth was 30 mm/year. The pitting ratio value of 3.4 is low due to the large value of its weight loss corrosion rate, which is 8.7 mm/year. According to theory, this pitting ratio value is considered too low to be categorized as localized corrosion. However, the pitting ratio is not a perfect representation of localized corrosion because it does not consider the magnitude of the steel's surface area [95]. It was obvious that pits were found on the steel surface, observed using 3D microscope (Figure 93) and SEM (Figure 94).

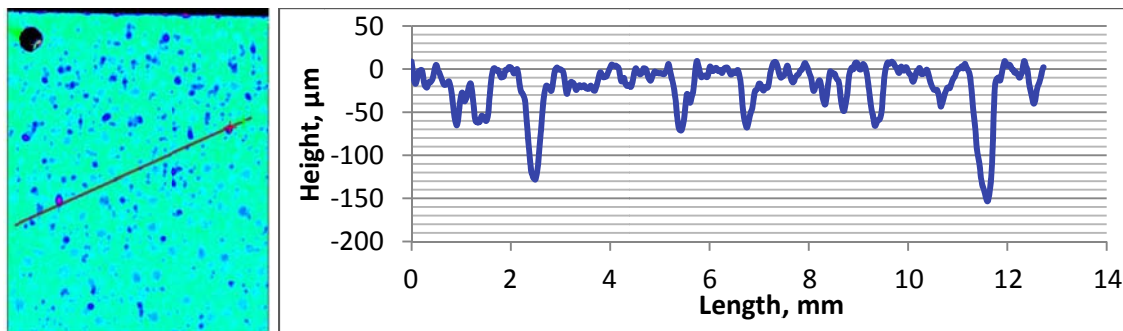


Figure 93. Surface profilometry of bare steel for test conditions 80°C, 90 bar  $\text{pCO}_2$ , 1.7 bar  $\text{O}_2$ .

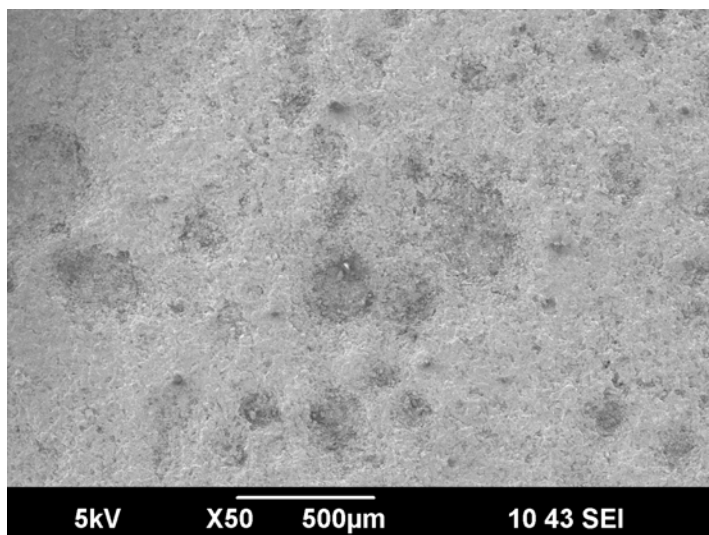


Figure 94. Localized corrosion on steel surface as seen under SEM.

### 5.6 The Proposed Corrosion Mechanism

The ingress of  $O_2$  in high  $CO_2$  partial pressure systems causes a more complex electrochemistry of  $CO_2$  corrosion. The additional cathodic reaction ( $O_2$  reduction reaction (14)) that takes place, results in an increased rate of anodic reaction to provide more electrons for the cathodic reactions. The dissolution of iron into ferrous ions is increased, which explains the overall higher corrosion rate. Previous researchers have suggested that the  $FeCO_3$  is very vulnerable to  $O_2$  and is easily damaged or dissolved by its presence [88], [107].

At low temperature, in this case  $25^\circ C$ , the temperature is too low for  $FeCO_3$  or  $Fe_2O_3$  to form effectively. Therefore, neither  $FeCO_3$  nor  $Fe_2O_3$ , was found on the steel surface. However, for the oxic environment at room temperature, in the presence of carbonate ions, formation of goethite,  $\alpha\text{-FeO(OH)}$ , [108] was observed as the greenish

layer that turned yellowish with air oxidation. The high  $\text{CO}_2$  partial pressure in the closed system leads to the increase of hydrogen, bicarbonate, and carbonate ion concentrations in the solution. The excess hydrogen ion and bicarbonate migrate to the steel surface to act as oxidants, causing dissolution of iron to form ferrous ions ( $\text{Fe}^{2+}$ ). Consequently the residual iron carbide, derived from pearlite and, enriched with alloying elements, becomes exposed (as evidenced by the previously shown SEM micrographs and EDS analyses). Figure 95 illustrates this corrosion mechanism.

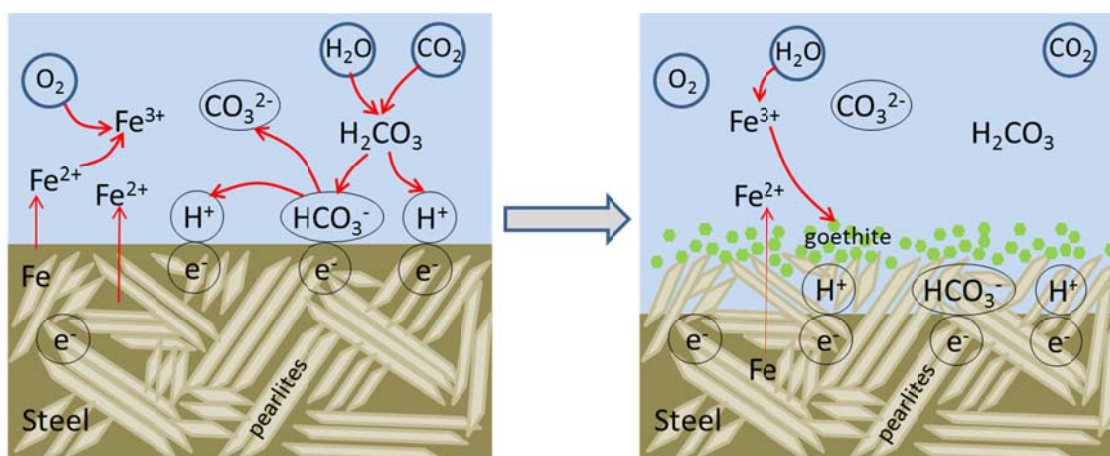


Figure 95. Proposed corrosion mechanism at low temperature and high  $p\text{CO}_2$  with  $\text{O}_2$  ingress in a closed system.

At high temperature, the formation of  $\text{FeCO}_3$  and oxides are thermodynamically and kinetically favored as the precipitation rate of these species increases. The presence of  $\text{O}_2$  interferes with the formation of  $\text{FeCO}_3$  due to the diminished ferrous ion concentration in solution. The ferrous ions are oxidized to ferric ions, which precipitate as iron oxides, and are deposited loosely and randomly on the steel surface. The heterogeneity of the deposition provides for localized environments with the steel surface

which is covered by  $\text{FeCO}_3$  is protected, whereas the steel surface under the oxide is not. This may lead to formation of galvanic cells, even if the exact mechanism is not clear. It is possible that the  $\text{O}_2$  that is trapped in the confined space gets consumed, and becomes depleted, creating a differential aeration cell, as typically seen in crevice corrosion [109]. In that theory, the local area underneath the iron oxide layer becomes the anode while the larger surface area of the steel that is directly exposed to the aerated bulk solution becomes the cathode. Supersaturation of  $\text{Fe}^{2+}$  and  $\text{CO}_3^{2-}$  in the local environment is hypothesized to promote the formation of  $\text{FeCO}_3$  in the pits as illustrated in Figure 96, but it appears to be less protective than the  $\text{FeCO}_3$  formed elsewhere.

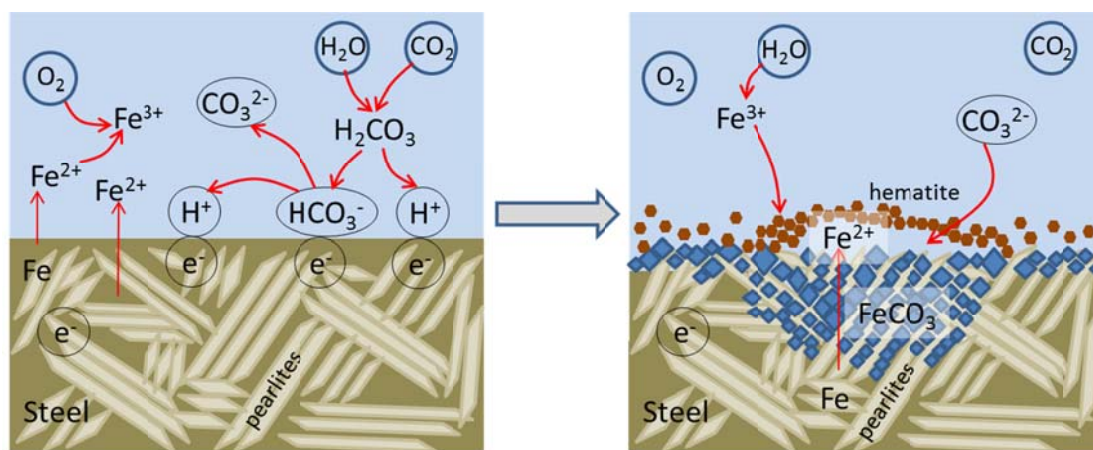


Figure 96. Proposed corrosion mechanism at high temperature and high  $p\text{CO}_2$  with  $\text{O}_2$  ingress in a closed system.

Further tests that are specific to studying the corrosion mechanisms under these conditions can be conducted to confirm their validity. Investigation of galvanic cells formed at high  $\text{CO}_2$  partial pressure might offer some answers about the mechanism of

localized corrosion. Electrochemical impedance spectroscopy (EIS) may be utilized to study the corrosion mechanism at high CO<sub>2</sub> partial pressure in the presence of O<sub>2</sub>.

### 5.7 The Effect of Flow

An impeller, fitted to the autoclave, with a rotational speed set at 1000 rpm conferred a flow field in the solution, corresponding to a peripheral velocity of about 1 m/s. The flow regime corresponds to a turbulent flow with a Reynolds number greater than 200. Figure 97 shows that the initial corrosion rate almost doubled due to the addition of flow in a CO<sub>2</sub> system. It then slowly decreased to about 0.2 mm/year after over 30 hours of test as compared to the lesser amount of time taken by the stagnant system. Figure 98 illustrates the same effect of flow on a CO<sub>2</sub>/O<sub>2</sub> system. This delayed behavior in the drop of corrosion rate shows that the mechanisms of both CO<sub>2</sub> and CO<sub>2</sub>/O<sub>2</sub> corrosion are influenced by mass transport of species to and from the metal surface. The highest recorded corrosion rate was over 60 mm/year in the oxic and turbulent environment. The lowered corrosion rate values are indicative of a protective barrier that had formed on the steel surface in spite of the presence of turbulent flow.

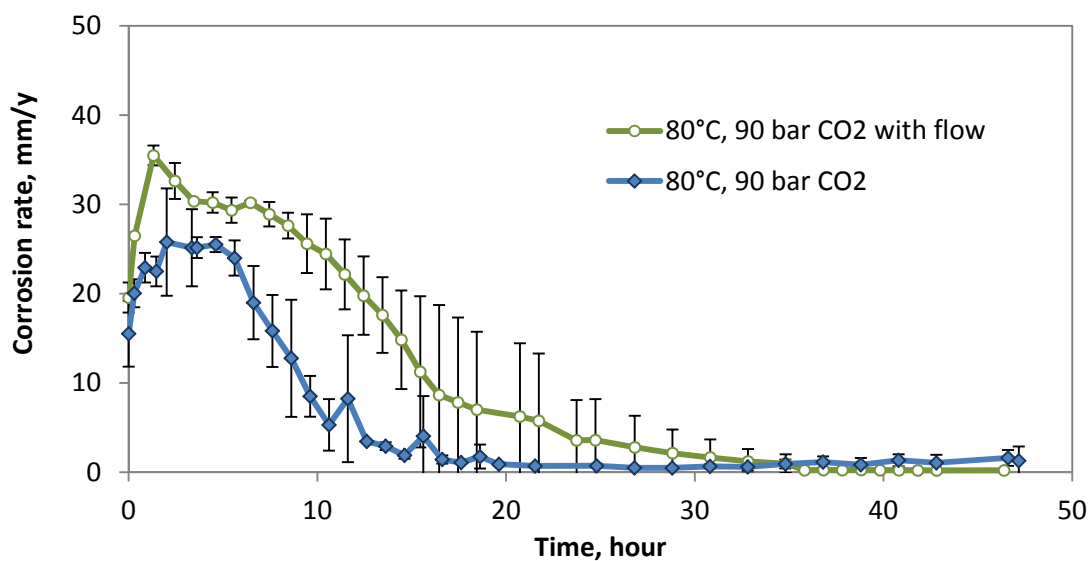


Figure 97. Effect of 1000 rpm flow rotational speed on the corrosion rates in equivalent  $\text{CO}_2$  systems.

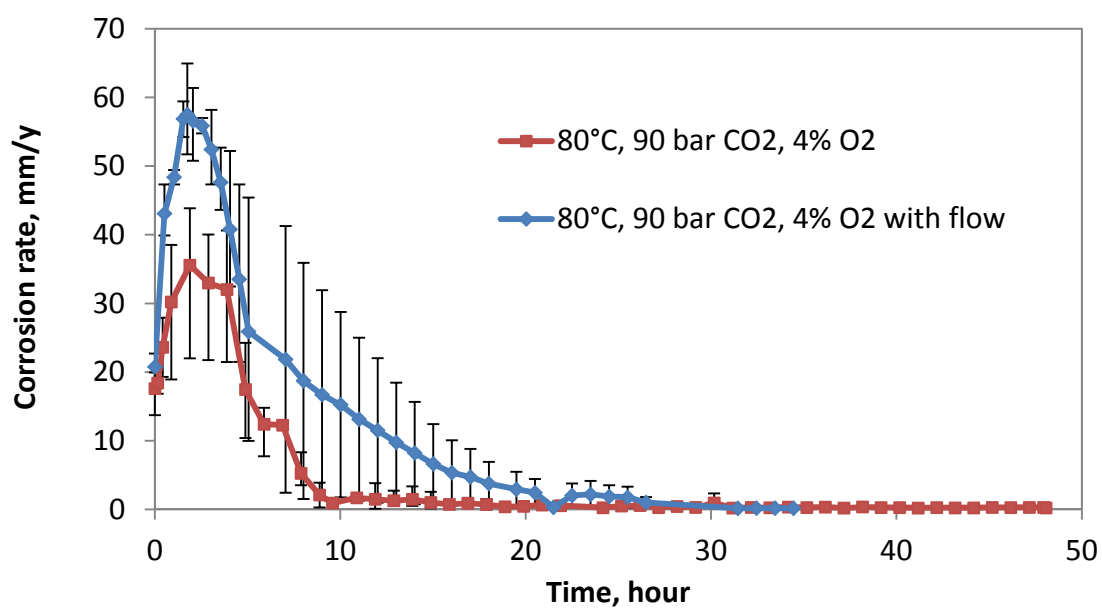


Figure 98. Effect of 1000 rpm flow on the corrosion rates in equivalent  $\text{CO}_2/\text{O}_2$  systems.

The effect of flow was also significant in the corrosion rate values that were measured by weight loss. Figure 99 illustrates that both CO<sub>2</sub> and CO<sub>2</sub>/O<sub>2</sub> flow systems recorded high corrosion rates as compared to their rates in the stagnant condition. Combination of high pressure CO<sub>2</sub> with O<sub>2</sub> and flow recorded the highest of over 35 mm/year.

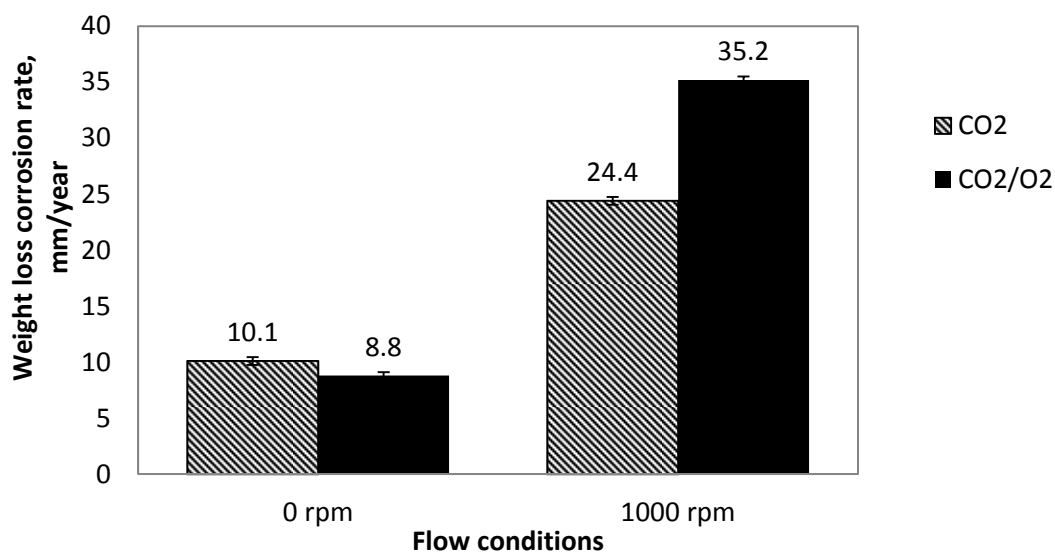


Figure 99. Effect of flow and O<sub>2</sub> on weight loss corrosion rate.

The surface of the steel specimen after 48 hours of exposure in the CO<sub>2</sub>/O<sub>2</sub> environment at 80°C, 90 bar CO<sub>2</sub>, and 1000 rpm rotational speed showed layers of corrosion product that were flaky and non-adherent, as shown in Figure 100. Observations under SEM, as shown in Figure 101, indicated the appearance of typical dense plate-like iron oxide crystals, with a high percentage of O in the EDS analysis shown in Figure 102. Crystals of FeCO<sub>3</sub> could not be seen on the sample.

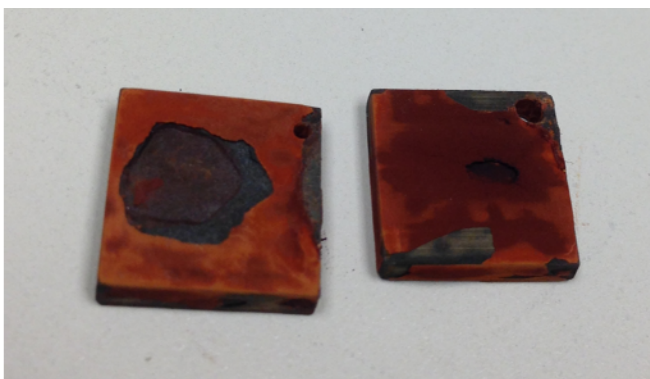


Figure 100. Steel specimens at 80°C 90 bar CO<sub>2</sub>, 4% O<sub>2</sub>, and 1000 rpm speed.

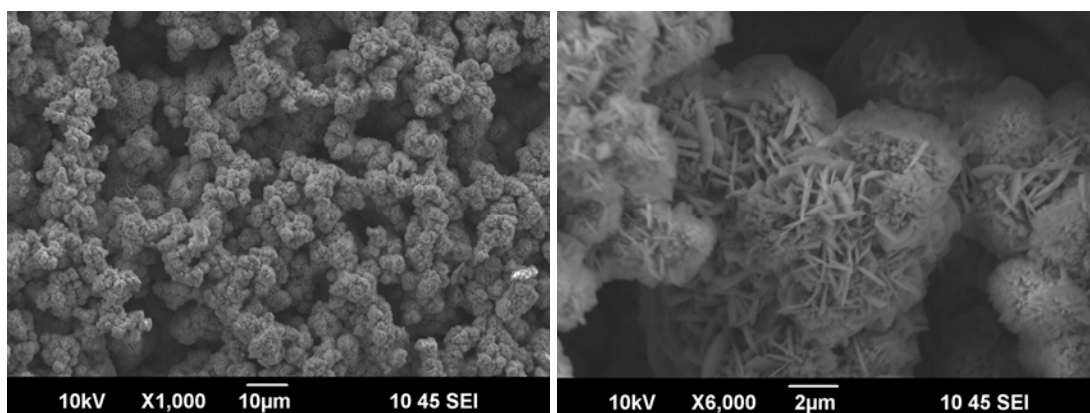


Figure 101. SEM of steel surface at 80°C 90 bar CO<sub>2</sub>, 4% O<sub>2</sub>, and 1000 rpm speed.

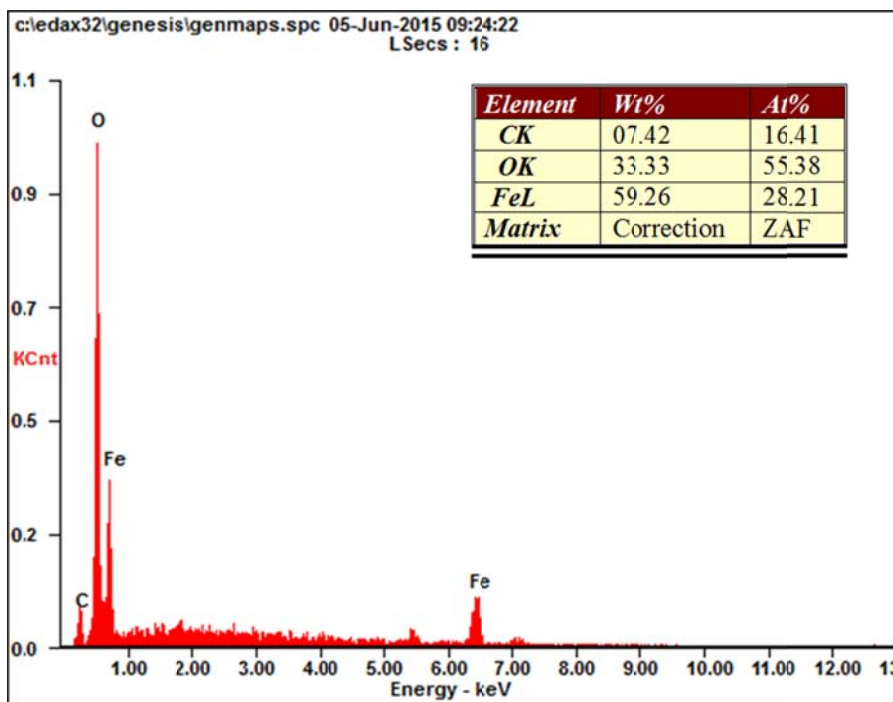


Figure 102. EDS of steel surface at 80°C, 90 bar CO<sub>2</sub>, 4% O<sub>2</sub>, and 1000 rpm rotational speed.

The specimen from the oxidic CO<sub>2</sub>/O<sub>2</sub> experiment was compared with the specimen in an anoxic CO<sub>2</sub> environment. The steel specimen from the anoxic flow experiment appeared severely corroded, as shown in Figure 103. The EDS analysis is shown in Figure 104. Analysis of a prismatic crystal, indicated by point '1' on the SEM micrograph, was indicative of FeCO<sub>3</sub> by the detection of elements Fe, C and O. EDS analysis on the flat non-crystalline part of the specimen, labelled as point '2', revealed the composition of the corroded steel substrate with high concentrations of alloying elements such as copper, molybdenum, manganese and nickel associated with carbide. Similar findings of the alloying elements in steel grade X65 have been reported when immersed in solution with a pH value of 6.0 and at temperatures 40, 60, and 80°C [110]

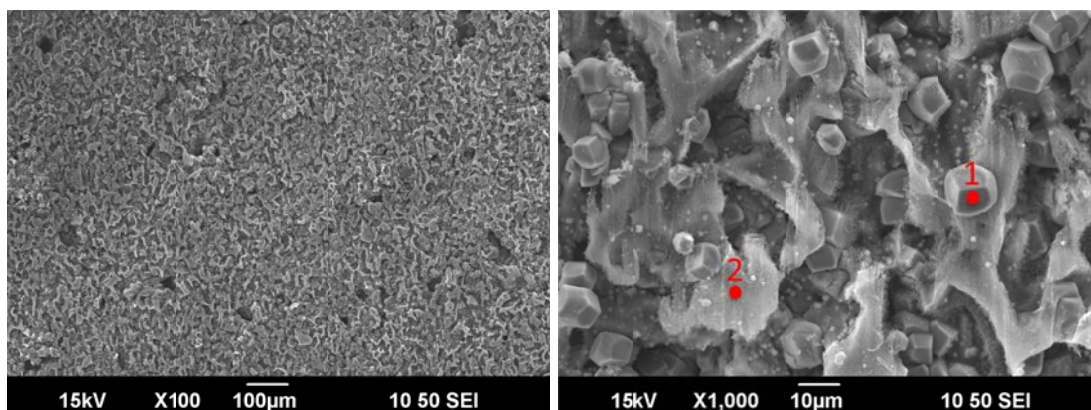


Figure 103. SEM of steel surface at 80°C 90 bar CO<sub>2</sub>, and 1000 rpm rotational speed.

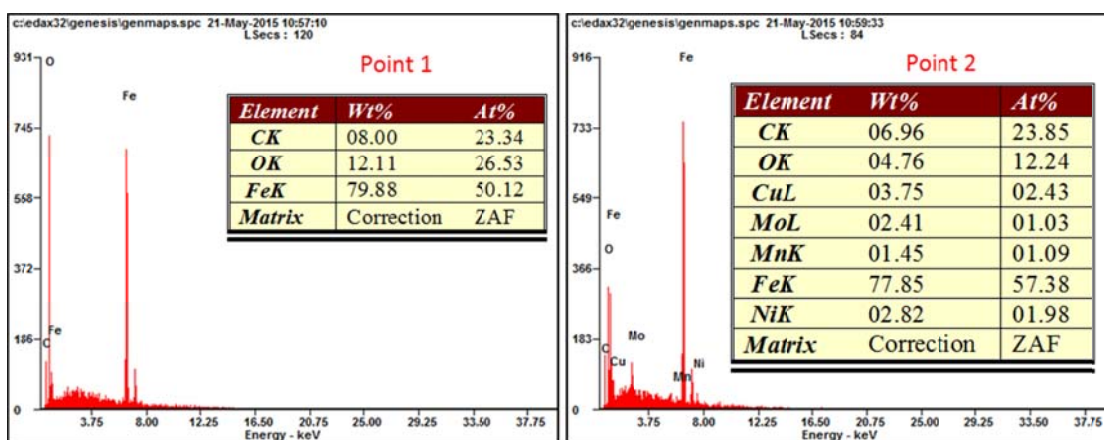


Figure 104. EDS analysis of two points on the steel as labeled in the previous Figure.

Figure 105 and Figure 106 show the cross-sectional view of steel specimens in both flow and stagnant conditions for CO<sub>2</sub> and CO<sub>2</sub>/O<sub>2</sub> systems. The corrosion product layer in Figure 105(a) showed the presence of voids in between the corrosion product which could be due to the interference of flow on FeCO<sub>3</sub> formation. The voids were even more obvious in Figure 106(a) where the oxide layer was flaky and non-adherent to the underlying FeCO<sub>3</sub>.

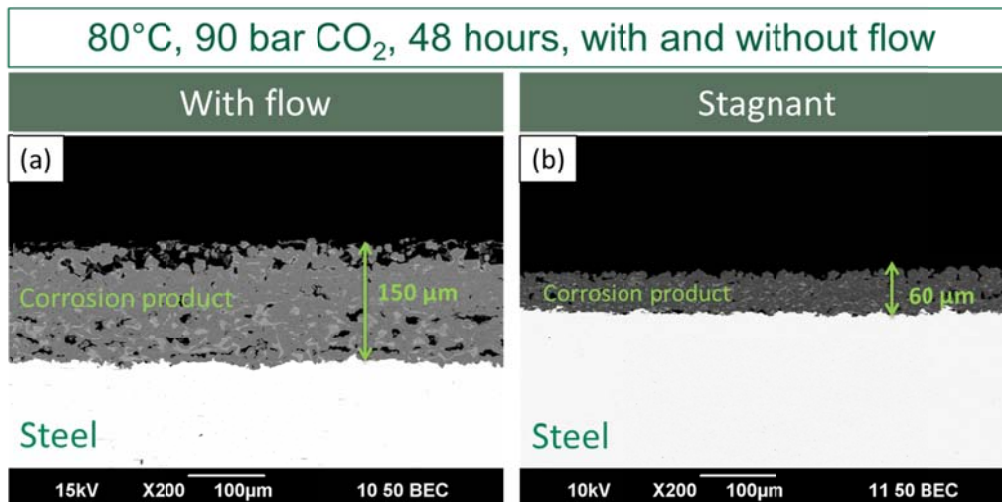


Figure 105. Cross-sectional views of coupon comparing the effect of flow at 80°C and 90 bar CO<sub>2</sub>.

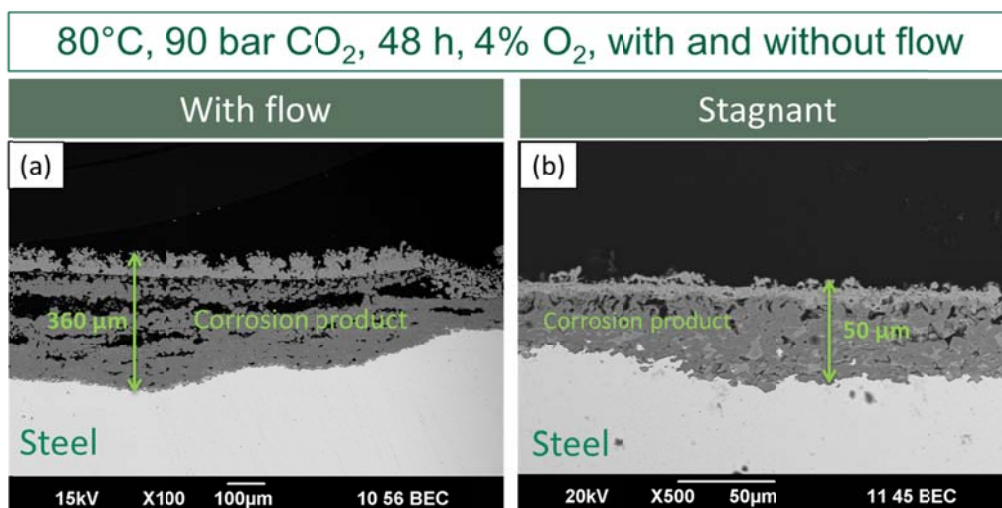


Figure 106. Cross-sectional views of coupon comparing the effect of flow in CO<sub>2</sub>-O<sub>2</sub> system at 80°C, 90 bar CO<sub>2</sub> and 4% O<sub>2</sub>.

The corrosion product was removed using a Clarke solution in order to observe the surface of the bare steel. Turbulent flow had caused the appearance of pits on the steel surface in both CO<sub>2</sub> and CO<sub>2</sub>/O<sub>2</sub> systems as illustrated in Figure 107 and Figure 108. The maximum pit depth observed was 93 μm for the anoxic system while the oxic system

proved to be more aggressive with pit depth up to 377  $\mu\text{m}$ . One specimen, however, did not exhibit pit-like features but instead appeared very severely corroded, as shown in Figure 109. The deepest penetration was recorded to be about 380  $\mu\text{m}$ .

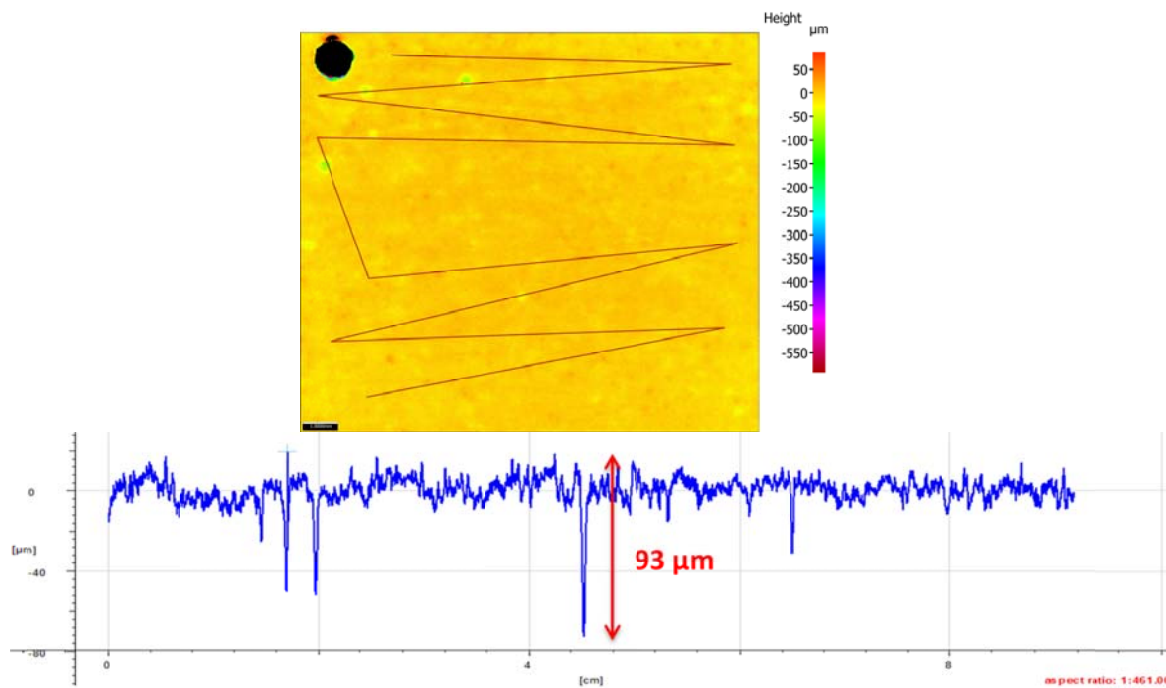


Figure 107. Surface profilometry of steel for experiment at 80°C, 90 bar CO<sub>2</sub>, 2 days, 1000 rpm

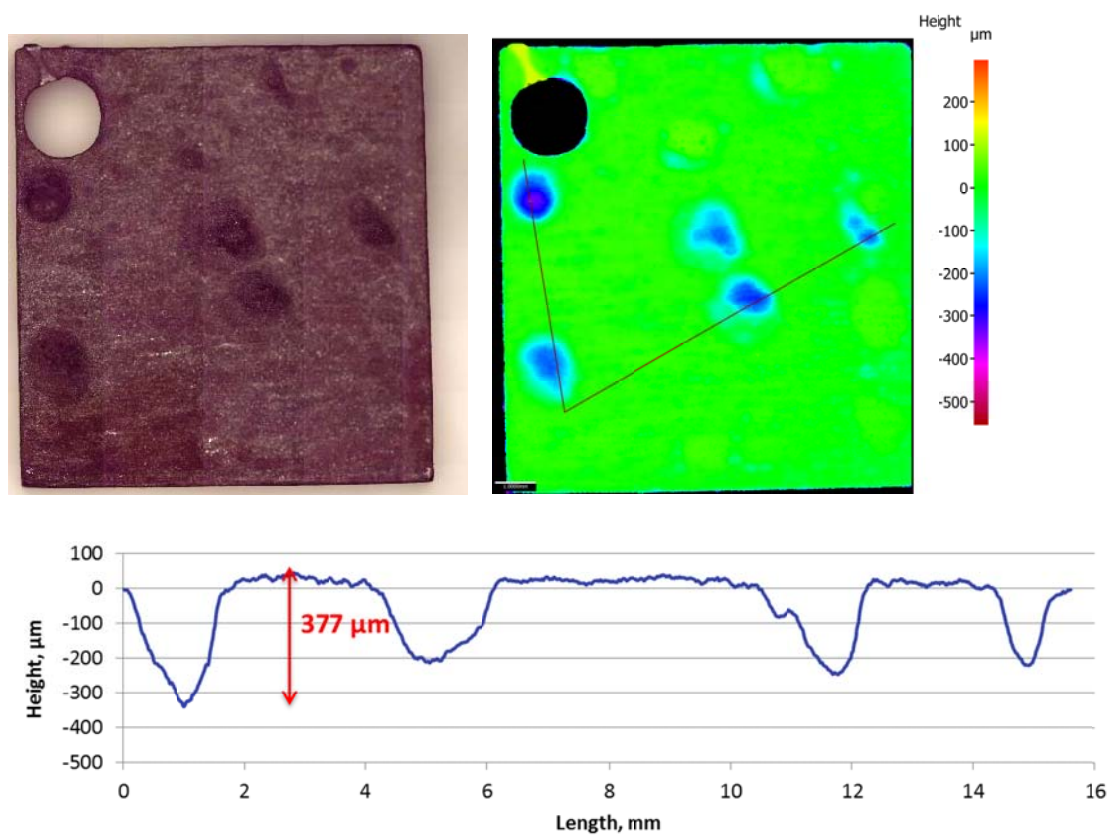


Figure 108. Surface profilometry of steel for experiment at 80°C, 90 bar CO<sub>2</sub>, 2 days, 4% O<sub>2</sub>, 1000 rpm

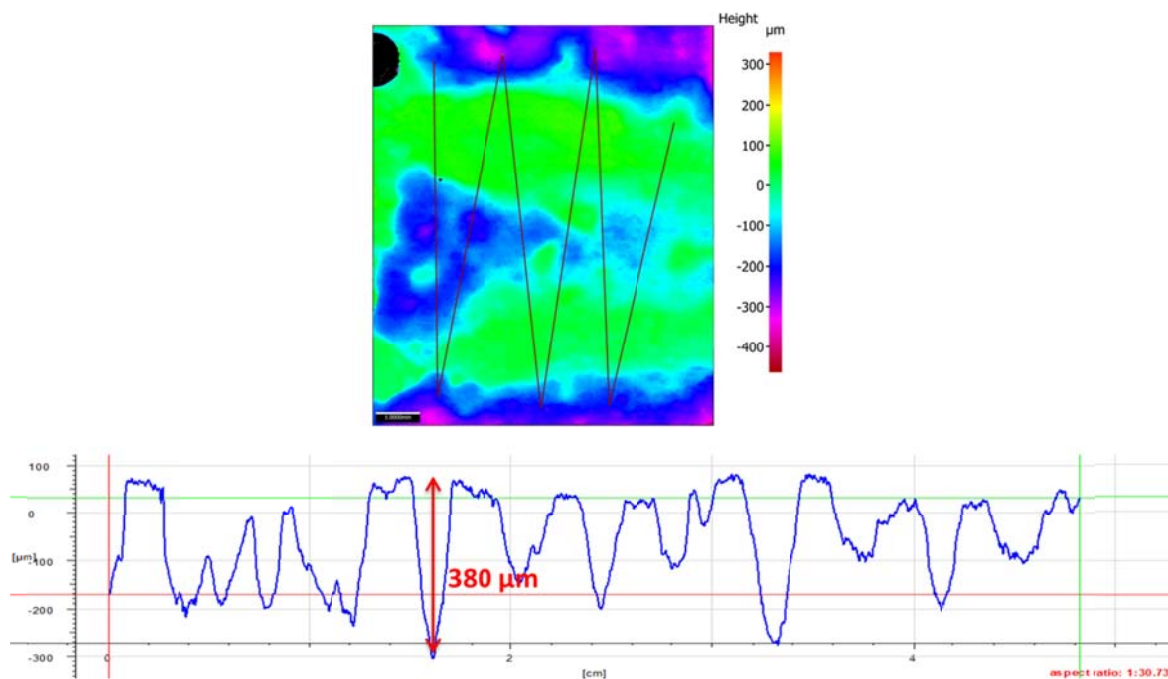


Figure 109. Surface profilometry of another specimen for experiment at 80°C, 90 bar CO<sub>2</sub>, 2 days, 4% O<sub>2</sub>, 1000 rpm

Based on the results from this set of experiments, the presence of flow resulted in a more severe corrosion than in a stagnant environment. The turbulent flow disrupted the formation of a protective layer on the steel surface by the enhanced transport of Fe<sup>2+</sup> ions away from the steel surface, thus lowering the saturation value with respect to FeCO<sub>3</sub> formation. More hydrogen ions are also being transported from the bulk to the steel surface, further enhancing the consumption of electrons, therefore increases the rate of iron dissolution. Flow also causes loose iron oxide precipitates to be removed from the surface, delaying the deposition of insoluble ferric oxides.

## 5.8 Chapter Summary and Conclusions

Table 9 summarizes the results that were drawn from the current work on the effect of O<sub>2</sub> in high pressure conditions.

Table 9: Results Summary of High Pressure Corrosion Experiments

T (°C)	pCO <sub>2</sub> (bar)	pO <sub>2</sub> (bar)	Flow condition, rpm	Final LPR corrosion rate (mm/year)	Weight loss Corrosion rate	Localized corrosion?
25	40	0	0	9.7	6.3	No
25	40	1.7	0	13.6	9.5	No
25	90	0	0	6.4	1.8	No
25	90	3.75	0	15.5	15.1	No
80	40	0	0	0.1	7.0	NA
80	40	1.7	0	0.7	9.2	Yes
80	90	0	0	1.3	10.1	NA
80	90	3.75	0	0.2	8.8	Yes
80	90	0	1000	0.2	24.4	Yes
80	90	3.75	1000	NA	35.2	Yes

The presence of O<sub>2</sub> was particularly detrimental to steel integrity. The experiments that were conducted at the 25°C caused severe uniform corrosion, devoid of any protective corrosion product layer on the steel surface. The final corrosion rates, based on the final  $R_p$  value measured by LPR, are considered to be high and regarded as unacceptable by the oil and gas industry. Experiments that were conducted at 80°C

showed possible initiation of localized corrosion on steel. The formation of thick and coherent corrosion products on the steel surface provided some defense from further active corrosion of the steel. Although the final corrosion rates were low (0.7 and 0.2 mm/year), they were still considered as unacceptable values for oil and gas applications which have been defined as a maximum of 0.1 mm/year [107], [111]. The highest corrosion rate observed was in the flow experiments.

The overall results showed that the corrosion rates were magnitudes higher than the corrosion rates observed at low pressure as discussed in Chapter 4. This is associated with elevated  $\text{CO}_2$  partial pressures causing an increase in the carbonic acid concentration.

## CHAPTER 6: MODELING

In-house corrosion prediction tools called Freecorp©, and Multicorp© were utilized for comparison of simulated corrosion rates to results.

### 6.1 Simulation at Low Pressure

Freecorp© is a simulation software that was developed by a team of research scientists and programmers at the Institute for Corrosion and Multiphase Technology (ICMT) to perform predictions of carbon steel corrosion at corrosion product layer-free conditions. The software was utilized to simulate corrosion, and related data for the FeCO<sub>3</sub>-free low pressure condition. Figure 110 shows that the corrosion rates presented in Chapter 4 are in agreement with the simulated results. The polarization curve shown in Figure 111 effectively describes the corrosion behavior change when O<sub>2</sub> is present in the system. The corrosion current increased due to the additional O<sub>2</sub> reduction reaction, reflected by the green vertical line, which shifted the total cathodic curve to the right. The other lines are labeled as different colors: orange (H<sup>+</sup> reduction), purple (H<sub>2</sub>O reduction), light blue (H<sub>2</sub>CO<sub>3</sub> reduction), red (total cathodic curve and Fe dissolution), and dark blue (sweep curve).

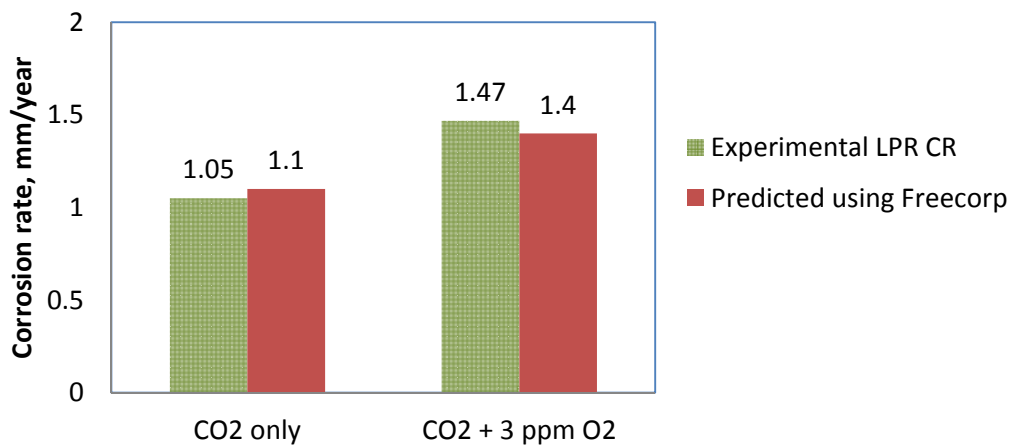


Figure 110. Comparison of corrosion rates between Freecorp© and experimental data at 25°C, 1 bar, pH 4.0, with and without 3 ppm O<sub>2</sub>

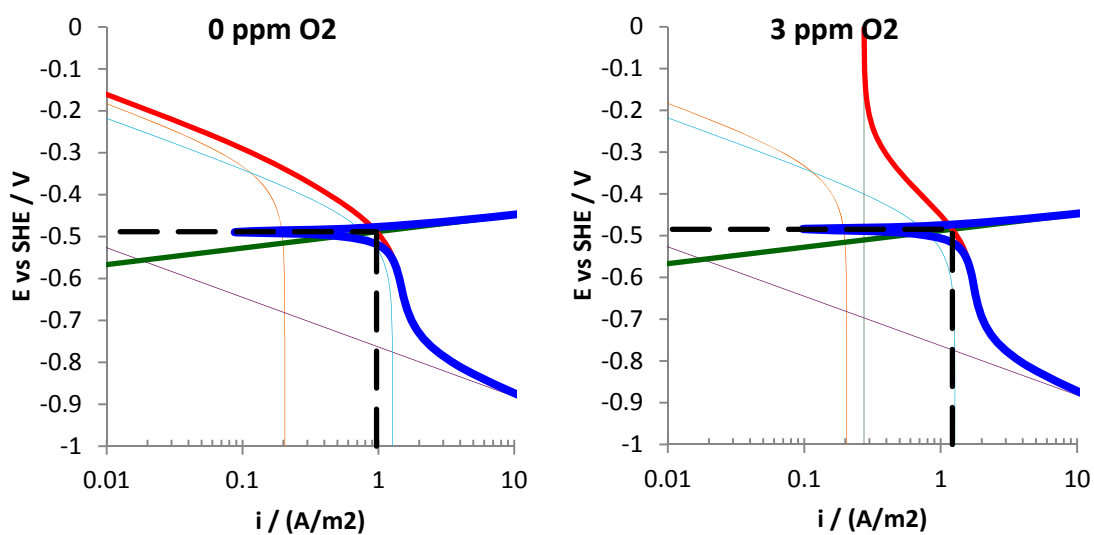


Figure 111. The effect of 3 ppm O<sub>2</sub> in CO<sub>2</sub> system at 25°C, 1 bar shown in Tafel plots using Freecorp©

Freecorp© tends to overpredict corrosion rates at higher temperature due to its inability to include the effect of corrosion product on the surface of steel. Simulation of corrosion at “corrosion product-forming” condition was performed using a more

advanced in-house proprietary model called Multicorp©. This corrosion prediction model was designed for use in pipelines in the oil and gas industry, therefore, it is unable to simulate the corrosion rate at a completely stagnant condition. All simulations using Multicorp© were set at the lowest allowable superficial water velocity, which is 0.01 m/s.

Figure 112 compares the results between experimental (red squares) and simulated data (blue line) for a 7-day experiment at 80°C, 0.5 bar CO<sub>2</sub> and pH value of 6.6. The simulated data showed a slightly lower corrosion rate than the experimental data. The immediate drop in both experimental and simulated corrosion rate is caused by the formation of corrosion product on the steel surface, which was observed and discussed earlier in Chapter 4. The drop in the corrosion rate corresponds to the drop in the surface porosity, which is shown in Figure 113. The presence of O<sub>2</sub> (denoted by the triangular plots) resulted in a much higher corrosion rate for the first 5 days of the test due to the additional O<sub>2</sub> reduction reaction in the system. The formation and accumulation of oxide precipitates on the steel surface partially mitigated further corrosion of the steel by limiting the area of the steel surface that is directly exposed to the corrosive environment.

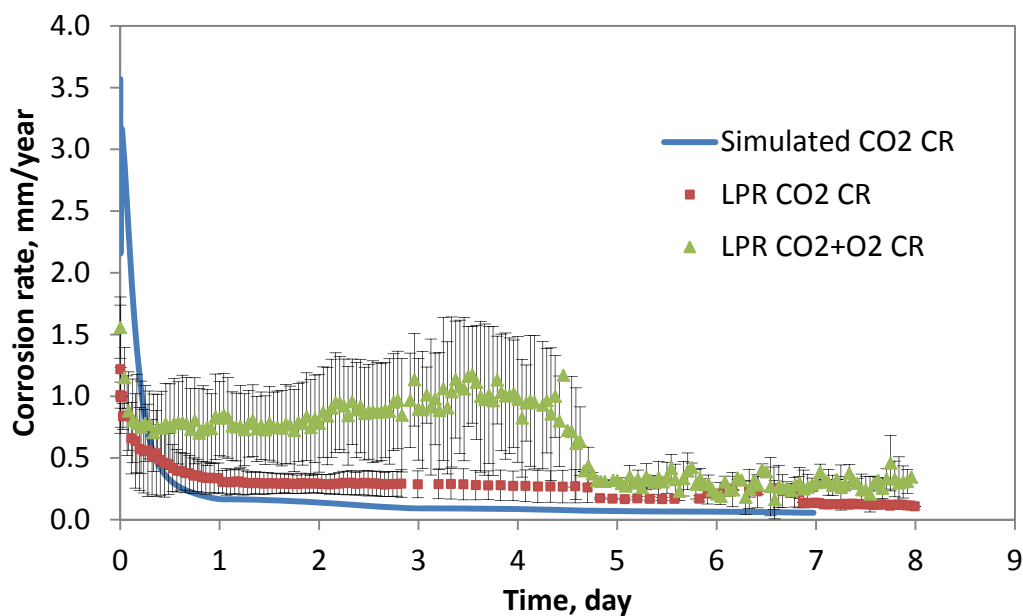


Figure 112. Comparison of corrosion rates between Multicorp© and experimental data of test at 80°C, pH 6.6 and 0.5 bar CO<sub>2</sub>, with and without O<sub>2</sub>

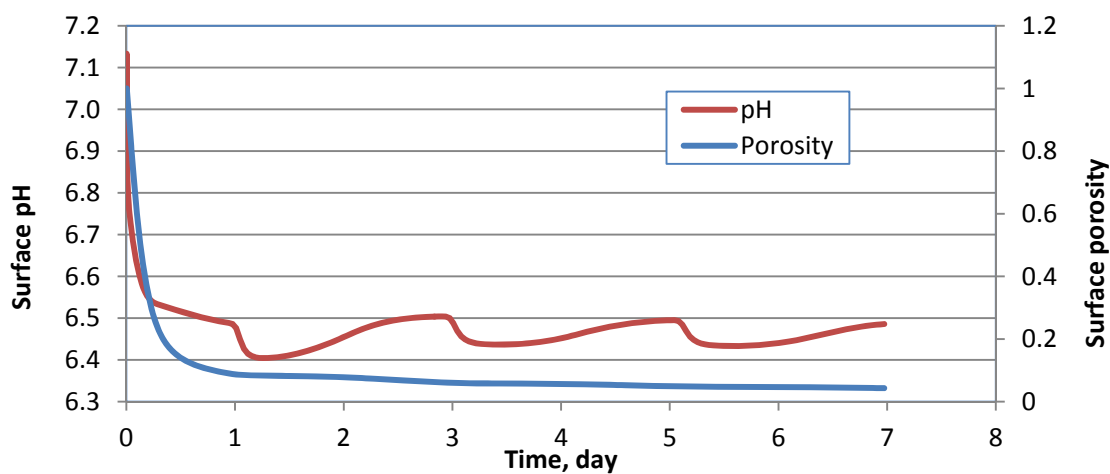


Figure 113. Simulated surface pH and porosity at 80°C, pH 6.6, and 0.5 bar CO<sub>2</sub>

## 6.2 Simulation at High Pressure

The latest version of Multicorp© was developed through a collaborative project between ICMT and oil and gas companies to accommodate the demand for a predictive

tool in near-critical and supercritical CO<sub>2</sub> conditions for steel pipelines in the oil and gas industry. This newest version of the software enables prediction of corrosion for pressures up to 200 bar.

### 6.2.1 Multicorp© High Pressure Simulation for Tests at 25°C

Experimental results at CO<sub>2</sub> partial pressures of 40 bar and 90 bar that was presented in Chapter 5 were compared with simulated results using Multicorp©, shown in Figure 114 and Figure 115. Both figures exhibited a fairly constant corrosion rate for 48 hours. The absence of a protective FeCO<sub>3</sub> layer on the steel that was observed in the laboratory experiment explains the constantly high corrosion rates. Multicorp© predicted a slightly higher corrosion rate due to the inability of the model to simulate corrosion behavior at stagnant conditions. The superficial fluid velocity was set at 0.01 m/s to simulate a near stagnant environment. The presence of O<sub>2</sub> affects the corrosion rate even at high pressure, as shown in the two figures. The increase in the corrosion rate at 90 bar is more significant than the increase at 40 bar CO<sub>2</sub>.

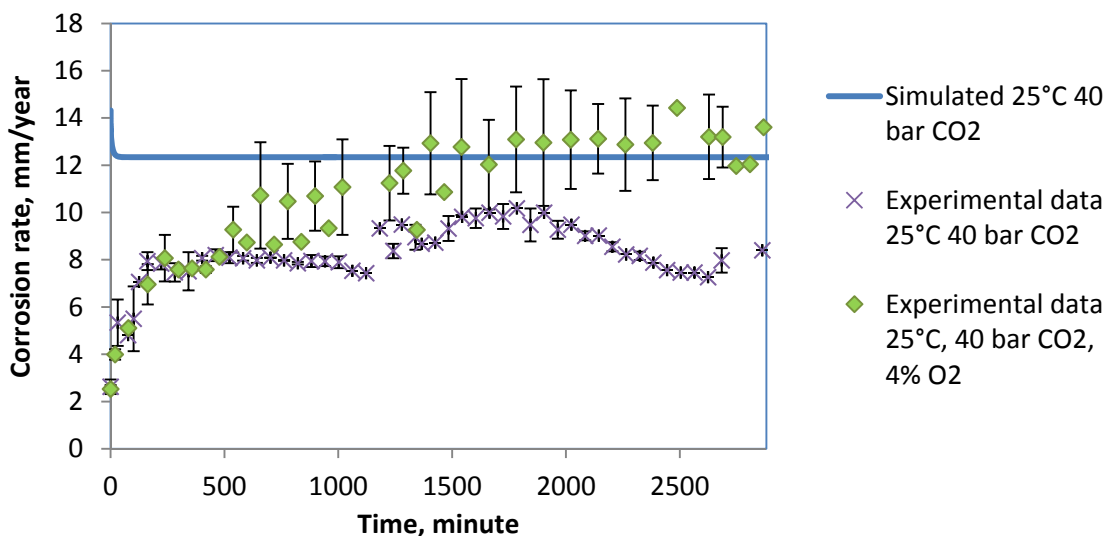


Figure 114. Comparison of simulated corrosion rate with experimental results for experiment at 40 bar CO<sub>2</sub>, 25°C, autogenous pH for 48 hours

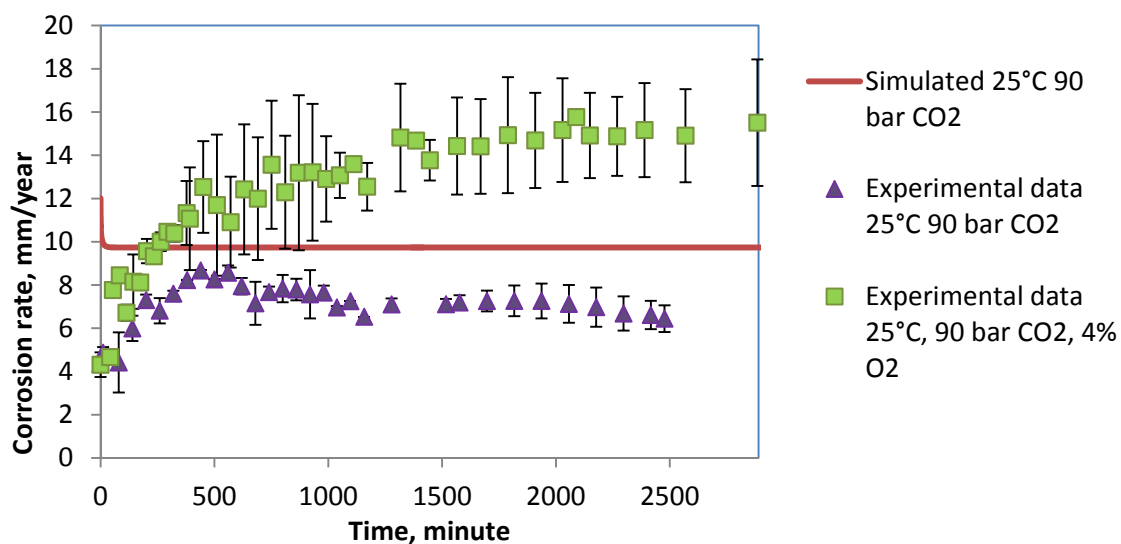


Figure 115. Comparison of simulated corrosion rate with experimental results for experiment at 90 bar CO<sub>2</sub>, 25°C, autogenous pH for 48 hours

Simulation of corrosion rate at different CO<sub>2</sub> partial pressures from 10 to 120 bar CO<sub>2</sub> at 25°C in a 48 hour period showed an interesting behavior. Figure 116 shows that

the corrosion rate increased as partial pressure was increased from 10 bar to 40 bar of gaseous CO<sub>2</sub>. However, as the partial pressure was increased to 90 bar then CO<sub>2</sub> is now in the liquid phase, and it exhibited a different behavior where the corrosion rate decreased with increasing partial pressure. The corrosion rates vary at different CO<sub>2</sub> partial pressures, and were fairly constant in the 48 hour period (2880 minutes) as shown in Figure 117.

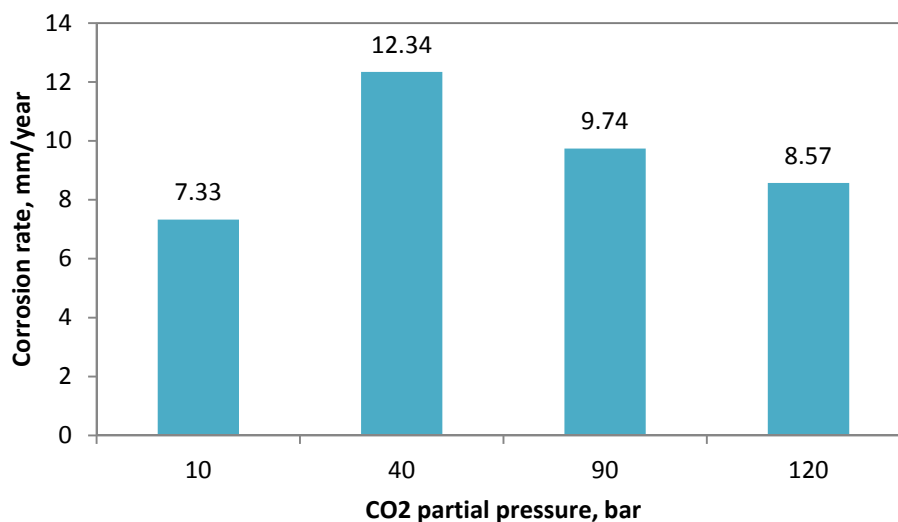


Figure 116. Predicted corrosion rates using Multicorp© at varying pressures at 25°C, autogenous pH for 2 days

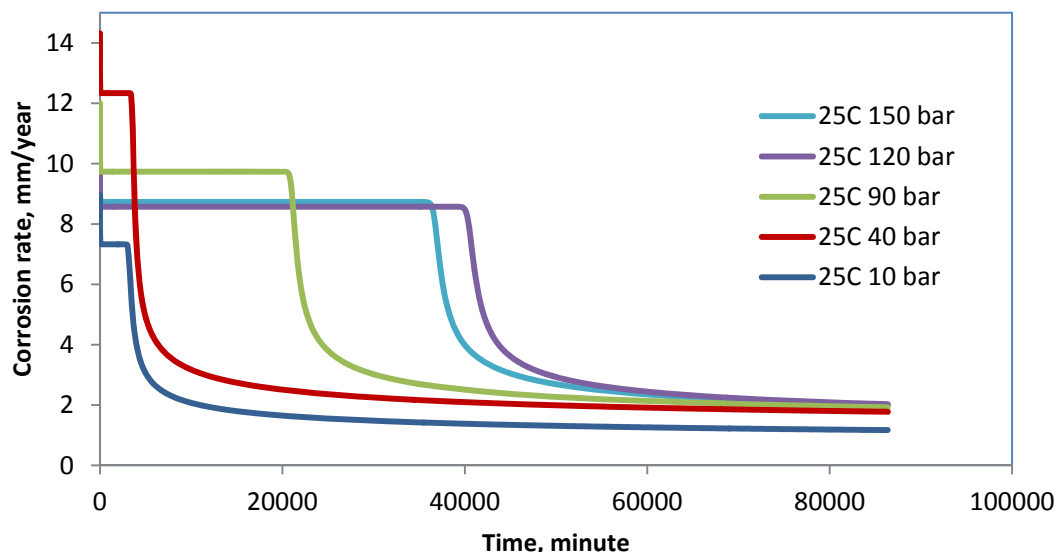


Figure 117. Predicted corrosion rates using Multicorp© at varying pressures at 25°C, autogenous pH for 60 days

Figure 117 shows that further simulation of corrosion rate at 25°C up to 60 days demonstrates that the corrosion rates eventually drop towards much lower values. The plot of the predicted porosity at the steel surface matches with the drop in corrosion rate, indicative of some form of corrosion product layer forming thereon, as shown in Figure 118. The increase in CO<sub>2</sub> partial pressure from 10 bar to 120 bar caused a delay in the formation of a corrosion product layer, as seen in the drop in the surface porosity. This is due to the increased concentration of carbonic acid that made the iron dissolution rate increase to a greater value than the precipitation rate at 25°C. This can be explained by the term Surface Scaling Tendency (SST) [112]:

$$SST = \frac{\text{pit precipitation rate, PPR}}{\text{corrosion rate, CR}} \quad (30)$$

Since the precipitation rate at 25°C is low relative to the corrosion rate, the corrosion product is porous and loose. As the partial pressure of CO<sub>2</sub> is increased, it increased the corrosion rate, thus lowering the value of SST and delaying the formation of any corrosion product.

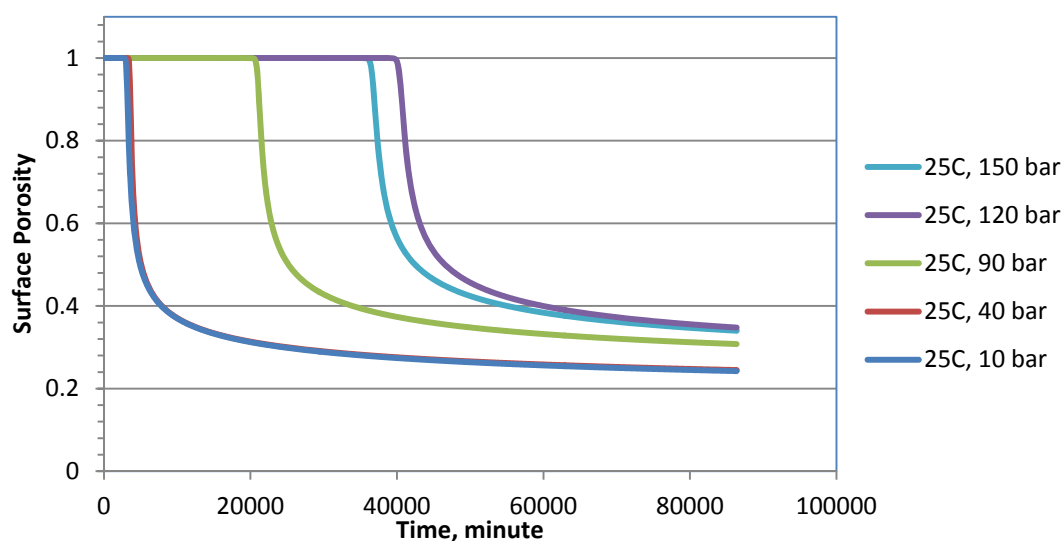


Figure 118. Simulated surface porosity at 25°C and autogenous pH for 60 days

The change in the surface pH is shown in Figure 119. The pH value at all simulated pressures decreases at the end of 60 days. Figure 120 compares simulated pH values of the bulk solution as well as at the steel surface. The pH value at the steel surface is much higher than the pH of the bulk solution.

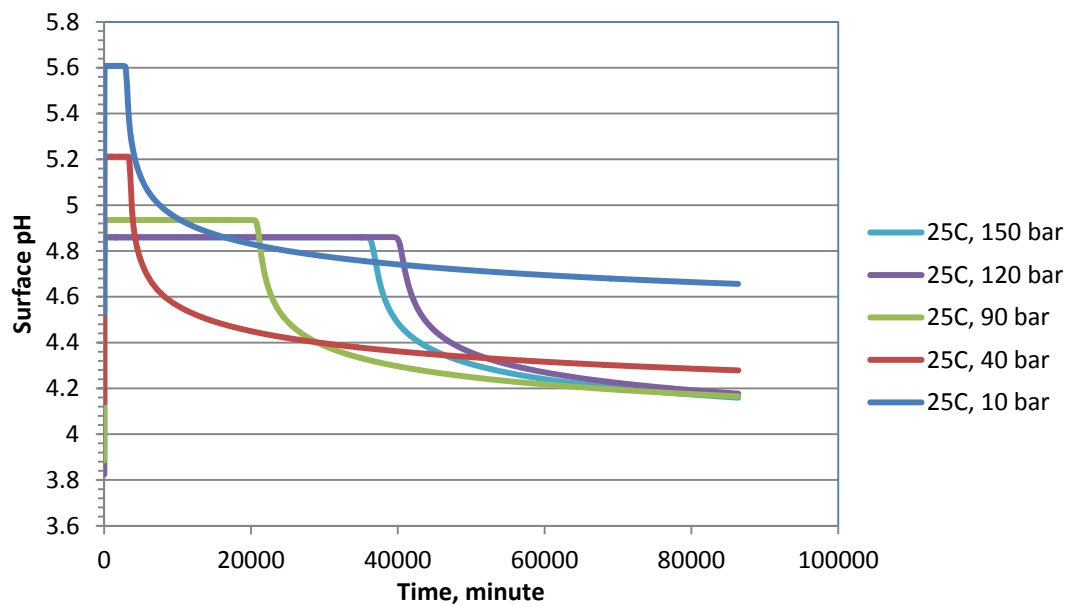


Figure 119. Predicted surface pH at 25°C and autogenous solution pH for 60 days

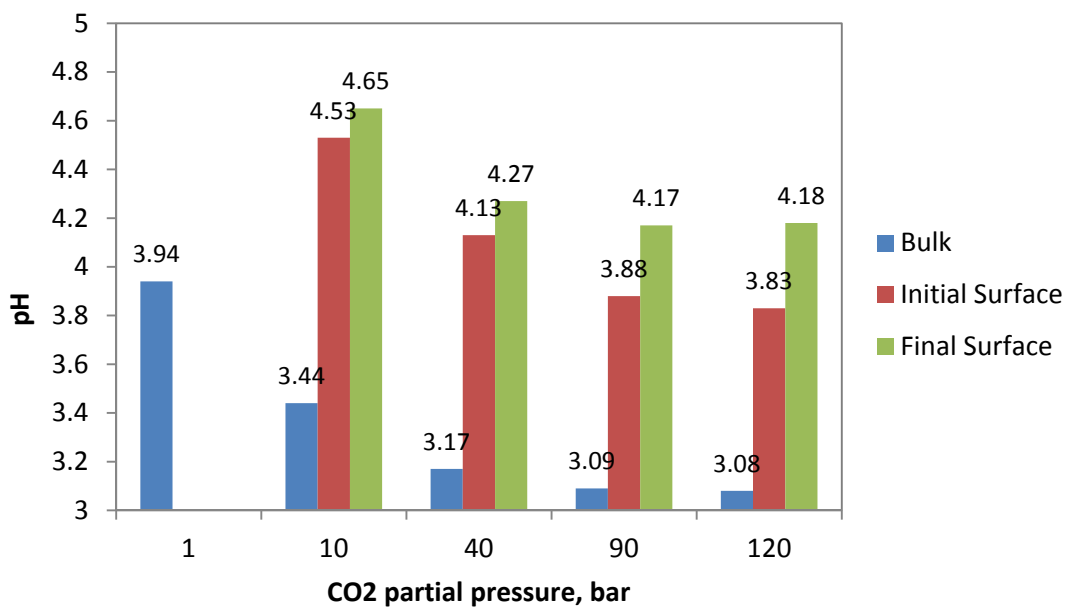


Figure 120. Predicted bulk and surface pH at 25°C

### 6.2.2 Multicorp© High Pressure Simulation for Tests at 80°C

Simulation of corrosion at 80°C resulted in a very high initial corrosion rate which then dropped rapidly within the first few hours of the corrosion process and gradually decreases afterwards, as shown in Figure 121. However, the corrosion rate after 48 hours was still considered unacceptably high. The poor correlation of the corrosion rate values is due to a number of possible factors. The simulated values were computed at the lowest allowable superficial fluid velocity of 0.01 m/s, therefore it does not truly represent corrosion rate values at stagnant condition. The simulation is also based on an infinite amount of solution which affects the supersaturation of species involved in the formation of  $\text{FeCO}_3$  or any other corrosion products.

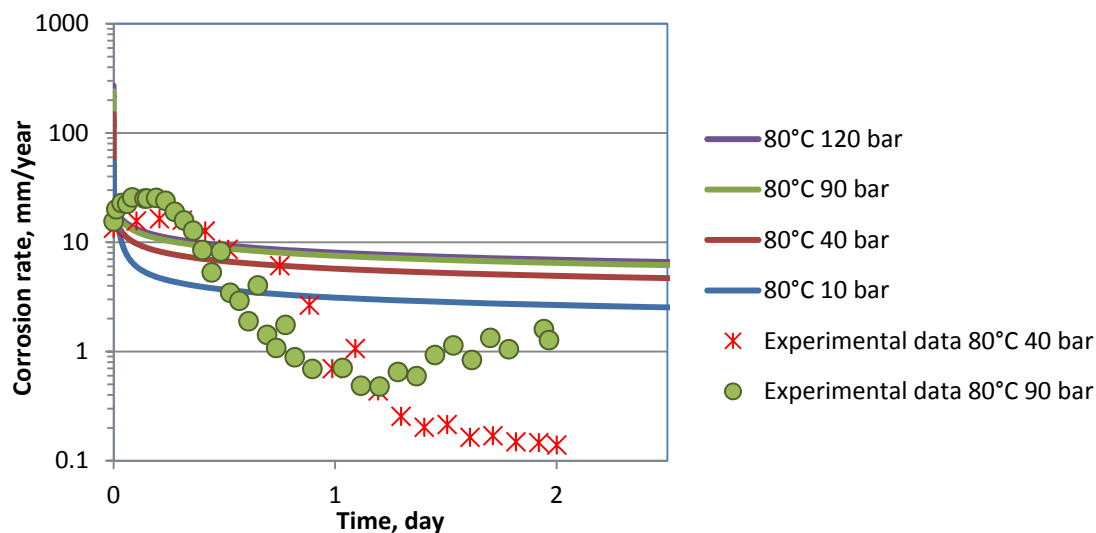


Figure 121. Predicted corrosion rates using Multicorp© at varying pressures at 80°C, autogenous pH

Figure 122 shows that the simulated surface porosity dropped simultaneously with the decrease in the predicted corrosion rate. Figure 123 shows that the surface pH almost instantaneously increased but then gradually decreases. The final value of the surface pH was higher than the initial pH of the solution, as shown in Figure 124.

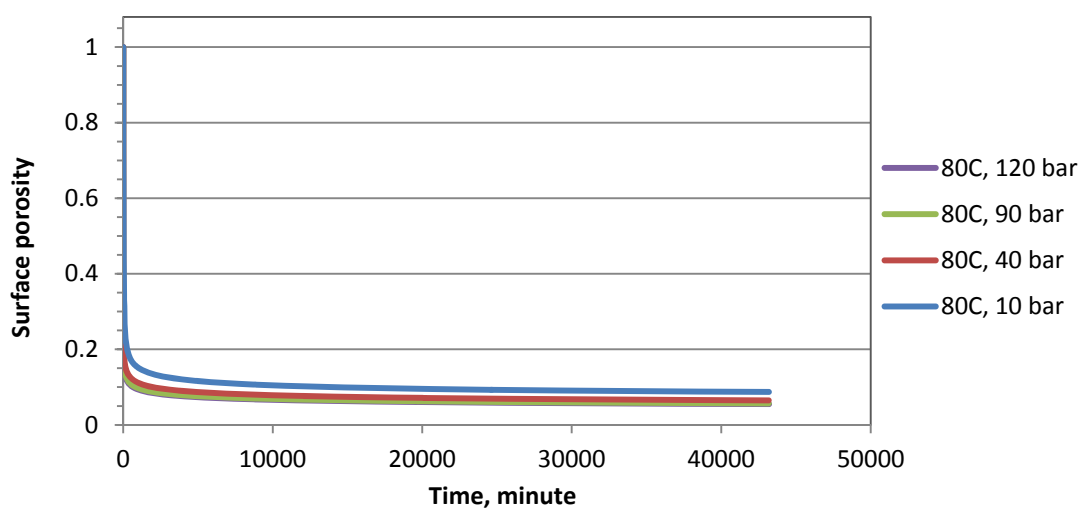


Figure 122. Simulated surface porosity at 80°C and autogenous pH for 30 days

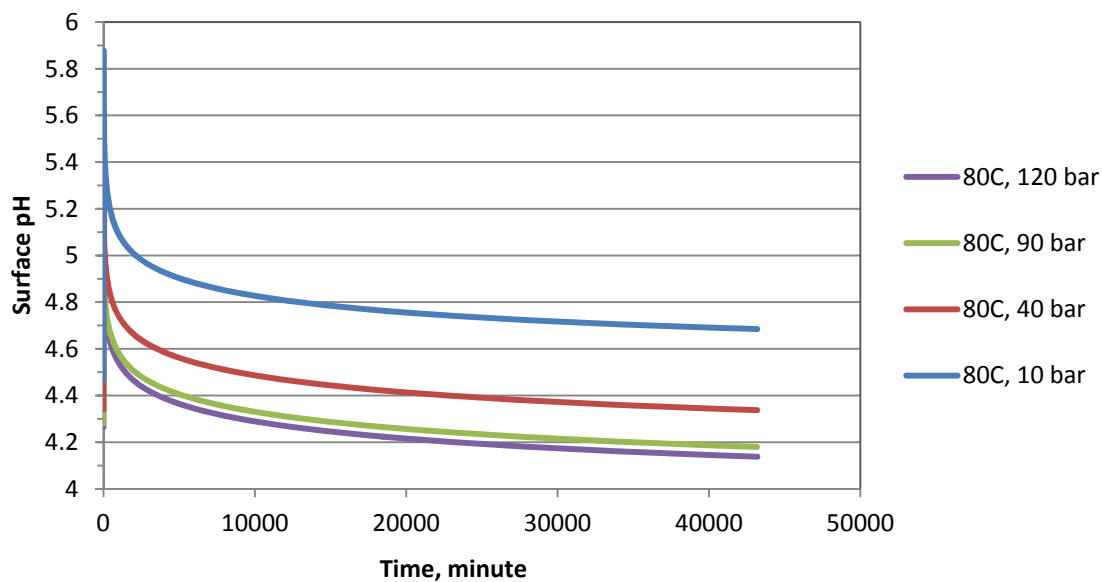


Figure 123. Predicted surface pH at 80°C and autogenous solution pH for 30 days

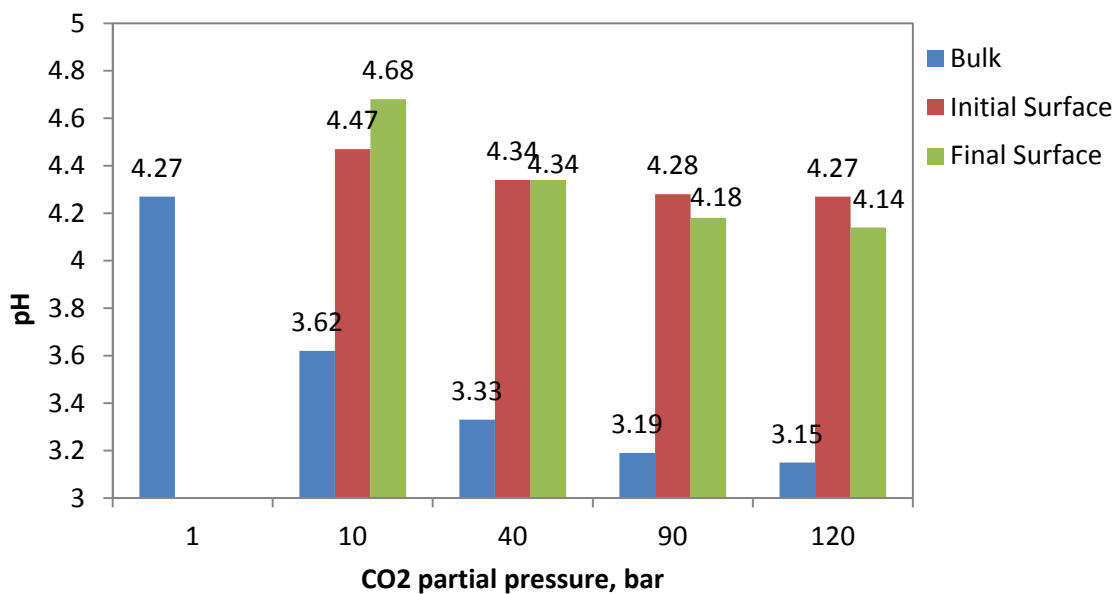


Figure 124. Predicted bulk and surface pH using Multicorp©

### 6.2.3 Multicorp© Simulation on the Effect of Flow

The effect of solution velocity on the corrosion rate of steel depends on several factors such as the passivity of the metal, salinity, O<sub>2</sub> concentration, and corrosion product or inhibitor film. For an active steel such as mild steel, its corrosion rate is affected by flow velocity only when it is diffusion-controlled, and the effect is only limited to low solution velocities [109]. The corrosion rate of an active steel will increase with increasing solution velocity but levels off as the velocity gets higher [18], [113]. The corrosion rate of an active-passive metal (stainless steel) is independent of flow at high solution velocity due to its passivity [18]. The increase in corrosion rate when velocity is increased is due to the O<sub>2</sub> reduction process. Hydrogen ions that are close to the steel surface are swept away by turbulent flow, enhancing the mass transport of O<sub>2</sub> towards the steel surface. Therefore, the effect of flow in the absence of O<sub>2</sub> is unseen [43]. Salinity of solution, *i.e.*, concentration of Cl<sup>-</sup> in the solution, also plays a role in the effect of flow on corrosion rate by interrupting passivation of steel. High salinity water, such as seawater, would exhibit increased corrosion rate with increasing solution velocity while this behavior is not exhibited in natural waters [43]. The effect of flow is less significant in the presence of an inhibitor film or a protective FeCO<sub>3</sub> layer on the steel surface, however, it can cause the initiation of pits [113].

The Multicorp© model is able to simulate for superficial water velocity up to 10 m/s. Simulation of corrosion was done at various velocities from 0.01 m/s to 10 m/s. Figure 125 and Figure 126 shows the effect of flow on the corrosion rate at 25°C and 80°C, respectively. Both figures show that the corrosion rate increases significantly as the

solution velocity is increased from 0.01 m/s to 1 m/s. The effect of flow is relatively insignificant at velocities higher than 1 m/s.

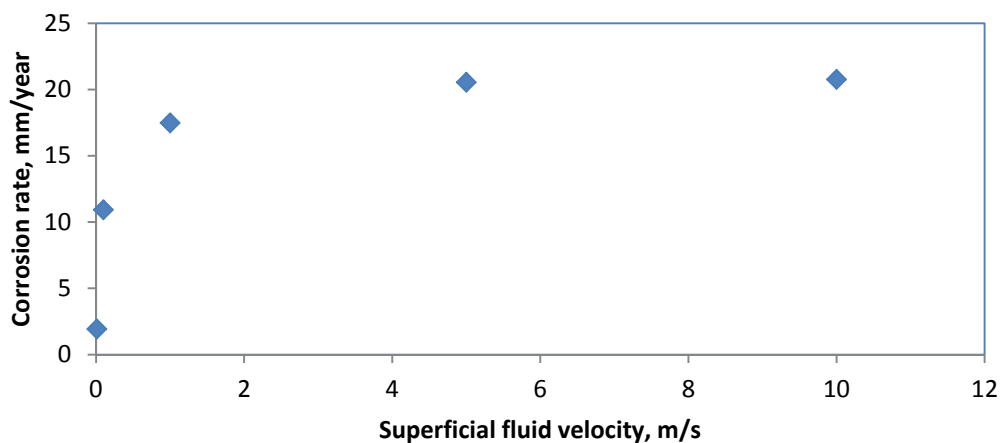


Figure 125. Simulated corrosion rate at varying flow velocities for non-FeCO<sub>3</sub> forming condition (25°C, 90 bar CO<sub>2</sub>, autogenous pH, 60 days)

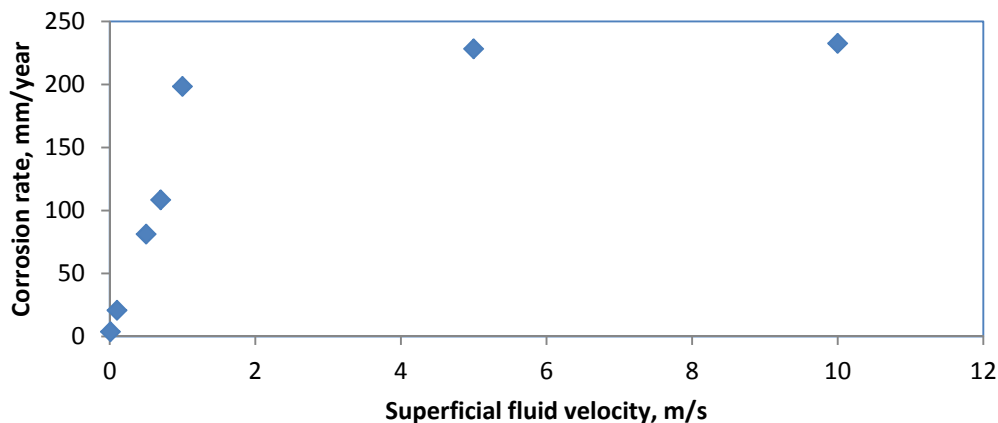


Figure 126. Simulated corrosion rate at varying flow velocities for FeCO<sub>3</sub> forming condition (80°C, 90 bar CO<sub>2</sub>, autogenous pH, 30 days)

The formation of corrosion product is also affected by flow. Simulation for 60 days at 25°C and 90 bar CO<sub>2</sub> showed a drop of corrosion rate at near stagnant

condition (0.01 m/s), typical of a protective film formation on the steel surface. This behavior is non-existent at higher velocities, which shows that flow interrupted the formation of a protective film/scale on the steel surface. The formation of a protective corrosion product at this lowest velocity is shown in Figure 128 as the decrease in surface porosity. The surface pH also appeared to be highest at the greatest fluid velocity, as shown in Figure 129. Turbulence and mixing in the flow enhances the transport of hydrogen ions from the bulk towards the surface of the steel.

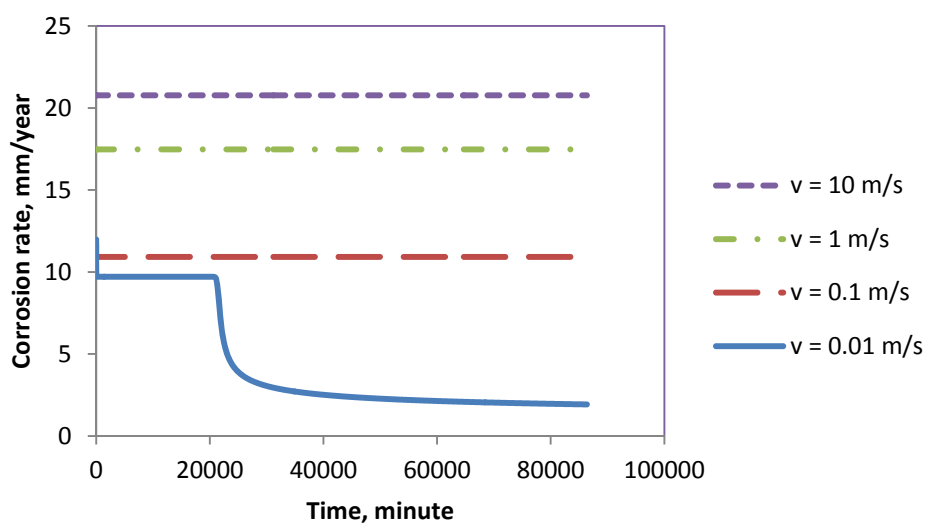


Figure 127. Evolution of simulated corrosion rate at varying flow velocities and non- $\text{FeCO}_3$  forming condition (25°C, 90 bar  $\text{CO}_2$ , autogenous pH, 60 days)

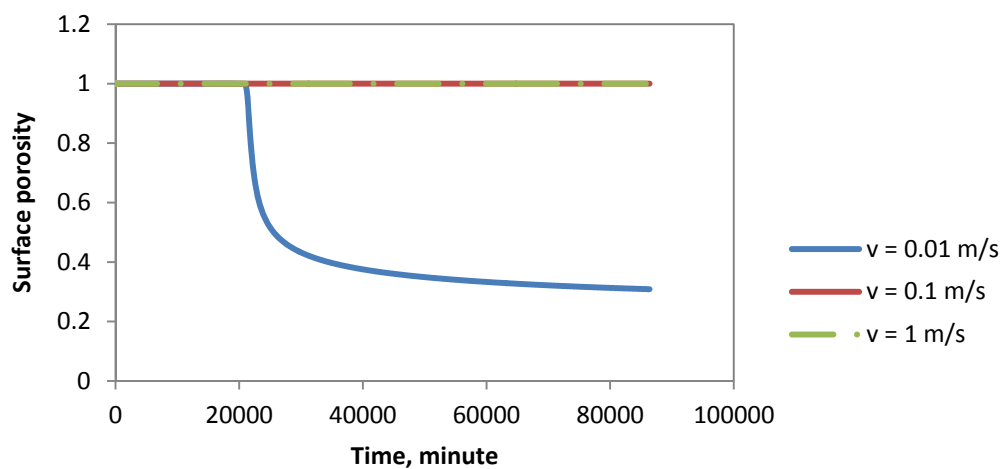


Figure 128. Simulated surface porosity at various flow velocities at 25°C, 90 bar CO<sub>2</sub>, autogenous pH for 60 days

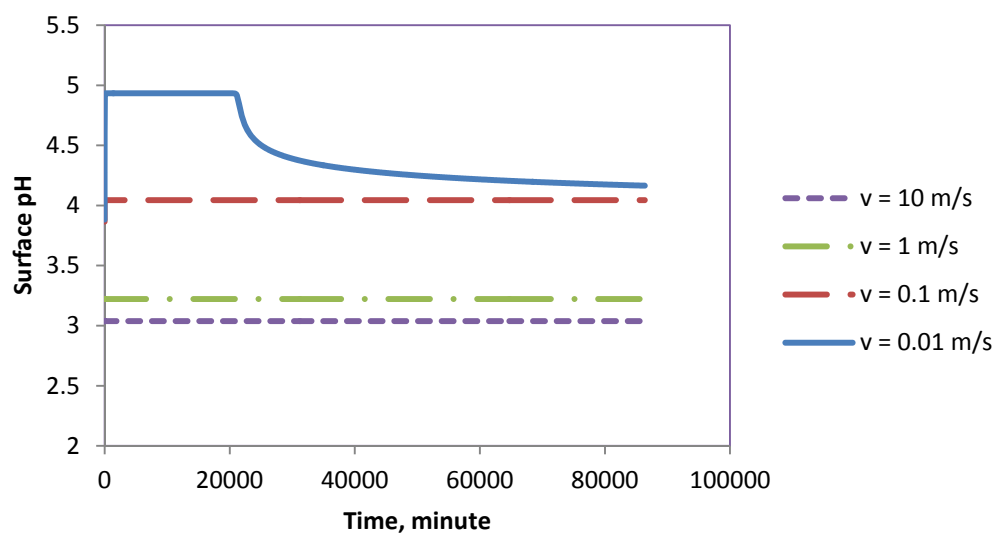


Figure 129. Simulated surface pH at various flow velocities at 25°C, 90 bar CO<sub>2</sub> and autogenous pH for 60 days

Prediction of corrosion rate at 80°C was compared with experimental data, as shown in Figure 130. The experimental data for the stagnant test is in closest agreement with the simulated corrosion rate at the lowest possible fluid velocity, 0.01 m/s.

However, experimental data for the test at 1000 rpm (this corresponds to about 1 m/s peripheral velocity), deviates greatly from the simulated data. This is due to the nature of the experiment that was a closed-system and non-refreshing, causing a great amount of change in the solution chemistry.

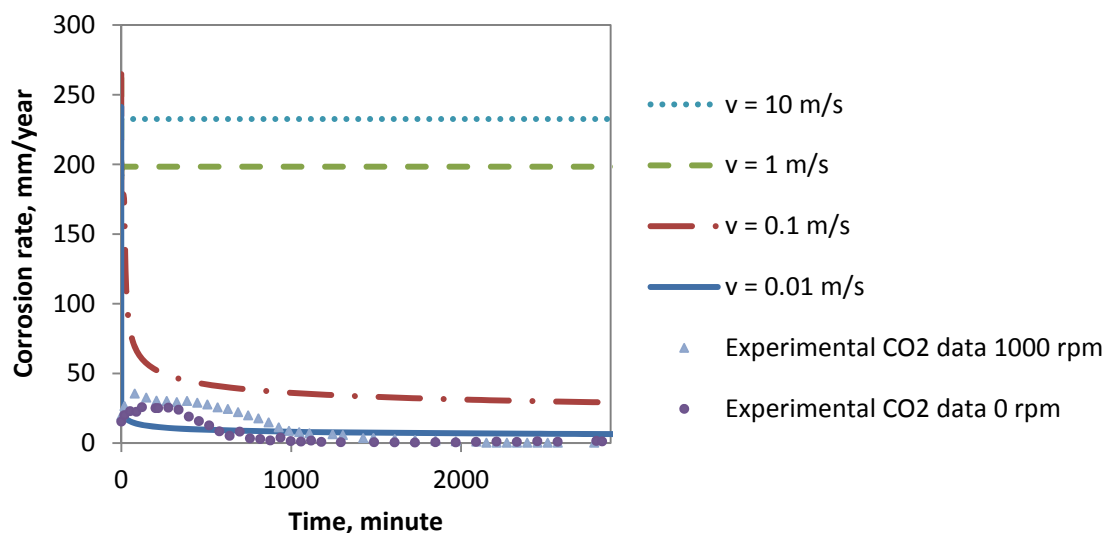


Figure 130. Predicted corrosion rate at various flow velocity at 80°C, 90 bar CO<sub>2</sub>, for 2 days at autogenous pH

### 6.3 Chapter Summary

The inclusion of O<sub>2</sub> in the Multicorp© model would benefit many decision makers in predicting and mitigating corrosion in CCS and CO<sub>2</sub>-EOR related industrial activities. Improved data such as for solubility of O<sub>2</sub> in CO<sub>2</sub> and in water at high pressures, and added capability to predict localized corrosion, will be beneficial when predicting the corrosion behavior of steel in CO<sub>2</sub>-containing oxic environments.

## CHAPTER 7: CONCLUSION AND RECOMMENDATIONS

The work in this dissertation has covered the study of carbon steel corrosion at supercritical and subcritical CO<sub>2</sub> relevant to the CCS and CO<sub>2</sub>-EOR sector in which O<sub>2</sub> is present as an aggressive contaminant in CO<sub>2</sub>. Observations from the experiments at gaseous and liquid CO<sub>2</sub> can be beneficial in terms of corrosion in CO<sub>2</sub> transmission line in the CCS network where the conditions are up to 30°C and 200 bar CO<sub>2</sub>. Results from experiments at supercritical CO<sub>2</sub> will be much more relevant to downhole condition (150°C and 500 bar CO<sub>2</sub>).

### 7.1 Overall Summary/Conclusion

While FeCO<sub>3</sub> was found to be advantageous in providing some form of protection to the steel surface, O<sub>2</sub> was destructive to it, see Chapter 4. O<sub>2</sub> was observed to cause degeneration of FeCO<sub>3</sub> crystals. The accumulation of iron oxides on the steel surface caused the occurrence of tubercles as occluded regions on the steel surface, creating a phenomenon similar to crevice corrosion that initiates the formation of pits. Oxides such as magnetite (Fe<sub>3</sub>O<sub>4</sub>), hematite ( $\alpha$ -Fe<sub>2</sub>O<sub>3</sub>), and goethite ( $\alpha$ -FeOOH) along with siderite (FeCO<sub>3</sub>) were the components of the tubercles.

Discussion in Chapter 5 has shown that the ingress of O<sub>2</sub> in high pressure CO<sub>2</sub> environment increased the overall corrosion rate of steel by suppressing the formation of FeCO<sub>3</sub> layer on the steel surface. Oxides similar to that in the low pressure tests were observed in the high pressure experiments at 80°C. Even though the presence of tubercles was not seen in high pressure experiments, pits were observed on the steel specimens in

the 80°C tests. XRD analyses detected iron carbide as the only significant corrosion product that was observed in the 25°C experiment, while EDS detected the presence of residual alloying elements such as Cu, Ni, Mn, and Mo on the steel surface. General uniform corrosion was observed at this low temperature.

The presence of flow heightened the severity of corrosion by disrupting the formation of a protective  $\text{FeCO}_3$  layer on the steel surface. This is due to the enhanced mass transport of species to/away from the steel surface, which decreased the saturation of ions with respect to  $\text{FeCO}_3$  formation. The combination of flow and  $\text{O}_2$  dramatically increased the overall general and localized corrosion rate.

Simulation of corrosion at high pressure and low pressure using in-house prediction models was beneficial. However, the models are not perfect. Predicted values of corrosion at low pressure using Multicorp© has shown almost perfect matching with experimental results. Simulation using Multicorp© for the high temperature low pressure conditions resulted in acceptable values as well. However, Multicorp© lacks in the calculation of the effect of  $\text{O}_2$  on  $\text{CO}_2$  corrosion. Prediction of corrosion rate at high pressure high temperature (HPHT) conditions showed the poorest correlation with experimental data.

## 7.2 Future Work/Recommendations

Based on the EDS analysis that was done on steel specimens shown in Chapter 5, the alloying elements and their enrichment has aroused a degree of curiosity. Future study on the effect of these alloying elements in steel can be conducted to understand their role

in corrosion of steel. The role of carbide as the skeletal remnants from corrosion of steel should also be further investigated. Other kinds of steels, such as 3Cr, 13Cr and other CRAs should also be tested to investigate their performance in oxic CO<sub>2</sub> corrosion environments.

The effect of O<sub>2</sub> may also differ in different kinds of brine, depending on the composition of the brine. Besides Na<sup>+</sup> and Cl<sup>-</sup>, the brine that is used at oil fields typically consist of other ions such as Ca<sup>2+</sup>, Mg<sup>2+</sup>, K<sup>+</sup>, and SO<sub>4</sub><sup>2-</sup>.

Based on the observations and high corrosion rate values in both low and high pressure situations, it is vital that corrosion inhibitor be employed in O<sub>2</sub>/CO<sub>2</sub> environment since it is universally accepted that corrosion rate should not exceed 0.1 mm/year. Mitigation of corrosion will help extend the life of equipment in CO<sub>2</sub>-EOR units. Investigation of the inhibition strategy for corrosion at high pressure with the ingress of O<sub>2</sub> should be conducted, especially in combatting the onset of localized corrosion underneath the thick corrosion product.

Prediction of corrosion using Multicorp© implies that the corrosion behavior of steel at low temperature potentially reaches its steady state at about 60 days. Therefore, longer tests can be conducted in order to give a better representation of the true corrosion behavior.

The overall setup design can also be improved. The change in the solution water chemistry should also be well-controlled either by using an ion-exchange unit, or simply using larger volume vessels. Quantification of the amount of O<sub>2</sub> and iron content throughout the duration of the experiment would be beneficial in determining the actual

kinetics of the corrosion product formation. A stable pH measurement device would be a valuable asset in future tests.

## REFERENCES

- [1] G. H. Koch, M. P. H. Brongers, N. G. Thompson, Y. P. Virmani, and J. H. Payer, "Corrosion Cost and Preventive Strategies in the United States.," Federal Highway Administration, McLean, VA, Technical Report FHWA-RD-01-156, 2002.
- [2] M. B. Kermani and D. Harrop, "The impact of corrosion on oil and gas industry," *SPE Prod. Facil.*, vol. 11, no. 3, pp. 186–190, 1996.
- [3] I. Herrera and G. F. Pinder, "Enhanced Oil Recovery," in *Mathematical Modeling in Science and Engineering*, John Wiley & Sons, Inc., 2012, pp. 149–164.
- [4] S. R. Reeves, "Demonstration of a novel, integrated, multi-scale procedure for high-resolution 3D reservoir characterization and improved CO<sub>2</sub>-EOR/sequestration management, SACROC Unit.," U.S. Department of Energy, DE-FC26-04NT15514, Mar. 2008.
- [5] L. E. Newton, "SACROC CO<sub>2</sub> project - Corrosion problems and solutions," in *Advances in CO<sub>2</sub> Corrosion*, vol. 2, Houston, TX: NACE International, 1985, pp. 235–249.
- [6] W. S. Han, B. J. McPherson, P. C. Lichtner, and F. P. Wang, "Evaluation of trapping mechanisms in geologic CO<sub>2</sub> sequestration: Case study of SACROC northern platform, a 35-year CO<sub>2</sub> injection site," *Am. J. Sci.*, vol. 310, no. 4, pp. 282–324, Apr. 2010.
- [7] R. F. Weeter and L. N. Halstead, "Production of CO<sub>2</sub> from a reservoir - a new concept," *J. Pet. Technol.*, vol. 34, no. 09, pp. 2144–2148, Sep. 1982.
- [8] T. D. Crameik and J. A. Plassey, "Carbon dioxide injection project SACROC Unit, Scurry County, Texas," in *Annual Meeting Papers, Division of Production*, Houston, TX, 1972, pp. 72–D001.
- [9] M. B. Kermani and A. Morshed, "Carbon dioxide corrosion in oil and gas production - A compendium," *Corrosion*, vol. 59, no. 8, pp. 659–683, 2003.
- [10] M. E. Parker, J. P. Meyer, and S. R. Meadows, "Carbon dioxide enhanced oil recovery injection operations technologies (Poster Presentation)," *Energy Procedia*, vol. 1, no. 1, pp. 3141–3148, Feb. 2009.
- [11] E. Akeer, B. Brown, and S. Nestic, "The influence of mild steel metallurgy on the initiation of localized CO<sub>2</sub> corrosion in flowing conditions," in *CORROSION/2013*, Orlando, FL, 2013, p. 2383.
- [12] J. Rogers and R. Grigg, "A literature analysis of the WAG injectivity abnormalities in the CO<sub>2</sub> process," *SPE Reserv. Eval. Eng.*, vol. 4, no. 5, Oct. 2001.

- [13] C. Preston, M. Monea, W. Jazrawi, K. Brown, S. Whittaker, D. White, D. Law, R. Chalaturnyk, and B. Rostron, "IEA GHG Weyburn CO<sub>2</sub> monitoring and storage project," *Fuel Process. Technol.*, vol. 86, no. 14–15, pp. 1547–1568, Oct. 2005.
- [14] S. Whittaker, B. Rostron, C. Hawkes, C. Gardner, D. White, J. Johnson, R. Chalaturnyk, and D. Seeburger, "A decade of CO<sub>2</sub> injection into depleting oil fields: Monitoring and research activities of the IEA GHG Weyburn-Midale CO<sub>2</sub> Monitoring and Storage Project," *Energy Procedia*, vol. 4, pp. 6069–6076, 2011.
- [15] B. M. Sass, H. Farzan, R. Prabhakar, J. Gerst, J. Sminchak, M. Bhargava, B. Nestleroth, and J. Figueroa, "Considerations for treating impurities in oxy-combustion flue gas prior to sequestration," *Energy Procedia*, vol. 1, no. 1, pp. 535–542, 2009.
- [16] A. Oosterkamp and J. Ramsen, "State of the art overview of CO<sub>2</sub> pipeline transportation with relevance to offshore pipelines," POLYTEC, Haugesund, Norway, POL-0-2007-138-A, 2008.
- [17] V. White, L. Torrente-Murciano, D. Sturgeon, and D. Chadwick, "Purification of oxyfuel-derived CO<sub>2</sub>," *Energy Procedia*, vol. 1, no. 1, pp. 399–406, 2009.
- [18] D. A. Jones, *Principles and Prevention of Corrosion*, 2nd ed. Upper Saddle River, NJ: Prentice Hall, 1996.
- [19] H. H. Uhlig, H. H. Triadis, and M. Stern, "Effect of oxygen, chlorides, and calcium ion on corrosion inhibition of iron by polyphosphates," *J Electrochem Soc*, vol. 102, pp. 59–66, 1955.
- [20] J. Collier, S. Papavinasam, J. Li, C. Shi, P. Liu, and J.-P. Gravel, "Effect of impurities on the corrosion performance of steels in supercritical carbon dioxide: Optimization of experimental procedure," in *CORROSION/2013*, Orlando, FL, 2013, p. 2357.
- [21] Y.-S. Choi, S. Nesic, and D. Young, "Effect of impurities on the corrosion behavior of CO<sub>2</sub> transmission pipeline steel in supercritical CO<sub>2</sub>-water environments," *Environ. Sci. Technol. Env. Sci Technol*, vol. 44, no. 23, pp. 9233–9238, 2010.
- [22] E. Gulbrandsen, J. Kvarekval, and H. Miland, "Effect of Oxygen Contamination on the Inhibition Studies of Carbon Dioxide Corrosion," *CORROSION*, vol. 61, no. 11, pp. 1086–1097, 2005.
- [23] R. L. Martin, "Corrosion consequences of oxygen entry into oilfield brines," in *CORROSION/2002*, Denver, CO, 2002, p. 02270.

- [24] G. Pipitone and O. Bolland, "Power generation with CO<sub>2</sub> capture: Technology for CO<sub>2</sub> purification," *Int. J. Greenh. Gas Control*, vol. 3, no. 5, pp. 528–534, Sep. 2009.
- [25] F. Yang, G.-B. Zhao, H. Adidharma, B. Towler, and M. Radosz, "Effect of oxygen on minimum miscibility pressure in carbon dioxide flooding," *Ind. Eng. Chem. Res.*, vol. 46, no. 4, pp. 1396–1401, 2007.
- [26] A. Oosterkamp and J. Ramsen, "State-of-the-Art Overview of CO<sub>2</sub> Pipeline Transport with relevance to offshore pipelines," POLYTEC, POL-O-2007-138-A, 2008.
- [27] H. Li, J. P. Jakobsen, Ø. Wilhelmsen, and J. Yan, "PVT<sub>xy</sub> properties of CO<sub>2</sub> mixtures relevant for CO<sub>2</sub> capture, transport and storage: Review of available experimental data and theoretical models," *Appl. Energy*, vol. 88, no. 11, pp. 3567–3579, Nov. 2011.
- [28] S. Nesic, "Carbon dioxide corrosion of mild steel," in *Uhlig's Corrosion Handbook*, 3rd ed., Hoboken, New Jersey: John Wiley & Sons, Inc., 2011, pp. 229–246.
- [29] C. deWaard and D. E. Milliams, "Carbonic acid corrosion of steel," *Corrosion*, vol. 31, no. 5, pp. 177–181, 1975.
- [30] C. deWaard and U. Lotz, "Prediction of CO<sub>2</sub> corrosion of carbon steel," in *CORROSION/93*, 1993, p. 69.
- [31] S. Nesic and W. Sun, "2.25 - Corrosion in Acid Gas Solutions," E.-C. T. J. A. Richardson, Ed. Oxford: Elsevier, 2010, pp. 1270–1298.
- [32] S. Nesic, J. Postlethwaite, and S. Olsen, "An electrochemical model for prediction of corrosion of mild steel in aqueous carbon dioxide solutions," *Corrosion*, vol. 52, no. 4, pp. 280–294, 1996.
- [33] W. Sun and S. Nešić, "Kinetics of corrosion layer formation: Part 1—Iron carbonate layers in carbon dioxide corrosion," *Corrosion*, vol. 64, no. 4, pp. 334–346, 2008.
- [34] A. Dugstad, "The importance of FeCO<sub>3</sub> supersaturation on the CO<sub>2</sub> corrosion of carbon steels," in *CORROSION/92*, 1992, p. 14.
- [35] S. Nešić and K.-L. Lee, "A mechanistic model for carbon dioxide corrosion of mild steel in the presence of protective iron carbonate films-Part 3: Film growth model," *Corrosion*, vol. 59, no. 7, pp. 616–628, 2003.

- [36] W. Sun, S. Nešić, and R. C. Woollam, “The effect of temperature and ionic strength on iron carbonate ( $\text{FeCO}_3$ ) solubility limit,” *Corros. Sci.*, vol. 51, no. 6, pp. 1273–1276, 2009.
- [37] W. Li, Y. Xiong, B. Brown, K. E. Kee, and S. Nestic, “Measurement of wall shear stress in multiphase flow and its effect on protective  $\text{FeCO}_3$  corrosion product layer removal,” in *CORROSION/2015*, Dallas, TX, 2015, p. 5922.
- [38] F. Farelas, B. Brown, and S. Nestic, “Iron Carbide and its Influence on the Formation of Protective Iron Carbonate in  $\text{CO}_2$  Corrosion of Mild Steel,” in *CORROSION/2013*, Orlando, FL, 2013, p. 2291.
- [39] V. Fajardo, B. Brown, D. Young, and S. Nešić, “Study of the solubility of iron carbonate in the presence of acetic acid using an EQCM,” in *CORROSION/2013*, Orlando, FL, 2013, p. 2452.
- [40] L. G. S. Gray, B. G. Anderson, M. J. Danysh, and P. R. Tremaine, “Mechanism of Carbon Steel Corrosion in Brines Containing Dissolved Carbon Dioxide at pH 4,” in *CORROSION/1989*, New Orleans, LA, 1989.
- [41] T. Tran, B. Brown, and S. Nestic, “Corrosion of Mild Steel in an Aqueous  $\text{CO}_2$  Environment – Basic Electrochemical Mechanisms Revisited,” in *CORROSION/2015*, Dallas, TX.
- [42] L. G. S. Gray, B. G. Anderson, M. J. Danysh, and P. R. Tremaine, “Effect of pH and temperature on the mechanism of carbon steel corrosion by aqueous carbon dioxide,” in *CORROSION/90*, Houston, TX, 1990, p. 40.
- [43] H. H. Uhlig and R. W. Revie, *Corrosion and corrosion control: an introduction to corrosion science and engineering*, 2nd ed. New York: John Wiley & Sons, 1985.
- [44] T. Tanupabrungrun, “Thermodynamics and kinetics of  $\text{CO}_2$  corrosion of mild steel at elevated temperatures,” Ohio University, Athens, OH, 2013.
- [45] Z. F. Yin, Y. R. Feng, W. Z. Zhao, Z. Q. Bai, and G. F. Lin, “Effect of temperature on  $\text{CO}_2$  corrosion of carbon steel,” *Surf. Interface Anal.*, vol. 41, no. 6, pp. 517–523, 2009.
- [46] S. Nestic and W. Sun, “Corrosion in acid gas solutions,” in *Shreir’s Corrosion*, 4th ed., vol. 2, 4 vols., T. J. A. Richardson, B. Cottis, R. Lindsay, S. Lyon, D. Scantlebury, H. Stott, and M. Graham, Eds. Amsterdam: Elsevier, 2010, pp. 1270–1298.
- [47] F. D. de Moraes, J. R. Shadley, J. Chen, and E. F. Rybicki, “Characterization of  $\text{CO}_2$  Corrosion Product Scales related to Environmental Conditions,” in *CORROSION/2000*, 2000, p. 30.

- [48] H. Fang, B. Brown, and S. Netic, "High Salt Concentration Effects On CO<sub>2</sub> Corrosion And H<sub>2</sub>S Corrosion," in *CORROSION/2010*, San Antonio, TX, 2010, p. 10276.
- [49] S. S. H. Rizvi, Z. R. Yu, A. R. Bhaskar, and C. B. C. Raj, "Fundamentals of Processing with Supercritical Fluids," S. S. H. Rizvi, Ed. Bishopbriggs, Glasgow: Chapman & Hall, 1994, pp. 1–26.
- [50] A. A. Clifford and J. R. Williams, "Introduction to Supercritical Fluids and Their Applications," vol. 13, J. R. Williams and A. A. Clifford, Eds. 2000, pp. 1–16.
- [51] W. A. Propp, T. E. Carleson, C. M. Wai, P. R. Taylor, K. W. Daehling, S. Huang, and M. Abdel-Latif, "Corrosion in Supercritical Fluids," US Department of Energy, DE96014006, 1996.
- [52] H. V. Poolen, *Fundamentals of enhanced oil recovery*. Tulsa, OK: PennWell Publishing Co., 1980.
- [53] Y. Zhang, X. Pang, S. Qu, X. Li, and K. Gao, "Discussion of the CO<sub>2</sub> corrosion mechanism between low partial pressure and supercritical condition," *Corros. Sci.*, vol. 59, pp. 186–197, 2012.
- [54] S. Wang, K. George, and S. Netic, "High pressure CO<sub>2</sub> corrosion electrochemistry and the effect of acetic acid," in *CORROSION/2004*, New Orleans, LA, 2004, p. 04375.
- [55] Y.-S. Choi and S. Nešić, "Corrosion behavior of carbon steel in supercritical CO<sub>2</sub>-water environments," in *CORROSION/2009*, Atlanta, GA, 2009, p. 09256.
- [56] K. O. Kongshaug and M. Seiersten, "Baseline experiments for the modelling of corrosion at high CO<sub>2</sub> pressure," in *CORROSION/2004*, New Orleans, LA, 2004, p. 04630.
- [57] S. M. Hesjevik, S. Olsen, and M. Seiersten, "Corrosion at High CO<sub>2</sub> Pressure," in *CORROSION/2003*, San Diego, CA, 2003, p. 3345.
- [58] S. Netic, M. Nordsveen, R. Nyborg, and A. Stangeland, "A mechanistic model for carbon dioxide corrosion of mild steel in the presence of protective iron carbonate films - Part 2: A numerical experiment," *Corrosion*, vol. 59, no. 6, pp. 489–497, 2003.
- [59] A. M. Nor, M. F. Suhor, M. F. Mohamed, M. Singer, and S. Netic, "Corrosion of Carbon Steel in High CO<sub>2</sub> Containing Environments - the Effect of High Flow Rate," in *CORROSION/2012*, Salt Lake City, UT, 2012, p. 1683.

- [60] E. M. Russick, G. A. Poulter, C. L. J. Adkins, and N. R. Sorensen, "Corrosive effects of supercritical carbon dioxide and cosolvents on metals," *J. Supercrit. Fluids*, vol. 9, no. 1, pp. 43–50, 1996.
- [61] M. F. Suhor, M. F. Mohamed, A. M. Nor, M. Singer, and S. Nestic, "Corrosion of mild steel in high CO<sub>2</sub> environment: effect of the FeCO<sub>3</sub> layer," in *CORROSION/2012*, Salt Lake City, Utah, 2012, p. 1434.
- [62] H. Li, Ø. Wilhelmsen, Y. Lv, W. Wang, and J. Yan, "Viscosities, thermal conductivities and diffusion coefficients of CO<sub>2</sub> mixtures: Review of experimental data and theoretical models," *Int. J. Greenh. Gas Control*, vol. 5, no. 5, pp. 1119–1139, 2011.
- [63] H. Li, J. Yan, J. Yan, and M. Anheden, "Impurity impacts on the purification process in oxy-fuel combustion based CO<sub>2</sub> capture and storage system," *Appl. Energy*, vol. 86, no. 2, pp. 202–213, Feb. 2009.
- [64] J. Stoll, J. Vrabec, and H. Hasse, "Vapor–liquid equilibria of mixtures containing nitrogen, oxygen, carbon dioxide, and ethane," *AIChE J.*, vol. 49, no. 8, pp. 2187–2198, 2003.
- [65] A. Fredenslund and G. A. Sather, "Gas-liquid equilibrium of the oxygen-carbon dioxide system," *J. Chem. Eng. Data*, vol. 15, no. 1, pp. 17–22, Jan. 1970.
- [66] A. Fredenslund, J. Mollerup, and O. Persson, "Gas-liquid equilibrium of oxygen-carbon dioxide system," *J. Chem. Eng. Data*, vol. 17, no. 4, pp. 440–443, 1972.
- [67] L. Garverick, *Corrosion in the Petrochemical Industry*. ASM International, 1994.
- [68] H. M. Herro, "MIC myths - Does pitting cause MIC?," in *CORROSION/98*, San Diego, 1998, p. 278.
- [69] X. Gao, "Localized corrosion initiation by O<sub>2</sub> in CO<sub>2</sub> environment," Institute for Corrosion and Multiphase Technology, Athens OH, CCJIP, Mar. 2013.
- [70] J. R. Baylis, "Factors other than dissolved oxygen influencing the corrosion of iron pipes," *Ind. Eng. Chem.*, vol. 18, no. 4, pp. 370–380, 1926.
- [71] R. I. Ray, J. S. Lee, B. J. Little, and T. L. Gerke, "The anatomy of tubercles: A corrosion study in a fresh water estuary," *Mater. Corros.*, vol. 61, no. 12, pp. 993–999, Dec. 2010.
- [72] P. Sarin, V. L. Snoeyink, J. Bebee, W. M. Kriven, and J. A. Clement, "Physico-chemical characteristics of corrosion scales in old iron pipes," *Water Res.*, vol. 35, no. 12, pp. 2961–2969, 2001.

- [73] L. McNeill and M. Edwards, "Iron pipe corrosion in water distribution systems," *Am. Water Works Assoc.*, vol. 93, no. 7, pp. 88–100, Jan. 2001.
- [74] U. Schwertmann, "Solubility and dissolution of iron oxides," *Plant Soil*, vol. 130, no. 1–2, pp. 1–25, Jan. 1991.
- [75] U. Schwertmann and R. M. Cornell, *Iron oxides in the laboratory. Preparation and characterization*. Wiley-VCH, Weinheim, Germany, 2000.
- [76] S. J. Oh, D. C. Cook, and H. E. Townsend, "Characterization of iron oxides commonly formed as corrosion products on steel," *Hyperfine Interact.*, vol. 112, no. 1–4, pp. 59–66, 01 1998.
- [77] T. Misawa, K. Asami, K. Hashimoto, and S. Shimodaira, "The mechanism of atmospheric rusting and the protective amorphous rust on low alloy steel," *Corros. Sci.*, vol. 14, no. 4, pp. 279–289, 1974.
- [78] T. Misawa, K. Hashimoto, and S. Shimodaira, "The mechanism of formation of iron oxide and oxyhydroxides in aqueous solutions at room temperature," *Corros. Sci.*, vol. 14, no. 2, pp. 131–149, 1974.
- [79] M. A. Legodi and D. de Waal, "The preparation of magnetite, goethite, hematite and maghemite of pigment quality from mill scale iron waste," *Dyes Pigments*, vol. 74, pp. 161–168, 2007.
- [80] G. T. Skaperdas and H. H. Uhlig, "Corrosion of steel by dissolved carbon dioxide and oxygen," *Ind. Eng. Chem.*, vol. 34, no. 6, pp. 748–754, 1942.
- [81] S. Wang, "Effect of oxygen on CO<sub>2</sub> corrosion of mild steel," Russ College of Engineering and Technology, Ohio University, Athens OH, 2009.
- [82] W. Liu, S. Dong, J. Zhang, X. Lin, J. He, and M. Lu, "Effect of oxygen on corrosion and erosion-corrosion behavior of N80 steel under high temperature and high pressure," in *CORROSION/2014*, San Antonio, TX, 2014, p. 4198.
- [83] X. Gao, "Mechanisms of localized corrosion initiation in CO<sub>2</sub> and H<sub>2</sub>S environments," ICMT, CCJIP Report, 2010.
- [84] X. Jiang, "Effect of oxygen contamination on CO<sub>2</sub> corrosion in presence of FeCO<sub>3</sub> film," ICMT, CCJIP Report, 2008.
- [85] D. John, B. Kinsella, S. Bailey, and R. D. Marco, "Flow dependence of carbon dioxide corrosion rates and the interference of trace dissolved oxygen," in *CORROSION/2007*, Nashville, TN, 2007, p. 07315.

- [86] Y.-S. Choi and S. Netic, "Effect of impurities on the corrosion behavior of carbon steel in supercritical CO<sub>2</sub> - water environments," in *CORROSION/2010*, San Antonio, TX, 2010, p. 10196.
- [87] Y.-S. Choi, S. Nešić, and D. Young, "Effect of impurities on the corrosion behavior of CO<sub>2</sub> transmission pipeline steel in supercritical CO<sub>2</sub>-water environments," *Environ. Sci. Technol.*, vol. 44, no. 23, pp. 9233–9238, Dec. 2010.
- [88] J. Zhang, X. Lin, S. Lu, T. Wang, W. Liu, S. Dong, C. Yang, and M. Lu, "Corrosion behavior and mechanism of N80 steel under high temperature and high pressure CO<sub>2</sub>-O<sub>2</sub> coexisting condition," in *CORROSION/2013*, Orlando, FL, 2013, p. 2479.
- [89] X. Lin, W. Liu, F. Wu, C. Xu, J. Dou, and M. Lu, "Effect of O<sub>2</sub> on corrosion of 3Cr steel in high temperature and high pressure CO<sub>2</sub>-O<sub>2</sub> environment," *Appl. Surf. Sci.*, vol. 329, pp. 104–115, Feb. 2015.
- [90] N. R. Rosli, Y.-S. Choi, and D. Young, "Impact of oxygen ingress in CO<sub>2</sub> corrosion of mild steel," in *CORROSION/2014*, San Antonio, TX, 2014, p. 4299.
- [91] F. Ayello, K. Evans, R. Thodla, and N. Sridhar, "Effect of impurities on corrosion of steel in supercritical CO<sub>2</sub>," in *CORROSION/2010*, San Antonio, TX, 2010, p. 10193.
- [92] R. L. Martin, "Corrosion consequences of oxygen entry into sweet oilfield fluids," in *SPE Permian Basin Oil and Gas Recovery Conference*, Midland, TX, 2001, p. SPE 70029.
- [93] A. T. Laudate, *The JEOL Institute Scanning Electron Microscope Operations Course*. 2008.
- [94] S. Richter, "Advanced use of the SEM: a seminar," presented at the Institute for Corrosion and Multiphase Technology, Ohio University, Athens OH, 2013.
- [95] B. Brown, "The likelihood of localized corrosion in an H<sub>2</sub>S/CO<sub>2</sub> environment," in *CORROSION/2015*, Dallas TX, 2015, p. 5855.
- [96] T. L. Gerke, J. B. Maynard, M. R. Schock, and D. L. Lytle, "Physiochemical characterization of five iron tubercles from a single drinking water distribution system: Possible new insights on their formation and growth," *Corros. Sci.*, vol. 50, no. 7, pp. 2030–2039, 2008.
- [97] R. I. Ray, J. S. Lee, B. J. Little, and T. L. Gerke, "The anatomy of tubercles: A corrosion study in a fresh water estuary," *Mater. Corros.*, vol. 61, no. 12, pp. 993–999, 2010.

- [98] P. Sarin, V. L. Snoeyink, J. Bebee, W. M. Kriven, and J. A. Clement, "Physico-chemical characteristics of corrosion scales in old iron pipes," *Water Res.*, vol. 35, no. 12, pp. 2961–2969, Aug. 2001.
- [99] P. Sarin, V. Snoeyink, D. Lytle, and W. Kriven, "Iron Corrosion Scales: Model for Scale Growth, Iron Release, and Colored Water Formation," *J. Environ. Eng.*, vol. 130, no. 4, pp. 364–373, 2004.
- [100] G. L. Miessler and D. A. Tarr, *Inorganic Chemistry*, 4th ed. Upper Saddle River, NJ: Pearson Prentice Hall, 2004.
- [101] H. K. Van Poolen and Associates, *Fundamentals of enhanced oil recovery*. PennWell Books, 1980.
- [102] Y.-S. Choi, D. Young, S. Nešić, and L. G. S. Gray, "Wellbore integrity and corrosion of carbon steel in CO<sub>2</sub> geologic storage environments: A literature review," *Int. J. Greenh. Gas Control*, vol. 16, Supplement 1, pp. S70–S77, Jun. 2013.
- [103] A. Dugstad and M. Halseid, "Internal corrosion in dense phase CO<sub>2</sub> transport pipelines - State of the art and the need for further R&D," in *CORROSION/2012*, Salt Lake City, UT, 2012.
- [104] D. W. DeBerry and W. S. Clark, "Corrosion due to use of carbon dioxide for enhanced oil recovery. Final Report. Sumx No. 78-003," SumX Corp., Austin, TX (USA), DOE/MC/08442-1, Sep. 1979.
- [105] S. D. Kapusta and S. C. Canter, "Corrosion control in CO<sub>2</sub> enhanced oil recovery," in *CORROSION/94*, Baltimore, MD, 1994.
- [106] A. Mohammed Nor, "The Effect of Turbulent Flow on Corrosion of Mild Steel in High Partial CO<sub>2</sub> Environments," Ohio University, 2013.
- [107] A. Dugstad, L. Børvik, S. Palencsar, and P. A. Eikrem, "Corrosion testing of steel armour wires in flexible pipes - a parametric study," in *CORROSION/2015*, Dallas, TX, 2015, p. 5829.
- [108] R. M. Cornell and U. Schwertmann, *The iron oxides: structure, properties, reactions, occurrences and uses*. Wiley-vch, 2003.
- [109] M. G. Fontana and N. D. Greene, *Corrosion engineering*. McGraw-Hill, 1967.
- [110] A. A. Al-Asadi, "Iron Carbide Development and its Effect on Inhibitor Performance," Ohio University, 2014.

- [111] A. Pfennig and R. Bäßler, “Effect of CO<sub>2</sub> on the stability of steels with 1% and 13% Cr in saline water,” *Corros. Sci.*, vol. 51, no. 4, pp. 931–940, Apr. 2009.
- [112] Y. Zheng, J. Ning, B. Brown, D. Young, and S. Netic, “Mechanistic Study of the Effect of Iron Sulfide Layers on Hydrogen Sulfide Corrosion of Carbon Steel,” in *CORROSION/2015*, Dallas, TX, 2015, p. 5933.
- [113] S. Nešić, “Key issues related to modelling of internal corrosion of oil and gas pipelines – A review,” *Corros. Sci.*, vol. 49, no. 12, pp. 4308–4338, Dec. 2007.
- [114] D. Tromans, “Temperature and pressure dependent solubility of oxygen in water: a thermodynamic analysis,” *Hydrometallurgy*, vol. 48, no. 3, pp. 327–342, 1998.

## APPENDIX A: AES ANALYSIS OF STEEL SPECIMEN


**LABORATORY  
TESTING INC.**

 2331 Topaz Drive, Hatfield, PA 19440  
 Phone: 800-219-9095 • Fax: 800-219-9096

**Certified Test Report**

ICM001-07-02-04366-1

*RCE Material  
5/8" stock*

 ISO/IEC 17025  
 Materials Testing Laboratory  
 NDT (PT, MT, UT)

**SOLD TO**

 Institute for Corrosion  
 Ohio University  
 340 1/2 W. State Street  
 Athens, OH 45701-2979

**SHIP TO**

 Institute for Corrosion  
 Multiphase Techn.- Ohio Univer  
 340 1/2 W. State Street  
 Athens, OH 45701  
 ATTN: Bruce N. Brown

**CUSTOMER P.O.**

CREDIT-CARD

**CERTIFICATION DATE**

2/15/2007

**SHIP VIA**

FAX AND MAIL

**DESCRIPTION**

Test Sample, Labeled 5

The referenced sample was submitted to chemical content evaluation and it was found to be in conformance to UNS G10180 with the following results:

ELEMENT	REQUIREMENTS		ACTUAL
	MIN	MAX	
Al			0.008%
As			0.006%
C	0.15	0.20	0.18%
Co			0.003%
Cr			0.12%
Cu			0.18%
Mn	0.60	0.90	0.75%
Mo			0.020%
Nb			0.002%
Ni			0.065%
P		0.030	0.011%
S		0.050	0.021%
Sb			0.009%
Si			0.16%
Sn			0.009%
Ta			0.028%
Ti			0.002%
V			0.003%
W			0.014%
Zn			0.004%
Zr			0.003%

**Procedures/Methods:** 86-SCA-0, Rev. 7, Direct Reading Atom Emissions Spectroscopy

The services performed above were done in accordance with LTI's Quality System Program Manual Revision 17 dated 12/3/04 and ISO/IEC 17025. These results relate only to the items tested and this report shall not be reproduced, except in full, without the written approval of Laboratory Testing, Inc. L.T.I. is accredited by NADCAP to ISO/IEC 17025, Material's Testing and NDT (MT, PT and UT). Reported results represent the actual attributes of the material / item tested. Testing was performed in accordance with all applicable specification and contract / purchase order requirements.

**MERCURY CONTAMINATION:** During the testing and inspection, the product did not come in direct contact with mercury or any of its compounds nor with any mercury containing devices employing a single boundary of containment.

**NOTE:** The recording of false, fictitious or fraudulent statements or entries on this document may be punished as a felony under Federal Statutes.

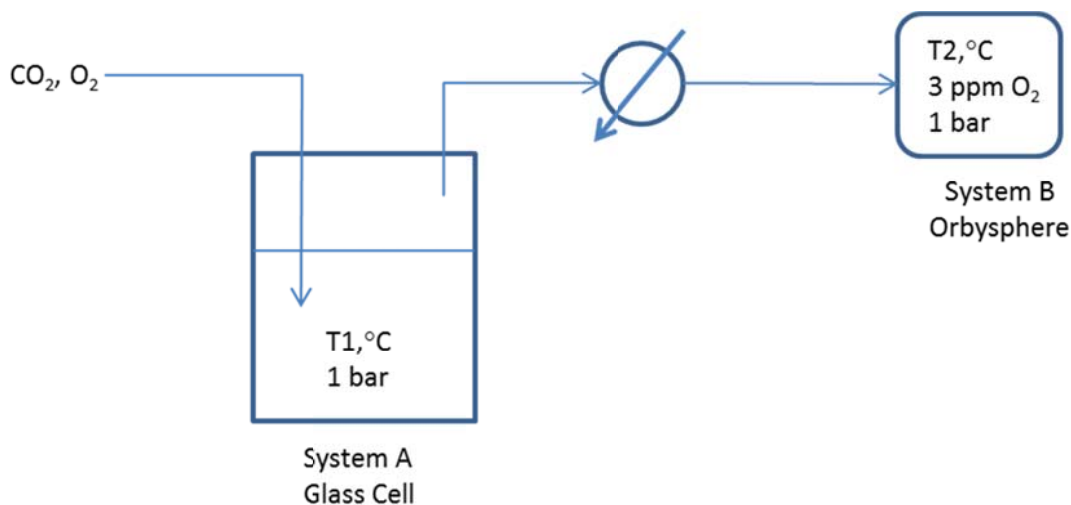
 Sherri L. Scheifele  
 QA Specialist

*Sherri L. Scheifele*

 By: \_\_\_\_\_  
 Authorized Signature

APPENDIX B: CALCULATION OF O<sub>2</sub> CONTENT IN WATER FROM ORBISPHERE

## DATA

System A: Glass Cell

$$P_{\text{total}} = 1 \text{ bar}$$

If  $T_1 = 80^\circ\text{C}$  (353.15 K), then partial pressure of water,  $p_w = 0.47$  bar (from Perry's Chemical Engineers' Handbook)

Unknowns =  $c_{\text{O}_2}$ ,  $p_{\text{O}_2}$ ,  $p_{\text{CO}_2}$ .

Using equation from Tromans (1998), and T is in Kelvin.

$$k = \exp \left\{ \frac{0.046T^2 + 203.35T \ln(T/298) - (299.378 + 0.092T)(T - 298) - 20.591 \times 10^3}{(8.3144)T} \right\}$$

So,  $k_{\text{O}_2} = 0.000793 \text{ mol/L}\cdot\text{bar}$

$$p_{\text{O}_2} + p_{\text{CO}_2} = p_{\text{Total}} - p_{\text{Water}} = 1 - 0.47 = 0.53 \text{ bar}$$

$$\text{So } p_{\text{CO}_2} = 0.53 - p_{\text{O}_2}$$

System B: Orbysphere

$$P_{\text{total}} = 1 \text{ bar}$$

If  $T_2 = 25^\circ\text{C}$  (298.15 K), then partial pressure of water,  $p_w = 0.03 \text{ bar}$  (from Perry's Chemical Engineers' Handbook)

The concentration of  $\text{O}_2$  (orbysphere) = 3 ppm = 3 mg/L =  $9.375 \times 10^{-5} \text{ mol/L}$

Unknowns =  $p_{\text{O}_2}$ ,  $p_{\text{CO}_2}$ .

Using the same equation from Tromans (1998), and T is in Kelvin.

$$k_{\text{O}_2} = 0.0012788 \text{ mol/L}\cdot\text{bar}$$

$$p_{\text{O}_2} = c_{\text{O}_2}/k_{\text{O}_2} = 9.375 \times 10^{-5} \text{ mol/L} / 0.0012788 \text{ mol/L}\cdot\text{bar} = 0.0733 \text{ bar}$$

$$p_{\text{CO}_2} = p_{\text{total}} - p_{\text{O}_2} - p_{\text{water}} = 1 - 0.0733 - 0.03 = 0.8967 \text{ bar}$$

The ratio of  $\text{O}_2/\text{CO}_2$  is  $0.0733/0.8967 = 0.082$

Since the ratio of  $\text{O}_2/\text{CO}_2$  in systems A and B are the same, therefore, in System A,

$$p_{\text{CO}_2} = 0.53/(1+0.082) = 0.49 \text{ bar}$$

$$p_{\text{O}_2} = 0.53-0.49 = 0.04 \text{ bar}$$

The concentration of  $\text{O}_2$  in the glass cell is,

$$c_{\text{O}_2} = k_{\text{O}_2} \times p_{\text{O}_2} = 3.18 \times 10^{-5} \text{ mol/L} = 1.02 \text{ mg/L} = 1.02 \text{ ppm}$$

Assumptions: The electrolyte NaCl concentration is low and negligible to consider the effect of NaCl.

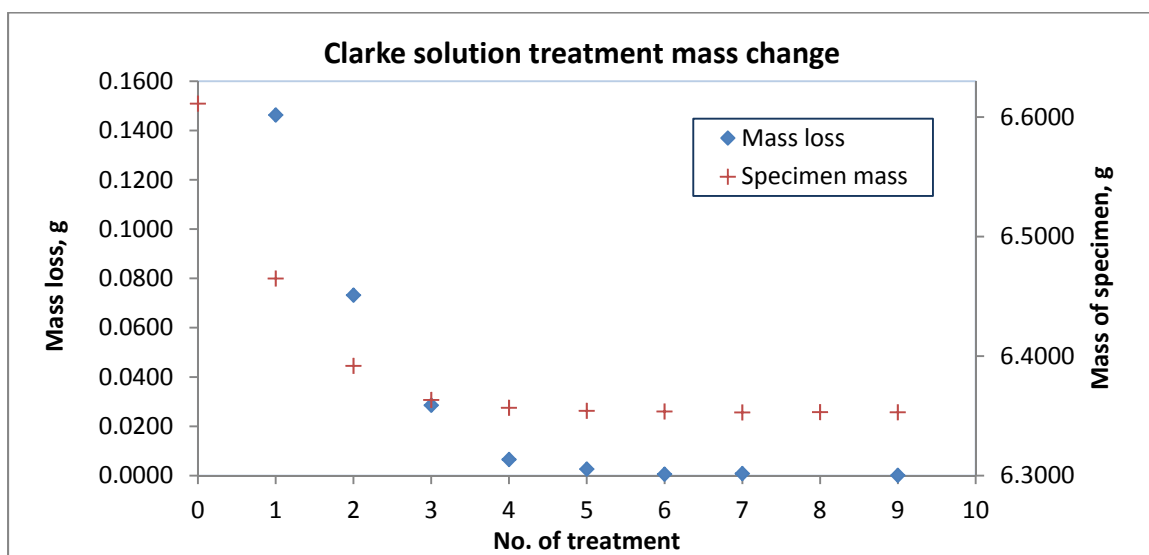
Data from Perry's Handbook		
T	Water Vapor Pressure	
°C	mmHg	bar
25	23.756	0.0317
30	31.824	0.0424
35	42.175	0.0562
40	55.324	0.0738
50	92.510	0.1233
60	149.38	0.1992
70	233.70	0.3116
80	355.10	0.4735
90	525.76	0.7010
100	760.00	1.0133

## APPENDIX C: CLARKE SOLUTION TREATMENT (ASTM G1-03)

The Clarke solution for removal of corrosion product on steel consists of the following:

- 1) 100 mL hydrochloric acid, HCl
- 2) 2 g Antimony trioxide,  $\text{Sb}_2\text{O}_3$
- 3) 5 g Stannous chloride,  $\text{SnCl}_2$

Clarke solution is a light brown formulation. The solution is corrosive; therefore the procedure was conducted in a fume hood. Details of the procedure are provided in ASTM G1-03 Standard Practice for Preparing, Cleaning, and Evaluating Corrosion Test Specimens. Measurements of weight loss was done at every cycle of Clarke treatment until the change in the mass was only in the 4<sup>th</sup> decimal point, as shown in the plot below.



APPENDIX D: SAMPLE CALCULATION OF CORROSION RATE FROM WEIGHT  
LOSS

In this example, the weight of a specimen, retrieved from an experiment at 80°C and 90 bar CO<sub>2</sub>, was determined using a digital balance during Clarke solution treatment, accurate up to 4 decimal points. The surface area of the specimen was determined prior to the start of the experiment by measuring the dimensions of the flat steel specimen. The following equation was used to determine the corrosion rate in the mm/y.

$$CR = \frac{W}{DAT}$$

The mass of the specimen before the start of the experiment,  $W_{\text{before}} = 6.6112$  g

The mass of the retrieved specimen after Clarke solution treatment,  $W_{\text{after}} = 6.3529$  g

The weight loss,  $W = 6.6112 - 6.3529 = 0.2583$  g

The density of the steel,  $D = 7.87 \text{ g/cm}^3 = 0.00787 \text{ g/mm}^3$

The surface area,  $A = 585.7705 \text{ mm}^2$

The time of exposure,  $T = 48 \text{ h} = 0.0056 \text{ y}$

Inserting all these values into the equation will result in a corrosion rate value of 10.23 mm/y.

APPENDIX E: SAMPLE CALCULATION OF CORROSION RATE FROM  
POLARISATION RESISTANCE

To calculate the corrosion rate, the true polarization resistance,  $R_p$ , was determined by deducting the solution resistance from the total polarization resistance that was obtained from LPR.

$$R_p = R_{p,total} - R_s$$

The solution resistance was obtained by conducting an Electrical Impedance Spectroscopy (EIS) on the specimen. The current density was then calculated using the Stern-Geary equation:

$$i = \frac{B}{R_p} = \frac{\beta_a \times \beta_c}{2.3 \times R_p \times (\beta_a + \beta_c)}$$

Where  $\beta_a$  and  $\beta_c$  are the anodic and cathodic Tafel slopes, set to a value of 0.12 V/decade each, resulting a Stern-Geary constant,  $B$ , value of 0.026 V. The corrosion current, in unit  $A/m^2$ , is obtained by dividing the current density with the surface area of the steel specimen that is exposed to the solution.

$$i_{corr} = \frac{i}{A}$$

The corrosion rate is then calculated using the equation:

$$CR = \frac{i_{corr} M_{Fe}}{\rho n F} \cdot \left[ \frac{mm}{year} \right] = \frac{i_{corr} M_{Fe}}{\rho n F} \cdot \frac{1000 mm}{1 year} \cdot 365 \times 24 \times 60 \times 60$$

Which is essentially  $CR = i_{corr} \times 1.16$

Where  $M_w$  is molecular weight of the Fe = 55.845 g/mol,

$\rho$  is the density = 7,870,000 g/m<sup>3</sup>,

$n$  is the number of charges = 2 (For every mol of iron lost, 2 mol of electrons are released).

$F$  is the Faraday's constant, 96,485 C/mol.

In one example on Aug 25, 2015, the  $R_{p,LPR}$  and  $E_{corr}$  was recorded using LPR while the  $R_s$  was determined using EIS. The exposed area of the steel specimen is 0.00054 m<sup>2</sup>.

$$R_{p,LPR} = 3.96 \, \Omega \qquad E_{corr} = -587 \, \text{mV} \qquad R_s = 3.1 \, \Omega$$

The true  $R_p = 3.96 - 3.1 = 0.86 \, \Omega$

$$i = \frac{B}{R_p} = \frac{0.026}{0.86} = 0.030233$$

$$i_{corr} = \frac{i}{A} = \frac{0.030233}{0.00054} = 55.986$$

Corrosion rate =  $i_{corr} \times 1.16 = 64.94 \, \text{mm/year}$

APPENDIX F: PREDICTED O<sub>2</sub> SOLUBILITY IN WATER

O<sub>2</sub> solubility in water was computed using Henry's Law vs. MultiFlash 4.2.

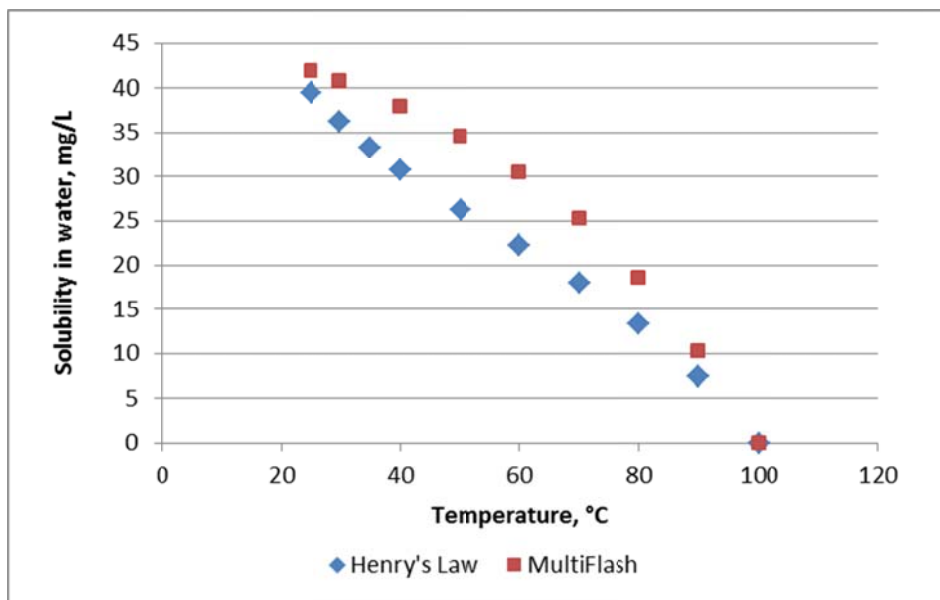


Figure E1: Solubility of oxygen in water as a function of temperature computed using two different methods of prediction.

The calculations and computations of the above plot are as follows:

### Part 1: MultiFlash 4.2

Simulation software, Multiflash 4.2 by Infochem was utilized to predict the mole fraction of oxygen in water at varying temperatures. Model set Cubic Plus Association (CPA-Infochem) with STRAPP/STRAPP/LGST transport properties was chosen as the calculation model. This model is based on the Redlich-Kwong-Soave model incorporated with the Wertheim theory of chemical association effect in a mixture.

The system was assumed to consist of only water and oxygen. Based on experimental conditions (3 L of solution in a 4 L vessel), the number of moles of water

and oxygen was calculated. The number of moles of oxygen, calculated using the Ideal Gas Law, is 0.16 moles. The number of moles in 3 L of water is 166.5 moles.

The software computes the mole fraction of each species in the water phase. The mol fraction was then converted into units of solubility, grams per mole. The results are shown in the following table.

Table E1: Results of computation using MultiFlash 4.2

Temperature		mol frac in water		Total	No. of moles		Mass, gram		$\rho_{Water}$	V water	O2 conc
K	C	xO2	xH2O	mol	nO2	nWater	mO2	mWater	(kg/m <sup>3</sup> )	L	gram/L
298.15	25	2.36E-05	0.999976	166.499	3.93E-03	166.495	1.26E-01	2996.91	996.95	3.006079	0.042
303.15	30	2.30E-05	0.999977	166.497	3.83E-03	166.4932	1.23E-01	2996.877	995.7	3.009819	0.041
313.15	40	2.15E-05	0.999978	166.491	3.59E-03	166.4873	1.15E-01	2996.772	992.2	3.020331	0.038
323.15	50	1.97E-05	0.99998	166.481	3.28E-03	166.4777	1.05E-01	2996.598	988.1	3.032687	0.035
333.15	60	1.74E-05	0.999983	166.463	2.90E-03	166.4602	9.27E-02	2996.283	983.2	3.047481	0.030
343.15	70	1.45E-05	0.999986	166.43	2.41E-03	166.4277	7.72E-02	2995.698	977.8	3.063712	0.025
353.15	80	1.08E-05	0.999989	166.356	1.79E-03	166.3542	5.74E-02	2994.375	971.8	3.081267	0.019
363.15	90	5.98E-06	0.999994	166.119	9.93E-04	166.118	3.18E-02	2990.124	965.3	3.097611	0.010
373.15	100	0.00E+00	0	0	0	0	0	0	958.4	0	0.000

## Part 2: Henry's Law

According to Henry's Law, the partial pressure of a gas above a liquid is directly proportional to the amount of gas that dissolves in the liquid at constant temperature.

$$p = k_H c$$

In this equation, the partial pressure of the gas above the liquid, and the concentration of the dissolved gas in the solution are denoted as  $p$  and  $c$ , respectively. The Henry's Law coefficient,  $k_H$ , is a value that depends on the solute, the solvent, and temperature.

An equation from Tromans (1998) was being used to determine the temperature-dependent Henry's Law coefficient for oxygen where T is the temperature in Kelvin [114]. This k value has a unit of mol/L·bar. The value of the inverse (unit L·bar/mol) was used in the solubility calculation shown in this report.

$$k = \exp \left\{ \frac{0.046T^2 + 203.35T \ln(T/298) - (299.378 + 0.092T)(T - 298) - 20.591 \times 10^3}{(8.3144)T} \right\}$$

The values for the vapor pressure of water at different temperatures were obtained from Perry's Chemical Engineering Handbook.

The total pressure of the system was set to 1 bar. Since the total system was assumed to consist of only water and oxygen, therefore the partial pressure of oxygen was calculated by deducting the vapor pressure of water from the total pressure

$$p_{O_2} = p_{total} - p_{water}$$

The resulting concentration of oxygen (in mol/L) was converted to units of solubility (g/mol). The results are shown in the following table.

Table E2: Results of solubility calculation using Henry's Law.

Temperature		pWater	pO2	kH (T) O2	O2 conc	
°C	K	bar	bar	L.bar/mol	mol/L	mg/L
25	298.15	0.031675	0.968325	783.9223	0.001235	39.52592
30	303.15	0.042432	0.957568	847.0861	0.00113	36.17227
35	308.15	0.056233	0.943767	907.898	0.00104	33.26299
40	313.15	0.073765	0.926235	965.6433	0.000959	30.6929
50	323.15	0.123347	0.876653	1069.483	0.00082	26.22936
60	333.15	0.199173	0.800827	1154.63	0.000694	22.19369
70	343.15	0.3116	0.6884	1218.654	0.000565	18.07566
80	353.15	0.473467	0.526533	1260.623	0.000418	13.36517
90	363.15	0.701013	0.298987	1280.914	0.000233	7.469054
100	373.15	1.013333	0	1280.948	0	0

### Discussion and Summary

Predicted value of oxygen solubility in water using two different methods was presented in this report. Both methods have given comparable values of solubility. The solubility of 1 bar pure oxygen in water at 25°C is 40 mg/L. Values of oxygen solubility that are commonly published are for water that is in contact with air. Since air is consist of 20% oxygen, therefore 40 mg/L multiplied by 0.2 will result in oxygen solubility of 8 mg/L of water.

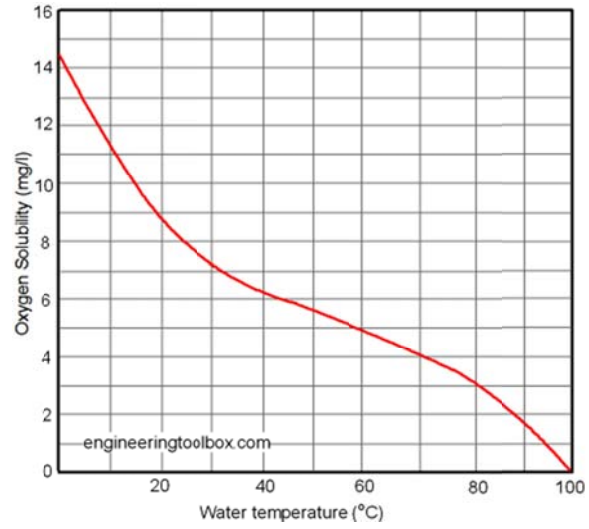


Figure E2. Source: engineeringtoolbox.com [2]

## APPENDIX G: SAMPLE CALCULATION FOR PITTING RATIO DETERMINATION

Example: At 80°C, 90 bar CO<sub>2</sub>, 48 hours, 1000 rpm

Weight loss corrosion rate, WL CR = 23.5 mm/year

Maximum pit depth (via profilometry) = 93 μm

Pit penetration rate, PPR,

$$PPR = \frac{0.093 \text{ mm}}{48 \text{ hour}} \times \frac{24 \text{ h}}{1 \text{ day}} \times \frac{365 \text{ day}}{1 \text{ year}} = 17 \text{ mm/year}$$

Pitting ratio, PR,

$$PR = \frac{PPR}{WL CR} = \frac{17}{23.5} = 0.7$$

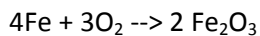
Therefore it is not prone to localized corrosion.

APPENDIX H: DETERMINATION OF O<sub>2</sub> CONSUMPTION FROM WEIGHT LOSS  
OF STEEL

**Calculation for complete conversion of Fe to Fe<sub>2</sub>O<sub>3</sub>**

Mass of Fe before =	2.4397 g =	0.043687 mole Fe
Mass of Fe after =	2.2819 g =	0.040861 mole Fe
Mass of Fe consumed =	0.1578 g =	0.002826 mole Fe

Stoichiometrically, 4 mols of Fe reacts with 3 mols of O<sub>2</sub> to form 2 mols of Fe<sub>2</sub>O<sub>3</sub>



Therefore,

Moles of Fe =		0.00283
Moles of O <sub>2</sub> =		0.00212
Moles of Fe <sub>2</sub> O <sub>3</sub>		0.00141

(This is the amount of O<sub>2</sub> consumed).

How much O<sub>2</sub> is in the system at this temperature?

T =	80	°C =	353.15	K
pO <sub>2</sub> =	3.75	bar		
kO <sub>2</sub> =	0.0007933	mol/L.bar		
cO <sub>2</sub> =	0.0030	mol/L		

Amount of O<sub>2</sub> left in the autoclave = **0.0009 moles**

Therefore the amount of O<sub>2</sub> is in excess to completely convert Fe to Fe<sub>2</sub>O<sub>3</sub>.

This calculation assumes the steel is not involved with the reaction with CO<sub>2</sub> to form FeCO<sub>3</sub>.



**OHIO**  
UNIVERSITY

Thesis and Dissertation Services